Lattice Boltzmann Method Based Framework for Simulating
Physico-Chemical Processes in Heterogeneous Porous Media
and Its Application to Cement Paste

Ravi Patel

UNIVERSITEIT
GENT

Supervisors

Prof. Geert De Schutter
Faculty of Engineering and Architecture - Ghent University

Prof. Klaas Van Breugel
Faculty of Civil Engineering & Geosciences - Delft University of Technology

Mentors

Dr. Janez Perko
Institute of Health, Environment and Safety - Belgian Nuclear Research Centre (SCK•CEN)

Dr. Diederik Jacques
Institute of Health, Environment and Safety - Belgian Nuclear Research Centre (SCK•CEN)

Doctoral committee

Prof. Luc Taerwe
Ghent university, Belgium
(*Chairman*)

Prof. Guang Ye
Delft University of Technology, Netherlands
(Secretary)

Prof. Geert De Schutter
Ghent University, Belgium
(*supervisor*)

Prof. Klaas Van Breugel
Delft University of Technology, Netherlands
(*supervisor*)

Dr. Janez Perko
Belgian Nuclear Research Centre, Belgium

Prof. Amir Raoof
University of Utrecht, Netherlands

Prof. Patrick Dangla
Université Paris-Est, France

Prof. Veerle Cnudde
Ghent University, Belgium

Last stanza of The Road Not Taken

"I shall be telling this with a sigh

Somewhere ages and ages hence:

Two roads diverged in a wood, and I —

I took the one less traveled by,

And that has made all the difference."

– Robert Frost

Summary

Concrete is one of the most widely used building materials and because of its durable nature has also been used for structures where very long service life plays an important role. For example, safety of near-surface radioactive waste disposal systems relies largely on cementitious components. In order to understand the performance of such a system it is essential to understand how the properties of concrete change over a very long period of time. This is referred to as the *ageing of concrete.*

Concrete undergoes weathering in service environment due to varieties of physico-chemo-mechanical processes, which change its physical structure. Slow chemical degradation processes such as calcium leaching alters the cement matrix mineralogy (due to dissolution of mineral phases) and consequently changes its transport and mechanical properties. These processes are often accelerated for experimental studies. As a result only limited amount of information exists concerning the influence of these processes on microstructure and properties of concrete under environmental conditions. To bridge this gap and to gain better insight into the material behaviour, it is of great use to develop a computational simulation suite, which can simulate the changes in the microstructures due to chemical degradation processes and is able to determine properties due to these changes. This thesis presents the development of such a tool and demonstrates its application to predict transport property (diffusivity) of cement paste and to simulate changes in microstructure due to calcium leaching.

The specific goals of this thesis are—

- To develop a numerical framework to simulate the changes in microstructure of cement paste due to reactive transport processes and to verify this framework through numerical benchmarks

- To develop the description of C-S-H diffusivity based on morphological parameters and to highlight contribution of different C-S-H pore spaces to the diffusivity of

hardened cement paste.

- To demonstrate the capability of the developed overall framework to from given cement paste microstructure

- To develop reactive transport model and apply it to calcium leaching in hardened cement paste

The proposed framework is based on the lattice Boltzmann (LB) method. The choice for this method lies in its advantages such as an explicit algorithm with inherent parallelism and simplistic application of zero flux boundary condition through a bounce-back rule on an arbitrary geometry, which allows for easy handling of geometry update due to dissolution or precipitation. The framework has been implemented in a newly developed simulation tool called *Yantra* (in Sanskrit means a tool or a device).

In first part of the thesis, two existing LB schemes viz., single relaxation time (SRT) and two relaxation time (TRT) method for mass transport at the pore-scale and multilevel porous media have been analysed. A new generalized local approach to implement general boundary conditions for solute transport has been developed. This approach is second-order convergent and outperforms existing methods to implement boundary conditions in the lattice Boltzmann method. Further, a new diffusion velocity SRT scheme has been developed that allows for fixing the relaxation parameter to a value that best suites the stability and accuracy with a flexibility of allowing for both variability of time step and spatial heterogeneity of diffusion coefficients. This approach has been further extended to simulate mass transport in a multi-level porous media. An adaptive relaxation scheme has been developed and applied for LB method to effectively adapt time stepping. The change in relaxation parameter is controlled such that the relative errors are kept below certain threshold value. This scheme is best suited for TRT method where changing of the relaxation parameters does not induce additional errors.

Further, a LB scheme for simulating multi-component reactive transport has been developed. Unlike existing approaches where heterogeneous reactions at the solid-fluid interface are treated as flux boundary, an alternative approach developed in this work treats heterogeneous reactions as pseudo-homogeneous reactions. Thus the heterogeneous reactions are simply treated as an additional source/sink term at the node next to the solid boundary, in turn allowing for uniform treatment of both heterogeneous and homogeneous reactions. This approach, thus enables coupling of LB schemes with any geochemical solver which makes it highly versatile. An approach to couple the LB schemes with the geochemical code *PHREEQC* is proposed. Each of the new proposed approaches have been verify for their numerical correctness through numerous benchmarks.

A series of simple examples highlighting the influence of parameters such as solution composition, surface area and location of mineral phases and pore network characteristics on dissolution of portlandite were carried out. Under diffusive transport conditions and

an assumption of thermodynamic equilibrium, it has been shown that different initial pH conditions do not influence the overall reaction kinetics (i.e. for different pH conditions equilibrium is achieved at same time). This is due to the fact that the dissolution process is diffusion-controlled. However lower pH values increase the amount of portlandite dissolved resulting in smaller grains at the end of simulation. Further, it was found that spatial distribution of the mineral grains is more important than their surface area. Different spatial distributions of grains may cause faster local equilibrium in certain parts of the domain resulting and thus inhibiting the further dissolution in that region. Finally, in order to study the influence of pore network on portlandite dissolution, four cases consisting of random porous media with portlandite as reacting phase are presented. All four cases have the same fraction of portlandite phase but differ in particle sizes, total porosity and tortuosity by introducing inert material. The results showed that characteristics of porous media affecting ion transport such as tortuosity and porosity have a more pronounced effect on dissolution compared to particle size and surface area.

The second part of the thesis discusses the application of the proposed framework to (i) computation of diffusivity from virtual microstructure of cement paste, and (ii) simulation of calcium leaching through cement paste microstructure. In order to better explain the diffusion process through cement paste, a new two-scale model for C-S-H diffusivity based on effective media theory has been proposed. This model allows separating the contribution from the different types of pores in C-S-H. The above explained LB framework, the two-scale model for C-S-H and microstructures generated from integrated kinetic models viz., HYMOSTRUC and CEMHYD3D provide a framework to explore the role of morphology and different pore spaces of cement paste on diffusivity. It was found that the diffusivity obtained from HYMOSTRUC generated microstructures was higher compared to that from CEMHYD3D generated microstructures and experimental data. The reason for this difference is a very low percolation threshold for HYMOSTRUC compared to CEMHYD3D. Further the role of low density (LD) C-S-H porosity and high density (HD) C-S-H porosity has been identified. It has been shown that diffusion of tracers, such as dissolved gases (e.g. oxygen, helium) and HTO measured in through-diffusion experiments, occurs only through LD C-S-H pores and that HD C-S-H pores does not contribute to transport. However, for electrical resistivity measurements, all gel pores contribute to the diffusion process. Due to this reason the relative diffusivity measured by electric resistivity as reported by different researchers is higher than through-diffusion experiments.

A simplified reactive transport model to simulate calcium leaching (from portlandite and C-S-H phase) through the microstructure of cement paste has been developed using the proposed framework. In this model, transport of Ca and Si species is carried out unlike a more common approach wherein only transport of Ca is considered. It was found that it is essential to consider Si transport to obtain correct profiles in the inlet of the domain where considerable leaching has occurred. The equilibrium curves were derived

from a geochemical model (implemented in *PHREEQC*) and implemented as a look-up table. A comparison with calculation carried out with reactive transport model in which reactions are computed using geochemical reaction approach reveals that the simplified model provides the same level of accuracy. The simplified model however reduces the computational time from days to few minutes. This in turn has made the simulation of the reactive transport processes occurring in the microstructure of cement paste due to calcium leaching (resulting in dissolution of portlandite and decalcification of C-S-H) feasible.

Keywords: lattice Boltzmann method, pore scale reactive transport modelling, reactive transport in multilevel porous media, microstructure modelling, diffusion in cement paste, calcium leaching

Samenvatting

Beton is één van de meest gebruikte bouwmaterialen. Dankzij het duurzaam karakter van beton wordt het ook gebruikt voor constructies waarvoor een zeer grote gebruiksduur een belangrijke rol speelt. Zo steunt de veiligheid van bergingsinstallaties voor radioactief afval in grote mate op cementgebonden componenten. Teneinde de prestaties van dergelijke systemen goed te begrijpen, is het essentieel om te begrijpen hoe betoneigenschappen veranderen over een lange tijdsperiode. Hiernaar wordt verwezen met verouderen van beton (*ageing of concrete*).

Beton ondergaat verwering in de gebruiksomgeving ten gevolge van een verscheidenheid aan fysico-chemo-mechanische processen. Hierdoor wordt de fysische structuur van het beton gewijzigd. Trage chemische aantastingsprocessen zoals kalkuitloging wijzigen de mineralogie van de cementmatrix (door het oplossen van mineralen), waardoor ook transporteigenschappen en mechanische eigenschappen gewijzigd worden. Chemische aantastingsprocessen in natuurlijke omgeving zijn meestal zeer traag, en worden in experimentele studies doorgaans artificieel versneld. Hierdoor is slechts een beperkte hoeveelheid informatie beschikbaar betreffende de invloed van de aantastingsprocessen op de microstructuur en op de eigenschappen van beton in natuurlijke omgeving. Om deze kenniskloof te overbruggen, en om een beter inzicht te krijgen in het materiaalgedrag, is het zeer nuttig om een numerieke simulatieomgeving (*computational simulation suite*) te ontwikkelen. Deze simulatieomgeving maakt het mogelijk wijzigingen in de microstructuur te simuleren ten gevolge van chemische aantastingsmechanismen, en laat toe om de gewijzigde eigenschappen te bepalen. Deze thesis beschrijft de ontwikkeling van een dergelijke simulatieomgeving, met de mogelijkheid om microstructurele wijzigingen in cementpasta door reactief transport te simuleren, en de gewijzigde transporteigenschappen (diffusiviteit) te voorspellen, toegepast op de problematiek van kalkuitloging.

Specifiek worden in de thesis volgende doelstellingen beoogd:

- De ontwikkeling van een numerieke omgeving voor de simulatie van wijzigingen in

de microstructuur van cementpasta ten gevolge van reactieve transportprocessen, en de validatie hiervan door middel van numerieke benchmarks

- De ontwikkeling van een beschrijvend model voor de diffusiviteit van C-S-H gebaseerd op morfologische parameters, en het toelichten van de bijdrage van de verschillende porositeiten in C-S-H op de diffusiviteit van cementpasta

- Het aantonen van de mogelijkheid van de ontwikkelde simulatieomgeving om diffusiviteitswaarden te bekomen voor een bepaalde microstructuur

- De ontwikkeling van reactieve transportmodellen en de toepassing hiervan op kalkuitloging in verharde cementpasta

De voorgestelde simulatieomgeving is gebaseerd op de lattice Boltzmann (LB) methode. De keuze van deze methode is gebaseerd op de voordelen zoals een expliciet algoritme met inherent parallellisme en eenvoudige toepassing van randvoorwaarden zonder flux door middel van een terugkaatsregel op een arbitraire geometrie, wat een eenvoudige aanpassing toelaat van de geometrie onder invloed van dissolutie of precipitatie. De simulatiemethode werd geïmplementeerd in een nieuw ontwikkelde simulatieomgeving genaamd *Yantra* (Sanskriet voor hulpmiddel of toestel).

Twee bestaande LB schemas voor massatransport op porinschaal en voor multiscale poreuze media werden geanalyseerd in deze studie, namelijk *single relaxation time* (SRT) and *two relaxation time* (TRT) method. Een nieuwe veralgemeende lokale benadering werd ontwikkeld voor de implementatie van algemene randvoorwaarden voor vloeistoftransport. Deze benadering is tweede-orde convergent, en presteert beter dan bestaande methoden voor de beschrijving van randvoorwaarden in de LB methode. Bovendien werd een nieuw SRT schema ontwikkeld voor de diffusiesnelheid dat toelaat om de relaxatieparameter vast te zetten op een waarde die best past voor de stabiliteit en de nauwkeurigheid, met de flexibiliteit om een variatie toe te laten zowel in de tijdsstap als in de ruimtelijke heterogeniteit van de diffusiecoëfficiënten. Deze aanpak werd verder uitgebreid voor de simulatie van massatransport in multiscale poreuze materialen. Een aanpassend relaxatieschema werd ontwikkeld en toegepast voor de LB simulaties voor een efficiënte aanpassing van de tijdsstappen. De wijziging in relaxatieparameter wordt dermate gecontroleerd dat de relatieve fouten beperkt worden. Dit schema is het meest aangewezen voor de TRT methode, waarin wijzigingen van de relaxatieparameters geen bijkomende fouten induceren.

Een LB schema werd ook ontwikkeld voor de simulatie van reactief transport met meerdere componenten. Een alternatieve aanpak van de heterogene reacties die optreden in het contactvlak tussen vaste stof en vloeistof werd voorgesteld. In tegenstelling tot bestaande methoden waarbij de heterogene reacties behandeld worden als een flux-randvoorwaarde,

behandelt de nieuwe methode de heterogene reacties als pseudo-homogene reacties. Hetero-gene reacties worden op deze wijze eenvoudig behandeld als een bijkomende bronterm in de knoop naast het vaste oppervlak, wat een uniforme behandeling van zowel heterogene als homogene reacties toelaat. Deze aanpak laat toe om LB schemas te koppelen met een externe geo-chemische module, wat het zeer veelzijdig maakt. De thesis stelt een aanpak voor om de LB schemas te koppelen met het geo-chemisch model *PHREEQC*. Alle nieuw voorgestelde methoden werden gevalideerd wat betreft numerieke correctheid door middel van een verscheidenheid aan benchmarks.

Een reeks eenvoudige voorbeelden werd nagerekend, waarbij de invloed van verschillende parameters op de dissolutie van portlandiet toegelicht werd, zoals de samenstelling van de oplossing, de specifieke oppervlakte en locatie van de mineralen, en de karakteristieken van het porinnetwerk. Bij diffusieve tranportcondities en mits het veronderstellen van thermodynamisch evenwicht werd aangetoond dat de globale reactiesnelheid niet beïnvloed wordt door de initiële pH-condities. Voor verschillende pH-condities werd evenwicht bereikt na eenzelfde tijdsperiode. Dit komt door het feit dat het dissolutieproces gecontroleerd wordt door diffusie. Echter, lagere pH-waarden veroorzaken een hoger gehalte aan opgelost portlandiet, wat resulteert in kleinere korrels op het einde van de simulatie. Verder werd vastgesteld dat de ruimtelijke distributie van de minerale korrels belangrijker is dan de specifieke oppervlakte. Verschillende ruimtelijke schikkingen van de korrels kunnen leiden tot een sneller lokaal evenwicht in bepaalde zones van het domein, wat de lokale dissolutie in deze zone verhindert. Teneinde de invloed van het porinnetwerk op de dissolutie van portlandiet te bestuderen, werden finaal vier gevallen beschouwd van willekeurige poreuze media met portlandiet al reactieve fase. De vier gevallen hebben eenzelfde fractie portlandiet, doch verschillen in deeltjesgrootte, totale porositeit en tortuositeit door het invoegen van een inert materiaal. De resultaten tonen aan dat tortuositeit en porositeit, twee parameters die de poreuze structuur karakteriseren, een meer belangrijke invloed hebben op de dissolutie in vergelijking met deeltjesgrootte en specifieke oppervlakte.

Het tweede deel van de thesis bespreekt de toepassing van de ontwikkelde simulatieomgeving op (i) de berekening van de diffusiviteit op basis van een virtuele microstructuur, en (ii) de simulatie van kalkuitloging in verharde cementpasta. Teneinde het diffusieproces in verharde cementpasta beter te begrijpen, werd voor de diffusiviteit van C-S-H een nieuw model met dubbele schaal voorgesteld, gebaseerd op de theorie van effectieve media. Dit model laat toe een onderscheid te maken tussen de bijdrage van de verschillende types van porin in C-S-H. De hoger beschreven LB methode, het C-S-H model met dubbele schaal, en gesimuleerde microstructuren door middel van kinetische modellen zoals HYMOSTRUC en CEMHYD3D, voorzien een omgeving voor de exploratie van de rol van de morfologie en de verschillende porinruimtes in cementpasta op de resulterende diffusiviteit. Er werd vastgesteld dat HYMOSTRUC steeds leidt tot hogere waarden in vergelijking met CEMHYD3D en experimentele data. De reden voor dit verschil is de

zeer lage percolatiedrempel voor HYMOSTRUC in vergelijking met CEMHYD3D. Voorts werd de rol van de porositeit van LD C-S-H en van HD C-S-H geïdentificeerd. Er werd aangetoond dat diffusie van tracers zoals opgeloste gassen (bv. zuurstof, helium) en HTO enkel gebeurt door poriën in LD C-S-H, terwijl de poriën van HD C-S-H niet bijdragen tot het transport. Echter, bij elektrische resistiviteitsmetingen dragen alle gelporiën bij tot het transport. Hierdoor ligt de relatieve diffusiviteit, gemeten door middel van elektrische resistiviteitsmetingen zoals gerapporteerd door verschillende onderzoekers, hoger dan de waarden bepaald door middel van diffusieproeven.

Door gebruik te maken van het de voorgestelde simulatieomgeving, werd een vereenvoudigd reactief-transportmodel ontwikkeld voor de simulatie van kalkuitloging (van portlandiet en C-S-H) uit de microstructuur van verharde cementpasta. In dit model wordt het transport van Ca en Si beschouwd, in tegenstelling tot doorgaans gebruikte modellen waarin enkel het transport van Ca beschouwd wordt. Er werd vastgesteld dat het beschouwen van het transport van Si essentieel is voor het bekomen van correcte profielen in het eerste deel van het domein waarin belangrijke uitloging opgetreden is. De evenwichtscurven werden bepaald met het geo-chemisch model (geïmplementeerd in *PHREEQC*), en werden gemplementeerd in tabelvorm. Een vergelijking met berekeningen met modellen waarbij de reacties begroot worden door middel van geo-chemische thermodynamica wijst uit dat het vereenvoudigd model een vergelijkbare nauwkeurigheid heeft. Het vereenvoudigd model vermindert echter de rekentijd van dagen naar minuten. Dit biedt extra mogelijkheden voor de simulatie van reactief transport in de microstructuur van verharde cementpasta onder invloed van kalkuitloging (resulterend in het oplossen van portlandiet en de decalcificatie van C-S-H).

Keywords: lattice Boltzmann methode, modelleren, reactief transport, poriënschaal, multiscale, microstructuur, diffusie, cementpasta, kalkuitloging

Acknowledgements

on experimental material science of concrete. I would also like to thank permanent members of my lunch group, Luca Fiorito, Delphine Durce and Dario Bisogni and other occasional members for their enjoyable lunch time debates and talks. I would like to thank the members of the "Boeretang kingdom" for making first two year of my stay in SCK•CEN dorms memorable.

Finally, I would like to thank my Grandmother Veenaben Patel, my Parents Ajitbhai Patel and kalavatiben Patel, my siblings Hiral Patel and Rashesh Patel and my brother-in-law Jagdish patel and his mother Daxa Patel for their constant support, patience, love and encouragement during the course of this work. Last but not least I would like to thank my fiancée Rachna and her family for their love, support, encouragement and most importantly being patient during the course of this work. Rachna I cant wait to start writing the new chapter of my life with you.

This thesis is dedicated to my family and teachers for their love and the things I learnt from them which has molded me to who I am today.

<div align="right">

Ravi Patel

February 2016

Mol, Belgium

</div>

Table of Contents

Appendix   186

A *Yantra: A lattice Boltzmann method based tool for multi-physics simulations in hetergoenous porous media*   187

B From Boltzmann equation to lattice Boltzmann equation   191

C Equilibrium distribution function in lattice Boltzmann method   193

D Multiscale Chapman-Enskog expansion   195

E Quasi stationary assumption for heterogeneous reactions   197

F Summary of mathematical expressions for different effective diffusivity models for cement paste   199

G A overview on effective media theories   205

H Extension of SciPy least square minimization method to account for bounds   209

I PID relaxation scheme for LB methods   213

References   217

List of Figures

List of Tables

Introduction

1.1 Motivation

This thesis is inspired from the very necessity to understand how the concrete would age
in a near surface Belgian nuclear waste disposal system (category A waste disposal facility
of Belgium is abbreviated as cAt). The major cementitious components of cAt are shown
in Fig. 1.1. These include module roof, walls, monoliths, base and sand-cement mixture
embankment, with their foreseen safety functions. The phenomenological understanding
of evolution of such a system is required for a very long period (around 1000 years which
is approximately 14 times average life expectancy of a human being). Therefore, the study
of aging of concrete becomes essential to gain an understanding of its performance.

Moreover, due to the high carbon penalty associated with cement production and its use,
there is an ongoing quest of developing sustainable concrete (concrete with less cement
content or no cement content!) and a growing need to improve the service life (up to 100
years) of concrete structures. Furthermore, sustainability and durability go hand in hand
and for a new concrete material to be sustainable it has to be durable. De Schutter [16] in
a recent publication states—

*"The erroneous idea saying that 'when it is strong enough, it is durable enough', is getting
more and more risk-full when considering alternative 'green' binder systems. While tra-
ditionally, strength is first and most important concrete property to be considered, a new
approach should be followed in which 'strength follows durability'"*.

Hence, the *"gerontology of concrete"*[1] becomes an increasingly important subject of study.

---

[1]Gerontology is the termed coined by lya I. Mechnikov in 1903 which refers to the study of the social,
psychological, cognitive, and biological aspects of aging. Gerontology of concrete thus refers to study of
varieties of aspects of ageing of concrete.
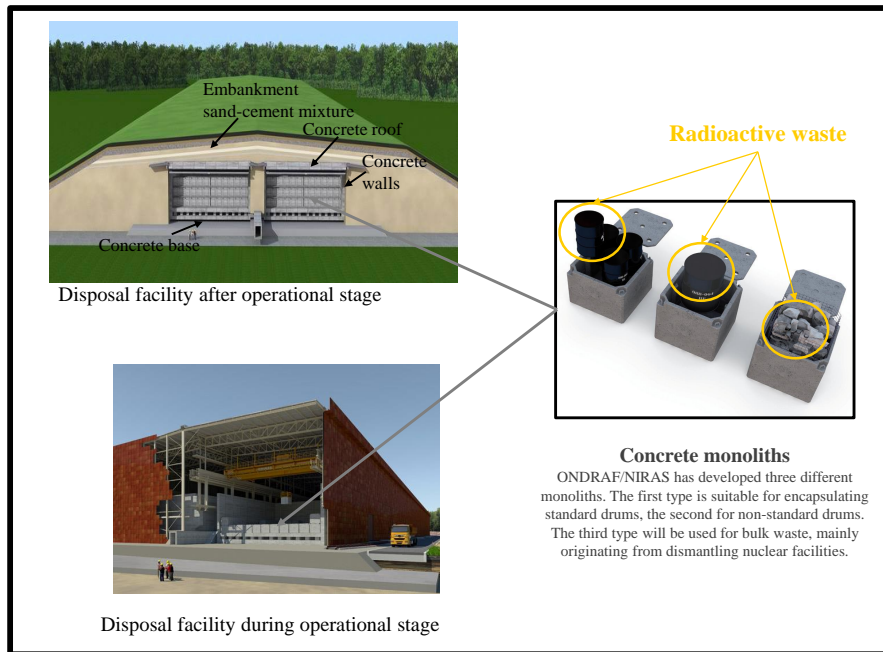
Figure 1.1: Near surface Belgian nuclear waste system (cAt). Figure adapted cAt website and NIRAS' report[1–3]

The ageing of concrete occurs due to wide range of physical-chemical-mechanical processes occurring during the service life. Of concern are the processes that deteriorate concrete performance. These processes can be broadly classified into two categories viz. physical causes or chemical causes [4] as shown in Fig. 1.2. The physical causes are further divided into two categories, surface wear or loss of mass due to abrasion, erosion and cavitation; and cracking due to normal temperature, humidity gradients, crystallization of salts in pores, structural loading, and exposure to temperature extremes such as freezing or fire. Similarly, the chemical causes are grouped into three categories, hydrolysis of the cement components by soft water; cation exchange reactions between aggressive fluids and cement paste; and reactions leading to the formation of expansive products such as in the case of sulfate attack, alkali-aggregate reaction, and corrosion of reinforcing steel in concrete. It should be noted that this classification is just for convenience and in actual conditions these processes are coupled (e.g. cracking can increase the flow of soft water and thus increase the leaching rate, and leaching further weakens concrete and makes it more susceptible to cracking).

1.2 Need for multi-scale models to simulate ageing of concrete

Designing experiments replicating the exact sequence of physical-chemical-mechanical events occurring during the ageing of concrete and studying all the aspects of mechanisms

Degradation of concrete

Physical causes

- **Surface wear**
  - Abrasion
  - Erosion
  - cavitation
- **Cracking**
  - **Volume change due to**
    1. Normal temperature and humidity gradient
    2. Crystallization pressure of salts in pores
  - **Structural loading**
    1. Overloading and Impact
    2. Cyclic loading
  - **Exposure to temperature extremes**
    1. Freeze – thaw cycles
    2. Fire

Chemical causes

- Exchange reactions between aggressive fluid and components of cement paste
- Reaction involving hydrolysis and leaching of the components of cement paste
- Reactions involving formation of expansive products

Chemical causes

B — Exchange reactions between aggressive fluid and components of HCP

- **1** Removal of Ca^{++} ions as soluble products
- **2** Removal of Ca^{++} ions as non-expansive insoluble products
- **3** Substitution reactions replacing Ca^{++} in C-S-H

A — Reaction involving hydrolysis and leaching of the components of HCP

- Increase in porosity and permeability

C — Reaction involving formation of expansive products

- Increase in internal stress

- Loss of alkalinity
- Loss of mass
- Increase in deterioration processes
- Loss of strength and rigidity
- Cracking, spalling, popouts
- Deformation

Detrimental of chemical reactions

A: calcium leaching by soft water
B1: carbonation, reactions with the solutions of ammonium chloride and ammonium sulphate
B2: Reactions with humic, hydrofluoric, or phosphoric acid
B3: Reactions with magnesium salts
C: Sulphur attack, alkali - aggregate reactions

Figure 1.2: Mechanisms causing deterioration of concrete (adapted from [4])

causing deterioration is a daunting task. Therefore *reductionism*[2] is often applied while studying deterioration of concrete both experimentally and numerically. Development of experimental procedure for coupled processes is not always possible. However, numerical models coupling different processes are relatively easy to develop. Moreover, many of the deterioration mechanism are slow in nature (e.g. the progression of leaching under natural condition is only upto few millimeters in hundred years! [17, 18]) and therefore often the degradation processes are experimentally studied under accelerated conditions. Thus, models form a crucial part in *gerontology* of concrete and can help to link the experimental observations with reality.

Macro
Scale of interest

Concrete/mortar is treated as a homogenous material.

Meso
Mortar, Concrete

Morphological feature of concrete/mortar consists of cement paste, sand, aggregate and Interfacial Transition Zone (ITZ). Additionally thermal cracks formed during hydration and air voids can exist at this level.

Micro
Cement paste

Cement paste consists of amorphous C-S-H phase; crystalline hydration products such as portlandite, AFm phases (most common AFm phases are mono sulphate hydrates), AFt phases (most common AFt phase is ettringite), hydrogarnet; clinkers and capillary pores. The micro cracks formed during hydration can also exist at this level.

Nano
C-S-H

C-S-H phase consist of solid phase and gel porosity. There exist two types of C-S-H viz., low density C-S-H formed during earlier stage of hydration and high density C-S-H formed during later stage of hydration

Figure 1.3: Multi-scale representation of concrete

To better capture the behaviour at macroscopic scale due to ageing and its impact on mechanical and transport properties, it is essential that the model accounts for changes in morphology of concrete and able to simulate multi-physics processes. However, the morphology of concrete presents a complex multi-scale nature as shown in Fig. 1.3 and changes occur along each of this spatial scale during ageing. C-S-H forms the lowest spatial scale (nano scale) of concrete. There is ample evidence to presume that C-S-H exists in two different forms with two distinct volume fractions viz., low density C-S-H (LD C-S-H) formed during early stage of hydration and (HD C-S-H) formed during later stage of hydration in the pore spaces confined by existing C-S-H [15, 19–23]. The porosity of the C-S-H matrix is commonly referred to as gel porosity. The gel pores can be further

---

[2]reductionism here refers to studying specific mechanism of deterioration and its influence on specific set of physical or chemical or mechanical property of concrete

classified into interlayer pores, small gel pores (inter globule pores) and large gel mesopores (inter LD pores) [22]. At micro scale concrete is represented by cement paste which consists of C-S-H matrix, unhydrated clinker phases, crystalline hydration products such as portlandite, AFm phases (most common AFm phases are mono sulphate hydrates), AFt phases (most common AFt phase is ettringite), hydrogarnet; and capillary pores. Additionally, at the micro scale, there might be micro cracks formed during hydration. The meso scale refers to concrete/mortar that is composed of cement paste, aggregates and interface between cement paste and aggregate the interface transition zone (ITZ). At this level additionally large air voids and cracks formed during hydration can exist. Thus, an accurate evaluation of concrete behavior due to aging requires the use of multi-scale and multi-physics models.

The need for multi-scale models for concrete has been long realized in cement science. Models have been proposed in order to provide the morphological description of concrete at each of these scales during hydration (see for instance [24–29]). These models are continuously being improved. Initiatives have also been undertaken to develop a multi-scale framework to transfer parameters from lower scale to higher scales to obtain physical and mechanical properties from these models (see for instance [29–33]).

There is still scope for improvement in these models in terms of providing reliable inputs for these models (e.g. diffusivity of C-S-H). Secondly, there is a need to extend or develop new multi-scale, multi-physics approaches for modeling ageing of concrete. The need for such approaches is echoed in the concluding remarks of Ref. [34] by Prof. Klaas Van Bruegel —

"Simulation models, based on sound material concepts, are of crucial importance for detecting weak links in the quality chain. Furthermore, multi-scale and multidisciplinary models, with a strong predictive power, will be essential for reliable service life predictions."

Furthermore, development of multi-scale, multi-physics strategies would in turn require development of models/tools to simulate changes due to aging in a wide range of length scales (i.e., nano, micro and meso scale).

1.3 Research Objectives

Research objectives of this thesis are set based on the need to develop multi-scale and multi-physics models in the field of *gerontology* of concrete. The specific objectives of this thesis are defined as:

- To develop a numerical framework to simulate changes in morphology of cement paste due to chemical degradation.

- Validate the numerical framework against several benchmark problems.

- To develop a more reliable approach to define transport parameters of C-S-H phase.

- Demonstrating the usefulness of the developed framework by simulating calcium leaching process.

1.4 Scope and limitations

The developed numerical framework considers only the reactive transport processes and its application is limited to the ordinary Portland cement paste (micro scale of concrete) in this study. However, the numerical framework developed in this study can be to meso and macro length scales. Further, following modelling simplifications are made in this study

- Cement paste is considered to be fully saturated, which is not usually the case.

- Electro-kinetic effects on ion transport are not considered.

- Chemo-mechanical coupling (e.g., chemical shrinkage of C-S-H due to leaching) is not considered.

- The influence of external temperature variations on chemical transport and reactions is not considered.

1.5 Research strategy

A variety of approaches to model reactive transport processes at the pore-scale[3] exist (e.g. dissolution, precipitation or adsorption) and they involve different numerical schemes such as finite volume method [35], pore network models [36, 37], smooth particle hydrodynamics [38, 39], hybrid approaches coupling different numerical methods[40–43] and lattice Boltzmann methods [44–51]. In this study, lattice Boltzmann (LB) method has been used as numerical framework. LB method presents a explicit algorithm with inherent parallelism and simplistic handling of zero flux boundary condition through a bounce-back rule[4]. Furthermore LB method also has certain advantages compared to other numerical approaches commonly used such as —

- Geometry update (boundary tracking and remeshing) due to dissolution or precipitation in traditional numerical methods (such as finite element and finite volume methods) is time consuming.

- Algorithmic simplicity compared to the other methods

- Better stability and flexibility in time stepping compared to explicit finite difference methods.

---

[3]pore-scale refers to the scale were pores and solids are explicitly resolved. Solids are considered to be non-diffusive at the pore-scale

[4]See chapter 2 for details

- A three dimensional voxelized pore structure can be directly used for LBM whereas for pore network method, an equivalent network representation of the pore structure needs to be extracted.

Applicability of LBM has been successfully demonstrated for dissolution and precipitation reactions [44–46, 49, 50]. This formulation has been further extended to incorporate ion-exchange reactions [51]. However, in these approaches the heterogeneous reactions at mineral grain boundary are conceptualized as as fluxes normal to the solid phase boundary, which makes it difficult to separate the transport and reaction calculations and consequent coupling of external geochemical codes. As a result, the applicability of LB method is yet limited to fixed chemical systems. This shortcoming has also been highlighted in [35] — *"Lattice Boltzmann models are also efficient and scalable for flow and transport problems, but they do not typically incorporate the wide range of geochemical reactions available in many geochemical models."*

To eliminate this shortcoming, an alternate approach has been developed in this thesis which enables coupling of LBM with external geochemical codes. Secondly, in case of cement paste two scales co-exist. While C-S-H acts as a continuum media, crystalline phases and clinker act as non diffusive phases and pore spaces are explicitly resolved making a cement paste a multi-level porous media [5]. Hence, a LBM for multi-level reactive transport has also been developed in this thesis. The developed methods have been implemented in a newly developed simulation tool called *Yantra* (in Sanskrit means a tool or a device). The design philosophy and features of *Yantra* are detailed in Appendix A. The developed framework has been applied to analyse the diffusivity of cement paste microstructures and has been further adapted to simulate the calcium leaching of cement paste. The diffusivity of C-S-H is determined by applying effective media theory. This approach has been further extended to determine changes in diffusivity of C-S-H due to leaching.

The input microstructures of the hydrated cement paste needed for these simulations are obtained using the existing *integrated kinetic models*[6]. Several integrated kinetic models exist, and have been reviewed in [28, 53]. These models simulate the microstructure formation of cement paste during hydration using some basic inputs such as initial phase composition of cement particles (clinkers), water to cement ratio, partial size distribution or surface area of clinkers, and kinetic rate parameters which have been calibrated using experimental data. These models can be divided into vector based models and lattice

---

[5]The term multi-level porous media is explained in Chapter 3.

[6]The term integrated kinetic models has been coined by Van Breugel [52] to refer to hydration models which describe the formation of inter particle contacts and their effect on the rate of reaction explicitly. These models, mostly computer-based simulation models, can be considered as operators, which generate, or have the potential to generate, micro-structural data in a direct way. Such an operator may consist of a set of mathematical formulae or computational procedures for describing (changes in) the state of the spatial distribution of the anhydrous cement, the reaction products, the moisture state, and, if possible, the state of stresses which develop during hydration [28].

based models [53].

In vector based models the cement particles are represented as spheres together with co-ordinates of their centers. The hydration product are grown concentrically to the cement particles. The dissolution of cement particles results in reduction in the radii of clinker and growth of C-S-H layers results in increase of radii of C-S-H layers. The rate of growth of C-S-H and reduction of clinkers is accounted for through a rate law. The redistribution of product phases when growing product phases overlap is also accounted for in such models. Phases such as calcium hydroxide grow spherically from initially defined nuclei. The well-known vector models are HYMOSTRUC [52, 54] and μic [55, 56] (which is a successor to Navi's model [57, 58]).

In lattice based models a 3D cement paste microstructure is digitized on a uniform cubic lattice and each volume element (voxel) is assigned certain material (e.g., water-filled porosity, clinker phase, etc). The two well known lattice based models are CEMHYD3D [59] and HydratiCA [60]. In CEMHYD3D the changes to the microstructure are simulated through a large number of rules that are evaluated locally and depend on the materials involved in the interaction, the temperature and, in some cases, global parameters describing the microstructure such as the water/cement mass ratio or the volume fraction of a phase. These rules are used to mimic the dissolution of solids, diffusion of dissolved species according to a random walk algorithm, and nucleation and growth of hydration products such as portlandite and C-S-H gel. HydratiCA is a reactive transport model based on kinetic cellular automation and it directly simulates transport of ions, dissolution and growth of mineral phases, complexation reactions at surface and nucleation of new phases. In this thesis HYMOSTRUC and CEMHYD3D are used to obtain the input microstructures of hydrated cement paste to cover both classes of cement paste microstructure models. Both HYMOSTRUC and CEMHYD3D are available for download through following links [61, 62] respectively, and almost all input parameters are self-explanatory in both the models. The HYMOSTRUC model used in this thesis is more advanced than the one available on-line and it includes also the nucleation and growth of portlandite. The theoretical background for this version of HYMOSTRUC model can be found in reference [63]

1.6 Summary of significant outcomes

- A new LB scheme (diffusion velocity lattice Boltzmann SRT scheme) has been developed which allows for fixing the relaxation parameter to a value which best suites the stability and accuracy with a flexibility of allowing for both variability of time step and spatial heterogeneity of diffusion coefficients. This approach has been further extended to simulate mass transport in a multi-level porous media.

- A new approach has been developed to implement a generalized transport boundary condition in LB scheme which is local and second order convergent.

- A new PID-controller (proportional, integral, differential) based adaptive relaxation scheme has been developed to accelerate transient LB simulation.

- A new approach has been developed to treat heterogeneous reactions in LB reactive transport schemes. This scheme has an ability to treat both homogeneous and heterogeneous reactions in the same way thus replacing homogeneous and heterogeneous reactions with an equivalent total single source/sink term. This allows for the coupling of LB schemes with the external geochemical codes.

- For the first time a successful coupling of LB schemes with the external geochemical code *PHREEQC* [64] has been demonstrated.

- Extension of LB reactive transport schemes to multi-level porous media has been demonstrated.

- A new two-scale model for C-S-H diffusivity based on effective media theory has been developed. Using this model, developed LB framework for transport and microstructures generated from integrated kinetic models viz., HYMOSTRUC and CEMHYD3D the role of LD C-S-H porosity and HD C-S-H porosity has been identified. It has been shown that for diffusion of tracers such as dissolved gases (e.g. oxygen, helium) and HTO occurs only through LD C-S-H pores and HD C-S-H pores do not contribute to transport. However, for electrical resistivity measurement all gel pores contributes to the diffusion process. Due to this reason, the relative diffusivity measured by electric resistivity techniques reported in literature is higher than through diffusion experiments and electro-migration techniques.

- A simplified reactive transport model to simulate calcium leaching (from portlandite and C-S-H phase) is developed. This model provides the same level of accuracy as the detailed chemical reactions computation using geochemical thermodynamics. The two scale diffusion model for C-S-H has been further extended to account for the leaching. Using this approach for the first time (as per the best of author's knowledge) the reactive transport processes occurring in the microstructure of cement paste due to calcium leaching (resulting in dissolution of portlandite and decalcification of C-S-H) has been simulated.

1.7 Outline of the thesis

The outline of the thesis is schematically depicted in Fig. 1.4. The thesis is divided into two parts. The numerical framework is presented in Part I. In chapter 2, a LB method is

introduced and specific details for solute transport in a pore-scale system are introduced. Two existing LB schemes viz., single relaxation method and two relaxation time method are discussed. A newly developed diffusion velocity LB schemes is also detailed in this chapter. Further, the existing approaches to implement generalized boundary conditions for solute transport are compared and a new local approach to apply general boundary conditions has been presented. In chapter 3, LB schemes to simulate solute transport in multi-level porous media are presented. Two LB schemes to simulate solute transport in multi-level porous media are discussed viz., diffusion velocity LB method and two relaxation time LB method. In Chapter 4 LB schemes for simulating reactive transport are presented. The LB scheme for simulating single mineral dissolution is first presented. Next, the new LB scheme for multi-component reactive transport and coupling of LB schemes with geochemical model *PHREEQC* is presented. Each of these chapters are accompanied with series of benchmarks and examples to demonstrate the validity and applicability of the developed schemes.

In Part II the developed framework is applied to obtain diffusivity from the microstructure, generated from integrated kinetic models, and to simulate microstructural changes due to calcium leaching in the cement paste. In Chapter 5 a critical appraisal of the existing experimental data for cement paste is carried out. Further, a review of approaches to estimate diffusivity and the models to obtain diffusivity from the microstructures is presented. The approaches to estimate diffusivity are further compared with the synthesised experimental data to reveal advantages and disadvantages of these approaches. This chapter thus provides a state of the art and identifies the knowledge gaps in modeling diffusivity of cement paste. In chapter 6, diffusivities are obtained from the microstructures generated CEMHYD3D and HYMOSTRUC models. A new two-scale model for diffusivity of C-S-H based on effective media theory has been presented. The diffusivity for a wide range of experimental data is simulated from the microstructure generated from integrated kinetic models and compared. Chapter 7 presents a review on the current understanding on mechanisms of leaching, its impact on properties of cement paste and both continuum and microstructural models developed for simulating leaching. Finally, in Chapter 8, the developed numerical framework is applied to simulate leaching in cement paste. A simplified approach to account for chemical reactions and the extension of the two-scale diffusivity model for C-S-H, to account for leaching, is presented. Changes on microstructure due to leaching are simulated on ordinary portland cement paste with two different water-cement ratios. Chapter 9 presents a retrospection of the work carried out in this thesis and the overall conclusions. It concludes with a brief discussion on a way forward to extend the present work to address more complex issues in modeling of aging concrete.

Figure 1.4: Oultine of the thesis

Chapter 1: Introduction

Part I: Numerical framework

Chapter 2: Lattice Boltzmann method for solute transport at pore scale

Chapter 3: Lattice Boltzmann method for solute transport in multilevel porous media

Chapter 4: lattice Boltzmann method for reactive transport

Part II: Applications to cement based materials

Literature review relevant to modeling work performed in this thesis

Chapter 5: Critical appraisal of experimental data and models for diffusivity of cement paste

Chapter 6: Determination of effective diffusivity from integrated kinetic models: role of morphology

Chapter 7: Leaching of cement paste: mechanisms, influence on properties and existing modelling approaches

Chapter 8: Modelling changes in microstructure of cement paste under calcium leaching

Chapter 9: Retrospection, Conclusions and Way forward

Part I: Numerical model development

Lattice Boltzmann method for solute transport at pore-scale

The pore-scale in this thesis refers to the explicit representation of the solids and pores spaces as shown in Fig. 2.1. For the definition of the pore-scale used in this thesis solids are considered non-diffusive. Thus diffusion occurs only through pore fluid.
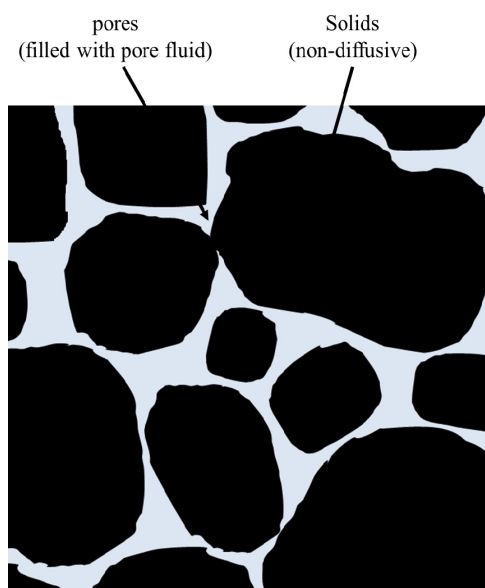
Figure 2.1: A representation of pore-scale system

In this chapter the lattice Boltzmann (LB) method is introduced to solve the governing equation (advection-diffusion equation) for solute transport at pore-scale. The details on governing equation are presented in Chapter 2.1. The LB methods to solve the governing equation are described in section 2.2. In this chapter first the general idea of LB methods is introduced and two existing LB formulations single relaxation time (SRT) LB method and two relaxation time (TRT) lattice Boltzmann method are presented. SRT LB is the most

simple LB formulation however it has certain disadvantages such as restrictive variability of relaxation parameter which in turn results in restrictive variability of diffusion coefficient and slower convergence to steady state. To eliminate this shortcoming a new SRT diffusion velocity LB formulation is developed. In the final part of this chapter approaches to implement initial and Boundary conditions in LB method are presented. A particular focus is laid in discussing and comparing different approaches to implement generalized boundary conditions for advection-diffusion equation. Also, a new local approach to implement generalized boundary condition for LB schemes with orthogonal lattices is proposed which is better in terms of accuracy and convergence compared to existing approaches. Finally, benchmarks and examples to highlight advantages of a SRT diffusion velocity LB method over SRT scheme are presented in section 2.3.

2.1 Governing equations

The solute transport at the pore-scale can be described using advection-diffusion equation.

$$\frac{\partial C}{\partial t} = -\vec{\nabla} \cdot \vec{J} \tag{2.1}$$

$$\vec{J} = -D_0 \vec{\nabla} C + \vec{u} C$$

where C is the concentration [NL^{-3}], $\vec{u}$ is the pore velocity vector [LT^{-1}], $\vec{J}$ is the flux vector and D_0 is the molecular diffusion coefficient of the solute in pore water [L^{2}T^{-1}]. As the solid phase is non-diffusive, a zero flux boundary condition is to be imposed at the surface of the solids

$$\vec{J} \cdot \hat{n} \mid_{\Gamma_s} = 0 \tag{2.2}$$

$\hat{n}$ is the unit normal vector and Γ_s represents the boundary of the non diffusive solid phase. The domain boundary conditions in general can be written as

$$A_1 C + A_2 \hat{n} \vec{\nabla} C = A_3 \tag{2.3}$$

A_1, A_2 and A_3 are constants. The special forms of the boundary condition can be deduced form Eq. (2.3) using different values of A_1, A_2 and A_3 as given below

Dirichlet boundary:	$A_1 = 1,$	$A_2 = 0$
Neumann boundary:	$A_1 = 0,$	$A_2 = 1$
Cauchy boundary:	$A_1 = \vec{u}_b,$	$A_2 = -D_0$ $\qquad A_3 = C_b \vec{u}_b$

C_b and $\vec{u}_b$ are concentration and pore velocity at boundary.

2.2 Lattice Boltzmann method

Lattice Boltzmann (LB) methods solves a discrete form of continuous Boltzmann equation. The Boltzmann transport equation describes the evolution of the density of particles $f(\vec{r}, t, \vec{e})$ [$N^1 L^{-3}$] at time t [T], at the point with position vector $\vec{r}$ [L], having same velocity $\vec{e}$ [$L^{-1}T$]. Alternatively $f(x, t, \vec{e})$ can also be thought of as the probability of finding a particle with velocity $\vec{e}$ near the point with position vector $\vec{r}$ at time t and hence it is also referred to as single particle distribution function. In this thesis $f(\vec{r}, t, \vec{e})$ is shortly referred to as distribution function. The Boltzmann transport equation in absence of external force is given as

$$\frac{\partial f}{\partial t} + \vec{e} \cdot \vec{\nabla} f = \Omega \tag{2.4}$$

Ω is the collision operator [1]. The left hand side of Eq. (2.4) is referred to as streaming operator and it relates to streaming of f from one point to another. This operator can be physically viewed as streaming of f from $\vec{r}$ to $\vec{r} + \vec{e}\Delta t$ in time interval Δt in case there is no collision i.e. right hand side of Eq. (2.4) is zero.

The discretization of the Boltzmann equation is carried out in space,time and velocity in order to obtain LB equation. The Boltzmann equation discretized with respect to velocity space can be written as

$$\frac{\partial f_i}{\partial t} + \vec{e}_i \cdot \vec{\nabla} f_i = \Omega_i, \qquad i = 1, 2, ..., q \tag{2.5}$$

$\vec{e}_i$ refers to discrete velocity vector. The velocity space in LB method is discretized in a regular lattice arrangement (as discussed later). Therefore in LB method, streaming occurs along the regular lattice. Hence the name *"Lattice Boltzmann"* method. Further discretization of Eq. (2.5) with respect to space and time gives (for details see Appendix B)

$$f_i(\vec{r} + \vec{e}_i \Delta t, t + \Delta t) = f_i(\vec{r}, t) + \Delta t \Omega_i(\vec{r}, t) \tag{2.6}$$

Eq. (2.6) is the *lattice Boltzmann equation*. The collision term in its general form for LB method can be written as

$$\Omega_i = -\Lambda_{ij} \left(f_j - f_j^{eq} \right) \tag{2.7}$$

Λ_{ij} is the matrix of the adjustable relaxation parameters, and f^{eq} is the single particle distribution function at equilibrium [$N^1 L^{-3}$] which is shortly referred to as equilibrium distribution function in this Thesis. The choice of the equilibrium distribution function and the type of lattice depends on the type of equation (physics) to be solved.

The distribution function and equilibrium function additionally need to satisfy a certain set of conditions in order to conserve certain physical quantities. For advection-diffusion

---

[1]In the original Boltzmann equation the collision operator is derived by considering interaction between two particles during collision.

only the conservation of mass is required during the collision step. This can be achieved by enforcing following condition

$$\sum_i f_i = \sum_i f_i^{eq} = C \tag{2.8}$$

In case of Navier-Stokes equation additionally conservation of momentum is needed during the collision step which can be achieved by following condition

$$\sum_i f_i \vec{e}_i = \sum_i f_i^{eq} \vec{e}_i = \rho_f \vec{u} \tag{2.9}$$

ρ_f being the density of the fluid $[\mathrm{ML}^{-3}]$. If energy has to be conserved in lattice Boltzmann method following condition has to be met,

$$\sum_i f_i (\vec{e}_i - \vec{u}) \cdot (\vec{e}_i - \vec{u}) = \sum_i f_i^{eq} (\vec{e}_i - \vec{u}) \cdot (\vec{e}_i - \vec{u}) = 2\rho_f E \tag{2.10}$$

where E is the energy $[\mathrm{ML}^2\mathrm{T}^{-2}]$. It can be shown that the solution of lattice Boltzmann equation (Eq. (2.6)) leads to solution of advection-diffusion equation (Eq. (2.1)) at the asymptotic limits through a multi-scale Chapman-Enskog expansion which is explained in detail in later part of this chapter.

Remark 2.2.1 (History of lattice Boltzmann method) *The predecessor to the lattice Boltzmann method are lattice gas automata wherein the fluid is represented as a set of particles moving on a defined lattice geometry and follows a simple set of collision rules. The break through in field of lattice gas automata to simulate fluid was achieved when Frisch et al. [65] demonstrated that particles moving on a defined lattice with a simple set of collision rules are able to mimic fluid flow. Soon after the drawbacks of lattice gas automata were realized such as large statistical noise, limited range of physical parameters, non-Galilean invariance, and implementation difficulty in three dimensions. To circumvent this drawback the lattice Boltzmann equation was introduced by Higuera and Jimenez [66]. In the original lattice Boltzmann method the equilibrium distribution functions and the relaxation matrix were derived from the underlying lattice gas automata models. Higuera et al. [67] further showed that the lattice Boltzmann equations can be derived independently of underlying lattice gas automata. Later on Qian et al. [68] suggested that the collision term can be replaced by a a linear term with a single relaxation parameter similar to one proposed by Bhatnagar et al. [69]. This is still the most popular LB scheme due to its algorithmic simplicity. However it has certain drawbacks (discussed later in this section). About a decade later, D'Humieres et al. [70] presented a theoretical framework for obtaining the matrix of relaxation parameters. They introduced this framework as Multi Relaxation Time (MRT) lattice Boltzmann method. The idea behind the MRT scheme is to relax the moments*

> *of distribution function rather than the distribution function as moments are related to physical quantities. The distribution function are transformed to moment space using the transformation matrix. The matrix of relaxation parameters is given by $M^{-1} \cdot \hat{S} \cdot M$. Here M is the transformation matrix which maps the distribution function to moment space and $\hat{S}$ is the matrix representing the relaxation parameter for the moments.*

2.2.1 Equilibrium distribution function

The equilibrium distribution function (EDF) is based on the Maxwell-Boltzmann distribution (see Appendix C for detail discussion). Linear part of Maxwell-Boltzmann distribution is enough for advection-diffusion equation, as it do not contain the second order terms of pore velocity [71].

$$
\begin{aligned}
f_i^{eq} &= w_i C \left(1 + \frac{\vec{e}_i \cdot \vec{u}}{e_s^2} \right) \qquad i > 0 \\
&= C - \sum_{i=1}^{i=q} f_i^{eq} \qquad i = 0
\end{aligned}
\tag{2.11}
$$

w_i are the lattice weights and e_s is the pseudo lattice speed of sound. The values of w_i and e_s depend on type of lattice. Alternatively the second order EDF (quadratic with respect to velocity terms) which is used for Navier-Stokes equation has also been used for advection-diffusion equation. It will be shown in later part of the discussion that second order EDF alongwith higher order lattice can recover advection-diffusion equation without any error terms upto second order during Chapman-Enskog expansion.

$$
\begin{aligned}
f_i^{eq} &= w_i C \left(1 + \frac{\vec{e}_i \cdot \vec{u}}{e_s^2} + \frac{\vec{e}_i \vec{e}_i : \vec{u}\vec{u}}{2e_s^4} - \frac{\vec{u} \cdot \vec{u}}{2e_s^2} \right) \qquad i > 0 \\
&= C - \sum_{i=1}^{i=q} f_i \qquad i = 0
\end{aligned}
\tag{2.12}
$$

2.2.2 Lattice structures

A lattice structure with q lattice directions in d dimensions is commonly referred to as "DdQq lattice" as suggested by Qian *et al.* [68]. The lattice structure defines the path for streaming of distribution function from current cell to the neighbouring cell. The number of neighbours in the lattice structure depends on the quantities to be conserved. For a regular lattice a unique set of velocity moments exist only up to certain order. This is referred to as *isotropy of the lattice*. The order of the moment upto which unique values exists are referred to as *order of isotropy of the lattice*. Furthermore, the lattices with more directions will have higher order of isotropy. For mass conservation lattices should be at least second order isotropic. For mass and momentum conservation lattices with at

least fourth order isotropy are required.

For advection-diffusion as only mass conservation is needed, the lattices should be at least second order isotropic. The formal definition of the second order isotropic lattice structures can be laid as, their exists w_i, e_s and velocity vectors $\vec{e_i}$ such that following conditions are satisfied.

$$\sum_i w_i = 1, \qquad \sum_i w_i e_{i\alpha} = 0, \qquad \sum_i w_i e_{i\alpha} e_{i\beta} = e_s^2 \delta_{\alpha\beta} \qquad (2.13)$$

Eq. 2.13 is written in indicial notations and α, β refers to spatial directions. *In this thesis indicial and vector notations are used interchangeably due to complexity of mathematical expressions. The notations are kept in vector form where ever possible.*

These criteria are easily met by lattices which are pointing toward its immediate neighbour. In three-dimensions immediate neighbour refers to cells sharing faces, edge or corners. For these lattices weights can be divided into three types: w_0 for rest or zero velocity, w_s for lattice velocity in orthogonal direction and w_l for lattice velocity in non orthogonal direction. The commonly used lattices with immediate neighbours are given below

D2Q5

$$e_s^2 = e/3 \qquad\qquad (2.14)$$
$$w_0 = 2/6 \qquad w_s = 1/6$$
$$\vec{e_0} = (0, 0)$$
$$\vec{e_1} = (e, 0) \qquad\qquad\qquad \vec{e_2} = (0, e)$$
$$\vec{e_3} = (-e, 0) \qquad\qquad\qquad \vec{e_4} = (0, -e)$$

D3Q7

$$e_s^2 = e/3.5 \qquad\qquad (2.15)$$
$$w_0 = 1/7 \qquad w_s = 1/7$$
$$\vec{e_0} = (0, 0, 0)$$
$$\vec{e_1} = (e, 0, 0) \qquad\qquad \vec{e_2} = (0, e, 0) \qquad\qquad \vec{e_3} = (0, 0, e)$$
$$\vec{e_4} = (-e, 0, 0) \qquad\qquad \vec{e_5} = (0, -e, 0) \qquad\qquad \vec{e_6} = (0, 0, -e)$$

D2Q9

$$e_s^2 = e/3 \tag{2.16}$$

$$w_0 = 4/9 \qquad w_s = 1/9 \qquad w_l = 1/36$$

$$\vec{e_0} = (0,0)$$

$$\vec{e_1} = (e,0) \qquad \vec{e_2} = (0,e) \qquad \vec{e_3} = (-e,0) \qquad \vec{e_4} = (0,-e)$$

$$\vec{e_5} = (e,e) \qquad \vec{e_6} = (-e,e) \qquad \vec{e_7} = (-e,-e) \qquad \vec{e_8} = (-e,e)$$

D3Q15

$$e_s^2 = e/3 \tag{2.17}$$

$$w_0 = 2/9 \qquad w_s = 1/9 \qquad w_l = 1/72$$

$$\vec{e_0} = (0,0,0)$$

$$\vec{e_1} = (e,0,0) \qquad \vec{e_2} = (0,e,0) \qquad \vec{e_3} = (0,0,e)$$

$$\vec{e_4} = (-e,0,0) \qquad \vec{e_5} = (0,-e,0) \qquad \vec{e_6} = (0,0,-e)$$

$$\vec{e_7} = (-e,-e,-e) \qquad \vec{e_8} = (-e,-e,e) \qquad \vec{e_9} = (-e,e,-e)$$

$$\vec{e_{10}} = (-e,e,e) \qquad \vec{e_{11}} = (e,e,e) \qquad \vec{e_{12}} = (e,e,-e)$$

$$\vec{e_{13}} = (e,-e,e) \qquad \vec{e_{14}} = (e,-e,-e)$$

D3Q19

$$e_s^2 = e/3 \tag{2.18}$$

$$w_0 = 1/3 \qquad w_s = 1/18 \qquad w_l = 1/36$$

$$\vec{e_0} = (0,0,0)$$

$$\vec{e_1} = (e,0,0) \qquad \vec{e_2} = (0,e,0) \qquad \vec{e_3} = (0,0,e)$$

$$\vec{e_4} = (-e,0,0) \qquad \vec{e_5} = (0,-e,0) \qquad \vec{e_6} = (0,0,-e)$$

$$\vec{e_7} = (-e,0,e) \qquad \vec{e_8} = (0,-e,-e) \qquad \vec{e_9} = (0,-e,e)$$

$$\vec{e_{10}} = (-e,-e,0) \qquad \vec{e_{11}} = (-e,e,0) \qquad \vec{e_{12}} = (-e,0,-e)$$

$$\vec{e_{13}} = (e,e,0) \qquad \vec{e_{14}} = (e,-e,0) \qquad \vec{e_{15}} = (e,0,e)$$

$$\vec{e_{16}} = (e,0,-e) \qquad \vec{e_{17}} = (0,e,e) \qquad \vec{e_{18}} = (0,e,-e)$$

where e is $\Delta r/\Delta t$. Δr being distance between two lattice nodes [L] and Δt is the discrete time step [T].

Table 2.1: Velocity moments of different lattices upto 4th order

moments of lattice weights	D2Q5, D3Q7	D2Q9, D3Q15, D3Q19
$\sum w_i$	1	1
$\sum w_i e_{i\alpha}$	0	0
$\sum w_i e_{i\alpha} e_{i\beta}$	$e_s^2 \delta_{\alpha\beta}$	$e_s^2 \delta_{\alpha\beta}$
$\sum w_i e_{i\alpha} e_{i\beta} e_{i\gamma}$	0	0
$\sum w_i e_{i\alpha} e_{i\beta} e_{i\gamma} e_{i\delta}$	$e_s^2 \delta_{\alpha\beta\gamma\delta}$	$e_s^4 \Delta_{\alpha\beta\gamma\delta}^4$

Remark 2.2.2 (Isotropy of velocity moments) *Chen* et al. *[72] has provided the formal definition of isotropy of velocity moments. A lattice is considered n^{th} order isotropic if following conditions are satsified:*

$$\sum_i e_{i\alpha 1} e_{i\alpha 2} \cdots e_{i\alpha n} = e_s^n \Delta_{\alpha 1 \alpha 2 \cdots \alpha n}^n \qquad n = 2, 4, 6, \cdots$$

$$\sum_i e_{i\alpha 1} e_{i\alpha 2} \cdots e_{i\alpha n} = 0 \qquad n = 1, 3, 5, \cdots$$

Here $\Delta_{\alpha 1, \alpha 2, \cdots, \alpha n}^n$ is the isotropic delta function. It is defined as the sum of $n/2$ products of Kronecker delta functions $\delta_{\alpha 1, \alpha 2} \cdots \delta_{\alpha n-1, \alpha n}$ in over all distinctive permutations of its sub-indices. There are $(n-1)!!(\equiv (n-1) \cdot (n-3) \cdots 3 \cdot 1)$ distinctive terms in $\Delta_{\alpha 1 \alpha 2 \cdots \alpha n}^n$. For instance

$$\Delta_{\alpha 1 \alpha 2}^2 = \delta_{\alpha 1 \alpha 2}$$

and

$$\Delta_{\alpha 1 \alpha 2 \alpha 3 \alpha 4}^4 = \delta_{\alpha 1 \alpha 2} \delta_{\alpha 3 \alpha 4} + \delta_{\alpha 1 \alpha 3} \delta_{\alpha 2 \alpha 4} + \delta_{\alpha 1 \alpha 4} \delta_{\alpha 2 \alpha 3}$$

Table 2.1 shows the velocity moments for various lattices listed above upto 4th order. It can be observed that orthogonal lattices only possesses 2nd order isotropy according to the definition provided above and hence they fail to recover Naiver-Stokes equation [65].

2.2.3 Single relaxation time lattice Boltzmann method

In single relaxation time (SRT) LB method the matrix of the adjustable relaxation parameters is replaced by the single relaxation parameter (τ). The resulting collision term is the one proposed by Bhatnagar *et al.* [69] and it is therefore also referred to as BGK collision term (Ω^{BGK}). The SRT LB equation is given as

$$f_i(\vec{r} + \vec{e}_i \Delta t, t + \Delta t) = f_i(\vec{r}, t) + \Delta t \Omega_i^{BGK}(\vec{r}, t) \tag{2.19}$$

$$\Omega_i^{BGK}(\vec{r}, t) = -\frac{1}{\tau} \left(f_i(\vec{r}, t) - f_i^{eq}(\vec{r}, t) \right)$$

It can be shown using multi-scale Chapman-Enskog expansion that at asymptotic limit Eq.(2.19) gives an advection-diffusion equation. The first step in Chapman-Enskog

expansion is to expand left hand side of Eq. (2.19) using Taylor series expansion. Then the space and time derivatives are expanded with respect to a small perturbation parameter ε. The time derivative is expanded as

$$\frac{\partial}{\partial t} = \varepsilon \frac{\partial}{\partial t_1} + \varepsilon^2 \frac{\partial}{\partial t_2} + O(\varepsilon^3) \tag{2.20}$$

and space derivative is expanded as

$$\vec{\nabla} = \varepsilon \vec{\nabla}^* + O(\varepsilon^2) \tag{2.21}$$

The distribution function is likewise expanded starting from zeroth order.

$$f_i = f_i^{(0)} + \varepsilon f_i^{(1)} + \varepsilon^2 f_i^{(2)} + O(\varepsilon^3) \tag{2.22}$$

The space and time derivatives are then replaced using Eq. (2.21) and Eq. (2.20) and distribution function is replaced using Eq. (2.22). The details of the derivation of Chapman-Enskog expansion upto this step are presented in Appendix (D). Eq. (2.20) implies that two time scales exist viz., advective time scale (t_1) and diffusive time scale (t_2). The advective component is mapped as $t_1 \to \varepsilon t$ and diffusive component is mapped as $t_2 \to \varepsilon^2 t$. The distribution function is thus mapped from $f_i(r, t)$ to $f_i(r^*, t_1, t_2)$. The Chapman-Enskog expansion thus allows to separate the phenomena occurring at different scales and by comparing the terms with same order of ε conservation laws and physical phenomena at each scale can be discussed separately. For SRT LB equation applying Chapman-Enskog expansion and comparing the terms with same order of ε leads to following relations

$$O(\varepsilon^0) : -\frac{\Delta t}{\tau} \left(f_i^{(0)} - f_i^{eq} \right) = 0 \tag{2.23}$$

$$O(\varepsilon^1) : \left[\frac{\partial}{\partial t_1} + \vec{e}_i \cdot \vec{\nabla}^* \right] f_i^{(0)} = -\frac{1}{\tau} f_i^{(1)} \tag{2.24}$$

$$O(\varepsilon^2) : \left[\frac{\partial}{\partial t_2} + \frac{\Delta t}{2} \frac{\partial^2}{\partial t_1^2} + \Delta t \frac{\partial}{\partial t_1} \vec{e}_i \cdot \vec{\nabla}^* + \frac{\Delta t}{2} \vec{e}_i \vec{e}_i : \vec{\nabla}^* \vec{\nabla}^* \right] f_i^{(0)} + \left[\frac{\partial}{\partial t_1} + \vec{e}_i \cdot \vec{\nabla}^* \right] f_i^{(1)}$$
$$= -\frac{1}{\tau} f_i^{(2)} \tag{2.25}$$

from $O(\varepsilon^0)$ it can be deduced that $f_i^{(0)} = f_i^{eq}$ and applying condition given by Eq. (2.8)

$$\sum_i f_i = \sum_i f_i^{(0)} = \sum_i f_i^{eq} = C \quad \text{and} \quad \sum_i f_i^{(1)} = \sum_i f_i^{(2)} = 0 \tag{2.26}$$

Taking zeroth order moment over $O(\varepsilon^1)$ equation and using Eq. (2.26) we get

$$\sum_i \left[\frac{\partial}{\partial t_1} + \vec{e_i} \cdot \vec{\nabla}^*\right] f_i^{(0)} = 0 \tag{2.27}$$

Substituting $O(\varepsilon^1)$ in $O(\varepsilon^2)$ equation we can rewrite $O(\varepsilon^2)$ in terms of $f_i^{(0)}$.

$$\left[\frac{\partial}{\partial t_2} + \left(\frac{\Delta t}{2} - \tau\right)\frac{\partial^2}{\partial t_1^2} + (\Delta t - 2\tau)\frac{\partial}{\partial t_1}\vec{e_i}\cdot\vec{\nabla}^* + \left(\frac{\Delta t}{2} - \tau\right)\vec{e_i}\vec{e_i} : \vec{\nabla}^*\vec{\nabla}^*\right] f_i^{(0)} = -\frac{1}{\tau}f_i^{(2)} \tag{2.28}$$

Taking zeroth order moment over Eq. (2.28)

$$\frac{\partial \sum_i f_i^{(0)}}{\partial t_2} + \left(\frac{\Delta t}{2} - \tau\right)\frac{\partial^2 \sum_i f_i^{(0)}}{\partial t_1^2} + (\Delta t - 2\tau)\frac{\partial}{\partial t_1}\vec{\nabla}^*\cdot\sum_i f_i^{(0)}\vec{e_i} + \left(\frac{\Delta t}{2} - \tau\right)\vec{\nabla}^{*2}\sum_i f_i^{(0)}\vec{e_i}\vec{e_i} = 0 \tag{2.29}$$

from Eq. (2.27) $\frac{\partial^2 \sum_i f_i^{(0)}}{\partial t_1^2}$ can be rewritten as

$$\frac{\partial^2 \sum_i f_i^{(0)}}{\partial t_1^2} = -\vec{\nabla}^* \cdot \sum_i f_i^{(0)}\vec{e_i} \tag{2.30}$$

substituting (2.30) in (2.29)

$$\frac{\partial \sum_i f_i^{eq}}{\partial t_2} + \left(\frac{\Delta t}{2} - \tau\right)\frac{\partial}{\partial t_1}\vec{\nabla}^* \cdot \sum_i f_i^{eq}\vec{e_i} + \left(\frac{\Delta t}{2} - \tau\right)\vec{\nabla}^{*2}\sum_i f_i^{eq}\vec{e_i} \cdot \vec{e_i} = 0 \tag{2.31}$$

substituting the relevant moments of f_i^{eq} in Eq. (2.31) advection diffusion equation can be recovered. Table 2.2 shows the moments of f_i^{eq} for different lattice structures and choice of EDF. The first LHS term of Eq. (2.31) irrespective of lattice structure or EDF can be written as

$$\frac{\partial \sum_i f_i^{eq}}{\partial t_2} = \frac{\partial C}{\partial t_2} \tag{2.32}$$

using Eq.(2.20) Eq. (2.27) and (2.21) in Eq. (2.32)

$$\frac{\partial \sum_i f_i^{eq}}{\partial t_2} = \frac{1}{\varepsilon^2}\left(\frac{\partial C}{\partial t} + \vec{\nabla}\cdot\vec{u}C\right) \tag{2.33}$$

The second LHS term of Eq. (2.31) irrespective of lattice structure and EDF can be written as

$$\left(\frac{\Delta t}{2} - \tau\right)\frac{\partial}{\partial t_1}\vec{\nabla}^* \cdot \sum_i f_i^{eq}\vec{e_i} = \left(\frac{\Delta t}{2} - \tau\right)\vec{\nabla}^* \cdot \left[\vec{u}\frac{\partial C}{\partial t_1} + C\frac{\partial \vec{u}}{\partial t_1}\right] \tag{2.34}$$

Table 2.2: Moments up to second orders of equilibrium distribution functions for different lattices

Lattices	moments	Linear	Quadratic
D2Q5,D3Q7	$\sum f_i^{eq}$	C	C
	$\sum f_i^{eq} e_{i\alpha}$	Cu_α	Cu_α
	$\sum f_i^{eq} e_{i\alpha} e_{i\beta}$	$Ce_s^2 \delta_{\alpha\beta}$	$C\left[\left(e_s^2 - \frac{u_\gamma u_\gamma}{2}\right)\delta_{\alpha\beta} + \frac{u_\gamma u_\delta \delta_{\alpha\beta\gamma\delta}}{2e_s^2}\right]$
D2Q9,D3Q15,D3Q19	$\sum f_i^{eq}$	C	C
	$\sum f_i^{eq} e_{i\alpha}$	Cu_α	Cu_α
	$\sum f_i^{eq} e_{i\alpha} e_{i\beta}$	$Ce_s^2 \delta_{\alpha\beta}$	$C\left[e_S^2 \delta_{\alpha\beta} + u_\alpha u_\beta\right]$

Considering no rapid time variation of flows $\frac{\partial \vec{u}}{\partial t_1} = 0$, assuming flow and using Eq. (2.27)

$$\left(\frac{\Delta t}{2} - \tau\right)\frac{\partial}{\partial t_1}\vec{\nabla}^* \cdot \sum_i f_i^{eq}\vec{e_i} = -\left(\frac{\Delta t}{2} - \tau\right)\vec{\nabla}^* \vec{u}\vec{u}\vec{\nabla}^* C \tag{2.35}$$

Assuming flow to be incompressible $\nabla \cdot \vec{u} = 0$ and using Eq. (2.21)

$$\left(\frac{\Delta t}{2} - \tau\right)\frac{\partial}{\partial t_1}\vec{\nabla}^* \cdot \sum_i f_i^{eq}\vec{e_i} = -\frac{1}{\varepsilon^2}\left(\frac{\Delta t}{2} - \tau\right)\vec{u} \cdot \vec{u}\vec{\nabla}^2 C \tag{2.36}$$

The third LHS term of Eq. (2.31) depends on type of EDF and lattice structure. For a linear EDF irrespective of the lattice structure using (2.21) the third LHS term can be rewritten as

$$\left(\frac{\Delta t}{2} - \tau\right)\vec{\nabla}^{*2}\sum_i f_i^{eq}\vec{e_i} \cdot \vec{e_i} = \frac{1}{\varepsilon^2}e_s^2\left(\frac{\Delta t}{2} - \tau\right)\vec{\nabla}^2 C \tag{2.37}$$

For orthogonal lattice structures with quadratic EDF the third LHS term of Eq. (2.31) becomes

$$\left(\frac{\Delta t}{2} - \tau\right)\vec{\nabla}^{*2}\sum_i f_i^{eq}\vec{e_i} \cdot \vec{e_i} = \frac{1}{\varepsilon^2}\left[\left(e_s^2 - \frac{u_\gamma u_\gamma}{2}\right)\delta_{\alpha\beta} + \frac{u_\gamma u_\delta \delta_{\alpha\beta\gamma\delta}}{2e_s^2}\right]\left(\frac{\Delta t}{2} - \tau\right)\nabla_{\alpha\beta}C \tag{2.38}$$

for higher order lattice structures with quadratic EDF the third LHS term of Eq. (2.31) is then written as

$$\left(\frac{\Delta t}{2} - \tau\right)\vec{\nabla}^{*2}\sum_i f_i^{eq}\vec{e_i} \cdot \vec{e_i} = \frac{1}{\varepsilon^2}\left(e_s^2 + \vec{u} \cdot \vec{u}\right)\left(\frac{\Delta t}{2} - \tau\right)\vec{\nabla}^2 C \tag{2.39}$$

Finally the advection-diffusion equation can be recovered by re substituting these terms back in Eq. (2.31).

- All lattice structures with linear EDF

$$\frac{\partial C}{\partial t} + \vec{\nabla}C \cdot \vec{u} = \left(\tau - \frac{\Delta t}{2}\right)\left(e_s^2 - \vec{u} \cdot \vec{u}\right)\vec{\nabla}^2 C \tag{2.40}$$

- Orthogonal lattice structures with quadratic EDF

$$\frac{\partial C}{\partial t} + \nabla_\alpha C u_\alpha = \left[e_s^2 \delta_{\alpha\beta} + \left(\frac{u_\gamma u_\delta \delta_{\alpha\beta\gamma\delta}}{2 e_s^2} - \frac{u_\gamma u_\gamma}{2} \delta_{\alpha\beta} - u_\alpha u_\beta \right) \right] \left(\tau - \frac{\Delta t}{2} \right) \nabla_{\alpha\beta} C$$

(2.41)

- Higher order lattice structures with quadratic EDF

$$\frac{\partial C}{\partial t} + \vec{\nabla} C \cdot \vec{u} = e_s^2 \left(\tau - \frac{\Delta t}{2} \right) \vec{\nabla}^2 C$$

(2.42)

Comparing equations Eq. (2.40), Eq. (2.41) and Eq. (2.42) the diffusion coefficient is obtained as

$$D_0 = e_s^2 \left(\tau - \frac{\Delta t}{2} \right)$$

(2.43)

It can be observed from Eq. (2.40), Eq. (2.41) and Eq. (2.42) that only higher order lattice structures with quadratic EDF recover the advection-diffusion equation without any error terms. This result has also been confirmed by other researchers [73, 74]. It can be further deduced that for the linear EDF and orthogonal lattice structure with quadratic EDF the error term vanishes under assumption $\frac{\vec{u} \cdot \vec{u}}{e_s^2} \approx 0$. Flekkoy [71] was the first to use linear EDF to recover advection diffusion equation. He argued that $\vec{u}$ is small in the incompressibility limit [2] and the term $\vec{u} \cdot \vec{u}$ represents only 1% of correction and hence these terms can be effectively neglected.

Remark 2.2.3 (removing error terms in case of linear EDF) *The error terms arising while recovering the advection-diffusion equation using linear EDF can be corrected by introducing a forcing term of form $w_i \vec{e}_i \cdot \vec{F}$ [74, 75]. This forcing term is added to collision term. During Chapman-Enskog expansion the the forcing term is expanded as $\vec{F} = \varepsilon \vec{F}^{(1)}$ and hence Eq. (2.24) can be rewritten as*

$$\left[\frac{\partial}{\partial t_1} + \vec{e}_i \cdot \vec{\nabla}^* \right] f_i^{(0)} = -\frac{1}{\tau} f_i^{(1)} + w_i \vec{e}_i \cdot \vec{F}^{(1)}$$

Correspondingly the $O(\varepsilon^2)$ in terms of $f_i^{(0)}$ can be written as

$$\left[\frac{\partial}{\partial t_2} + \left(\frac{\Delta t}{2} - \tau \right) \frac{\partial^2}{\partial t_1^2} + (\Delta t - 2\tau) \frac{\partial}{\partial t_1} \vec{e}_i \cdot \vec{\nabla}^* + \left(\frac{\Delta t}{2} - \tau \right) \vec{e}_i \vec{e}_i : \vec{\nabla}^* \vec{\nabla}^* \right] f_i^{(0)} +$$

$$\tau \left[\frac{\partial}{\partial t_1} + \vec{e}_i \cdot \vec{\nabla}^* \right] w_i \vec{e}_i \cdot \vec{F}^{(1)} = -\frac{1}{\tau} f_i^{(2)}$$

---

[2]Incompressibility refers to the assumption that if the flow remains within a Mach number limit (normally less than 0.3) the fluid flow is treated as incompressible flow

Taking the zeroth moment over above equation we get

$$\left[\frac{\partial}{\partial t_2} + \left(\frac{\Delta t}{2} - \tau \right) \frac{\partial^2}{\partial t_1^2} + (\Delta t - 2\tau) \frac{\partial}{\partial t_1} \vec{e_i} \cdot \vec{\nabla}^* + \left(\frac{\Delta t}{2} - \tau \right) \vec{e_i} \vec{e_i} : \vec{\nabla}^* \vec{\nabla}^* \right] \sum_i f_i^{(0)} +$$
$$\tau e_s^2 \vec{\nabla}^* \cdot \vec{F}^{(1)} = 0$$

Further using Eq. (2.24), the term $\frac{\partial^2}{\partial t_1^2} \sum_i f_i$ can be replaced by $-\frac{\partial}{\partial t_1} \vec{e_i} \cdot \vec{\nabla}^* \sum_i f_i$ resulting in

$$\left[\frac{\partial}{\partial t_2} \left(\frac{\Delta t}{2} - \tau \right) \frac{\partial}{\partial t_1} \vec{e_i} \cdot \vec{\nabla}^* + \left(\frac{\Delta t}{2} - \tau \right) \vec{e_i} \vec{e_i} : \vec{\nabla}^* \vec{\nabla}^* \right] \sum_i f_i^{(0)} + \tau e_s^2 \vec{\nabla}^* \cdot \vec{F}^{(1)} = 0$$

Further continuing the derivation for recovering the advection-diffusion equation from above equation it can be observed that in order to recover the advection-diffusion equation without error term following condition should be satisfied

$$\left(\tau - \frac{\Delta t}{2} \right) \frac{\partial C \vec{u}}{\partial t} - \tau e_s^2 \vec{F} = 0$$

which leads to

$$\vec{F} = \frac{1}{e_s^2} \left(1 - \frac{\Delta t}{2\tau} \right) \frac{\partial C \vec{u}}{\partial t} = \frac{1}{e_s^2} \left(1 - \frac{\Delta t}{2\tau} \right) \left[C \frac{\partial \vec{u}}{\partial t} + \vec{u} \frac{\partial C}{\partial t} \right] =$$
$$\frac{1}{e_s^2} \left(1 - \frac{\Delta t}{2\tau} \right) \left[C^{(t+\Delta t)} \frac{\vec{u}^{(t+\Delta t)} - \vec{u}^{(t)}}{\Delta t} + \vec{u}^{(t+\Delta t)} \frac{C^{(t+\Delta t)} - C^{(t)}}{\Delta t} \right]$$

In case the rest velocity is present in the lattice structure $\frac{\partial C}{\partial t}$ can be expressed in terms of $f_0^{neq} = f_0 - f_0^{eq}$ using Eq. (2.24) as

$$\frac{\partial C}{\partial t} = -\frac{1}{\tau w_0} f_0^{neq}$$

Remark 2.2.4 (Implementation) *LB methods has a Lagrangian nature. Hence conventionally, LB methods is implemented in two steps: collide and stream. In collide step the collision term is evaluated and in place modification of distribution function is made. In the stream step the distribution functions are advected to the neighbouring node based on a given lattice structure. The collide-stream algorithm for the two dimensional SRT lattice Boltzmann method is shown in Algorithm 2.1. As shown in the pseudo code during streaming step two copies of distribution function are required. This can be avoided by using a swap algorithm [76]. Collide-stream algorithm needs at least two passes over the memory which is memory band width intensive. To circumvent this several fused algorithms (applying collide and stream in one go) have been proposed (for details of fused algorithms and comparison*

Algorithm 2.1: SRT method for D2Q*q* lattice

```
   /* Given intial concentration (C) and velocity field (u) initialize
      particle probability distribution functions (f) to equilibrium
      distribution function (feq)                                      */
 1 while t<tf do
   |   /* Run simulation till final time(tf) is reached                */
 2 |   t= t + dt ;
   |   /* collide                                                      */
   |   /* lx and ly are domain length in x and y direction             */
 3 |   for i=1 to lx do
 4 |   |   for j= 1 to ly do
   |   |   |   /* compute concentration                                */
 5 |   |   |   C[i,j] = 0;
 6 |   |   |   for k=1 to q do
 7 |   |   |   |   C[i,j] = C[i,j] + f[i,j,k];
 8 |   |   |   end
   |   |   |   /* tau is the relaxation parameter that is based on
   |   |   |      diffusion coefficient                                 */
 9 |   |   |   omega = dt/tau ;
10 |   |   |   for k=1 to q do
11 |   |   |   |   f[i,j,k] = (1-omega) * f[i,j,k]+ omega * feq(C[i,j],k,ux[i,j],uy[i,j]) ;
12 |   |   |   end
13 |   |   end
14 |   end
   |   /* stream                                                       */
15 |   for i=1 to lx do
16 |   |   for j= 1 to ly do
17 |   |   |   for k=1to q do
18 |   |   |   |   NextI = i + e[k];
19 |   |   |   |   NextJ = j + e[k];
20 |   |   |   |   if 1 ≤ NextI ≤ lx & 1 ≤ NextJ ≤ ly then
21 |   |   |   |   |   fnew[NextI,NextJ,k] = f[i,j,k];
22 |   |   |   |   end
23 |   |   |   end
24 |   |   end
25 |   end
26 |   f = fnew ;
27 end
   /* apply boundary conditions                                        */
```

between different algorithms refer [77, 78]).

Remark 2.2.5 (D2Q5 vs D2Q9) *Suga [79] carried out stability analysis for D2Q5 and D2Q9 lattices with linear EDF. His conclusions showed that the stability conditions of the D2Q9 are more restrictive than those of D2Q5. Further, his numerical experiments suggest that for a grid Peclet number greater than 10, D2Q9 gives more accurate results than D2Q5 lattice for a given Courant number. However in his study the e_s^2 for D2Q5 and D2Q9 lattices are different viz. 1/2 and 1/3 respectively. Hence for a given Courant number D2Q5 and D2Q9 lattices yields different relaxation parameters. It has been shown by Servan-Camas [74] that the accuracy of SRT scheme is dependent on relaxation parameter. Servan-Camas [74] further showed that for a grid Peclet number 40, D2Q5 lattice with corrected linear EDF (see Remark 2.2.3) shows good match with analytical method. Moreover, D2Q5 is more efficient than D2Q9 lattice both in terms of both memory and computation. Hence D2Q5 lattice is a good choice for pore scale solute transport and for higher Peclet number the correction to linear EDF should be taken into account.*

2.2.4 Two relaxation time lattice Boltzmann method

In two relaxation time (TRT) lattice Boltzmann method the symmetric and anti-symmetric parts of the particle distribution function are relaxed separately using two different relaxation parameters. The symmetric (f^+) and anti-symmetric parts (f^-) of the particle distribution functions are defined as

$$f_i^+ = \frac{f_i + f_{-i}}{2} \qquad \& \qquad f_i^- = \frac{f_i - f_{-i}}{2} \tag{2.44}$$

where f_i and f_{-i} refers to distribution functions corresponding to lattice velocity $\vec{e}_i$ and $\vec{e}_{-i}$ respectively; $\vec{e}_i = -\vec{e}_{-i}$. The above definition of symmetric and anti-symmetric part naturally imposes a condition that all the even moments of anti-symmetric part and odd moments of symmetric parts are zero. The two relaxation time lattice Boltzmann equation is written as follows [73]

$$f_i(\vec{r} + \vec{e}_i \Delta t, t + \Delta t) = f_i(\vec{r}, t) + \Delta t \Omega_i^{TRT}(\vec{r}, t) \tag{2.45}$$

$$\Omega_i^{TRT}(\vec{r}, t) = -\frac{1}{\tau_+} \left(f_i^+(\vec{r}, t) - f_i^{eq+}(\vec{r}, t) \right) - \frac{1}{\tau_-} \left(f_i^-(\vec{r}, t) - f_i^{eq-}(\vec{r}, t) \right) \tag{2.46}$$

Here, τ_+ and τ_- are relaxation parameters for the symmetric part and anti-symmetric part respectively. Applying Chapman-Enskog expansion to TRT scheme given by Eq. (2.45)

and separating the terms with same order of ε we get

$$O(\varepsilon^0) : -\frac{\Delta t}{\tau_+}\left(f_i^{+(0)} - f_i^{eq+}\right) - \frac{\Delta t}{\tau_-}\left(f_i^{-(0)} - f_i^{eq-}\right) = 0 \tag{2.47}$$

$$O(\varepsilon^1) : \left[\frac{\partial}{\partial t_1} + \vec{e_i}\cdot\vec{\nabla}^*\right]f_i^{(0)} = -\frac{1}{\tau_+}f_i^{+(1)} - \frac{1}{\tau_-}f_i^{-(1)} \tag{2.48}$$

$$O(\varepsilon^2) : \left[\frac{\partial}{\partial t_2} + \frac{\Delta t}{2}\frac{\partial^2}{\partial t_1^2} + \Delta t\frac{\partial}{\partial t_1}\vec{e_i}\cdot\vec{\nabla}^* + \frac{\Delta t}{2}\vec{e_i}\vec{e_i} : \vec{\nabla}^*\vec{\nabla}^*\right]f_i^{(0)} + \left[\frac{\partial}{\partial t_1} + \vec{e_i}\cdot\vec{\nabla}^*\right]f_i^{(1)}$$
$$= -\frac{1}{\tau_+}f_i^{+(2)} - \frac{1}{\tau_-}f_i^{-(2)} \tag{2.49}$$

from $O(\varepsilon^0)$ terms under the condition imposed by Eq. (2.8) we get

$$\sum_i f_i = \sum_i f_i^{(0)} = \sum_i f_i^{+(0)} = C \qquad \text{and}$$

$$\sum_i f_i^{(1)} = \sum_i f_i^{(2)} = \cdots = 0 \qquad \text{and}$$

$$\sum_i f_i^{+(1)} = \sum_i f_i^{+(2)} = \cdots = 0 \tag{2.50}$$

Taking zeroth moment over $O(\varepsilon^1)$ terms Eq. (2.27) can be recovered. Finally taking zeroth moment over $O(\varepsilon^2)$ terms

$$\sum_i\left[\frac{\partial}{\partial t_2} + \frac{\Delta t}{2}\frac{\partial^2}{\partial t_1^2} + \Delta t\frac{\partial}{\partial t_1}\vec{e_i}\cdot\vec{\nabla}^* + \frac{\Delta t}{2}\vec{e_i}\vec{e_i} : \vec{\nabla}^*\vec{\nabla}^*\right]f_i^{(0)} + \vec{\nabla}^*\cdot\sum_i f_i^{(1)}\vec{e_i} = 0 \tag{2.51}$$

using Eq. (2.27)

$$\frac{\partial^2\sum_i f_i^{(0)}}{\partial t_1^2} = -\frac{\partial}{\partial t_1}\vec{e_i}\cdot\vec{\nabla}^*\sum_i f_i^{(0)} \tag{2.52}$$

Taking first moment over $O(\varepsilon^1)$ terms it can be shown that

$$\vec{\nabla}^*\cdot\sum_i f_i^{(1)}\vec{e_i} = \vec{\nabla}^*\cdot\sum_i f_i^{-(1)}\vec{e_i} = -\tau_-\sum_i\left[\frac{\partial}{\partial t_1}\vec{e_i}\cdot\vec{\nabla} + \vec{e_i}\vec{e_i} : \vec{\nabla}^*\vec{\nabla}^*\right]f_i^{(0)} \tag{2.53}$$

substituting Eq. (2.52) and Eq. (2.53) in Eq. (2.51)

$$\frac{\partial\sum_i f_i^{eq}}{\partial t_2} + \left(\frac{\Delta t}{2} - \tau_-\right)\frac{\partial}{\partial t_1}\vec{\nabla}^*\cdot\sum_i f_i^{eq}\vec{e_i} + \left(\frac{\Delta t}{2} - \tau_-\right)\vec{\nabla}^{*2}\sum_i f_i^{eq}\vec{e_i}\cdot\vec{e_i} = 0 \tag{2.54}$$

Eq. (2.54) is same as Eq. (2.31) with τ now replaced by τ_-. Following the further derivation as shown in Section 2.2.3 it can be shown that similar to SRT scheme the scheme advection-diffusion equation can be recovered at asymptotic limits.

- All lattice structures with linear EDF

$$\frac{\partial C}{\partial t} + \vec{\nabla} C \cdot \vec{u} = \left(\tau_- - \frac{\Delta t}{2} \right) \left(e_s^2 - \vec{u} \cdot \vec{u} \right) \vec{\nabla}^2 C \tag{2.55}$$

- Orthogonal lattice structures with quadratic EDF

$$\frac{\partial C}{\partial t} + \nabla_\alpha C u_\beta = \left[e_s^2 \delta_{\alpha\beta} + \left(\frac{u_\gamma u_\delta \delta_{\alpha\beta\gamma\delta}}{2 e_s^2} - \frac{u_\gamma u_\gamma}{2} \delta_{\alpha\beta} - u_\alpha u_\beta \right) \right] \left(\tau_- - \frac{\Delta t}{2} \right) \nabla_{\alpha\beta} C \tag{2.56}$$

- Higher order lattice structures with quadratic EDF

$$\frac{\partial C}{\partial t} + \vec{\nabla} C \cdot \vec{u} = e_s^2 \left(\tau_- - \frac{\Delta t}{2} \right) \vec{\nabla}^2 C \tag{2.57}$$

and the diffusion coefficient is given as

$$D_0 = e_s^2 \left(\tau_- - \frac{\Delta t}{2} \right) \tag{2.58}$$

While τ_- is related to the diffusion coefficient, τ_+ is the free parameter which can be adjusted to improve the stability or accuracy of the scheme.

Remark 2.2.6 (SRT vs. TRT vs. MRT) *One can view the MRT scheme as the most general case of LB method. The TRT scheme can then be considered as a subset of the MRT scheme and the SRT scheme in turn is the subset of TRT scheme. SRT scheme due to its simplicity is still widely used LB scheme. However, the errors associated with the solution of SRT scheme are highly dependent on the relaxation parameter [80, 81]. Moreover, the accuracy of the bounce-back scheme (bounce-back scheme is described later in this chapter) also depends on the relaxation parameter [82–85]. Furthermore the computed permeability at pore-scale is affected by the choice of relaxation parameter [86]. For pore-scale simulation this in turn implies that the relaxation parameter has to be kept fixed and preferably close to one. The disadvantage of keeping relaxation parameter close to one is that the computation of diffusivity or permeability using SRT scheme requires relatively large number of iterations to reach steady state and hence it is computationally inefficient. Later in this section the diffusion velocity SRT scheme is introduced which can be used to increase time step (in turn reducing number of iterations) keeping relaxation parameter constant and thus improving efficiency of SRT scheme.*

In MRT scheme, while some relaxation parameters are related to physical moments other set of relaxation parameters can be tweaked to remove the dependency of error on relaxation parameters [86]. Similarly, for the TRT scheme which has two relaxation parameters, only one relaxation parameter is linked to physical quantity and the other relaxation parameter

can be tweaked to remove the errors associated with the choice of the relaxation parameter [87, 88]. Hence this allows for the choice of higher values of relaxation parameters which in turn reduces the number of iterations needed to reach steady state. On other hand, MRT is computationally the most expensive and SRT is the least expensive scheme of all the three schemes

Remark 2.2.7 (Choice of magic parameter) *The stability and accuracy of TRT scheme is related to the choice of the so called magic parameter ($\boldsymbol{M}$) which is defined as*

$$\boldsymbol{M} = (\tau_- - \frac{1}{2})(\tau_+ - \frac{1}{2})$$

For any values of τ_+ and τ_- the TRT scheme shows same stability if the value of $\boldsymbol{M}$ is kept to $\frac{1}{4}$ [89]. The third order advection terms can be successfully eliminated for $\boldsymbol{M}$ equal $\frac{1}{12}$ [90]. Similarly for pure diffusion equation the fourth order error terms can be eliminated for the value of $\boldsymbol{M}$ equal to $\frac{1}{6}$ [91]. The solid boundary can be set exactly at the midway for the bounce back condition in case of Poiseuille's flow through inclined channel for $\boldsymbol{M}$ equal to $\frac{3}{16}$ [92].

2.2.5 A local approach to compute total flux

Taking the first moment over $O(\varepsilon^1)$ terms (Eq. (2.24)) we get

$$\frac{\partial}{\partial t_1} \sum_i f_i^{(0)} \vec{e}_i + \vec{\nabla}^* \cdot \sum_i f_i^{(0)} \vec{e}_i \cdot \vec{e}_i = -\frac{1}{\tau} \sum_i f_i^{(1)} \vec{e}_i \tag{2.59}$$

Substituting the of moments of $f_i^{(0)} = f_i^{eq}$ as listed in Table 2.2.

$$\frac{\partial C\vec{u}}{\partial t_1} + e_s^2 (\mathbb{1} + I_n \vec{u} \cdot \vec{u}) \vec{\nabla}^* C = -\frac{1}{\tau} \sum_i f_i^{(1)} \vec{e}_i \tag{2.60}$$

Instead of using the $\sum_i f_i^{(0)} \vec{e}_i \cdot \vec{e}_i$ as listed in Table 2.2 the above substitution is used for the sake of generality. For higher order lattices with quadratic EDF I_n is equal to 1 and for linear EDF I_n is equal to 0. Following the argumentation presented for deriving Eq. (2.36) the term $\frac{\partial C\vec{u}}{\partial t_1}$ can be replaced by $-\vec{u} \cdot \vec{u} \nabla^* C$. Substituting this in above equation

$$e_s^2 \left(\mathbb{1} + (I_n - 1)\vec{u} \cdot \vec{u} \right) \vec{\nabla}^* C = -\frac{1}{\tau} \sum_i f_i^{(1)} \vec{e}_i \tag{2.61}$$

Using Eq. (2.20), Eq. (2.21) and Eq. (2.22) we get

$$\vec{\nabla} C = -\frac{1}{\tau e_s^2 \left(\mathbb{1} + (I_n - 1)\vec{u} \cdot \vec{u} \right)} \left[\sum_i f_i \vec{e}_i - \vec{u} \sum_i f_i \right] \tag{2.62}$$

The total flux as given in Eq. (2.1) can be written in terms of f_i using above equation as

$$\vec{J} = \frac{D_0}{\tau e_s^2 \left(\mathbb{1} + (I_n - 1)\vec{u} \cdot \vec{u}\right)} \left[\sum_i f_i \vec{e}_i - \vec{u} \sum_i f_i\right] + \vec{u} \sum_i f_i \qquad (2.63)$$

For TRT scheme τ in above equation is replaced with τ_-.

Remark 2.2.8 (case of corrected linear EDF) *As discussed in Remark 2.2.3 Linear EDF can be corrected by removing numerical diffusion by introducing a forcing term at of $O(\varepsilon^1)$. Eq. (2.60) can be rewritten as*

$$e_s^2 \vec{\nabla}^* C = -\frac{1}{\tau} \sum_i f_i^{(1)} \vec{e}_i - \frac{\Delta t}{2\tau} \frac{\partial C\vec{u}}{\partial t_1}$$

Eq. (2.62) then becomes

$$\vec{\nabla} C = -\frac{1}{\tau e_s^2} \left[\sum_i f_i \vec{e}_i - \vec{u} \sum_i f_i + \frac{\Delta t}{2} \frac{\partial C\vec{u}}{\partial t}\right]$$

Finally the total flux is given by

$$\vec{J} = \frac{D_0}{\tau e_s^2} \left[\sum_i f_i \vec{e}_i - \vec{u} \sum_i f_i + \frac{\Delta t}{2} \frac{\partial C\vec{u}}{\partial t}\right] + \vec{u} \sum_i f_i$$

As explained in Remark 2.2.3 $\frac{\partial C\vec{u}}{\partial t}$ can be obtained using following equation

$$\frac{\partial C\vec{u}}{\partial t} = \left[C^{(t+\Delta t)} \frac{\vec{u}^{(t+\Delta t)} - \vec{u}^{(t)}}{\Delta t} - \frac{1}{\tau w_0} \vec{u}^{(t+\Delta t)} f_0^{neq}\right]$$

2.2.6 Diffusion velocity single relaxation time lattice Boltzmann method

[3] In SRT scheme, the time step depends on the magnitude of diffusion coefficient (see Section 2.2.7 Eq. (2.76)). The variability in both time step and spatial heterogeneity of diffusion coefficients are accommodated through the variation of the relaxation time. The relaxation time however, should be selected in an interval $(0.5, 5]$ to have reliable results for diffusion equation [94]. Moreover the accuracy of no flux boundary applied using bounce-back condition (for details on bounce back condition see Section 2.2.8) depends on the value of relaxation parameter [82–85]. The relaxation parameter should be close to unity to ensure the second order accurate bounce-back scheme. The diffusion velocity

---

[3]This section is based on the published paper titled "Single relaxation time lattice Boltzmann scheme for advective-diffusion problems with large diffusion coeffcient heterogeneities and high advective transport" [93]

formulation allows for fixing the relaxation parameter to a value which best suites the stability and accuracy with a flexibility of allowing for both variability of time step and spatial heterogeneity of diffusion coefficients.

The central idea of diffusion velocity formulation is to divide diffusion coefficient into a reference value D_{ref} which is constant over entire domain and a fluctuating value $\tilde{D}$ which represents a deviation from the reference. This can be written as

$$D_0 = D_{ref} + \tilde{D} \tag{2.64}$$

The reference part, is used to define the physical time scale as in Eq (2.76) (i.e. D_{ref} instead of D_0). The fluctuating part, on the other hand, is transferred to a new velocity (hence termed "diffusion velocity") which contributes to a new advection term. A similar procedure has been used to achieve stability of advection dominant mass transport problems, e.g. in atmospheric phenomena [95]. With the definition of the reference diffusion coefficient Eq.(2.64), the corresponding fluxes as in Eq.(2.1) become

$$\vec{J} = -D_{ref}\vec{\nabla}C - \tilde{D}\vec{\nabla}C + \vec{u}C \tag{2.65}$$

The second term in Eq. (2.65) represents flux from the fluctuating part which is transferred to an advection term as

$$-\tilde{D}\vec{\nabla}C = \vec{u}_d C \tag{2.66}$$

from which the diffusion velocity $\vec{u}_d$ can be derived

$$\vec{u}_d = -\frac{\tilde{D}\vec{\nabla}C}{C} \tag{2.67}$$

This diffusion velocity is an additional advection term in the advection-diffusion transport equation

$$\vec{J} = -D_{ref}\vec{\nabla}C + (\vec{u} + \vec{u}_d)\,C \tag{2.68}$$

By this, the total mass balance is still respected. The diffusion velocity can be calculated in several ways, either directly from the macroscopic concentrations where the concentration gradient are calculated by a finite difference scheme, or by the use of the $O(\varepsilon^1)$ of Chapman-Enskog expansion.

Local approach to compute diffusion velocity

To compute diffusion velocity as given by Eq. (2.67) one needs to compute concentration gradients. Using Eq. (2.62) concentration gradients can be computed in terms of distribution function as

$$\vec{\nabla}C = -\frac{1}{\tau e_s^2}\left[\sum_i f_i\vec{e}_i - (\vec{u} + \vec{u}_d)\sum_i f_i\right] \tag{2.69}$$

Substituting Eq. (2.69) in Eq. (2.67) and on rearrangement, the diffusion velocity can be obtained using following equation

$$\vec{u}_d = \frac{\frac{\tilde{D}}{\tau\, e_s^2}}{\left(1 + \frac{\tilde{D}}{\tau\, e_s^2}\right)} \left(\frac{\sum_i f_i\, \vec{e}_i}{\sum_i f_i} - \vec{u}\right). \tag{2.70}$$

The diffusion velocity $\vec{u}_d$ is finally added to velocity term before computing the collision step. Above approach is fully local and was found to be more stable compared to the use of finite difference scheme to compute the concentration gradient. The proposed approach is easy to implement into existing LB scheme and comes with a marginal increase in computational efforts.

Implications of diffusion velocity formulation

The diffusion velocity formulation carries several implications. The basic purpose of the formulation is to numerically solve, within an LB framework, problems with large variation in diffusion coefficients with adequate accuracy, stability and the efficiency. As the physical time step is inversely related to the diffusion coefficient (see Section 2.2.7 Eq. (2.76)), time step can be increased by transferring part of the diffusion flux in the advection term, i.e. by setting $D_{ref} < D_0$. Time stepping flexibility, however, has its upper bound which still ensures reasonably accurate solution. Accuracy of the solution decreases with the increase of time step due to the explicit nature of the LBM and possibly larger numerical diffusion due to higher diffusion velocity in case of linear EDF and orthogonal lattices. Apart form the accuracy issues, the introduced diffusion velocity affects the stability as well. Because the diffusion velocity formulation introduces an additional velocity, even in pure diffusion systems it is necessary to examine its effect on the accuracy and stability when $D_{ref} \neq D$. To highlight this effect let us consider a simple one dimensional case where left boundary is a concentration boundary and diffusion occurs inward in the domain. For this case, if only diffusion is considered the field velocity is zero and the grid Courant number (Cr) is thus defined as

$$Cr = \frac{\Delta t |\vec{u}_d|}{\Delta x} \tag{2.71}$$

In LB simulations Δt and Δx are usually set to 1 and hence the $Cr = |\vec{u}_d|$. For stability reasons the maximum Courant number that can be achieved in LB simulation is one and $|\vec{u}_d| < 1$. In case of very large time steps (i.e. $D_{ref} < D_0$) $|\vec{u}_d|$ as given by Eq. (2.67) will be maximum when $\frac{\Delta C}{C} \to 1$ and hence $|\tilde{D}| < 1$ to ensure $Cr < 1$. In case of external velocity field, $Cr < 1 \implies |\vec{u}_d| + |\vec{u}| < 1$.

In pure diffusion case the grid Peclet number (Pe) is defined as

$$Pe = \frac{|\vec{u}_d|\Delta x}{D_{ref}} \tag{2.72}$$
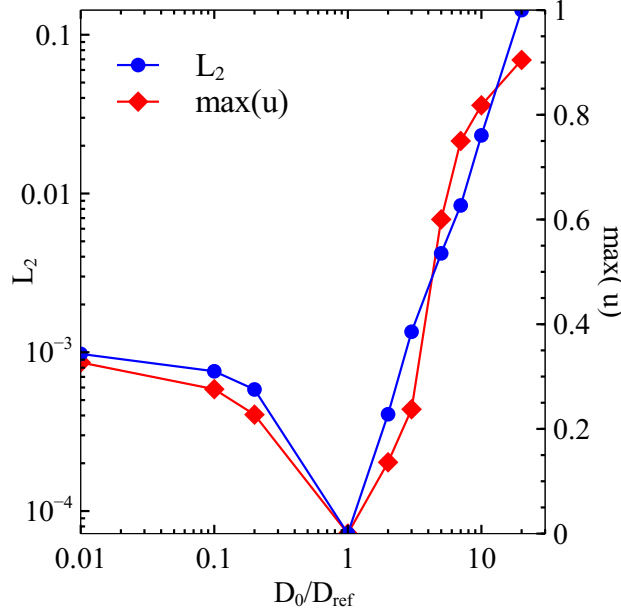
Figure 2.2: Behaviour of diffusion velocity formulation in terms of accuracy and stability for pure diffusion

As Δx is usually taken as 1, the value of Pe equals to $\frac{|\vec{u}_d|}{D_{ref}}$. Further under the arguments presented above for very high time steps

$$Pe \approx \frac{|\tilde{D}|}{D_{ref}} = \left| 1 - \frac{D_0}{D_{ref}} \right| \tag{2.73}$$

This equation suggests that if Pe^{max} is the maximum Peclet number achievable for SRT scheme then the D_{ref} should be selected such that $\frac{D_0}{D_{ref}} \leq (Pe^{max} + 1)$ to ensure stable and accurate solutions. The stability and accuracy of SRT scheme has been studied in detail in Refs. [74, 79]. In case if advection is considered Pe is defined as

$$Pe \approx \frac{|\vec{u}_d + \vec{u}|\Delta x}{D_{ref}} \tag{2.74}$$

The above equation suggests that in case of advection-diffusion equation the D_{ref} should be selected such that $\frac{D_0}{D_{ref}} \leq \left(Pe^{max} + 1 - \frac{|\vec{u}|\Delta x}{D_0} \right)$ to ensure stable and accurate solution. It can be further noted that in Eq. (2.74) D_{ref} now defines the grid Peclet number instead of D_0. Hence if the $D_{ref} > D_0$ the grid Peclet number can be effectively reduced even if relaxation parameter is kept close to 1. Thus stable and accurate solution can be achieved even at very high Peclet number. However as time step is inversely proportional to diffusion coefficient (as given by Eq. (2.76)) selecting higher D_{ref} reduces the time step. Another constraint for orthogonal lattices and schemes with linear EDF as discussed previously is that $\frac{\vec{u}\cdot\vec{u}}{e_s^2} \ll 1$ to avoid errors associated with numerical diffusion.

The points made above can be highlighted by a simple one-dimensional diffusion problem in a 0.1 m long domain, discretized in 100 nodes and with diffusion coefficient $D_0 = 10^{-11}$
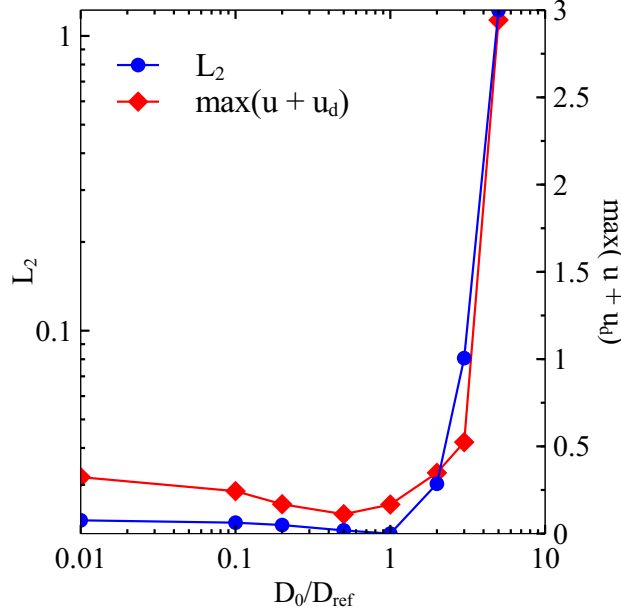
Figure 2.3: Behaviour of diffusion velocity formulation in terms of accuracy and stability for advection-diffusion case

m^2/s. Initially, the concentration in the domain is 0 mol/m^3 and a constant concentration of 1 mol/m^3 at the left boundary. D2Q5 lattice with linear EDF was chosen for simulation. Relaxation time τ is set to 1 which leads to time step $\Delta t = 0.193$ days when $D_0 = D_{ref}$. Relative error with respect between the numerical solution and analytical solution[96] is represented in terms of L_2 error norm which is given as

$$\|L_2\| = \sqrt{\frac{\sum \left(C_{num} - C_{any}\right)^2}{\sum \left(C_{any}\right)^2}} \tag{2.75}$$

here C_{num} and C_{any} being the concentration matrix obtained by numerical solution and analytical solution respectively. The relative errors are computed at t = 200 days for different values of refrence diffusion and are shown in Fig. 2.2. It can be seen in Fig. 2.2 that higher diffusion velocity are associated with higher relative error. Suga [79] has showed that for D2Q5 lattice with linear EDF the grid Peclet number greater than 10 results oscillatory behaviour for any set of the parameters. Therefore based on above discussion $D_0/D_{ref} \leq 11$ to avoid oscillations. It can be seen in Fig. 2.2 that for the choice of D_0/D_{ref} above 10 very high relative error value is observed.

To simulate the advection-diffusion the case for diffusion discussed above is extended by additional field velocity u=10^{-8} m/s. This choice of velocity gives grid Peclet number of 1. In this case from above discussions it can be deduced that $D_0/D_{ref} \leq 10$ to avoid oscillations. It can be observed from Fig 2.3 that for the choice of D_0/D_{ref} around 5 very high relative error value are observed and instability was observed in simulations for D_0/D_{ref} greater than 7.

2.2.7 Conversion from LBM units to physical units

Lattice Boltzmann computations are usually carried out in lattice length units (lu) and lattice time units (ltu) which are different from physical units. Hence, for real-world problems conversion is required between two unit systems. This can be done by dimensional mapping between these two systems for base quantities (viz., mass, length, amount of substance and time) through conversion factors. Multiplying these conversion factors with quantities in lattice units, corresponding quantities can be derived in terms of physical units. Mass mapping is not required for advection diffusion equation and factor for amount of substance N_0 can be set to 1. Length mapping is imposed by the choice of discretization. The lattice spacing Δr is usually set to 1 lu and corresponding length factor L_0 would be equal to the spacing between the lattice nodes in physical units. Time mapping is obtained from the diffusion coefficient. Δt is usually set to 1 ltu. The diffusion coefficient in terms of lattice units for a given relaxation parameter τ can be determined using Eq. (2.43). Correspondingly the conversion factor for time is determined as

$$T_0 = L_0^2 \frac{e_s^2 \left(\tau - \frac{1}{2}\right)}{D_0} \tag{2.76}$$

As Δt in LB units is 1 the time step in terms of physical units would be equal to T_0. The conversion factors for derived quantities such as molar concentration, flux and velocity can be expressed in terms of conversion factors for base quantities as $N_0^1 L_0^{-3} T_0^0$, $N_0^1 L_0^{-2} T_0^{-1}$ and $N_0^1 L_0^{-1} T_0^0$, respectively.

2.2.8 Initial and Boundary conditions

In this section procedures to implement initial and boundary conditions for transport equation are presented.

Initial conditions

The initial conditions are usually specified in terms of macroscopic variables i.e. C and $\vec{u}$. As the primary variable in lattice Boltzmann equation is distribution function f_i, it needs to be initialized in beginning of simulation. The equilibrium distribution function is used as initial condition for f_i.

Zero flux Boundary at Solid nodes

As given by Eq. 2.2 a normal gradient at solid boundary is enforced as zero. This essentially can be implemented in lattice Boltzmann method using bounce back condition. The bounce back condition essentially implies that the unknown incoming f_i's are set to

the outgoing f_i's in opposite lattice direction i.e.

$$f_i = f_{-i} \tag{2.77}$$

In case of higher order lattices above condition induces no slip conditions i.e. both normal and tangential components are zero. Pure slip boundary condition to ensure that only normal components are forced to zero can be implemented through specular reflection bounce back condition [97, 98]. In specular reflection, for orthogonal direction bounce back condition is applied whereas the diagonal f_i are reflected as a ray of light.

Care should be taken while implementing the bounce-back boundary condition. Bounce-back scheme is second order accurate only in the case when the boundary is located midway between the two links.

Periodic boundary conditions

Periodic boundary can be used in the case were the solution pattern is repeating itself. It is quite straight forward to implement the periodic boundary in lattice Boltzmann method. The periodic boundary can be imposed by assigning the outgoing distribution function to the incoming distribution function at other end. The typical two dimensional domain is shown in Fig. 2.4. The unknown distribution in left boundary as shown in Fig. 2.4 are f_1, f_5 and f_8. The unknown distribution in right boundary as shown in Fig. 2.4 are f_6, f_3 and f_7. The periodic boundary condition at left boundary can be imposed by

$$f_i(0, y, t + \Delta t) = f_i(l_x, y, t), \qquad i = 1, 5, 8 \tag{2.78}$$

and correspondingly at the right boundary the periodic boundary is imposed as

$$f_i(l_x, y, t + \Delta t) = f_i(0, y, t), \qquad i = 3, 6, 7 \tag{2.79}$$

The above periodic boundary condition ensures that

$$C(0, y, t + \Delta t) = C(l_x, y, t + \Delta t) \tag{2.80}$$
$$\hat{n} \cdot \vec{\nabla} C(0, y, t + \Delta t) = -\hat{n} \cdot \vec{\nabla} C(l_x, y, t + \Delta t)$$

Generalized boundary conditions

[4] The generalized boundary conditions as given by Eq. (2.3) are defined in terms of macroscopic variable. However, in lattice Boltzmann method implementation of boundary condition means determining the values of unknown distribution function (see Fig. 2.4).

---

[4]This section has been presented at DSFD 2014 conference
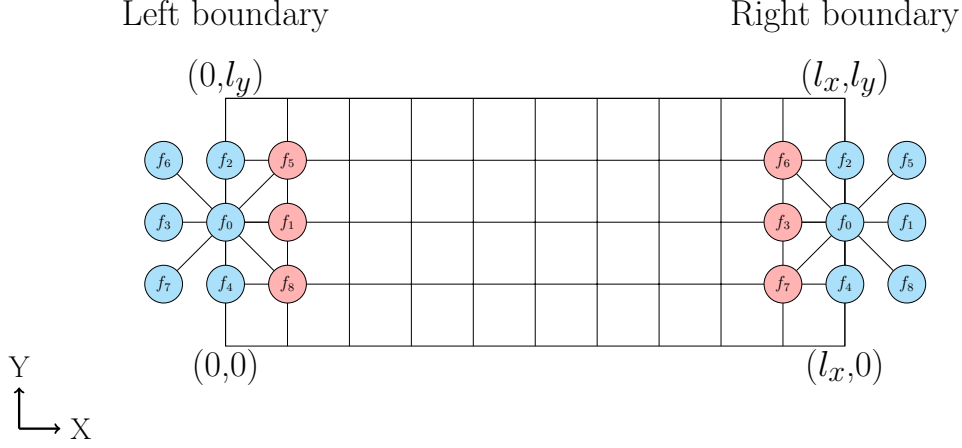
Figure 2.4: Sketch of the typical 2D domain with D2Q9 lattice. The unknown distribution functions at the boundary are marked red and the known distribution function at boundary are marked blue. l_x and l_y are the length of domain in x and y direction.

Several methods exist to determine the values of unknown distribution functions which represent a specific physical boundary condition. This section first reviews the existing approaches used to define different boundary conditions in LB and presents a new boundary condition utilizing the definition of gradient as given by Eq. (2.62) (Approach IV)

I **Bounce back of non-equilibrium part**

Zhang *et al.* [99] proposed this approach to implement generalized boundary conditions for advection-diffusion equation. The primary assumption in this approach that the non-equilibrium distribution function (f_i^{neq}) of opposite velocity direction are bounced back with negative sign i.e. $f_i^{neq} = -f_{-i}^{neq}$. This in turn gives

$$
\begin{aligned}
f_i(\vec{r}_b) + f_{-i}(\vec{r}_b) &= f_i^{eq}(\vec{r}_b) + f_{-i}^{eq}(\vec{r}_b) \\
&= 2w_i C(\vec{r}_b) \left[1 + I_n \left(\frac{\vec{e}_i \vec{e}_i : \vec{u}\vec{u}}{2e_s^4} - \frac{\vec{u} \cdot \vec{u}}{2e_s^2} \right) \right]
\end{aligned}
\tag{2.81}
$$

where I_n is one if quadratic EDF is used and zero if linear EDF is used. $\vec{r}_b$ is the position vector of boundary. The gradient of concentration required in Eq. (2.3) can be computed using finite difference scheme and correspondingly the concentration at the boundary can be calculated from prescribed boundary conditions as

$$
C(\vec{r}_b) = \frac{A_3 - A_2 C(\vec{r}_f) \frac{\hat{n} \cdot e_i}{\Delta x}}{A_1 - A_2 \frac{\hat{n} \cdot e_i}{\Delta x}}
\tag{2.82}
$$

$\vec{r}_f$ is the position vector of the fluid node adjacent the the boundary. This approach can be viewed as an extension of the anti-bounceback scheme (as described in [100]) wherein the concentrations at the wall are determined by above equation.

II **Extrapolation of non-equilibrium part**

The idea behind this boundary condition is that the distribution function can be separated into equilibrium and non-equilibrium part [101, 102].

$$f_i(\vec{r}_b) = f_i^{eq}(\vec{r}_b) + f_i^{neq}(\vec{r}_b) \tag{2.83}$$

Generally $f_i^{neq} \ll f_i^{eq}$ and hence it can be approximated as $f_i^{neq}(\vec{r}_b) = f_i(\vec{r}_f) - f_i^{eq}(\vec{r}_f)$. The unknown distribution functions at boundary can be correspondingly determined as

$$f_i(\vec{r}_b) = f_i^{eq}(\vec{r}_b) + f_i(\vec{r}_f) - f_i^{eq}(\vec{r}_f) \tag{2.84}$$

The concentration at the boundary needed to compute f_i^{eq} can be obtained using Eq. (2.82).

III **Regularized boundary condition**

In this approach all the particle distribution functions at the boundary are replaced with the regularized distribution function [103, 104] as given below

$$f_i(\vec{r}_b) = f_i^{eq}(\vec{r}_b) + f_i^{(1)}(\vec{r}_b) \tag{2.85}$$

For advection-diffusion equation the $f_i^{(1)}$ can be defined as

$$f_i^{(1)} = -\tau w_i \vec{e}_i \cdot \vec{\nabla} C \tag{2.86}$$

This choice of $f_i^{(1)}$ respects the constraints needed to recover advection diffusion equation i.e. $\sum_i f_i^{(1)} = 0$ as given by Eq. (2.27) and $\sum_i f_i^{(1)} \vec{e}_i = -\tau e_s^2 \vec{\nabla} C$ as given by Eq. (2.61) (if $\vec{u} \cdot \vec{u}$ term is ignored). This choice of $f_i^{(1)}$ is similar to the one used by Huang *et al.* [104]

The gradient needed in Eq. (2.86) can be obtained using forward difference scheme which is a non local approach. Alternatively $f_i(\vec{r}_b)$ can be first computed using Eq. (2.85). $f_i^{(1)}$ for the unknown velocity direction can be taken as $f_{-i}^{(1)}$. This is valid due to the choice of $f_i^{(1)}$ as given by Eq. (2.86). $f_i^{(1)}$ can be computed as $f_i - f_i^{eq}$. Once all f_i are determined, gradient can be obtained using Eq. (2.62). Once gradients are computed all the particle distribution functions at boundary are replaced with the regularized distribution functions. The concentration at the boundary can be computed using Eq. (2.82).

IV **Bounce back of non-equilibrium part with computation of gradient using Eq.** (2.62)

In case of orthogonal lattices with linear EDF under the assumption $f_i = -f_{-i}$ Eq. (2.81) can be rewritten as

$$C(\vec{r}_b) = \frac{f_i + f_{-i}}{2w_i} \tag{2.87}$$

Using (2.62) $\hat{n} \cdot \vec{\nabla} C$ is given as

$$\hat{n} \cdot \vec{\nabla} C = \frac{1}{\tau e_s^2} \left[(f_i \vec{e}_i + f_{-i} \vec{e}_{-i}) - \vec{u} \left(\frac{f_i + f_{-i}}{2w_i} \right) \right] \cdot \hat{n} \tag{2.88}$$

Substituting above equations in Eq. (2.3) and rearranging, the unknown f_i at the boundary can be computed as

$$f_i = \frac{A_3 - f_{-i} \left[\frac{A_1}{2w_i} + \frac{A_2}{\tau e_s^2} \left(\frac{\vec{u}}{2w_i} - \vec{e}_{-i} \right) \cdot \hat{n} \right]}{\frac{A_1}{2w_i} + \frac{A_2}{\tau e_s^2} \left(\frac{\vec{u}}{2w_i} - \vec{e}_i \right) \cdot \hat{n}} \tag{2.89}$$

It is interesting to note that the above equation gives a bounce back scheme for Neumann boundary condition and anti bounce back scheme for Dirichlet boundary condition.

V **Difference of boundary concentration and incoming distribution functions**
In case of orthogonal lattices only one distribution function at boundary is unknown. In this case the unknown distribution function can be simply obtained as the difference between the concentration at the boundary and the sum of incoming distribution function. That is

$$f_i = C(\vec{r}_b) - \sum_{j \neq i} f_j \tag{2.90}$$

The concentration at the boundary wall can be then calculated using Eq. (2.82).

Comparision between different approaches to implement boundary conditions

A SRT scheme using $D2Q5$ lattice with corrected linear EDF is used to make comparison between different approaches to implement boundary conditions. The dimensions of simulation domain was taken as 200×30 lu. Simulations were carried out for four different relaxation parameters viz., 0.6, 0.8, 1 and 2.The corresponding diffusion coefficient can be obtained using Eq. (2.43). The accuracy and convergence of different approaches for both Dirichlet and Cauchy boundary conditions were tested. For the case of Dirichlet boundary, the left boundary was set as constant concentration boundary with values of A_1, A_2 and A_3 as 1, 0 and 50 respectively. All other boundary conditions were set as zero flux boundaries. In case of Cauchy boundary, A_1, A_2 and A_3 were set as $\vec{u}$, $-D_0$ and $50\vec{u}$ respectively for left boundary. All other boundaries were set as zero flux boundaries.
Fig. 2.5 and Fig. 2.6 shows performance of different approaches for Dirichlet boundary conditions and Cauchy boundary conditions respectively for different grid Peclet number at the end of 300 ltu. For these simulations the velocity was set as $Pe \times D_0$ and zero for x and y directions respectively. The L_2 error norm is computed using Eq. (2.75) and the
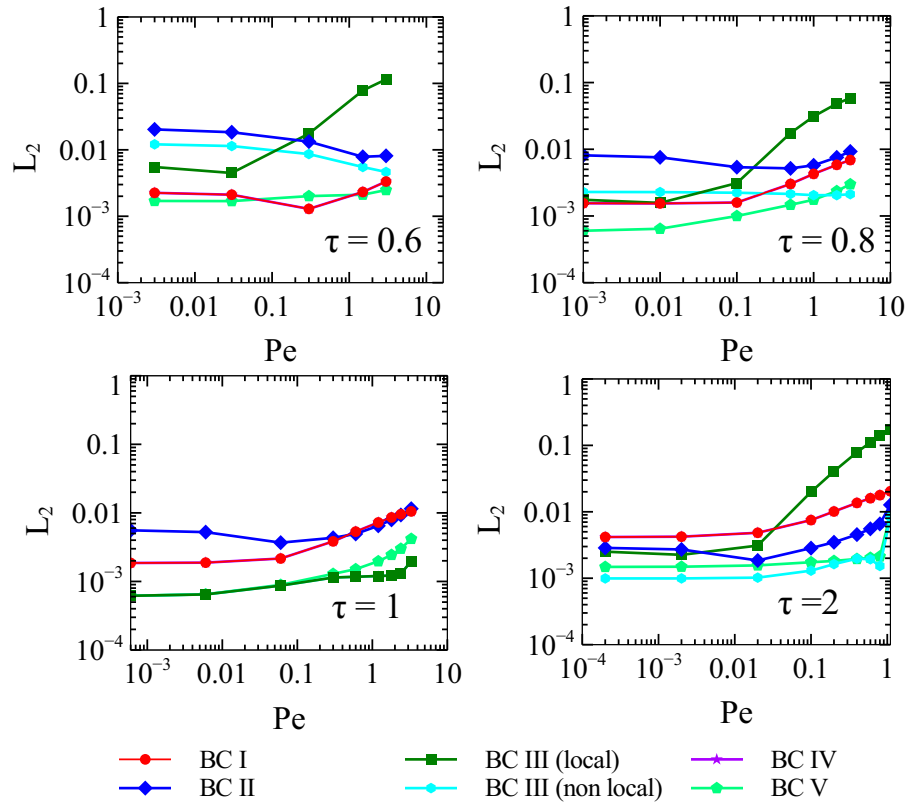
Figure 2.5: Performance of different lattice Boltzmann implementation for Dirichlet boundary condition at different grid Peclet numbers.
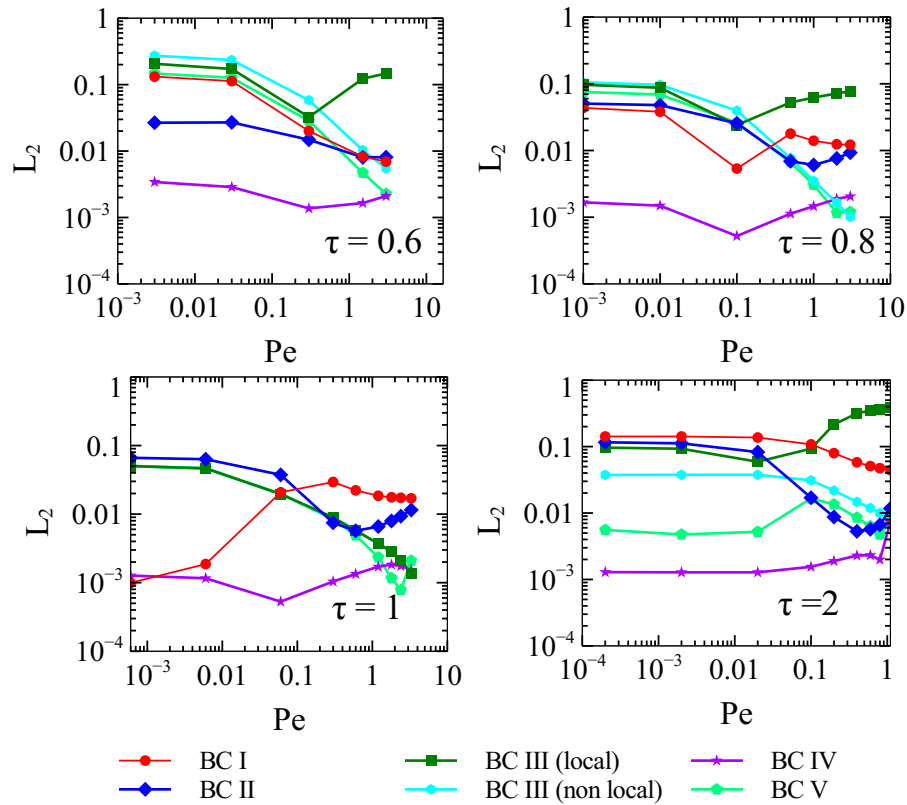
Figure 2.6: Performance of different lattice Boltzmann implementation for Cauchy boundary condition at different grid Peclet numbers.
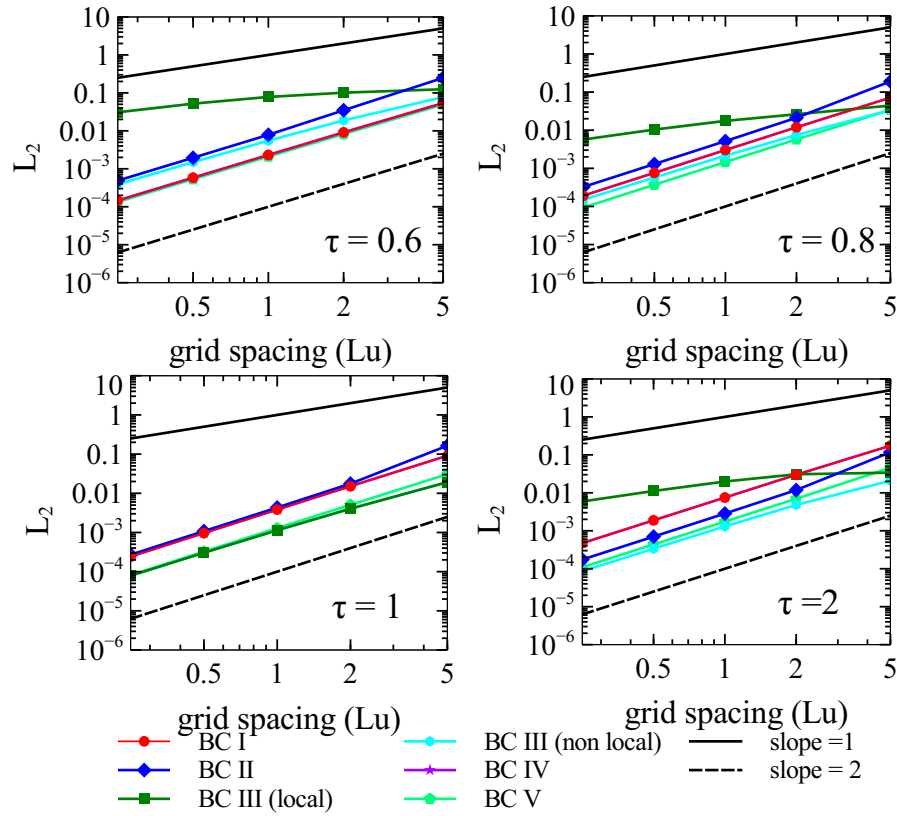
Figure 2.7: Convergence of different lattice Boltzmann implementation for Dirichlet boundary condition (velocity in x-direction equal to 0.05 Lu/Ltu)
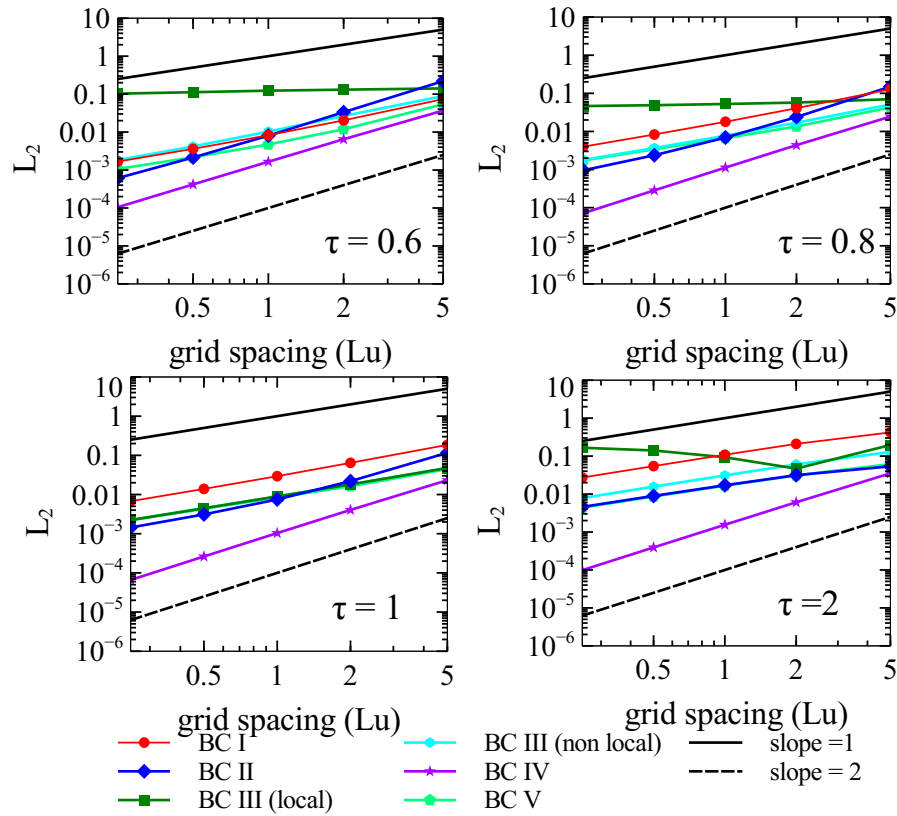
Figure 2.8: Convergence of different lattice Boltzmann implementation for Cauchy boundary condition (velocity in x-direction equal to 0.05 Lu/Ltu)

relevant analytical solution can be found in Ref [96]. The grid spacing was kept as 1 lu for these simulations. The convergence of different implementations for Dirichlet and Cauchy boundary are shown in Fig. 2.7 and Fig. 2.8 respectively. For these simulations the velocity in x direction was kept constant at 0.05 Lu/Ltu. To keep the relaxation parameter constant in these simulation the time steps were appropriately scaled as explained in section 2.2.7. As seen in Fig. 2.7 all approaches are second order convergent for Dirichlet boundary condition. However for Cauchy boundary condition approach IV is the only second order convergent boundary condition. All other approaches show only first order convergence for Cauchy boundary condition as they use first order finite difference scheme to approximate the gradients. These figures also show that the local regularized approach show first order convergence for Cauchy boundary and second order convergence for concentration boundary only for $\tau = 1$ and for other values of the relaxation parameters it does not show a good convergence behaviour. The possible reason for this can be that as the collision step is not regularized in these simulations, the reconstructed $f_i^{(1)}$ used to compute gradients do not preserve the moments correctly.

The numerical analysis reveals that both in terms of accuracy and convergence at different Peclet number and relaxation parameters approach IV outperforms other approaches. The advantage of using this approach is that it is fully local which is unique for a second order convergent boundary condition. This approach for orthogonal lattices can be viewed as an extension of bounce-back/anti-bounce-back condition and hence can be easily applied for arbitrary domain geometry. However, it is not straight forward to extend this approach to higher order lattices due to the contribution of the unknown diagonal term in $\sum f_i e_i$ which makes the system of equations non-linear.

2.3   Benchmarks and Examples

In the previous section existing LB methods for solute transport at pore-scale were introduced. Further a newly developed diffusion velocity LB scheme was introduced which allows for arbitrary variability of dissipative parameters keeping the relaxation time constant and can be used to accelerate simulations by increasing the D_{ref} to be lower than D_0. These features of SRT diffusion velocity LB scheme are highlighted through simple benchmarks and examples. All simulations in this section have been carried out using D2Q5 lattice with linear EDF. For diffusion velocity SRT scheme the relaxation parameter τ is set to 1 unless specified. The problem definitions in some benchmarks and examples are not truly representative of a pore-scale media but they are presented in this section to highlight different features of SRT diffusion velocity LB scheme.
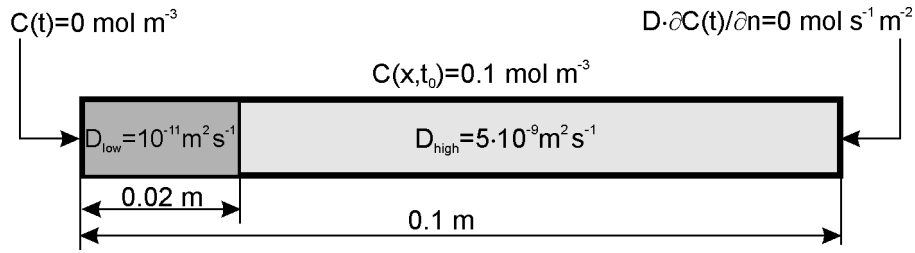
Figure 2.9: Definition of the diffusion problem with large variations of spatial diffusion coefficients.

2.3.1 Spatial variability of diffusion coefficients using diffusion velocity scheme

The ability of the diffusion velocity formulation to deal with highly contrasting diffusion coefficient within a domain is demonstrated using a simple one dimensional model as shown in Fig. 2.9. Initial domain concentration is set to 0.1 mol/m³. Left boundary condition is of Dirichlet type with concentration 0 mol/m³ and right boundary is no-flux Neumann boundary. The domain is 10 cm long, discretized in 100 nodes and is divided into two domains. The left domain is 2 cm (20 nodes) long with a low diffusion coefficient ($D_{low} = 10^{-11}$ m²/s). The diffusion coefficient in the remaining 8 cm (80 nodes) is 500 times higher ($D_{high} = 5 \times 10^{-9}$ m²/s). Results are given at time 500 days. The reference solution is obtained using a Comsol Multiphysics finite element code with sufficiently fine discretization to ensure a grid independent solution. Relaxation time τ is set to 1. The obvious decision for setting the reference diffusion to the lowest time step ($D_{ref} = D_{high}$) gives a good agreement with the reference solution as shown in (Fig. 2.10(a)). However, based on the given discretization, the physical time step would be 33.3 seconds which leads to 1296000 iterations to reach 500 days. Reduction of calculation time can be accommodated through a lower reference diffusion D_{ref}. The method was tested for (e.g. $D_{ref} = D_{low}$) which reduces the number of iterations to 2592 iterations. The agreement between results is good until $D_{ref} = D_{low}/7$ (370 iterations). Diffusion velocity in this case is 0.85 in lattice units which is below the stability limit value of one. For $D_{ref} = D_{low}/8$ onwards ($D_{ref} = D_{low}/10$ in Fig. 2.10(b)), diffusion velocity in lattice units exceeds one which results in oscillatory solution.

On a similar, but slightly more complex diffusive case which includes contrasting diffusion coefficients it is of interest to compare the two approaches which deal with the variation of diffusion coefficients in SRT scheme; the first one being by the variation of the relaxation time and the second one by the diffusion velocity scheme. Three regions with different diffusion coefficients are defined in order to impose multiple contrasting conditions within the domain. The diffusion coefficient in the first and last 2 cm equals $D_{low} = 10^{-11}$ m²/s from the previous example, while the middle domain has a higher diffusion. Three cases are presented in which D_{high} is respectively 100, 500, and 2000 times the value of D_{low}. The reference diffusion D_{ref} is set to D_{low} in all cases which results in 2592 iterations to
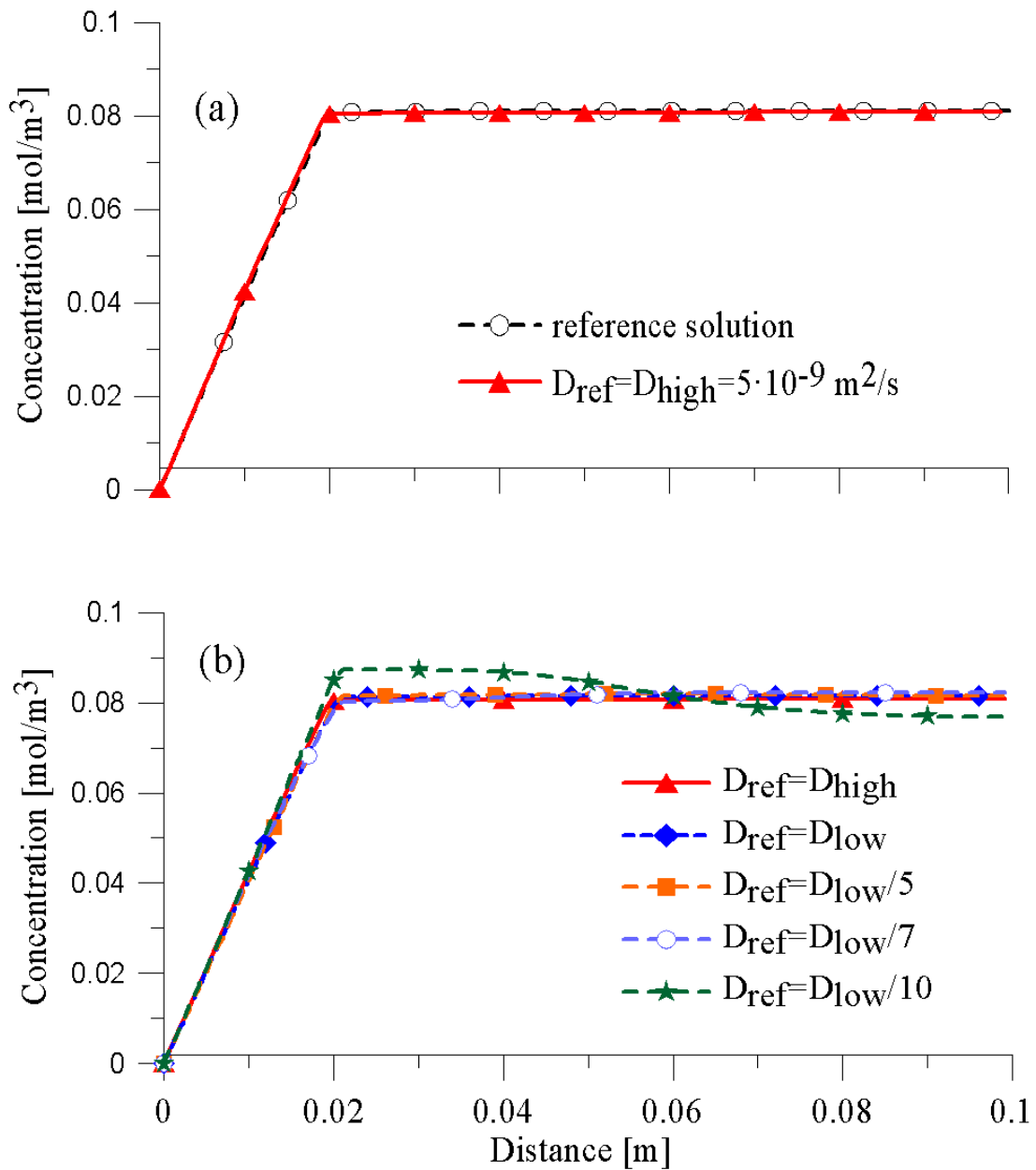
Figure 2.10: Solution of two domain problem with contrasting diffusion coefficients in domains; comparison with the reference solution at 500 days (a) for LB time step based on $D_{ref} = D_{high}$ and (b) influence of time step to the accuracy of the results.

C(t)=0 mol m^{-3}

D·∂C(t)/∂n=0 mol s^{-1} m^{-2}

C(x,t$_0$)=0.1 mol m^{-3}

D$_{low}$

D$_{high}$

D$_{low}$

0.02 m

0.02 m

0.1 m
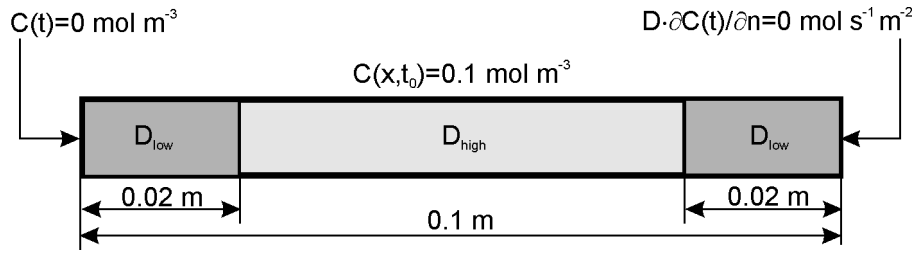
Figure 2.11: Definition of the diffusion problem with spatially variable diffusion coefficients in three domains.

reach the final time of 500 days. Corresponding relaxation time τ values which provide the same number of iterations are $\tau = 1$ in the first and the last region, while the values in the middle region depend on D_{high}; consequently, $\tau = 50.5$, $\tau = 250.5$ and $\tau = 1000.5$ for $D_{high} = 100$,$D_{high} = 500$, and $D_{high} = 2000$ times the value of D_{low}, respectively. Initial and boundary conditions are the same as in the previous case. Because of lower diffusion coefficient on the left hand side region there is a high concentration gradient until the transition point to higher diffusion coefficient. There the concentration profile is almost flat (i.e. with low concentration gradient). The low diffusion coefficient in the last 2 cm causes again a steeper concentration gradient towards the right hand side boundary.

Fig. 2.12 illustrates that the approach using the relaxation time is only stable for lower ratios of the diffusion coefficients. As such, with a ratio of only 100, both approaches are in good agreement with the reference solution as shown in Fig. 2.12(a). Increase of diffusion coefficient ratios causes the relaxation time formulation to give non-physical results (decrease of concentration on interface of domain with different diffusion coefficients) (Fig. 2.12(b)). This instability increases with larger contrasts in diffusion coefficients and is clearly observed in Fig. 2.12(c) for the ratio of 2000. The instability related to the τ variability can be reduced by the lower reference τ on the account of lower time step and consequent more iterations to reach the same final time. Similar accuracy as obtained by the diffusion velocity formulation in Fig. 2.12(c) can only be obtained by five times more time steps when τ is varied (results not shown). On the other hand, the diffusion velocity formulation provides correct results in all cases even for much larger ratios. This demonstrates that the diffusion velocity formulation outperforms substantially the classical SRT formulation when dealing with large variation of diffusion coefficients.

2.3.2 Spatial and temporal variability of diffusion coefficients using diffusion velocity scheme

One dimensional cases in section 2.3.1 served for the analysis of diffusion velocity formulation behaviour in terms of accuracy and stability. The additional analysis demonstrates the applicability of the diffusion velocity formulation to higher space dimensions and for non-linear problems. Non-linearity in this 2D problem is introduced through the diffusion
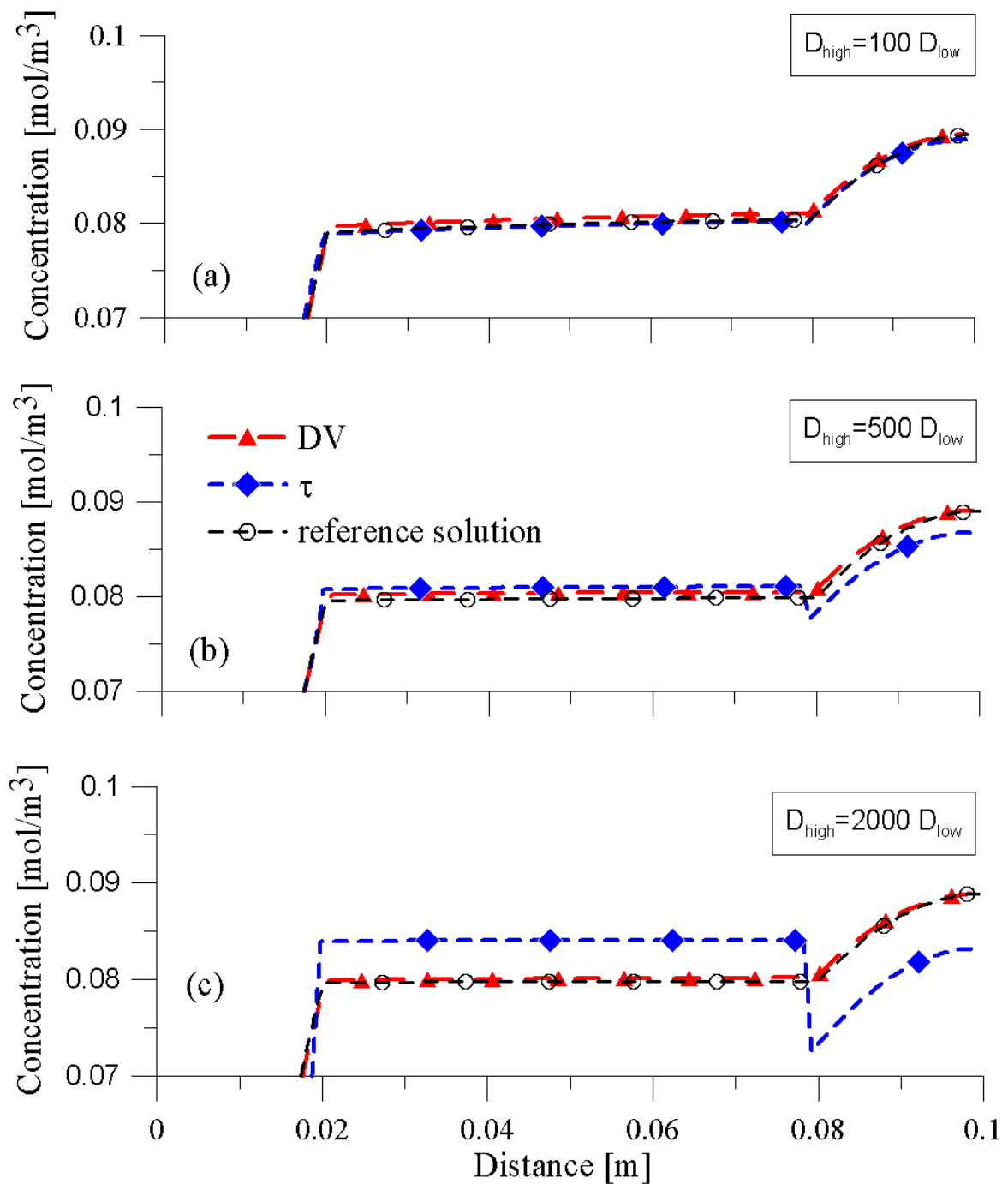
Figure 2.12: Comparison of numerical solution at 500 days for the domain with three different diffusion coefficients for classical SRT formulation (denoted as τ) and for new diffusion velocity (DV) formulation. Y-axis between 0 mol/m^3 and 0.07 mol/m^3 is not shown in figures.
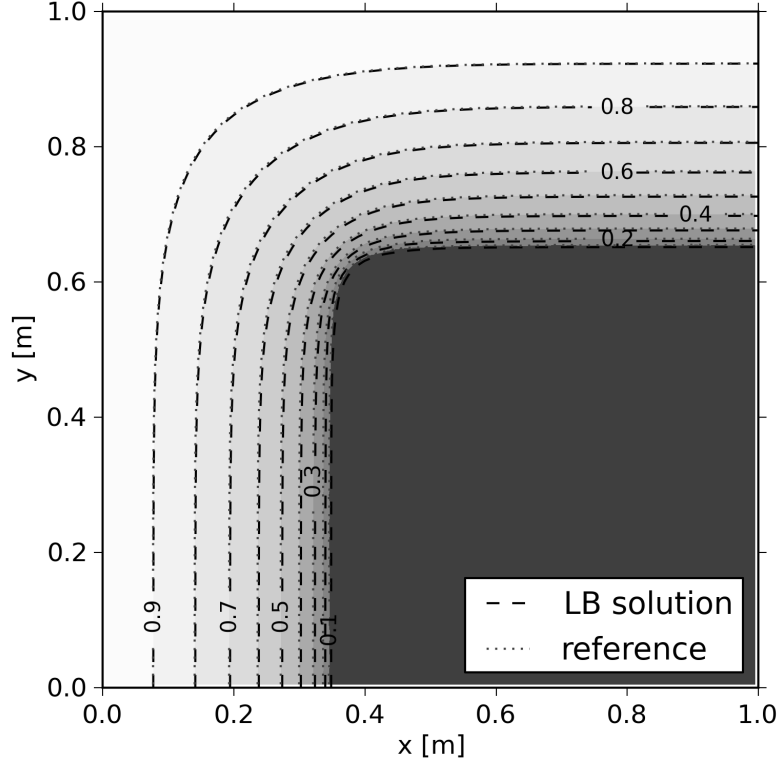
Figure 2.13: Results for 2D porous medium equation with $n = 2$ at final time 0.1 s. Lighter grey colour denotes higher C values and darker lower C values

coefficient dependent on the primary variable. The numerical example is taken from the field of porous medium equations applicable to many physical problems from gas flow through porous medium, or non-linear heat transfer (e.g. heat propagation by radiation occurring in an ionized gas) [105]. The general formulation of this equation is

$$\frac{\partial C}{\partial t} = \nabla \cdot (aC^n \nabla C), \quad n \geq 0 \tag{2.91}$$

where n and a are positive constants. For the purpose of numerical analysis we chose a 2D analysis with mixed Dirichlet and Neumann boundary conditions with $a = 1$ and $n = 2$. The computational domain of 1m $\times$ 1m is initially at value $C = 0.01$. Dirichlet boundary conditions are at the left and the top boundaries with a value $C = 1$. Hence, the values of diffusion coefficient aC^n extend over four orders of magnitude and vary with time as a consequence of field concentration evolution. Bottom and right boundaries are no-flux boundaries. Similar to previous cases the relaxation time τ is set to a constant value of 1. The reference diffusion coefficient value $D_{ref} = 1$. The domain is discretized in 100×100 nodes. The solution is compared to the results obtained by a COMSOL Multiphysics finite element method (FEM) based code at time 0.1 s. COMSOL model was discretized into 9440 FEM elements which resulted in sufficiently small oscillations in the regions with low diffusion coefficients when C is close to 0.01. No oscillations, however, are observed for diffusion velocity LB formulation. Results in Fig. 2.13 demonstrate a very good agreement

$C(t)=0$ mol m^{-3}

$C(x,t_0)=0.1$ mol m^{-3}

$D \cdot \partial C(t)/\partial n = 0$ mol s^{-1} m^{-2}

u_a

$D_{low}=10^{-11}$ m^2 s^{-1}

0.5 m
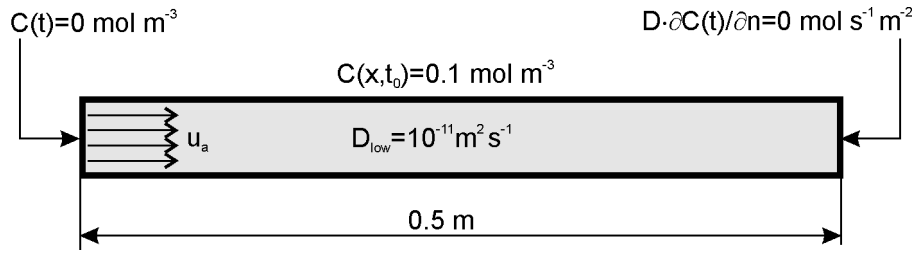
Figure 2.14: Problem definition for advection cases.

between the reference and the diffusion velocity LB solution while no stable solution was found for the classical SRT formulation.

2.3.3 Applying diffusion velocity to highly advective transport problems

As discussed previously the stability of the solution for advection-diffusion transport can be considerably improved by reduction of time step which can be achieved through the increase of the reference diffusion D_{ref}. The first example represents advection cases with low grid Pe numbers, 1 and 10, respectively. 0.5 m long domain is discretized with 500 elements. Initial and boundary conditions are shown in Fig. 2.14. With a physical diffusion $D = 10^{-11}$ m^2/s the corresponding Pe numbers are $Pe = 1$ and $Pe = 10$ for velocities 10^{-8} m/s and 10^{-7} m/s, respectively. The classical SRT using $\tau = 1$ still provides stable solution for $Pe = 1$, while for $Pe = 10$ solution diverges (results not shown). For mesh $Pe = 1$ and time step based on the physical diffusion, the results are in very good agreement with the reference solution. Since there is some margin to the stability limit, the reference diffusion can be lowered by a factor 2 i.e. double the time step, while still providing an accurate solution. Further acceleration worsens the accuracy. When total velocity exceeds 1 in terms of lattice units it leads to unstable solution. The results for $Pe = 1$ are presented in Fig. 2.15(a). Two times higher reference diffusion still produces unstable results while further increase (shown for five and ten times diffusion increase) results in a stable solution Fig. 2.15(b).

In order to demonstrate more severe advection problems, one case with a mesh Pe number of 1000 is presented. Such Pe number gives oscillatory results for any relaxation factor τ in SRT [79]. Moreover, when making comparison to the commercial FEM based code, the solution demonstrated visible oscillations. A non-oscillatory FEM solution is only possible with the introduction of artificial diffusion. With the diffusion velocity scheme, stability is obtained by a 10^4 times increased reference diffusion. Further increase in the reference diffusion gives very similar solution as shown in Fig. 2.16.
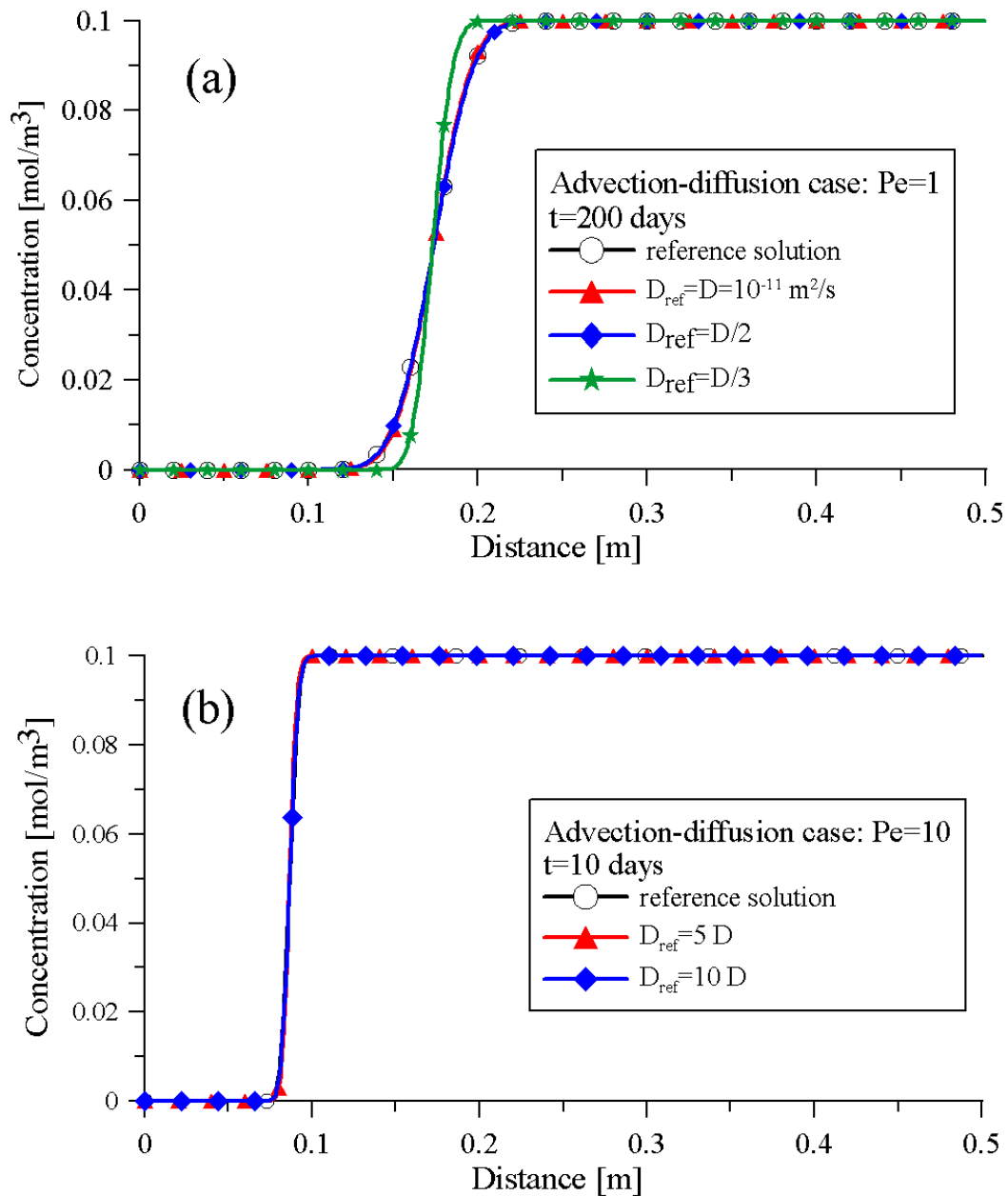
Figure 2.15: Comparison of diffusion/advection problem between the reference solution and different reference diffusion parameters used in diffusion velocity formulation for $Pe = 1$ (a) and $Pe = 10$ (b).
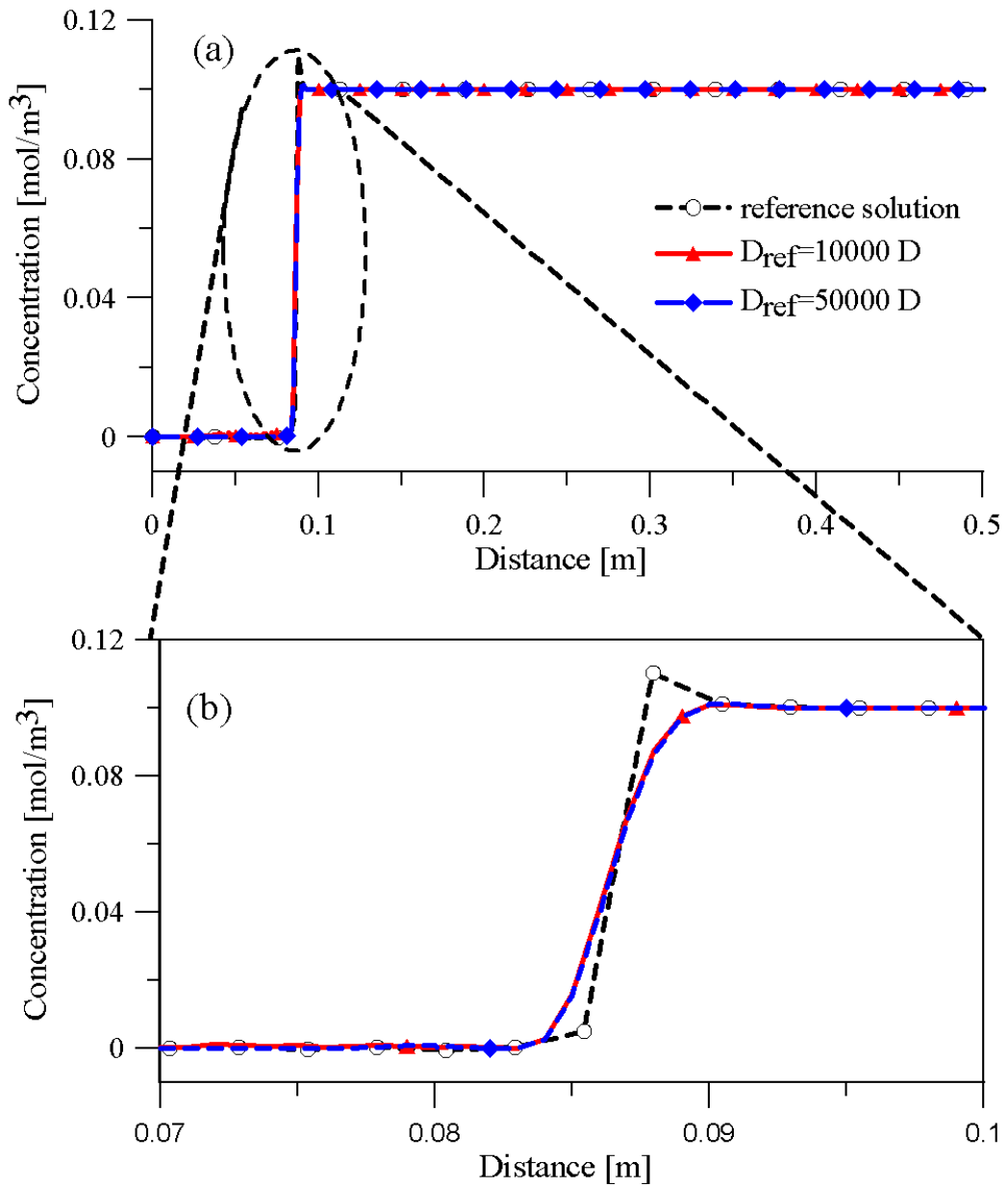
Figure 2.16: Comparison of highly advection problem with $Pe = 1000$; solution at 0.1 day (a) and magnification of the relevant transition (b).

2.4 Conclusions

In this chapter different LB schemes for solute transport at pore-scale have been presented. First existing SRT and TRT LB schemes have been presented along with the Chapman-Enskog expansion. Using the first order terms of Chapman-Enskog expansion a local approach to compute total flux for advection-diffusion equation has been derived. Furthermore a local approach to apply a general boundary condition for orthogonal lattices has been proposed. The numerical experimentation and comparison with other approaches to implement the general boundary condition reveals that the proposed approach outperforms the other methods. Further analysis shows that for the Cauchy boundary condition only the proposed approach gives the second order convergence.

A SRT diffusion velocity LB scheme has been proposed to accommodate for larger spatial variations of diffusion coefficient and with improved stability in advection dominated problems. It is computationally efficient while at the same time provides a considerable flexibility in comparison to the classical SRT LB scheme. The benchmark examples have demonstrated that the proposed formulation allows for much larger variations of diffusion coefficients compared to the variation of relaxation parameter and better accuracy for the same chosen time step. For the pure diffusion case, the formulation is stable in the large spectra of reference diffusion coefficients. The flexibility in the choice of the reference diffusion coefficient can be exploited in two ways: to minimize computational time by increasing the time step and to improve the stability of advection dominated problems. In the latter case, the reference diffusion is set to a higher value. It has been shown that the accuracy for this scheme depends on the total lattice velocity. The bounds for D_0/D_{ref} can be defined in terms of maximum grid Peclet numbers that can be achieved for a given SRT scheme. The values of $D_0/D_{ref} \leq P_e^{max} + 1$ and $D_0/D_{ref} \leq P_e^{max} + 1 - \frac{|\vec{u}|\Delta x}{D_0}$ for pure diffusion and advection-diffusion equations respectively to ensure stable and accurate solution. This conditions are not the exact bounds but give a conservative choice for D_0/D_{ref}. It has been observed that in some cases accurate results are obtained even if these bounds are violated.

In advection dominated cases, the choice of the reference diffusion depends on the magnitude of fluid velocity. With larger fluid velocity the reference diffusion has to be increased, which for a given spatial discretization decreases the Pe and Cr numbers and hence ensures stability. However, the stability is improved at the cost of smaller time step and consequent larger number of iterations to achieve particular physical time. Analysis also shows that for such cases a reference diffusion coefficient exists for which the solution is more accurate compared to the classical SRT formulation.

Lattice Boltzmann method for solute transport in multilevel porous media

In many cases all pore spaces cannot be explicitly represented due to separation of scale and computational limitations. In such cases both continuum scale and pore-scale co-exist. Schematic representations of such system relevant to cement based materials are shown in Fig. 3.1. As shown in Fig. 3.1 in case of cement paste C-S-H is a diffusive solid (through which mass transport can occur) and other solid phases such as clinker and portlandite are relatively non-diffusive (through which mass transport does not occur). Moreover the cement paste contains capillary pores which are filled with pore fluid. Thus when microstructure is resolved, both continuum and pore scales co-exist. Such a system is defined in this thesis as a *Multilevel system* or *multilevel porous media* [1]. The term *multilevel* is use to distinguish *multiscale* from *multilevel* as in scale representation of concrete cement paste only represents one scale. Similarly at mesoscale of a cracked concrete both continuum scale and pore scale co-exists as shown in Fig. 3.1.

In this chapter lattice Boltzmann (LB) schemes to simulate solute transport through multilevel porous media are discussed. The mass transport in multilevel porous media is governed by advection-diffusion equation and the governing equations are presented in 3.1. The LB schemes for multilevel porous media are presented in section 3.2. In particular, extension of SRT diffusion velocity scheme and an existing TRT scheme to simulate mass transport are discussed in this section. A benchmark validating the proposed SRT diffusion velocity formulation for multilevel porous media is presented in section 3.3.

---

[1] The use of the term multilevel is inspired for the similar use for distinguishing multiscale treatment from multilevel treatments in numerical methods [106]

CSH
(diffusive solid)

clinker
(non- diffusive solid)

capillary pores
(filled with pore fluid)

(b)

Cement paste
(diffusive solid)

Aggregates
(non-diffusive solid)

Crack
(filled with pore fluid)

(a)
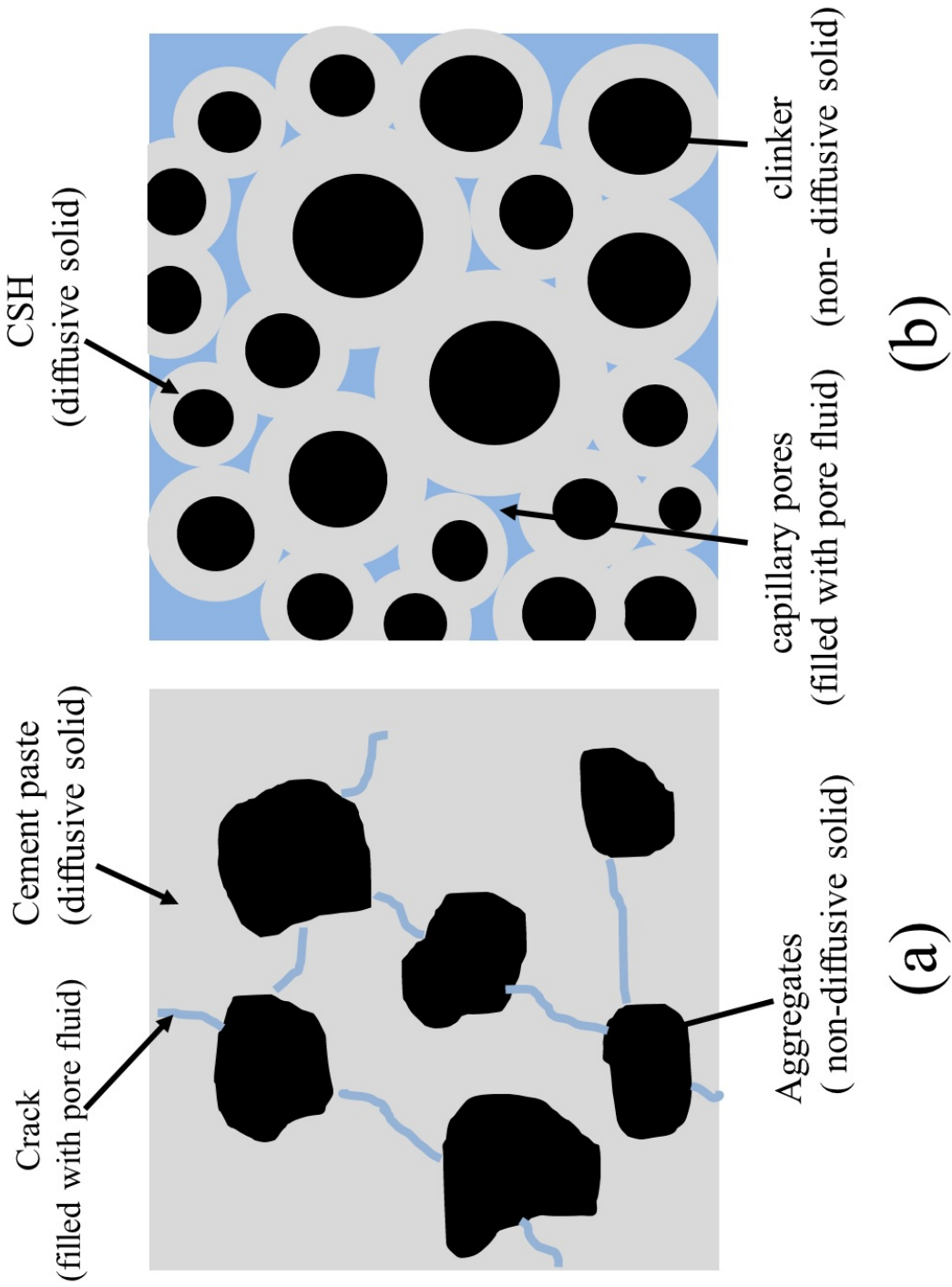
Figure 3.1: A schematic representation of multilevel porous media (a) cracked concrete (b) cement paste (only C-S-H and clinker are considered as the solid phases for illustration)

3.1   Governing equations

The solute transport in the mutlilevel porous media can be described using advection-diffusion equation.

$$\frac{\partial \phi C}{\partial t} = -\vec{\nabla} \cdot \vec{J} \tag{3.1}$$

$$\vec{J} = -\phi D_p \vec{\nabla} C + \phi \vec{u} C$$

where C is the concentration in liquid phase $[\mathrm{NL}^{-3}]$, $\vec{u}$ is the pore velocity vector $[\mathrm{LT}^{-1}]$, $\vec{J}$ is the flux vector $[\mathrm{NL}^{-3}\mathrm{T}^{-1}]$, ϕ is the porosity of the media and D_p is the pore diffusion coefficient of the media $[\mathrm{L}^2\mathrm{T}^{-1}]$. The pore diffusion coefficient can be related to molecular diffusion coefficient (D_0) as

$$D_p = \frac{\delta D_0}{\zeta^2} \tag{3.2}$$

δ is the constrictivity of the media and and ζ is the tortuosity of the media. For pure liquid phase the values of ϕ and D_p would be one and D_0 respectively. In Eq. (3.1) the dispersion term in the diffusive solid phase is neglected.

Further at the surface of non-diffusive solid phase a zero flux boundary condition has to be imposed.

$$\vec{J} \cdot \hat{n} \mid_{\Gamma_s} = 0 \tag{3.3}$$

$\hat{n}$ is the unit normal vector and Γ_s represents the boundary of the non diffusive solid phase. The domain boundary conditions in general can be written as

$$A_1 C + A_2 \hat{n} \vec{\nabla} C = A_3 \tag{3.4}$$

A_1, A_2 and A_3 are constants. The standard boundary condition from above equations can be deduced as

Dirichlet boundary:	$A_1 = 1$,	$A_2 = 0$
Neumann boundary:	$A_1 = 0$,	$A_2 = 1$
Cauchy boundary:	$A_1 = \phi \vec{u}_b$,	$A_2 = -\phi D_p$	$A_3 = \phi C_b \vec{u}_b$

C_b and $\vec{u}_b$ are concentration and velocity at boundary.

3.2   Lattice Boltzmann method

In this section two different LB schemes for handling solute transport in multilevel porous media are discussed. The first scheme is the extension of diffusion velocity LB method for multilevel porous media whereas second scheme is the extension of TRT scheme.

3.2.1 Diffusion velocity lattice Boltzmann scheme for multilevel porous media

[2] As presented in Chapter 2 diffusion velocity LB scheme can be used for accounting for large spatial variability of diffusion coefficient. To extend diffusion velocity LB scheme to multilevel porous media Eq. (3.1) can be rewritten as

$$\frac{\partial C}{\partial t} = -\vec{\nabla} \cdot \vec{J} + (1 - \phi)\frac{\partial C}{\partial t} + C\frac{\partial \phi}{\partial t} \tag{3.5}$$

$$\vec{J} = -D_e \vec{\nabla} C + \vec{u}_e C$$

D_e is the effective diffusion coefficient [L^2T^{-1}] which is equal to ϕD_p and $\vec{u}_e$ is the darcy velocity which is equal to $\phi \vec{u}$. Eq. (3.5) can be viewed as the Eq. (2.1) (Governing equation in Chapter 2) with additional forcing term $\boldsymbol{F} = (1 - \phi)\frac{\partial C}{\partial t} + C\frac{\partial \phi}{\partial t}$ and spatially varying diffusion coefficient D_e.

In diffusion velocity LB scheme the collision term is similar to SRT scheme as explained in Chapter 2. The additional forcing term arising from the multilevel porous media equation can be added to the LB equation as

$$f_i\left(\vec{r} + \vec{e}_i\Delta t, t + \Delta t\right) = f_i(\vec{r}, t) + \Omega_i^{SRT}(\vec{r}, t) + w_i \boldsymbol{F} \tag{3.6}$$

$$\Omega_i^{SRT}(\vec{r}, t) = -\frac{1}{\tau}\left(f_i(\vec{r}, t) - f_i^{eq}(\vec{r}, t)\right)$$

The time derivatives needed for the forcing term can be computed using first order finite difference as

$$\frac{\partial C}{\partial t} = \frac{C^{(t)} - C^{(t-\Delta t)}}{\Delta t} \qquad \& \qquad \frac{\partial \phi}{\partial t} = \frac{\phi^{(t)} - \phi^{(t-\Delta t)}}{\Delta t} \tag{3.7}$$

The spatial variation of diffusion coefficient is incorporated through diffusion velocity. As explained in Chapter 2 in diffusion velocity the flux associated fluctuating part of diffusion coefficient is transferred to advective part through diffusion velocity. In case of Eq. (3.5) the fluctuating part of diffusion coefficient is $\tilde{D} = D_e - D_{ref}$. Substituting this in Eq. (2.70) of Chapter 2 the diffusion velocity can be obtained as

$$\vec{u}_{d,e} = \frac{\frac{D_e - D_{ref}}{\tau e_s^2}}{\left(1 + \frac{D_e - D_{ref}}{\tau e_s^2}\right)}\left(\frac{\sum_i f_i \vec{e}_i}{\sum_i f_i} - \vec{u}_e\right). \tag{3.8}$$

$\vec{u}_{d,e}$ is the diffusion velocity [LT^{-1}]. This velocity has to be added to the velocity field (i.e. $\vec{u}_e = \vec{u}_e + \vec{u}_{d,e}$) while computing the collision term. The initial conditions, boundary conditions and unit conversion can be done using the procedures given in Chapter 2.

---

[2]This section is based on the published paper titled "Diffusion velocity lattice Boltzmann formulation applied to transport in macroscopic porous media" [93]

3.2.2 TRT scheme for Multilevel porous media

Vikhansky and Ginzburg [107] have proposed a TRT scheme for multilevel porous media. The general idea of the TRT scheme as discussed in Chapter 2 is to relax the symmetric and anti-symmetric part of distribution functions using two different relaxation parameters. In order to recover the multilevel porous media equation the appropriate equilibrium distribution function has to be chosen. Vikhansky and Ginzburg [107] have proposed the following equilibrium distribution function for orthogonal lattices

$$f_i^{eq} = \frac{C}{2} \left(c_\phi + \phi \vec{e_i} \cdot \vec{u} + I_n \phi \vec{e_i} \vec{e_i} : \vec{u}\vec{u} \right) \qquad \forall i > 0 \tag{3.9}$$

$$f_0^{eq} = \phi C - \sum_{i>0} f_i \tag{3.10}$$

Where c_ϕ is the positive parameter which can be tuned to adjust the diffusion coefficient. However the value of c_ϕ has to be chosen within stability bounds as discussed later. Correspondingly the moments of the equilibrium distribution function upto 2nd order would be

$$\sum_i f_i^{eq} = \phi C \tag{3.11}$$

$$\sum_i f_i^{eq} \vec{e_i} = \phi C \vec{u}$$

$$\sum_i f_i^{eq} \vec{e_i} \cdot \vec{e_i} = \sum_i f_i^{eq} e_{i\alpha} e_{i\beta} = C(c_\phi + I_n \phi u_\gamma u_\delta \delta_{\alpha\beta\gamma\delta})$$

Following the Chapman-Enskog procedure as described in chapter 2 for TRT scheme, it can be shown that from the $O(\varepsilon^2)$, using the equilibrium distribution function given by Eq. (3.9) following equation is recovered

$$\frac{\partial \phi C}{\partial t} + \frac{\partial}{\partial x_\alpha} \phi C u_\alpha = \nabla_\alpha \left(\tau_- - \frac{\Delta t}{2} \right) \nabla_\beta \left(c_\phi \delta_{\alpha\beta} + I_n \phi u_\gamma u_\delta \delta_{\alpha\beta\gamma\delta} - \phi u_\alpha u_\beta \right) C \tag{3.12}$$

Comparing Eq. (3.12) with Eq. (3.1) the effective diffusion coefficient and pore diffusion coefficient can be related to anti-symmetric relaxation parameter (τ_-) as

$$\phi D_p = D_e = c_\phi (\tau_- - \frac{\Delta t}{2}) \tag{3.13}$$

The additional terms in Eq. (3.12) of order $\vec{u} \cdot \vec{u}$ corresponds to the error terms. For $I_n = 1$ the diagonal part of the error terms are cancelled out for orthogonal lattice. This model can be further extended to higher order lattices but is not discussed here. The necessary

and stability conditions for this scheme are given as [107]

$$I_n = 0 : u_e^2 \leq \phi c_\phi, \qquad c_\phi \in \left[0, \frac{\phi}{d}\right] \tag{3.14}$$

$$I_n = 1 : u_e^2 \leq \min\left\{\phi(\phi - dc_\phi), \frac{d}{d-1}\phi c_\phi\right\}, \qquad c_\phi \in \left[0, \frac{\phi}{d}\right] \tag{3.15}$$

In general both c_ϕ and τ_- can be varied in order to accommodate the spatial and temporal variations of diffusion coefficient [107]. However, it can be seen from Eq. (3.12) that c_ϕ should be kept constant spatially to remove it out of the gradient operator. Therefore it is advisable to set c_ϕ as "$c_\phi^{fact}\min(\phi)$" throughout the domain. The c_ϕ^{fact} is the tunable parameter and its value should be less than $\frac{1}{d}$. In this study the c_ϕ^{fact} is taken as $1/3$ and $1/3.5$ for two-dimensional and three-dimensional systems unless specified.

Remark 3.2.1 (Approach to compute flux for multilevel TRT scheme) *Similar to section 2.2.5 of Chapter 2, a local approach to compute total flux can be derived for the above scheme. Taking the first moment over $O(\varepsilon^1)$ terms (Eq. (2.48)) we get*

$$\frac{\partial}{\partial t_1}\sum_i f_i^{(0)}\vec{e_i} + \vec{\nabla}^* \cdot \sum_i f_i^{(0)}\vec{e_i}\vec{e_i} = -\frac{1}{\tau_-}\sum_i f_i^{(1)}\vec{e_i}$$

$f_i^{(0)} = f_i^{eq}$ *as shown in Eq. (2.50) of Chapter 2. Substituting the moments as given by Eq. (3.11) in above equation we get,*

$$\frac{\partial \phi C\vec{u}}{\partial t_1} + \nabla_\alpha^* C(c_\phi \delta_{\alpha\beta} + I_n\phi u_\gamma u_\delta \delta_{\alpha\beta\gamma\delta}) = -\frac{1}{\tau_-}\sum_i f_i^{(1)}\vec{e_i}$$

The term $\frac{\partial \phi C\vec{u}}{\partial t_1}$ as given by Eq. (2.36) can be replaced with $-\phi u_\alpha u_\beta \nabla_\alpha^* C$. Substituting this in above equation we get

$$(c_\phi \delta_{\alpha\beta} + I_n\phi u_\gamma u_\delta \delta_{\alpha\beta\gamma\delta} - \phi u_\alpha u_\beta)\nabla_\alpha^* C = -\frac{1}{\tau_-}\sum_i f_i^{(1)}\vec{e_i}$$

Using Eq. (2.20) and Eq. (2.21) and substuting the term $\varepsilon \sum f_i^{(1)}\vec{e_i}$ with $\sum f_i\vec{e_i} - \sum f_i^{eq}\vec{e_i}$ we get

$$\nabla_\alpha C = -\frac{1}{\tau_-(c_\phi \delta_{\alpha\beta} + I_n\phi u_\gamma u_\delta \delta_{\alpha\beta\gamma\delta} - \phi u_\alpha u_\beta)}\left(\sum f_i\vec{e_i} - \sum f_i^{eq}\vec{e_i}\right)$$

Using the above equation the total flux as given in Eq. (3.1) is given as

$$\vec{J} = \sum_i f_i\vec{u} + \frac{\phi D_p}{\tau_-(c_\phi \delta_{\alpha\beta} + I_n\phi u_\gamma u_\delta \delta_{\alpha\beta\gamma\delta} - \phi u_\alpha u_\beta)}\left(\sum f_i\vec{e_i} - \sum f_i^{eq}\vec{e_i}\right)$$

Remark 3.2.2 (Other approaches) *Zhang* et al. *[108] has proposed an SRT based approach to solve Eq.(3.1) . In their approach they choose equilibrium distribution function as given below to recover the Eq.(3.1) from Chapman-Enskog expansion.*

$$f_i^{eq} = w_i C \left(1 + 3\frac{\vec{e} \cdot \vec{u}}{\Phi}\right) \forall i > 0$$

$$f_0^{eq} = \phi' C - \sum_i f_i$$

$$\phi' = \frac{\phi}{\Phi}$$

where Φ is the constant scalar which is introduced to ensure $\frac{\phi}{\Phi} > \frac{2}{3}$ so that f_0^{eq} is positive. For $\Phi = 1$ the minimum porosity in the domain should be greater than $\frac{2}{3}$ to ensure f_0^{eq} is the porosity. The variability of the diffusion coefficient is then taken into account by varying the relaxation parameter in the domain. This approach has limitation in terms of variability of ϕ and D_e. Walsh and Saar [109] have presented two different SRT schemes to handle variability of porosity in the domain. Their first model takes into account the variability of porosity by adding an additional term to the collision step of LB method to account for the temporal derivative. Their second approach decomposes the relaxation parameter into symmetric and antisymmetric components. They further suggested to use semi-implicit collision term to improve the stability. The variability in diffusion coefficient in both models is accounted for by varying the relaxation parameter. The number of memory access operations is increased by approximately 50% in their model as they need to excess values from the neighbouring nodes. Servan-Camas [74] used the TRT scheme similar to the one presented above wherein c_ϕ was chosen differently for each direction to account for anisotropy. In order to correct for the spatial derivative of c_ϕ he introduces and additional forcing term.

3.3   Benchmarks

[3] In this section a set of benchmark examples are presented to validate the newly proposed SRT diffusion velocity LB scheme for multilevel porous media. The first example describes a 2D rectangular area with dimensions $0.1m \times 0.1m$. The area is divided into four zones as shown in Fig. 3.2 (left). Each zone is characterized by a different pore diffusion coefficient in the first variant and additionally by a different porosity in the second variant. For this zones the pore diffusion coefficients are taken as: (zone 1) $D_p = 10^{-10}$ m^2/s, (zone 2) $D_p = 10^{-11}$ m^2/s, (zone 3) $D_p = 10^{-12}$ m^2/s and (zone 4) $D_p = 5 \cdot 10^{-10}$ m^2/s. The contrast in diffusion coefficient of different zones is 500 times between zone 3 and zone 4 and one order of magnitude between zone 1 and zone 2. The initial concentration is 2

---

[3]This section is based on the published paper titled "Diffusion velocity lattice Boltzmann formulation applied to transport in macroscopic porous media" [93]
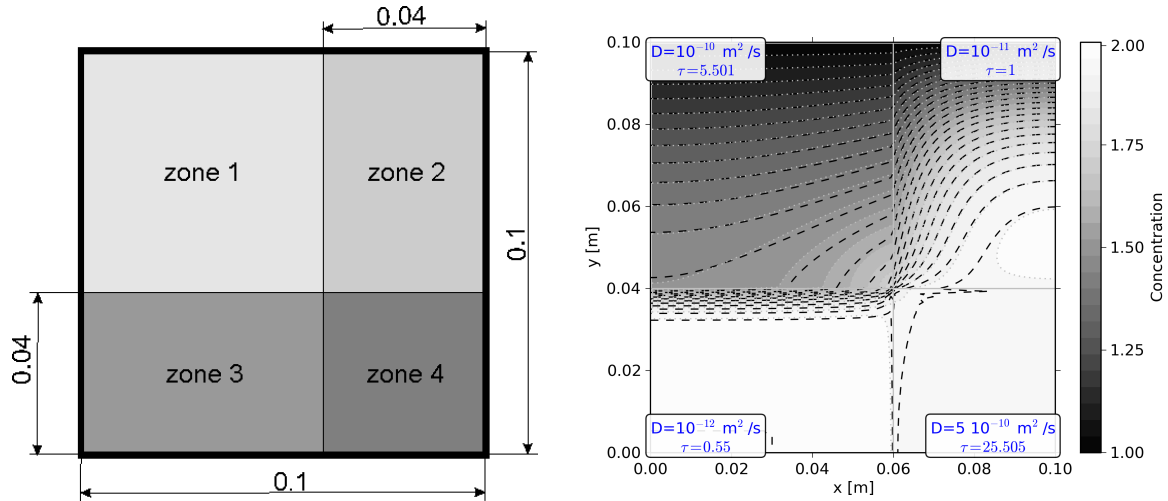
Figure 3.2: Geometry and dimensions (left) and solution based on constant porosity value $\phi = 1$ calculated with classical SRT formulation (right). Relaxation times τ are indicated for each zone.

mol/m^3 in the whole domain. Top boundary is at constant concentration 1 mol/m^3 while all other boundaries are zero flux boundaries. Domain is discretized by 150×150 nodes. Results are compared at 200 days.

The purpose of the first variant with uniform porosity $\phi = 1$ is to compare classical SRT versus diffusion velocity formulation in 2D without taking porosity variation into account. Results in Fig. 3.2 (right) and Fig. 3.3 are presented in terms of contour field with superimposed reference solution obtained by FEM code COMSOL Multiphysics. Zone 1 and zone 2 are adjacent to the low concentration boundary. Migration of species in zone 1 is faster due to a higher diffusion coefficient.

Concentration gradients in zone 2 close to the boundary are much higher because of slower diffusion in this zone. The gradients become lower close to zone 1 because of the influence of a higher diffusion there. Concentrations in zone 3 and zone 4 are more spatially homogeneous, because in zone 3 the effective diffusion coefficient is low and mass is not migrated far into this zone and, on contrary, in zone 4 due to high diffusion coefficient which allows mass to evenly distribute within this zone. Low diffusion coefficient in zone 3 also causes large concentration gradients between zone 1 and zone 3.

Results calculated with a classical SRT formulation using the variation of relaxation time are shown in Fig. 3.2 (right). Relaxation times τ are based on the diffusion coefficient in zone 2. This results in 2333 iterations to reach the final time of 200 days. Agreement with the reference solution is generally good. However, concentration at interfaces with contrasting diffusion coefficients (between zone 2, 3 and 4) exhibit instabilities. The most visible are between zones 2 and 4.

The same calculation as above is performed with the diffusion velocity formulation and shown in Fig. 3.3 (left). Relaxation time in this case is set to $\tau = 1$ and the reference diffusion used is the one from zone 2. This results, as in the case above, in 2333 iterations
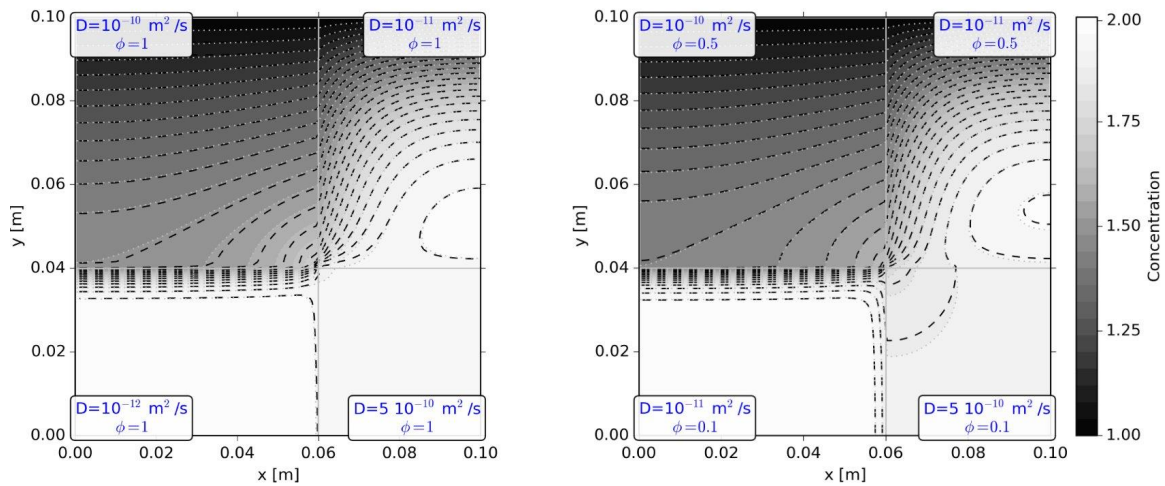
Figure 3.3: Concentration contours for the problem with constant porosity $\phi = 1$ (left) and spatially variable porosities $\phi = 0.5$ and $\phi = 0.1$ (right). Colours represent reference FEM solution and dashed black lines LB solution.

to reach 200 days. Results in Fig. 3.3 (left) show much better agreement with the reference solution, without any oscillations.

The second variant introduces the variation of porosity in addition to contrasting diffusion coefficients. A higher porosity $\phi = 0.5$ is assigned to zone 1 and zone 2 while a low porosity $\phi = 0.1$ defines zone 3 and zone 4. The difference between Fig. 3.3 (left) with constant porosity $\phi = 1$ and Fig. 3.3 (right) is mostly in the bottom part where the difference in porosity is the largest.

3.4   Conclusions

In this section two LB schemes to model solute transport through multilevel porous media are presented. The first approach is an extension of SRT diffusion velocity formulation to multilevel porous media. The second approach is based on TRT LB scheme wherein the governing equation for solute transport through multilevel porous media is recovered using a special form of the distribution functions. A benchmark has been presented for the newly developed SRT diffusion velocity scheme. This scheme presented a good agreement with FEM results for both high and low porosity systems.

Lattice Boltzmann method for reactive transport

In this chapter LB methods for reactive transport at pore-scale and multilevel porous media are presented. In section 4.1 the governing equation for multi-component reactive transport at pore scale and multilevel porous media and the assumptions associated with it are first discussed. LB scheme for single component reactive transport is introduced in section 4.2. The discussion is further extended to multi-component reactive transport in section 4.3. A novel approach is presented in this section to deal with heterogeneous reactions which enables the same treatment for both homogeneous and heterogeneous reaction terms. This in turn allows coupling of any LB transport method to an external geochemical solver. The details of the coupling of the LB transport model with external geochemical solver *PHREEQC* is also presented in section 4.3. A static approach to evolve the mineral phase boundary as a result of dissolution or precipitation is discussed in section 4.4. Finally benchmarks validating coupling of the LB method with *PHREEQC* are presented in section 4.5. Examples illustrating the influence of various parameters such as pH, surface area and morphology of porous media on dissolution of portlandite are finally presented in section 4.6.

4.1   Governing equations

The changes in aqueous concentrations due to reactive transport processes are given by the following equations [110]

$$\frac{\partial C^j}{\partial t} = -\vec{\nabla} \cdot \vec{J}^j + R^j_{hom} \tag{4.1}$$

$$\vec{J^j} = -\phi z_i \frac{D_p^j C^j}{\mathcal{R}T}\mathcal{F}\vec{\nabla}\Psi - \phi D_p^j \left(\vec{\nabla}C^j + C^j \ln \gamma^j\right) + \phi \vec{u}C^j$$

where C^j is the concentration in liquid phase of jth species $[N^1 L^{-3}]$, R_{hom}^j is the contribution from the homogeneous equilibrium and non-equilibrium reactions to aqueous concentration of jth species $[N^1 L^{-3}T^{-1}]$, z_i is the valence number of jth species, γ^j is the activity coefficient of jth species, D_p^j is the pore diffusion coefficient of jth species $[L^2 T^{-1}]$, $\vec{u}$ $[L^1 T^{-1}]$ is the pore velocity field of the fluid and ϕ is the porosity. For pore-scale and liquid phase in case of multilevel porous media, the value of ϕ and $D_p j$ are equal to one and D_0^j respectively. D_0^j being the diffusion coefficient of the ion in water $[L^2 T^{-1}]$. Ψ is the electrical potential $[M^1 L^2 T^{-2}Q^{-1}]$. $\mathcal{F}$, $\mathcal{R}$ and T are Faraday's constant (96,488.46 C/mol), universal gas constant (8.3143 J/mol/° K), and temperature [°K] respectively. The first term of the flux in Eq. (4.1) represents electro-kinetic effect on transport, the second term represents the diffusive transport and the last term represents advective transport. To obtain the electrochemical potential the mass conservation equation has to be coupled with the Poisson equation

$$\vec{\nabla} \cdot \vec{\nabla}\Psi + \frac{\mathcal{F}}{\epsilon}\sum_i^N \left(z_i C^i\right) = 0 \tag{4.2}$$

where N is the total number of species and ϵ is the medium permittivity $[M^{-1}L^{-3}T^2 Q^2]$. Additionally non-equilibrium heterogeneous surface reactions occurring at the mineral surface (solid-fluid interface) for j^{th} species under quasi stationary assumption can be written as (see Appendix E)

$$\vec{J^j} \cdot \hat{n}|_{\Gamma = \Gamma_s} = -\frac{V}{A_s}R_{het}^j \tag{4.3}$$

where Γ_s repesents the boundary of the reactive solids, A_s is the surface area of the solid $[L^2]$, V is the total volume of the solid domain $[L^3]$ and R_{het}^j is a source/sink term for heterogeneous reactions to aqueous concentration of jth species $[N^1 L^{-3}T^{-1}]$. Correspondingly the change in the concentration of jth species in solid is given as

$$\frac{\partial C^{j,s}}{\partial t} = -R_{het}^j \tag{4.4}$$

In case of equilibrium heterogeneous reactions for mineral phases, the boundary condition at the boundary of the Mth mineral phase can be simply represented as

$$C^j|_{\Gamma = \Gamma_{s,M}} = C_{eq,M}^j \tag{4.5}$$

$C_{eq,M}^j$ being the concentration to be maintained for jth component to be in equilibrium

with Mth mineral phase. Correspondingly the change in the solid concentration is given as

$$\frac{\partial C^{j,s}}{\partial t} = -\left(C^j_{eq,M} - C^j\right) \tag{4.6}$$

For dilute solutions the activity of jth species approaches towards unity. In such a case an assumption can be made that $\ln \gamma^j \to 0$. Further if it is assumed that diffusion coefficient is same for all species the charge balance of the solution is satisfied as a result of which the electro-kinetic term is cancelled out [110]. Under these assumptions Eq. 4.1 reduces to the advection-diffusion equation with an additional source/sink term arising from chemical reactions as given below

$$\frac{\partial C^j}{\partial t} = -\vec{\nabla} \cdot \vec{J^j} + R^j_{hom} \tag{4.7}$$

$$\vec{J^j} = -\phi D_p \vec{\nabla} C^j + \phi \vec{u} C^j$$

D_p is usually taken as the average diffusion coefficient of all the species [111]. Eq. 4.7 has been used in many existing reactive transport codes (see [112] for review on existing reactive transport codes) for continuum scale and is also commonly used for pore-scale simulations [35, 37–43, 113]. In this thesis too the electro-kinetic effects are neglected. It should be noted that electro-kinetic effects can have important influence especially in low pH systems (i.e. when concentration of H$^+$ ion is high) [114]. Molins *et al.* [35] have shown for calcite reaction system at pH 4 that the contribution of electro-migration plays a significant role in pore-scale simulations.

The chemical species to be transported can be further distinguished into the primary species and secondary species which can be related to primary species through the stoichiometry of chemical reactions. The number of transport equations to be solved can be thus reduced by expressing the transport equations in terms of total concentration of the primary species.The total concentration is defined as the stoichiometric sum of the concentrations of all primary and secondary species [115]. For further discussions in this chapter on multi-component reactive transport C^j represents the total concentration of jth primary species.

4.2 Lattice Boltzmann method for single component reactive transport

In this section the LB scheme for pore-scale reactive transport is introduced through a single component system. For single component system, the mass transport Eq. (4.7) with first order kinetics for homogeneous reaction reduces to

$$\frac{\partial C}{\partial t} = -\vec{\nabla} \cdot \vec{J} + k_{hom} C \tag{4.8}$$

$$\vec{J} = -\phi D_0 \vec{\nabla} C + \vec{u} C$$

k_{hom} is the first order reaction rate for homogeneous reaction $[T^{-1}]$.

The heterogeneous reaction at the mineral surface can either be non-equilibrium (kinetic) or equilibrium based as discussed previously. For single component system, the source/sink term in aqueous concentration resulting from the rate controlled heterogeneous surface reactions is expressed as

$$R_{het} = -k_{het}(C - C_{eq}) \tag{4.9}$$

Correspondingly at solid-fluid interface the heterogeneous reaction can be expressed as a boundary condition as given below

$$-D_0 \hat{n} \cdot \vec{\nabla} C|_{\Gamma = \Gamma_s} = \frac{V}{A_s} k_{het}(C - C_{eq}) \tag{4.10}$$

k_{het} is the first order rate constant for the heterogeneous reaction $[T^{-1}]$ and C_{eq} is the concentration at equilibrium $[N^1 L^{-3}]$. The change in the solid concentration due to heterogeneous reaction is given by

$$\frac{\partial C^s}{\partial t} = k_{het}(C - C_{eq}) \tag{4.11}$$

For equilibrium heterogeneous reactions, the boundary condition at the solid-fluid surface can be simply written as

$$C|_{\Gamma = \Gamma_s} = C_{eq} \tag{4.12}$$

The corresponding change in the solid concentration is given by

$$\frac{\partial C^s}{\partial t} = C_{eq} - C|_{\Gamma = \Gamma_s} \tag{4.13}$$

The LB schemes presented in Chapter 2 and Chapter 3 can be extended to solve Eq. (4.8) by simply adding a forcing term to Eq. (2.6)

$$f_i(\vec{r} + \vec{e_i}\Delta t, t + \Delta t) = f_i(\vec{r}, t) + \Delta t \Omega_i(\vec{r}, t) + F_R^{hom}(\vec{r}, t) \tag{4.14}$$

$$F_R^{hom} = w_i R_{hom} \qquad \text{where } R_{hom} = k_{hom} C$$

F_R^{hom} being the additional forcing term for the homogeneous reaction.

The heterogeneous reaction term represented by Eq. (4.10) and Eq. (4.12) can be imposed on the boundary of solid surface using methods discussed in section 2.2.8. In this chapter, all simulations are carried out using orthogonal lattices with linear EDF. For orthogonal lattice with linear EDF the rate controlled heterogeneous reaction given by Eq. (4.10) can be imposed by substituting $A_1 = \frac{V}{A_s} k_{het}$, $A_2 = D_0$ and $A_3 = \frac{V}{A_s} k_{het} C_{eq}$ in Eq. (2.89).

Moreover as $\vec{u}$ at solid surface is zero, Eq. (2.89) reduces to

$$f_i = \frac{k_{het}C_{eq} - f_{-i}\left[\frac{V}{A_s}\frac{k_{het}}{2w_i} - \frac{D_0}{\tau e_s^2}\vec{e}_{-i}\cdot\hat{n}\right]}{\frac{V}{A_s}\frac{k_{het}}{2w_i} - \frac{D_0}{\tau e_s^2}\vec{e}_i\cdot\hat{n}} \tag{4.15}$$

Substituting $D_0 = e_s^2\left(\tau - \frac{\Delta t}{2}\right)$ as given by Eq. (2.43) we get

$$f_i = \frac{k_{het}C_{eq} - f_{-i}\left[\frac{V}{A_s}\frac{k_{het}}{2w_i} - \left(1 - \frac{\Delta t}{2\tau}\right)\vec{e}_{-i}\cdot\hat{n}\right]}{\frac{V}{A_s}\frac{k_{het}}{2w_i} - \left(1 - \frac{\Delta t}{2\tau}\right)\vec{e}_i\cdot\hat{n}} \tag{4.16}$$

Eq. 4.16 is the correct formulation for the flux boundary for heterogeneous reaction and not the one as proposed by Kang *et al.* [45]. Kang *et al.* [45] "assumed" $D_0 = e_s^2\tau$ in order to derive the heterogeneous boundary conditions. This assumption is only valid if the Crank-Nicholson scheme is used to discretize discrete Boltzmann equation in time [116] which was not so in their case. The equilibrium heterogeneous reaction as given by Eq. (4.12) can be imposed by substituting $A_1 = 1$, $A_2 = 0$ and $A_3 = C_{eq}$ in Eq.(2.89)

$$f_i = 2w_i C_{eq} - f_{-i} \tag{4.17}$$

4.3 Lattice Boltzmann method for multi-component reactive transport

[1]The approach presented in the previous section can be extended to multi-component reactive transport (Eq. (4.7)) by using a separate distribution function for each jth primary species

$$f_i^j(\vec{r} + \vec{e}_i\Delta t, t + \Delta t) = f_i^j(\vec{r}, t) + \Delta t\Omega^j(\vec{r}, t) + F_R^{hom,j}(\vec{r}, t) \tag{4.18}$$

$$F_R^{hom,j} = w_i R_{hom}^j$$

It should be noted that the Eq. 4.18 is same for both pore-scale and multilevel LB method and hence the discussion in this section is applicable to *all LB schemes* described in previous chapters.

Heterogeneous reactions at the fluid-solid interface are conventionally implemented in LB schemes for reactive transport as an boundary condition as given in Eq. (4.3) [44, 45, 49, 51]. This in turn, requires special treatment of interface nodes compared to other nodes and

---

[1]This section is based on the published papers titled —

"A versatile pore-scale multicomponent reactive transport approach based on lattice Boltzmann method: Application to portlandite dissolution" [117]

"Lattice Boltzmann based multicomponent reactive transport model coupled with geochemical solver for pore scale simulations" [118]

a specific derivation for boundary condition for each mineral reactions at the interface. Examples of such implementations for mineral dissolution/precipitation can be found in [44, 45] and ion-exchange and mineral dissolution/precipitation can be found in [51]. Several geochemical reaction modelling codes have been developed during last decade to handle different types of chemical reactions [64, 119–121]. Commonly the coupling of a transport code with a external geochemical code for conventional numerical method is carried out using an explicit operator splitting approach [112, 115]. In this approach, a transport step is first executed and then the reaction step is carried out using an external geochemical code wherein each discrete volume element is treated as batch reactor. Finally the reaction source/sink terms are computed and the concentrations are suitability modified to the next time step. Therefore, in order to couple the external geochemical codes with the pore-scale or multilevel LB schemes through operator splitting approach an uniform treatment of both homogeneous and heterogeneous reactions is required so that all nodes can be treated as a batch reactor in geochemical reaction code. This can be achieved by treating the heterogeneous reactions as pseudo-homogeneous reaction. That is, under the assumption that $\Delta r \ll L$ (Δr being grid spacing and L domain length), the heterogeneous reaction can be treated as an additional source/sink term at the fluid node adjacent to a solid boundary. The LB equation (Eq. (4.18)) at the interface can be then written as

$$f_i^j(\vec{r} + \vec{e}_i \Delta t, t + \Delta t) = f_i^j(\vec{r}, t) + \Delta t \Omega^j(\vec{r}, t) + F_R^{hom,j}(\vec{r}, t) + F_R^{het,j}(\vec{r}, t) \qquad (4.19)$$

$$F_R^{het,j} = w_i R_{het}^j$$

In general Eq. (4.19) can be written as

$$f_i^j(\vec{r} + \vec{e}_i \Delta t, t + \Delta t) = f_i^j(\vec{r}, t) + \Delta t \Omega^j(\vec{r}, t) + F_R^{tot,j}(\vec{r}, t) \qquad (4.20)$$

$$F_R^{tot,j} = w_i R_{tot}^j$$

where R_{tot} represents the combined homogeneous and heterogeneous reactions (at fluid-solid interface) which can be computed using the external geochemical solver $[N^1 L^{-3} T^{-1}]$.

To validate the pseudo-homogeneous treatment for heterogeneous reactions, a two dimensional example analogous to one defined by Kang et $al.$ [45] is used. In this example single component reactive transport is considered. The domain consist of size 50 mm $\times$ 30 mm. Solute is diffused from the left hand side boundary and a constant concentration boundary condition of 100 mol/m^3 is maintained. No flux boundary is applied at the right hand side boundary and the bottom boundary. The top boundary is the heterogeneous rate controlled reaction boundary as given by Eq. (4.10). Equilibrium concentration C_{eq} is taken as 50 mol/m^3. Simulations are carried out for two reaction rates, 1×10^{-7} s^{-1} and 1×10^{-6}s^{-1} representing slow and fast reaction rates respectively. The initial
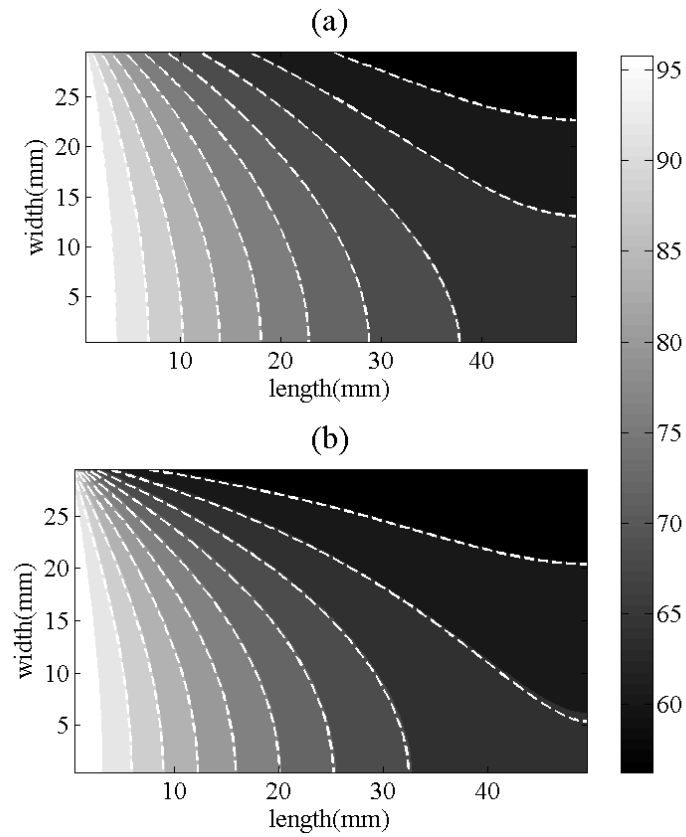
Figure 4.1: Contours of solute concentration at steady state - rectangular domain with first order kinetic reaction along top boundary: a) k $= 1 \times 10^{-7}$s^{-1}, b) k $= 1 \times 10^{-6}$ s^{-1}. Dashed lines indicate results obtained from LB
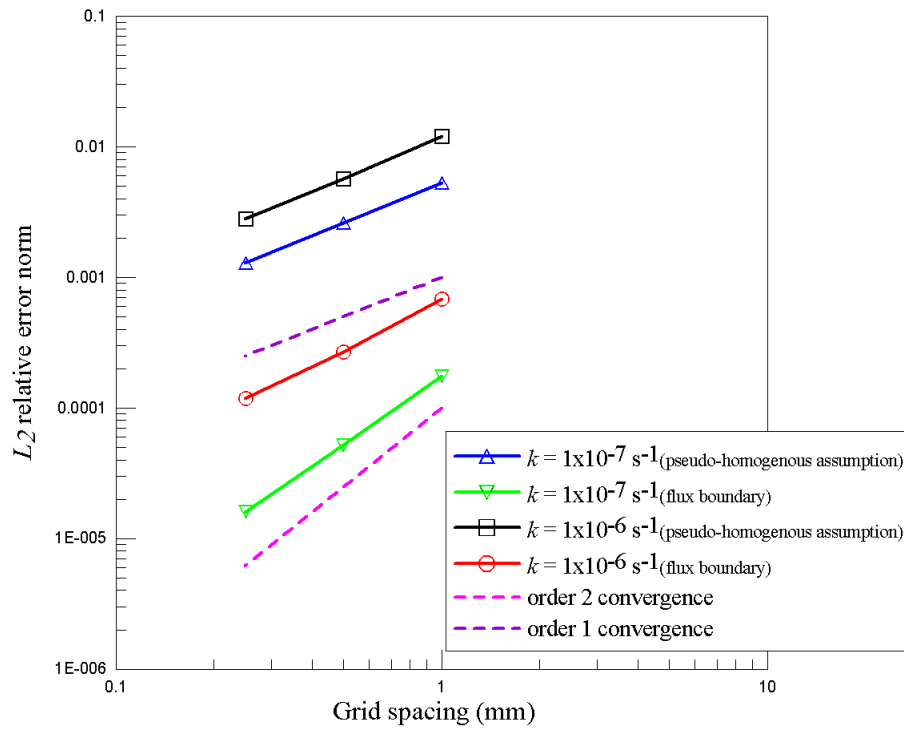
Figure 4.2: Convergence with respect to grid spacing for rectangular domain with linear kinetic reaction along top boundary

concentration is set to C_{eq}. Simulations were carried out until steady state is reached i.e. when the difference between the molar concentrations at all nodes in domain between two consecutive time steps is less than 10^{-10} mol/m^3.

The analytical solution for molar concentration for this problem is given as [44, 122]

$$C(x,y) = (C(t=0) - C_{eq}) \sum_{n=1}^{\infty} \frac{\cosh\left[\beta_n(x - L_x)\right] \sin(\beta_n L_y)}{M_n^2 \beta_n \cosh(\beta_n L_x)} \cos(\beta_n y) + C_{eq} \qquad (4.21)$$

$$M_n^2 = \frac{L_y}{2} \left(1 + \frac{\sin(2\beta_n L_y)}{2\beta_n L_y}\right)$$

where L_x and L_y are the length of domain along x and y direction repsectively. β_n is determined by solving following transcendental equation

$$\beta_n L_y \tan(\beta_n L_y) = \frac{kL_y}{D_0} \qquad (4.22)$$

A good agreement is observed between the analytical solution and pseudo-homogeneous treatment for heterogeneous reaction for both cases as shown in Fig. 4.1 thus verifying the proposed approach. The comparison of accuracy and convergence behaviour of two implementation approaches for heterogeneous reactions in LB schemes viz., pseudo-homogeneous treatment and as boundary condition is shown in Fig 4.2. The results shows that pseudo-homogeneous treatment is less accurate compared to the implementation of heterogeneous reaction as boundary condition for a given discretization. However, the flexibility pseudo-homogeneous treatment provides outweighs this drawback.

4.3.1 Coupling with the External Geochemical solver

In this work the coupling of external geochemical solver *PHREEQC* [64] with the LB method was carried out. *PHREEQC* has capabilities for simulating a broad range of equilibrium reactions between water and minerals, ion exchangers, surface complexes, solid solutions, and gases. It also has a general kinetic formulation that allows modelling of non-equilibrium mineral dissolution and precipitation, microbial reactions, decomposition of organic compounds, and other kinetic reactions. Thus coupling with *PHREEQC* provides access to this wide range of geochemical models which was lacking in previous LB frameworks for multi-component reactive transport. In case of cementitious system it enables incorporation of a range of geochemical reactions involved in cementitious materials [123, 124] using a pre-compiled thermodynamic database [125, 126].

The coupling of the LB method with *PHREEQC* using the operator splitting approach is equivalent to sequential non-iterative approach used for conventional numerical methods [112, 115]. The communication between LB and *PHREEQC* is carried out through
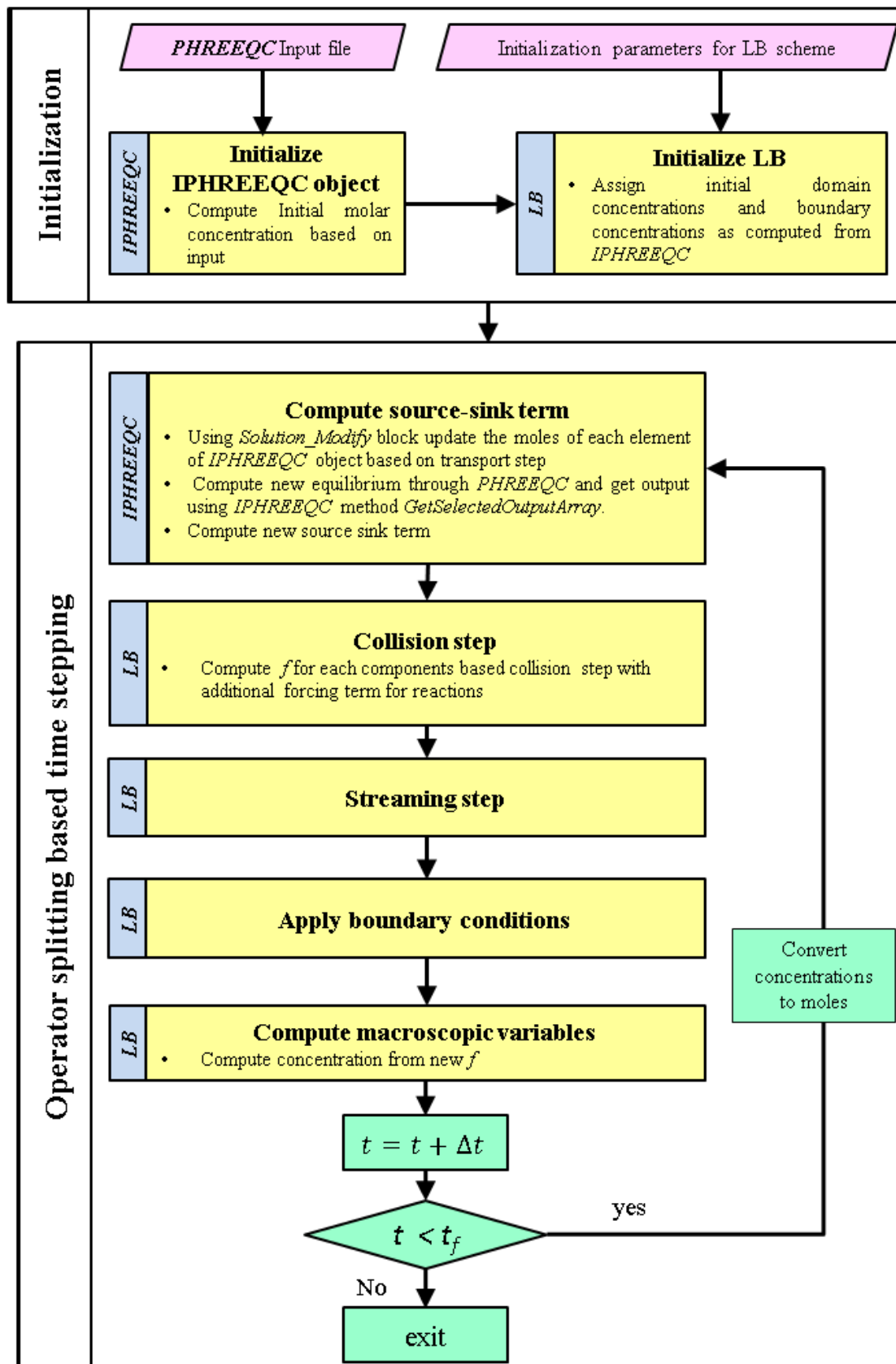
Figure 4.3: Schematic alogrithim for coupling of LB scheme with *PHREEQC*

IPHREEQC API [127]. The molar concentrations for initial and boundary conditions are obtained through *PHREEQC*. At the beginning of each time step, based on concentrations obtained from the transport step the moles of each component are computed by multiplying the concentration with water content. The moles of components are then updated in *IPHREEQC* object using *Solution_Modify* method of *PHREEQC* and new equilibrium concentrations are computed. The new concentrations can be obtained after reactions from *IPHREEQC* using *GetSelectedOutputArray* method. The source/sink term due to reaction is then computed as

$$R_{tot}^j = \phi \left(\frac{C_{react}^j - C_{trans}^j}{\Delta t} \right) \tag{4.23}$$

where C_{trans}^j is the aqueous concentration after the transport step before executing the reaction step and C_{react}^j is the aqueous concentration after reaction step from geochemical model. Following this, the collision step and the streaming steps are executed. The boundary conditions are then applied and new concentrations are computed from the updated distribution functions. The detailed schematic algorithm for coupling is presented in Fig 4.3

Remark 4.3.1 (Time step criteria) *One of the drawbacks of explicit coupling is that the time step must be small enough to avoid operator splitting errors. For the sequential operator splitting approach the time step should satisfy the Courant (for advection) and von Neumann (for diffusion) criteria in order to ensure accurate results[112].*

$$\text{Courant criteria:} \qquad \frac{|\vec{u}|\Delta t}{\Delta r} \leq 1$$

$$\text{von Neumann criteria:} \qquad \frac{D_0 \Delta t}{\Delta r^2} < 0.5$$

For relaxation parameter equal to one according to Eq. (2.43) of Chapter 2, $\frac{D_0 \Delta t}{\Delta r^2} \approx 0.17$. Hence for this choice of relaxation parameter von Neumann criteria is automatically satisfied. The Courant criteria can be used to choose appropriate grid spacing in case of the advection-diffusion equation.

4.4   Solid phase evolution onsite of reaction

[2]Change in pore geometry due to dissolution/precipitation of solid phase is made through static update rules using an approach similar to that proposed by Kang *et al.* [45]. In implementation used in this thesis, the volume occupied by a single mineral at a given lattice node is updated after the reaction step, based on the number of moles mineral dissolved or precipitated during the reaction as

$$V_m(\vec{r}, t + \Delta t) = V_m(\vec{r}, t) + \bar{V}_m \left[N_m(\vec{r}, t + \Delta t) - N_m(\vec{r}, t) \right] \tag{4.24}$$

where V_m is the volume occupied by a solid mineral phase m at given lattice node $[L^3]$, $\bar{V}_m$ is the molar volume for a solid mineral phase m $[N^{-1}L^3]$, and N_m is the number of moles of solid mineral phase m present at a node which is updated after every reaction step[N]. In case of multiple mineral phases at a given lattice node, the total volume occupied by the solid phase V_{tot}, is then the sum of the volumes occupied by all mineral phases at that node given by

$$V_{tot}(\vec{r}, t + \Delta t) = \sum_m V_m(\vec{r}, t + \Delta t) \tag{4.25}$$

Now we can define the volume fraction occupied by solid mineral phases (ϕ_m) as $\phi_m = V_{tot}/V_{eff}$, where V_{eff} is effective volume which is defined as the maximum volume mineral phases can occupy at a given node. When ϕ_m reaches a predefined threshold value (ϕ_m^{thres}) the pore geometry is updated. For the implementation purpose, both the fluid node and solid node at interface are marked as interface nodes. The track of dissolving and precipitating mineral phases is kept respectively at the solid interface node and the fluid interface node. When $\phi_m \leq \phi_m^{thres}$ at the interface solid node, it is converted into a fluid node. Similarly, in case of precipitation when $\phi_m > \phi_m^{thres}$ at the interface fluid node, it is converted into a solid node. The choice of ϕ_m^{thres} as 0.5 rather than at complete dissolution ($\phi_m^{thres} = 0$) or full precipitation ($\phi_m^{thres} = 1$) as proposed by Kang *et al.* [45], gives more accurate solution of moving boundary problems. In case of multilevel porous media the porosity after dissolution or precipitation of solid mineral phases in a diffusive solid the porosity can be obtained as $1 - \phi_m$.

To validate the proposed approach for geometry update a one dimensional single-component equilibrium based dissolution of a planar solid with Stefan moving boundary condition is

---

[2]This section is based on the published papers titled —

"A versatile pore-scale multicomponent reactive transport approach based on lattice Boltzmann method: Application to portlandite dissolution" [117]

"Lattice Boltzmann based multicomponent reactive transport model coupled with geochemical solver for pore scale simulations" [118]
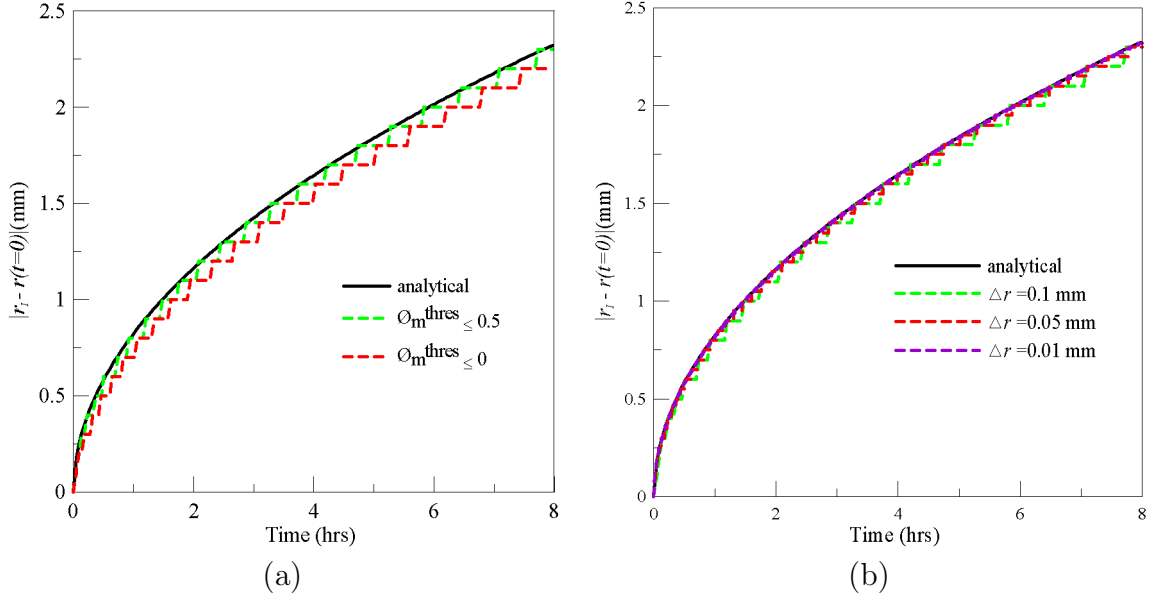
Figure 4.4: Diffusion controlled dissolution a) Influence of choice of ϕ_m^{thres}, b) Influence of grid resolution on front propogation

modelled for which analytical solution is given as [128]

$$r_I(t) - r_I(t = 0) = 2k_I\sqrt{D_0 t} \tag{4.26}$$

k_I is given by solution of the following transcendental equation

$$\pi^{1/2}k_I \exp(k_I^2)\text{erfc}(-k_I) = \frac{C_{eq} - C_0}{C_m - C_{eq}}$$

where r_I is the position of solid-fluid interface [L], C_m is the concentration in mineral phase [NL^{-3}], C_0 is the initial aqueous concentration [NL^{-3}].

The model setup consists of a quasi one-dimensional domain of size 20 mm × 5 mm. The initial aqueous concentration C_0 is assigned as 0.1 mol/m³. The last 3 mm domain is taken as the solid with initial concentration C_m of 1 mol/m³. Hence, the fluid-solid interface, r_I is initially located at 17 mm from the inlet. An equilibrium concentration C_{eq} of 0.4 mol/m³ is maintained at the fluid-solid interface. The diffusion coefficient D_0 is taken as 1×10^{-9} m²/s.

Fig. 4.4(a) shows a comparison of the results obtained from the proposed LB scheme with the analytical solution for $\phi_m^{thres} = 0$ and $\phi_m^{thres} = 0.5$. It clearly shows that the choice of $\phi_m^{thres} = 0.5$ is more accurate. In Fig. 4.4, the movement of interface is in discrete steps as update of the geometry is carried out in a static way. Fig. 4.4(b) shows that, for $\phi_m^{thres} = 0.5$, a higher number of nodes gives continuous movement of the fluid-solid interface. However, the movement of the fluid-solid interface is fairly independent of the number of nodes and in good agreement with the analytical solution is obtained for all discretization.

4.5 Benchmarks

[3]In this section, benchmarks are presented illustrating the correctness of coupling between *PHREEQC* and the LB schemes. These benchmarks demonstrate the versatility of the developed approach in handling a wide range of geochemical system.

A benchmark illustrating the ability of current approach to handle ion exchange reaction is presented in Section 4.5.1. Portlandite dissolution without geometry update is described in Section 4.5.2. The transport in both this benchmarks were solved using SRT LB scheme for pore-scale. The relaxation parameter was kept as one.

All the above benchmarks are illustrative for coupling of pore-scale LB method with *PHREEQC*. In order to validate the coupling of *PHREEQC* with the multilevel LB schemes a benchmark on dissolution of C-S-H phase taking into account the influence of porosity on diffusion coefficient is presented in Section 4.5.3. The C-S-H is conceptualized as solid solution. Validation was carried out for both transport schemes for multilevel porous media as described in chapter 3 viz., the diffusion velocity SRT scheme and TRT scheme. For diffusion velocity SRT scheme the relaxation parameter is kept as one and the reference diffusivity is chosen as molecular diffusion coefficient D_0. The fluctuating component of diffusion coefficient is recomputed every iteration. For TRT scheme for multilevel porous media the maximum relaxation parameter is kept as one inside the domain. To ensure this, conversion factors and relaxation parameters are updated at the end of each time step. All benchmarks are pseudo-one dimensional systems and hence the computations were carried out using D2Q5 lattice with linear EDF.

4.5.1 Ion exchange

Chemical composition of effluent from a column containing a cation exchanger is simulated and the result of LB scheme is compared with COMSOL Mutliphysics (this benchmark is based on example 11 described in [64]). Coupling of IPHREEQC with COMSOL Mutliphysics was carried out using the approach presented in [129]. The model setup consists of an 8 cm long column containing initially 1 mM of $NaNO_3$ solution and 0.2 mM of KNO_3 solution in equilibrium with 1.1 mM of cation exchanger. The column is then injected with a 0.6 mM $CaCl_2$ solution. At each time step, the exchanger is in equilibrium with Na, K and Ca. Thus the components to be transported are H, O, Na, K, NO_3, Cl and Ca. The water flow velocity in domain is assumed to be 2.77×10^{-6} m/s and the diffusion coefficient is 5.54×10^{-9} m²/s. The left boundary is the Cauchy boundary which

---

[3]This section is based on the published papers titled —

"A versatile pore-scale multicomponent reactive transport approach based on lattice Boltzmann method: Application to portlandite dissolution" [117]

"Lattice Boltzmann based multicomponent reactive transport model coupled with geochemical solver for pore scale simulations" [118]
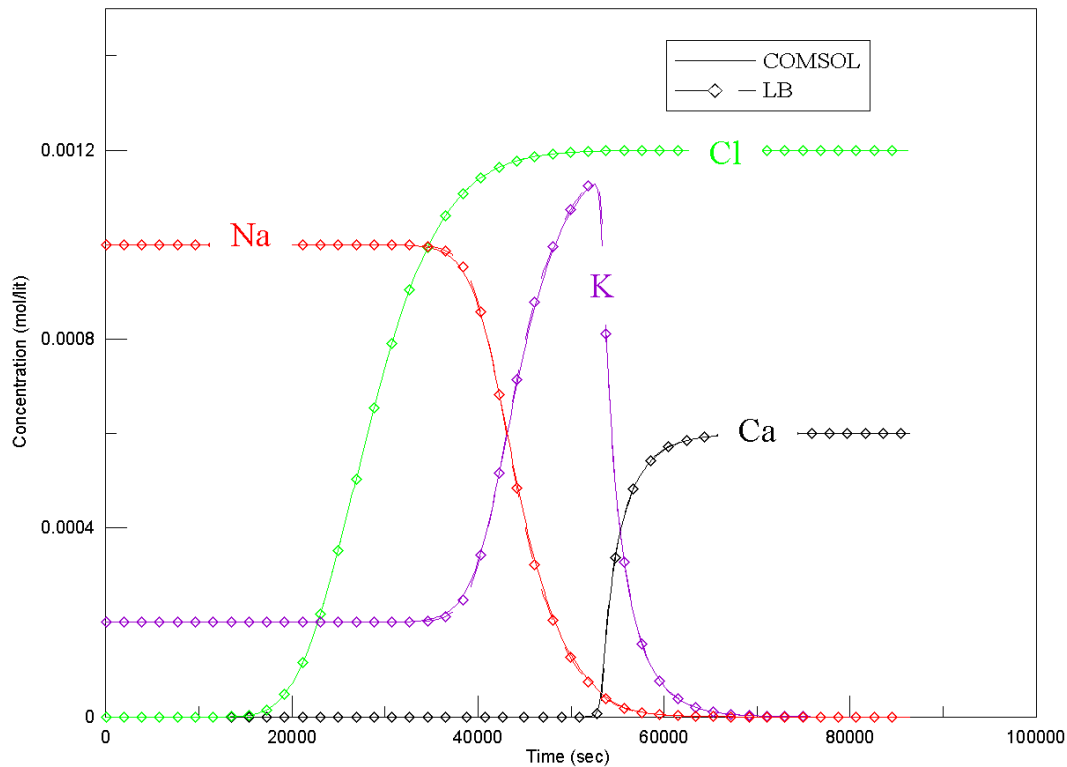
Figure 4.5: Cation Ion exchange: Evolution of concentrations of different components at right boundary with time

is equal to the product of fixed boundary concentration and velocity applied. All other boundaries are set as zero flux boundary. Fig. 4.5 shows a comparison between the LB results and COMSOL Mutliphysics and indicates an excellent agreement.

4.5.2 Portlandite dissolution without geometry update

The model setup consists of a rectangular domain of size 3 cm × 1 cm with grid spacing of 0.025cm. An aqueous phase in the domain is initially in equilibrium with portlandite (Ca ≈ 20 mM, pH ≈ 12.5 at 25°C). 4 mM solid portlandite mineral phase is initially present at the right hand side boundary. An aggressive water solution with pH 3 (obtained by adjusting Cl ion concentration to maintain charge balance) is in contact at the left hand side boundary of the domain. A zero flux condition is imposed at top and bottom boundaries. This model setup can be interpreted conceptually as a location in the pore structure of hardened cement paste where portlandite is in contact with pore water. Change in pore water composition (i.e. decrease in pH) initiates dissolution of portlandite. The components to be transported in this case are Ca, Cl, H and O. The diffusion coefficient is assumed to be 1×10^{-9} m²/s.

Comparison was made with the reactive transport module of *PHREEQC*. Fig. 4.6 shows the evolution of portlandite concentration and pH respectively, at the right hand side boundary obtained with LB-PHREEQC approach and *PHREEQC*. The transient pH
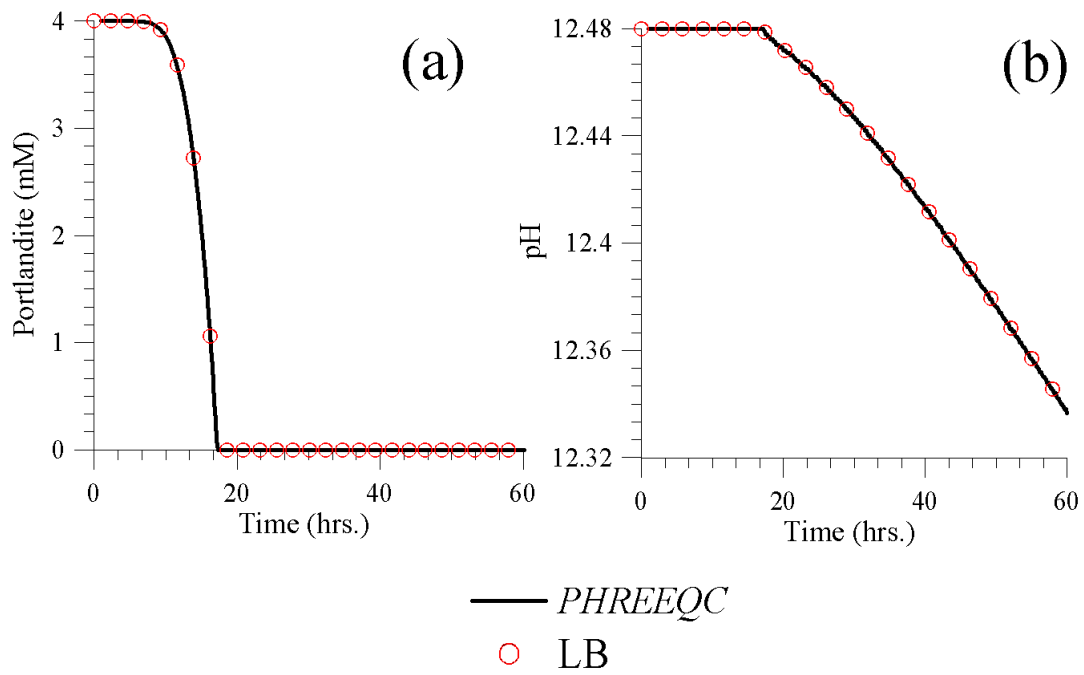
Figure 4.6: Portlandite dissolution without geometry update: Variations of (a) Portlandite concentration and (b) pH with time along the right hand side boundary.
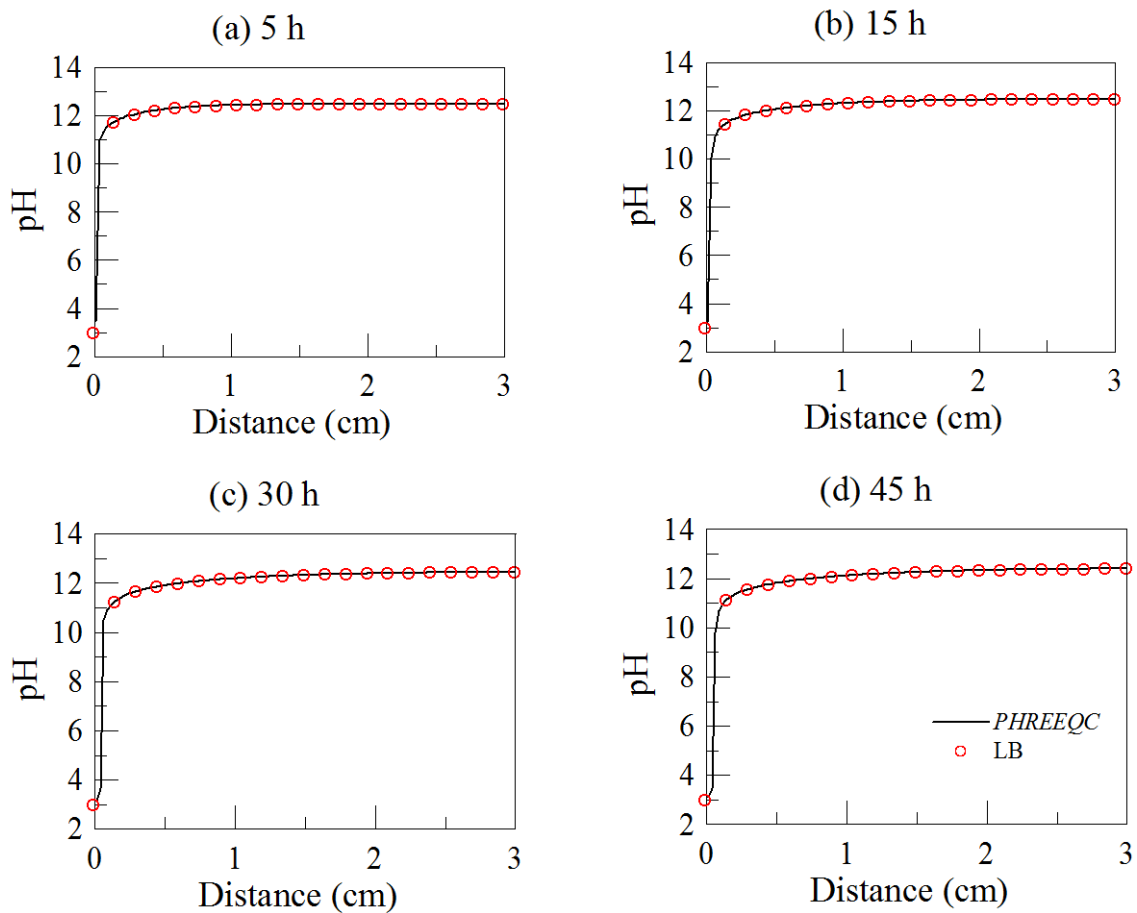
Figure 4.7: Portlandite dissolution without geometry update: Transient pH profiles along the cross-section at the centre of the domain at (a) 5 h, (b) 15 h, (c) 30 h, and (d) 45 h.
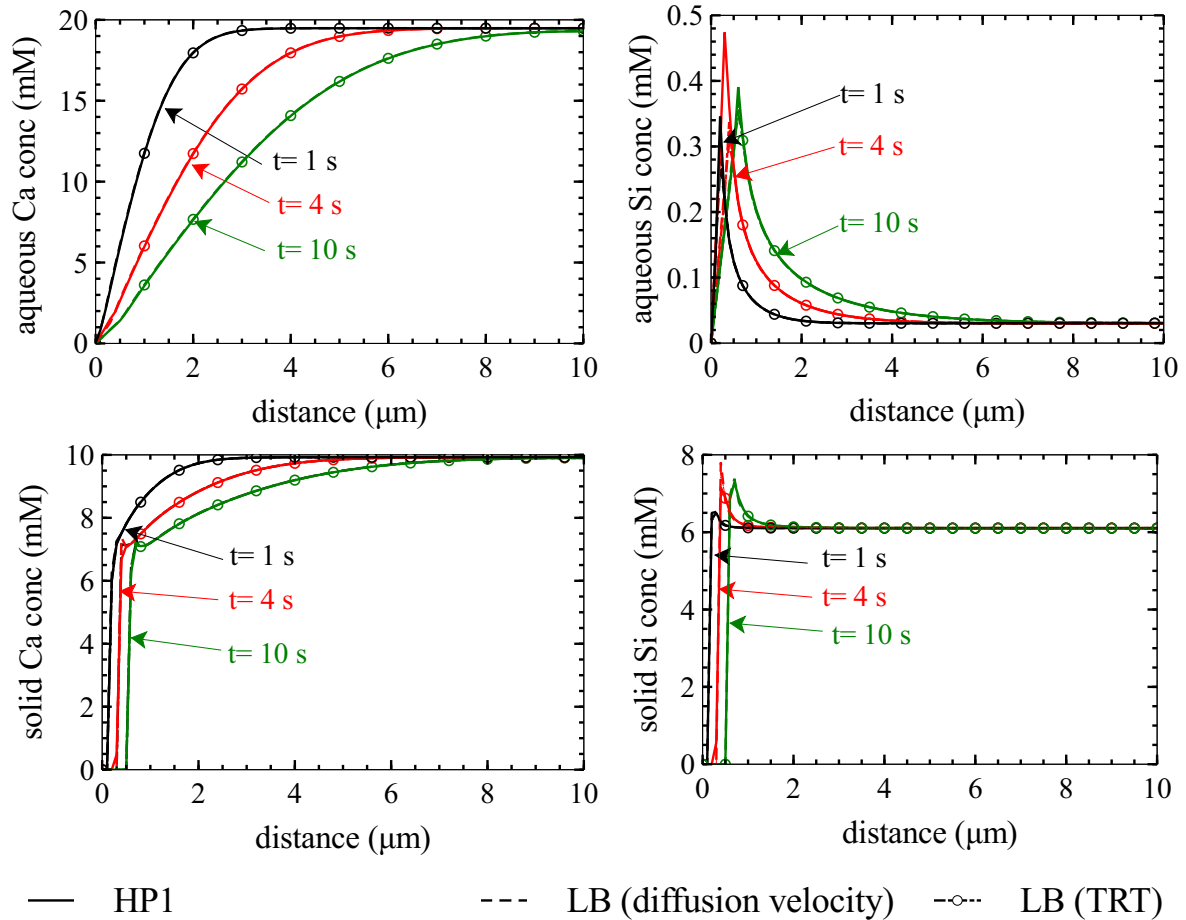
Figure 4.8: C-S-H dissolution: porfiles for Ca and Si concentration in aqueous and solid phases at different times

profiles obtained at 5h, 15h, 30h and 45h, along the cross-section using both codes can be seen in Fig. 4.7.

4.5.3 C-S-H dissolution

The model setup consists of a rectangular domain of size 10 μm $\times$ 0.5 μm with grid spacing of 0.1 μm. The domain contains C-S-H solid phase and has initial porosity of 0.448 which corresponds to the cement paste with water cement ratio of around 0.45. An aqueous phase in the domain is initially in equilibrium with portlandite (Ca $\approx$ 20 mM, pH $\approx$ 12.5 at 25°C). A demineralized water with pH 7 is in contact at the left hand side boundary of the domain. A zero flux condition is imposed on other boundaries. The components to be transported for this benchmark are Ca, Si, H and O. The molecular diffusion for all components D_0 is assumed to be 2.2×10^{-10}m²/s which is one order lower than diffusivity of ion in pure water to account for the constrictivity effects in gel pores. The evolution of diffusivity due to porosity for this benchmark is carried out using the Millington and Quirk
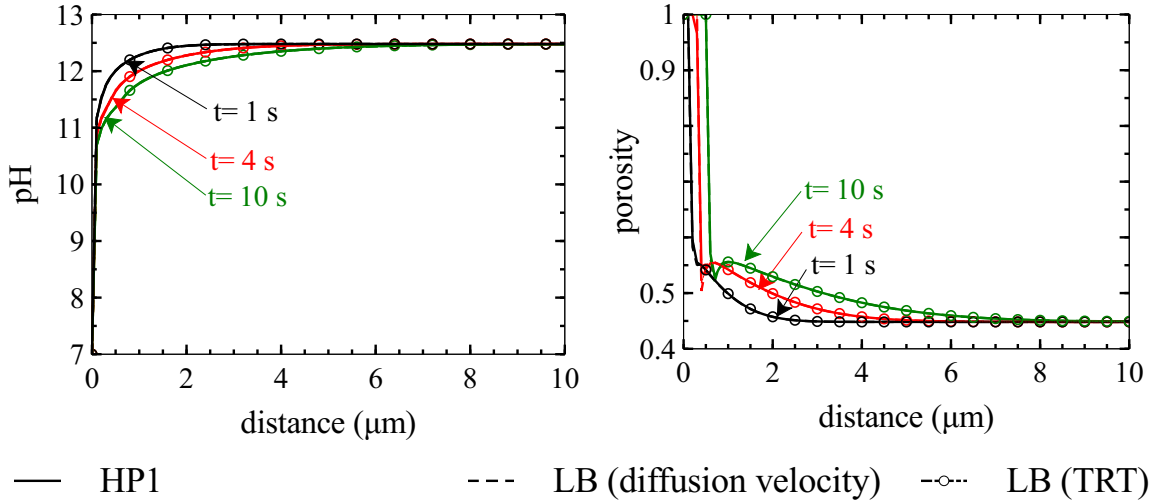
Figure 4.9: C-S-H dissolution: porfiles for pH and porosity change at different times

model [130]. According to this model the pore diffusivity D_p can be related to porosity as

$$D_p = \phi^{1/3} D_0 \tag{4.27}$$

A more detailed model for C-S-H diffusivity accounting for changes in different morphological aspects of C-S-H as a consequence of leaching has been developed in Chapter 8. The C-S-H reaction in *PHREEQC* is modelled using a CSHQ solid solution model proposed by Kulik [131].

As the setup is quasi one dimensional a comparison of the results was carried out with one dimensional reactive transport code HP1 [132]. Fig. 4.8 shows the profile at different times for Ca and Si in solid and liquid phases. Fig. 4.9 shows the profiles of pH and porosity at different time. Excellent agreement is observed between LB schemes and HP1.

4.6 Examples

[4]In this section different examples highlighting the influence of various parameters such as solution composition, surface area, location of mineral phases and pore network characteristic on dissolution of portlandite are presented. The example in Section 4.6.1 demonstrates the influence of solution pH on dissolution kinetics. The influence of mineral location and surface area on dissolution kinetics is presented in Section 4.6.2. Both simulations were

---

[4]This section is based on the published papers titled —

"A versatile pore-scale multicomponent reactive transport approach based on lattice Boltzmann method: Application to portlandite dissolution" [117]

"Application of porescale reactive transport model to study the influence of pore network characteristics on calcium leaching in cementitious material" [133]
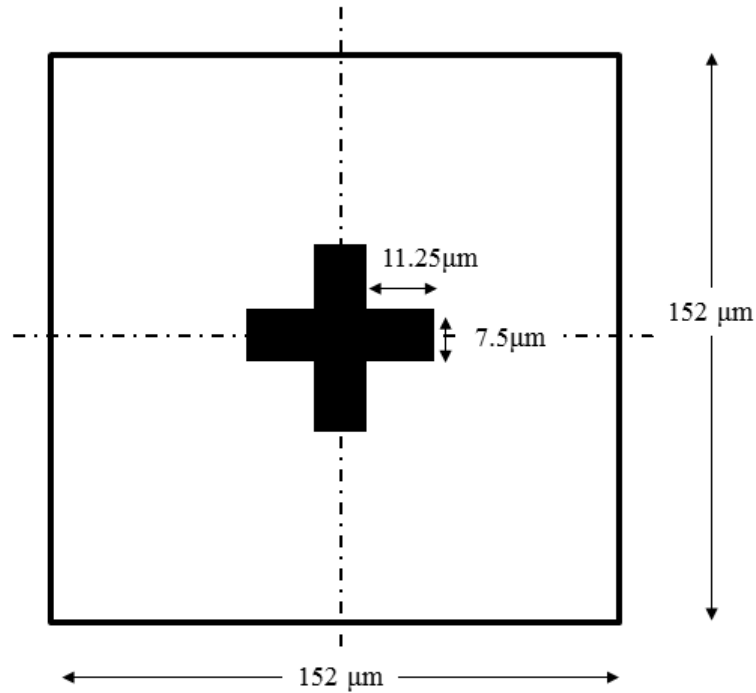
Figure 4.10: Geometry setup for simulations in Section 4.6.1. Region in black represents portlandite grain. In Section 4.6.2 this geometry is referred to as case 1.

carried out using LB reactive transport model wherein the reaction term is computed using *PHREEQC*. The transport is carried out using pore-scale SRT LB scheme with D2Q5 lattice and linear EDF. The diffusion coefficient for all the components was taken as 1×10^{-9} m^2/s.

The example in Section 4.6.3 illustrates the influence of pore network properties on dissolution of mineral phase. This example is carried out using a single component reactive transport model with only Ca as the component to be transported. The heterogeneous reactions were considered as equilibrium reactions. The discussion on equivalence of this approach compared to LB transport model coupled with the geochemical solver is presented in Chapter 8. The equilibrium concentration C_{eq} was set to 19.49 mM which corresponds to the equilibrium concentration of portlandite when in contact with deionized water. The transport is carried out using the pore-scale SRT LB scheme with D2Q5 lattice and linear EDF. The diffusion coefficient for Ca component was taken as 1.3×10^{-9} m^2/s for this example.

4.6.1 Influence of pH on portlandite dissolution

In this example the effects of different pH values of the surrounding solution on averaged dissolution kinetics, equilibrium solubility and change in geometry of solid portlandite mineral grain are shown. The model setup consists of 152 μm $\times$ 152 μm with a grid spacing of 1 μm and a solid portlandite grain with a hypothetical cross shape at the centre
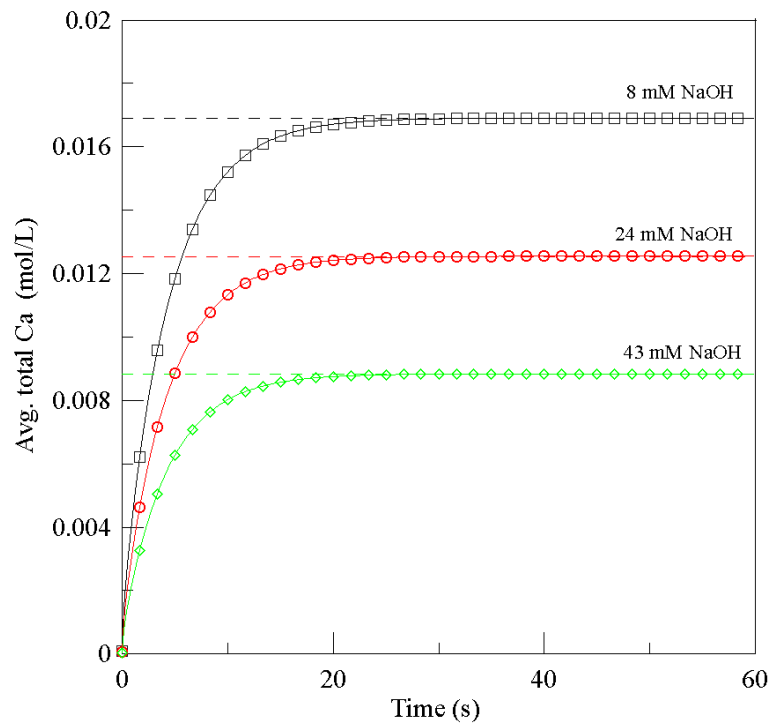
Figure 4.11: Average total Ca concentration with different NaOH solutions. Dashed lines indicate equilibrium computed using PHREEQC assuming the problem setup as a batch reactor
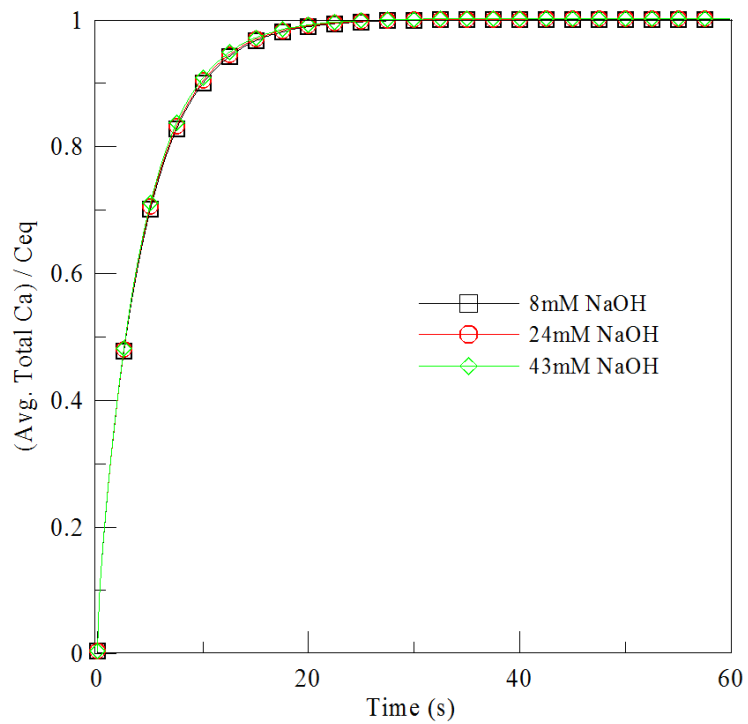
Figure 4.12: Normalized average total Ca concentration with respect to equilibrium for different NaOH solutions.
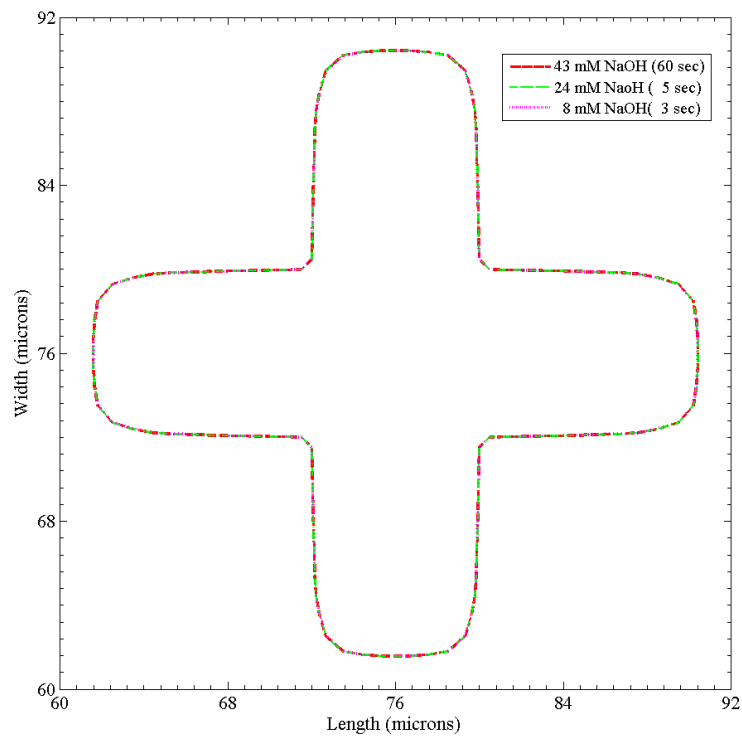
(a)
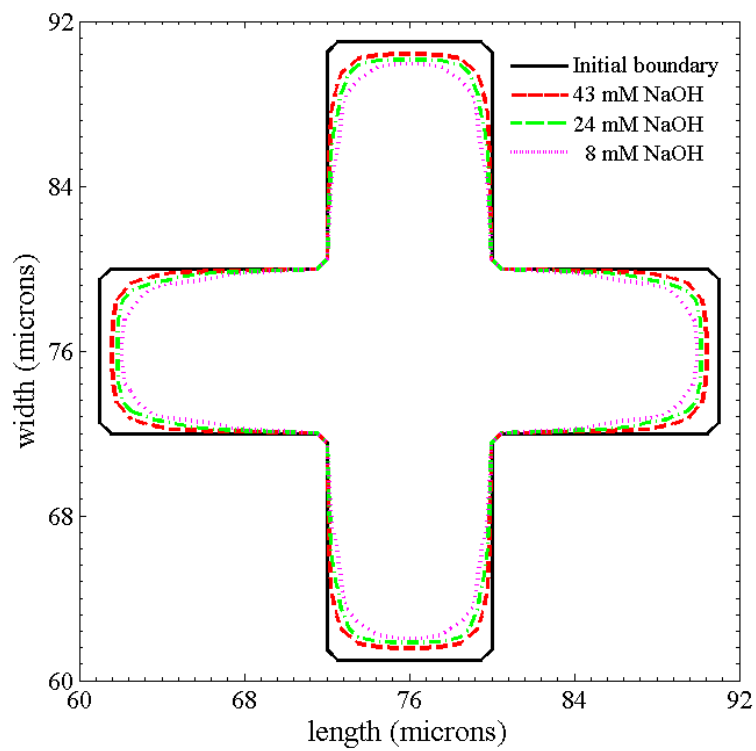
(b)

Figure 4.13: Boundary contour for solid grain for 43 mM, 24 mM and 8 mM NaOH solution (a) when the average concentration in domain is equal to the one corresponding to equilibrium concentration of 43 mM NaOH solution (b) at 60 sec.

of domain as shown in Fig. 4.10. The shape of the portlandite grain is chosen to include inner and outer corners, but kept symmetric so that change of geometry can be visually verified. The domain is initially filled with an aqueous NaOH solution and simulations were carried out for different molar concentrations of NaOH viz., 8 mM (pH $\approx$ 11.867, ionic strength $\approx 7.965 \times 10^{-3}$ at 25°C), 24 mM (pH $\approx$ 12.326, ionic strength $\approx 2.371 \times 10^{-2}$ at 25°C) and 43 mM (pH $\approx$ 12.567, ionic strength $\approx 4.214 \times 10^{-2}$ at 25 °C). All boundaries are no flux boundaries to simulate a closed system. The amount of portlandite in the solid grain is 5M (instead of $\approx$30 M in case of hardened cement paste) to clearly observe the influence of dissolution on geometrical changes before equilibrium is reached.

Fig. 4.11 shows the evolution of the average aqueous total Ca concentration with time. The average total Ca concentration at equilibrium corresponds to the equilibrium Ca concentration. Solutions with a lower NaOH content (lower pH) require a higher amount of portlandite to be dissolved to reach equilibrium. On the other hand, equilibrium is reached at the same time for all three cases and the profile of total Ca concentration normalized with respect to the equilibrium concentration over time coincide with each other as a consequence of a diffusion-controlled dissolution process (Fig. 4.12). This can be also confirmed from Fig. 4.13(a) which shows that the portlandite grain boundary for all the three cases overlap each other when the average concentration in the domain corresponds to the equilibrium concentration with 43 mM NaOH solution. The final portlandite grain boundary at the end of simulations for all the three cases is shown in Fig. 4.13(b) which shows that solutions with lower NaOH content undergoes more dissolution.

4.6.2   Influence of surface area and spatial arrangement

Surface area is an important parameter influencing the dissolution rate of minerals. However, not only the surface area, but also the spatial arrangement of different mineral grains determines the average dissolution rate. For example, if two mineral grains are located close to each other, the narrow channel formed between two grains might reach local equilibrium, prohibiting further dissolution of the grains from these surfaces. Hence, surface area and location of mineral grains contribute to average dissolution rate and to the evolution of microstructure during dissolution.

To illustrate these processes, the cross-shaped grain from the Section 4.6.1 is further divided into four equal 'L' shaped parts as shown in Fig. 4.14, which doubles the surface area compared to that in the Section 4.6.1. Simulations were carried out for two spatial arrangements of these grains as shown in Fig. 4.14. In case 2 (Fig. 4.14(a)), grains are separated from each other forming a narrow channel of 2 μm between them, whereas in case 3 (Fig. 4.14(b)), they are separated more distantly from each other. Boundary conditions are similar to those in the previous example. Initial concentration of NaOH solution is set to 8 mM in the domain.
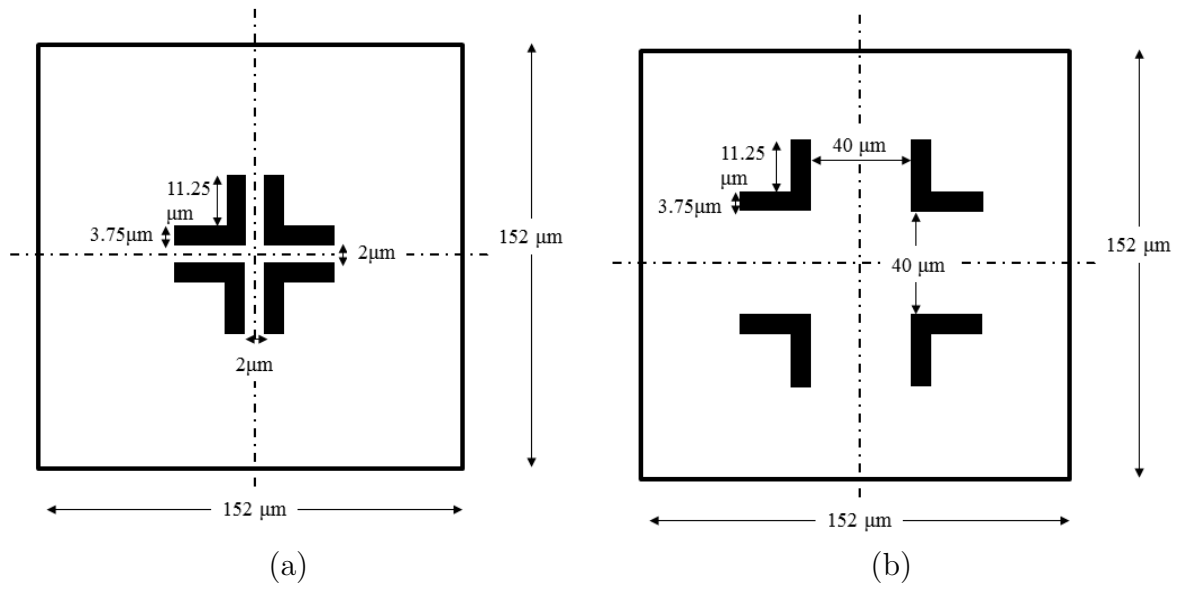
Figure 4.14: Geometry setup for simulations in section 4.6.2. Region in black represents portlandite grain. a) referred as case 2, b) referred as case 3 in text
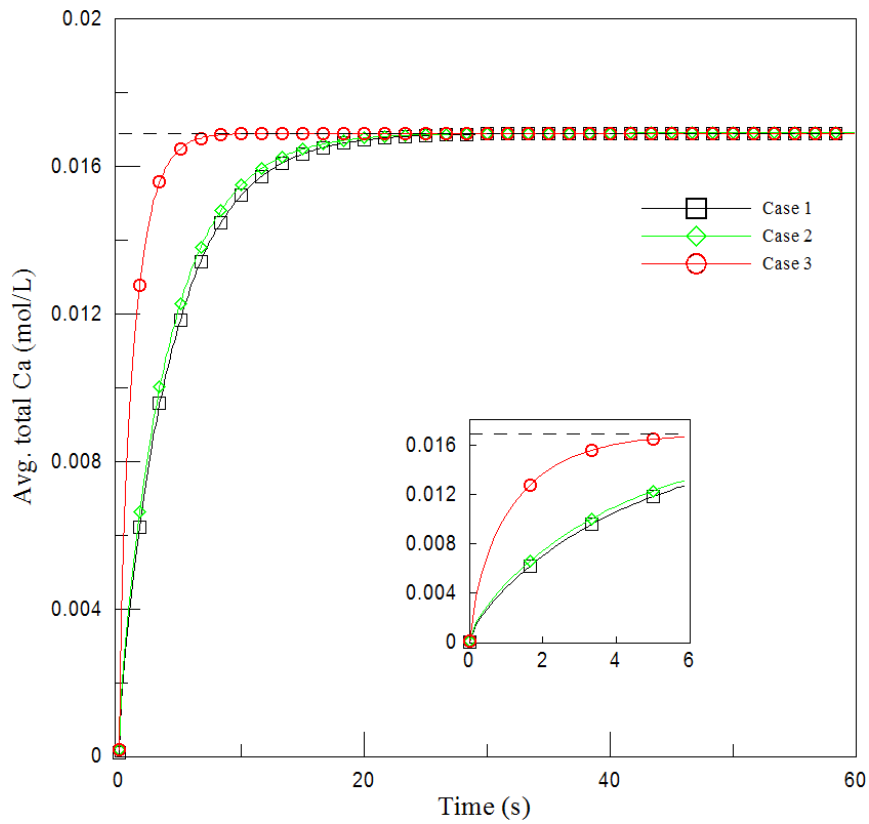
Figure 4.15: Average total Ca concentration showing influence of surface area and relative location of portlandite grain. The first 6 sec of profile is magnified in inset. Dashed line indicates equilibrium computed using *PHREEQC*.
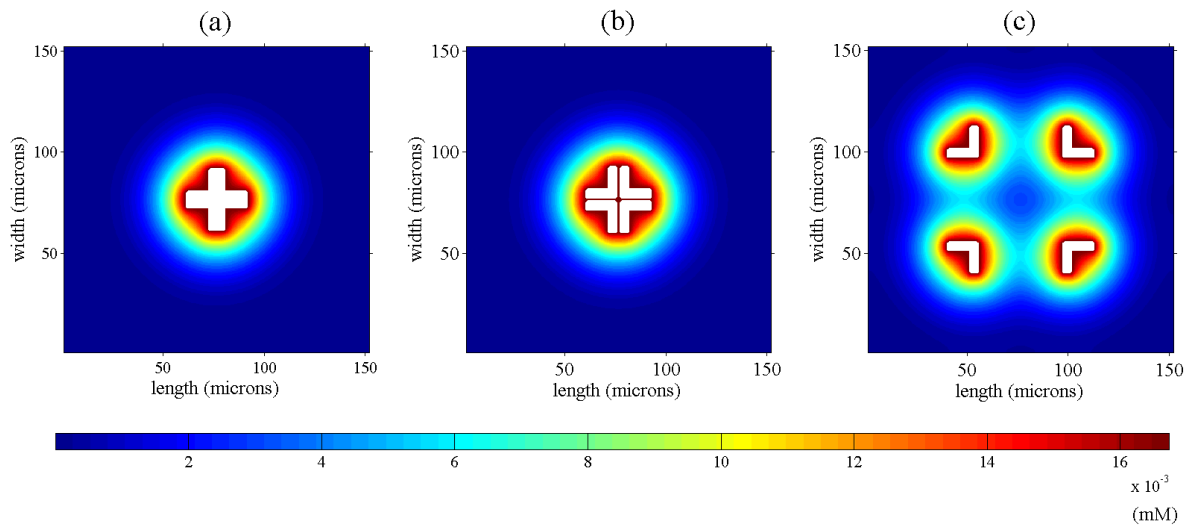
Figure 4.16: Total Ca concentration contour at 0.1668 s: a) Case 1, b) Case 2, c) Case 3 of Section 4.6.2
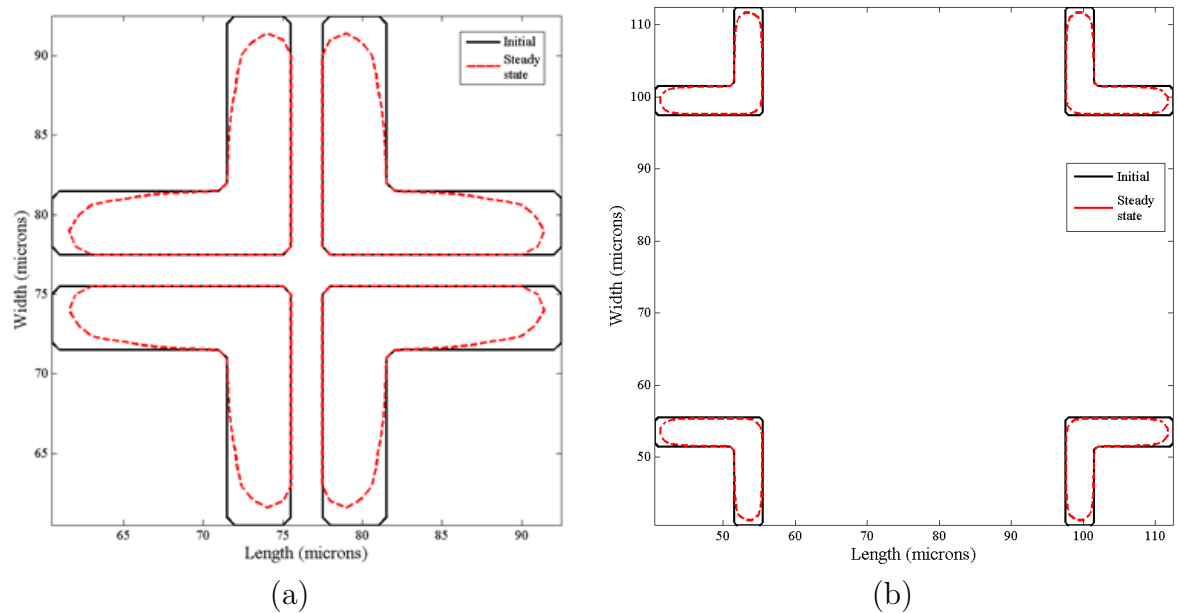
Figure 4.17: Boundary contour for solid grains: a) Case 2 of Section 4.6.2, b) Case 3 of Section 4.6.2
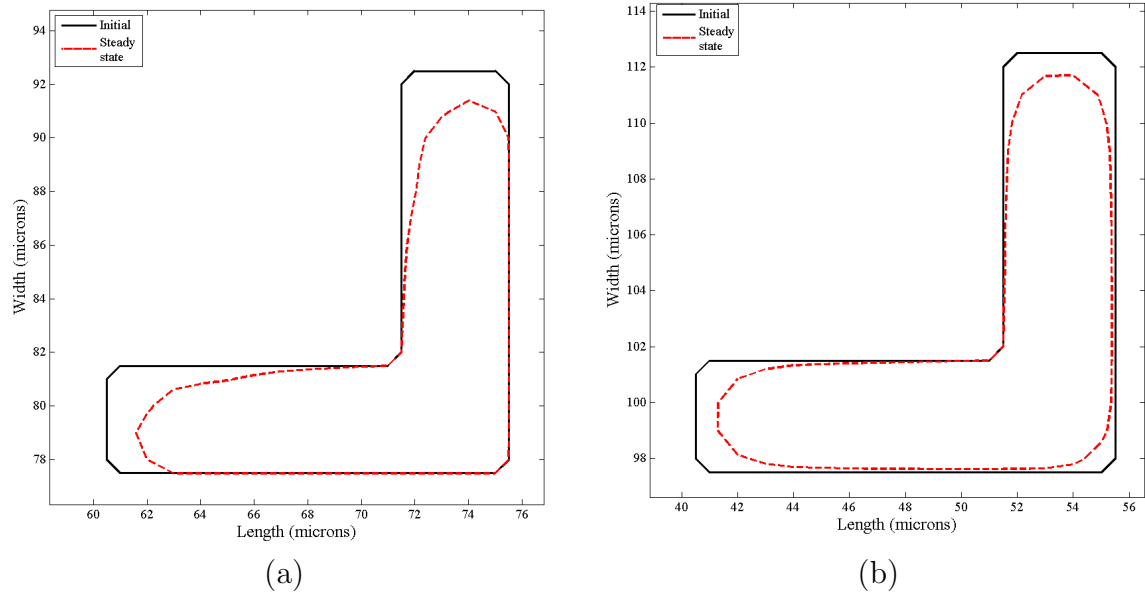
Figure 4.18: Boundary contour for top-left 'L' solid grain: a) Case 2, of Section 4.6.2, b) Case 3 of Section 4.6.2

Fig. 4.15 shows the evolution of the average total Ca concentration with time. In case 2, the narrow channel between the grains quickly reaches local equilibrium (concentration gradient inside the narrow channel is close to zero) soon after the start of portlandite dissolution as indicated in Fig. 4.16(b) which shows the total Ca concentration profile at time 0.1668 s. This inhibits further dissolution of the inner surfaces. Thus, even though the total surface area is twice than that in case 1, the accessible reactive surface area is almost the same as in case 1. Therefore, only small differences in average dissolution rate and total Ca concentration are observed between cases 1 and 2 (see Fig. 4.15). When the grain surfaces are sufficiently apart from each other (as in case 3), concentration gradients exist in all directions (see Fig.4.16c), and hence all faces dissolve faster. This result in a higher average dissolution rate and shorter time to reach equilibrium for case 3 compared to cases 1 and 2 (see Fig. 4.15). Fig. 4.17 shows the altered grain shapes for cases 2 and 3 at end of simulation. Fig. 4.18 magnifies the top-left 'L' shaped grains for case 2 and 3. Fig. 4.18 clearly shows that inner surfaces do not tend to dissolve in case 2 whereas all surfaces are dissolving in case 3. This example effectively demonstrates the influence of surface areas and spatial arrangements of grains on the average dissolution rate and suggests that in case of complex pore structure such as one of hardened cement paste heterogeneities might play an important role in determining average dissolution rate.

4.6.3 Influence of pore network on dissolution

To investigate the influence of the pore network characteristics on leaching, a random porous media consisting of a portlandite mineral as an only reacting phase is considered. In
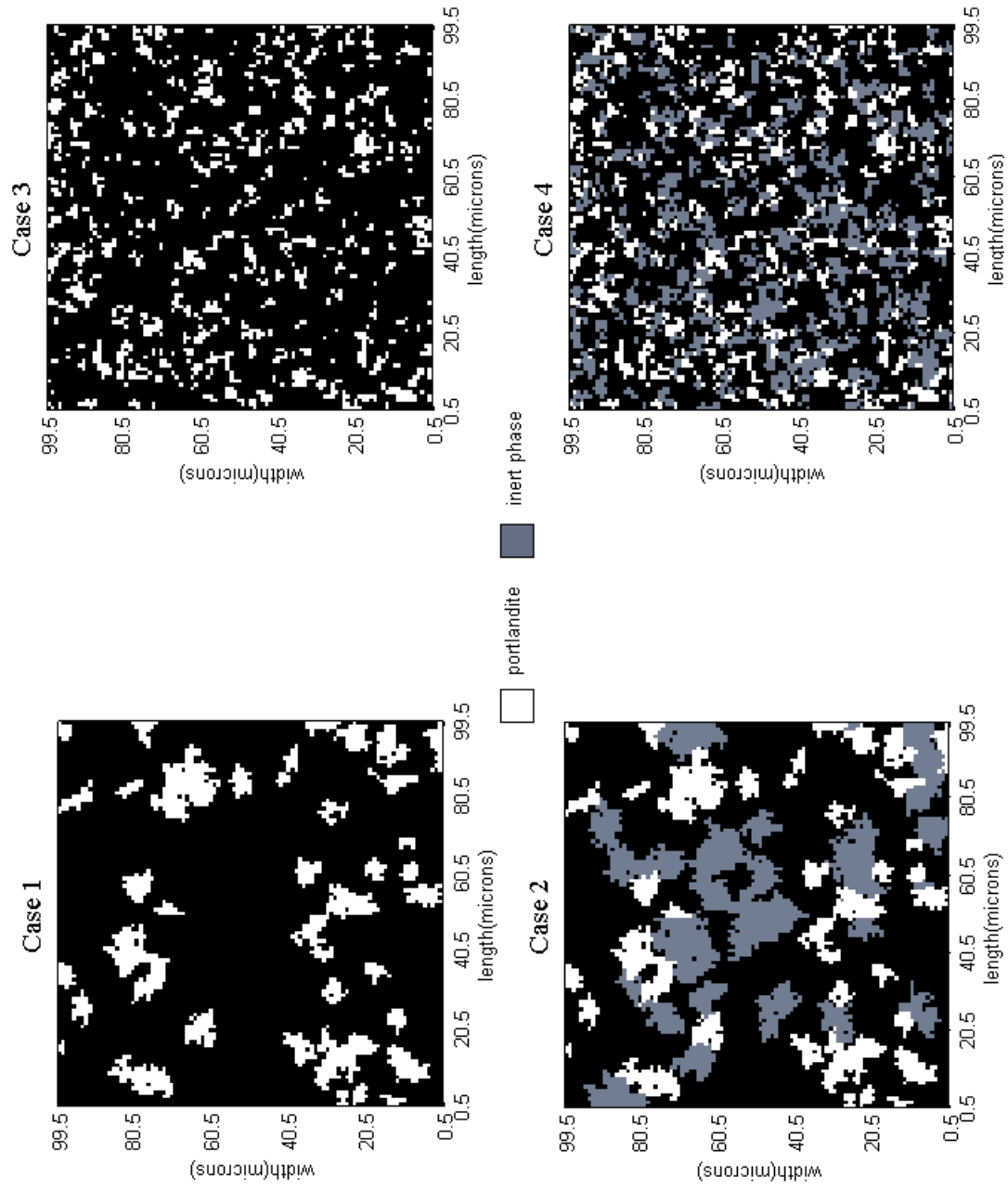
Figure 4.19: Generated porous media for Section 4.6.3

Table 4.1: Characterization of generated porous media

	C_d	ϕ_{port}	ϕ_I	N_p	A_{max}	A_{min}	A_{mean}	P_R/A_p	D_{eff}/D_0
Case 1	0.005	0.15	0.0	35	174	6	42.914	0.9786	0.5903
Case 2	0.05	0.15	0.2	35	174	6	42.914	0.7856	0.1650
Case 3	0.005	0.15	0.0	276	35	1	5.4348	2.2167	0.5701
Case 4	0.05	0.15	0.2	276	35	1	5.4348	1.6827	0.1132

particular, the influence of particle size and tortuosity is investigated through 4 cases shown in Fig. 4.19. The random porous media is generated using the Quartet Structure Generation Set (QSGS) algorithm [134]. This algorithm requires parameters such as directional probabilities for growth in a Von Neumann neighbourhood, core probabilities determining initial number of seeds for growth, the phase fractions and interaction probabilities between two phase if the growth of phases is correlated to generate random porous media. The directional probabilities for QSGS algorithm in orthogonal direction is taken as 0.001 and 0.00025 in diagonal directions to ensure exact phase fractions. The core probability for each case is given in Table 4.1. In all four cases the fraction of portlandite mineral is set to 0.15. Case 1 and Case 3 consist only of portlandite mineral. To increase tortuosity in Case 2 and Case 4, an inert phase with fraction of 0.2 was introduced, keeping the same portlandite mineral phase arrangement as that in Case 1 and Case 3 respectively. The generated random porous media for all four cases is shown in Fig. 4.19. Table 4.1 summarizes parameters of initial microstructure such as fraction of portlandite (ϕ_{port}), fraction of inert phase (ϕ_I), number of particles of portlandite mineral (N_p), maximum area of portlandite mineral particle (A_{max}), minimum area of portlandite mineral particle (A_{min}), mean area of portlandite mineral particle (A_{mean}), ratio of reactive perimeter (P_R) over total area of portlandite mineral grain (A_p) , and ratio of effective diffusivity of media to diffusivity of ion in water (D_e/D_0). The simulation domain consists of 100 μm $\times$ 100 μm with pore water initially in equilibrium with portlandite. The left boundary was set to a constant Ca concentration boundary of 0M. Top, bottom and right boundaries were set as no flux boundaries. Simulations were carried out up to 600s.

Time evolutions of average aqueous Ca concentration and average portlandite concentration are shown in Fig. 4.20(a) and Fig. 4.20(b) respectively. Whereas a similar rate of dissolution is obtained for Case 1 and Case 3 (both has a porosity of 0.85), Case 2 has higher rate compared to Case 4 (both has a porosity of 0.65). Although there is large variation of P_R/A_p between the different cases (Table 1), D_e/D_0 for Case 1 and Case 3 varies by factor of 1.035, whereas it varies by factor of 1.458 for Case 2 and Case 4. This suggests that tortuosity has a more pronounced effect than surface area (i.e. particle size) on the overall dissolution behaviour. Also, lower porosity results in lower D_e/D_0, which leads to lower dissolution rate. Case 2 and Case 4 has lower dissolution rate compared to Case 1 and Case 3 which is evident from Fig. 4.20.
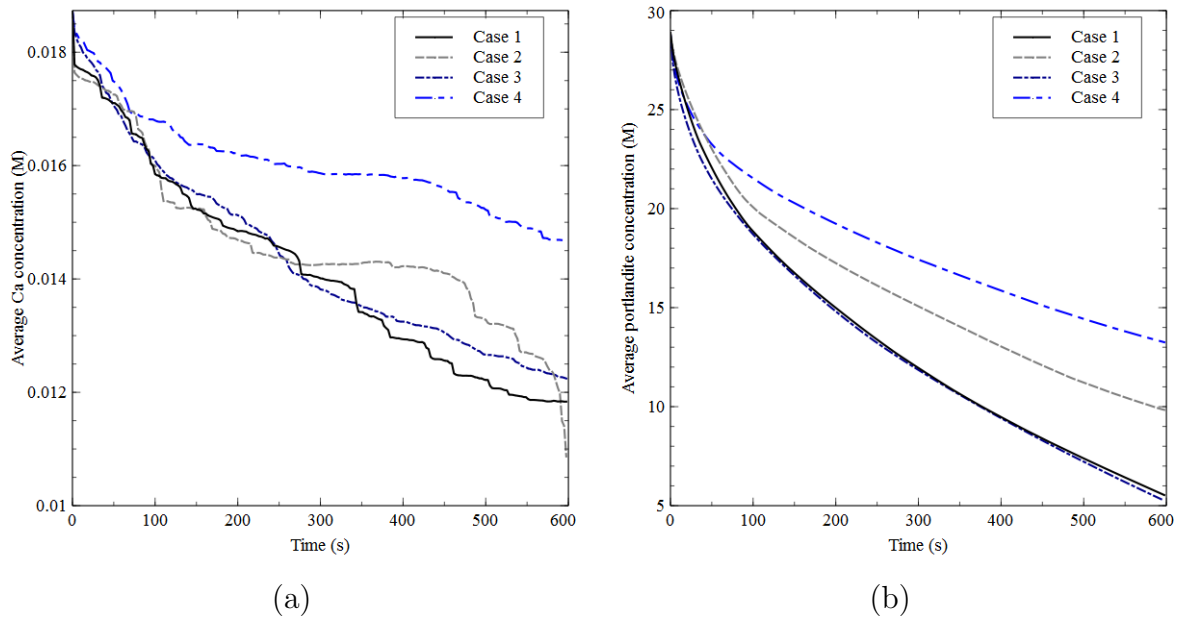
Figure 4.20: Time evolution of (a) average Ca concentration and (b) average portlandite concentration. Averages are taken over phase volume
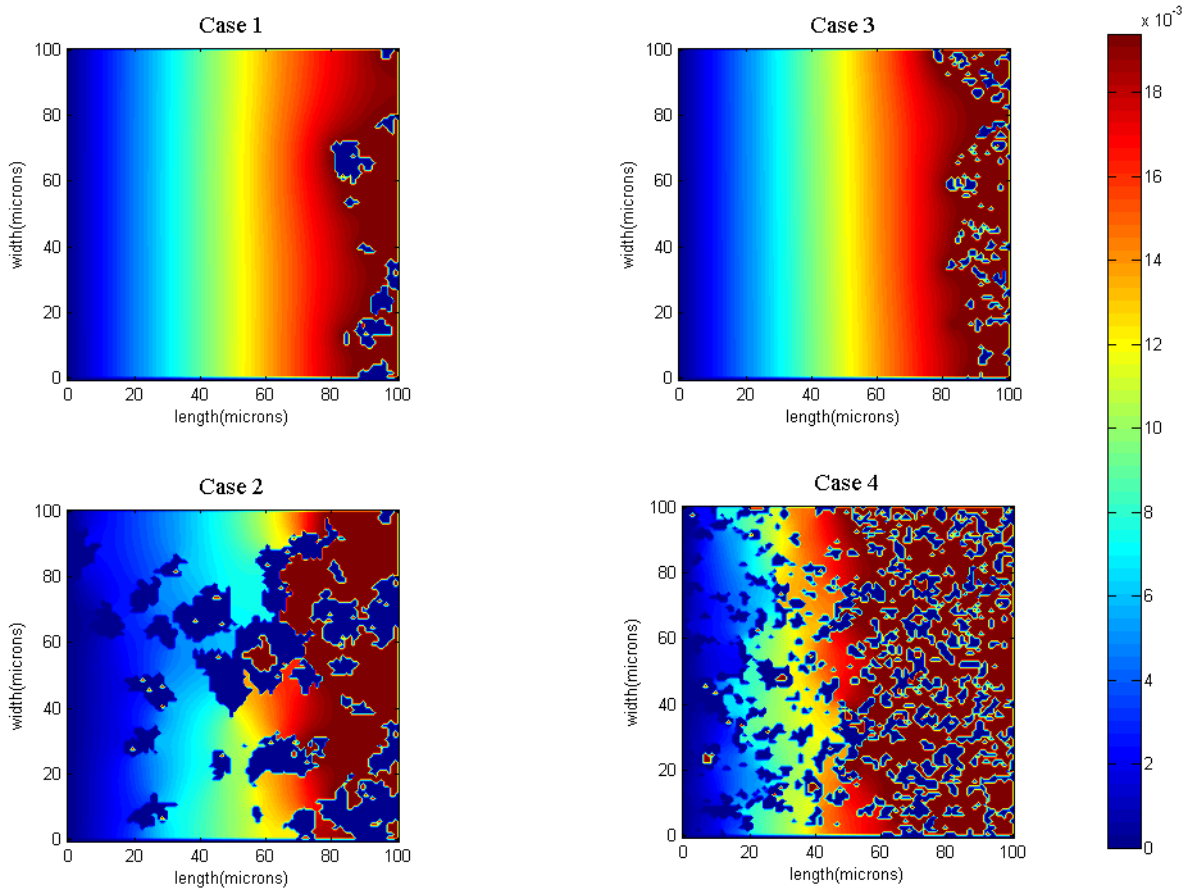
Figure 4.21: Ca profiles at the end of simulation (600s)
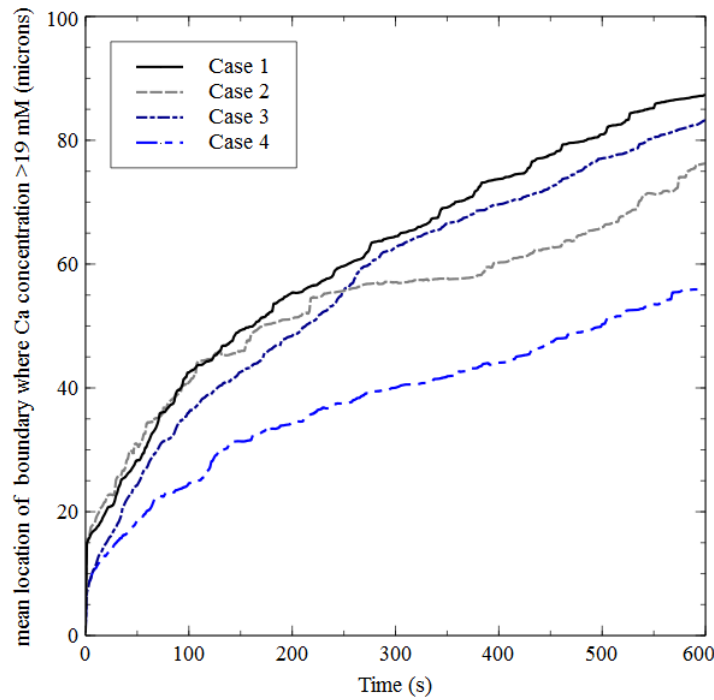
Figure 4.22: Time evolution of mean location of boundary where Ca is greater than 19mM

Figure 4.21 shows the Ca concentration contours at 600 s. the dissolution front moves slower for Case 2 and Case 4 compared to Case 1 and Case 2 with Case 4 the slowest front movement of all cases. To quantify front movement over time, the front position was defined as the mean distance along the horizontal axis at which the concentration is greater than 19mM. Fig. 4.22 shows this front position over time. There are smaller differences in front movement between Cases 1 and 2 as compared to Cases 3 and 4. Moreover for lower porosities (Cases 2 and 4), the front movement is slower compared to the cases with higher porosities (Cases 1 and Case 3) as shown in Fig 4.22.

The results suggest that the tortuosity of the porous media is more significant than the particle shape and the surface area for dissolution in random porous media. Further it indicates that the initial transport properties of media such as porosity and tortuosity have a dominant influence on dissolution behaviour.

4.7 Conclusions

In this chapter, extension of LB schemes for pore-scale and multilevel porous media to incorporate single component and multi-component reactive transport processes are presented. In case of multi-component reactive transport scheme a pseudo-homogeneous treatment is proposed to deal with heterogeneous reactions. Even though, the benchmark shows that this approach is less accurate compared to the conventional approach to treat heterogeneous reactions as boundary conditions, flexibility the proposed approach offers outweighs this drawback. The main advantage of a pseudo-homogeneous treatment is

the ability to treat both homogeneous and heterogeneous reactions in same way thus replacing homogeneous and heterogeneous reactions with a single source/sink term. This allows for the coupling of LB schemes for pore-scale and multilevel porous media with external geochemical codes which have been developed over several decades. This makes the approach more versatile to incorporate new geochemical reaction networks. In this work, a successful coupling of LB schemes with geochemical code *PHREEQC* have been presented for the first time. This coupling has been validated with wide range of benchmark examples. An approach to update the boundary of non-diffusive solid phase as a result of dissolution or precipitation has been presented and validated. It has been found that the changing of boundary at threshold volume fraction of 0.5 is more accurate than updating the boundary on complete dissolution or precipitation as proposed by Kang *et al.* [45] which is commonly used in literature.

A series of examples highlighting the influence of parameters such as solution composition, surface area and location of mineral phases and pore network characteristics on dissolution of portlandite have been presented. Under diffusive transport conditions and a thermodynamic equilibrium approach, different initial pH conditions do not influence the overall reaction rate. However lower pH values increase the amount of portlandite dissolved resulting in smaller grains at the end of simulation. Further for diffusion controlled dissolution, spatial arrangement of mineral grains is more important that the surface area. The spatial arrangement of grains may cause local equilibrium in certain parts of the domain inhibiting local dissolution processes at the grain surface.

Finally, in order to study influence of pore network on portlandite dissolution four cases consisting of random porous media with portlandite as reacting phase were presented. All four cases had the same fraction of portlandite phase but differ in particle sizes or total porosity (by introducing inert material). The latter also increased the tortuosity. The results show that characteristics of porous media affecting ion transport such as tortuosity and porosity have a more pronounced effect on dissolution compared to particle size and surface area for diffusion controlled dissolution.

The results from these simple examples highlights the importance of ion transport at the pore-scale as a crucial factor for determining the overall dissolution rate. In a real microstructure of hardened cement paste, the results from these simplified simulations suggest that the heterogeneity (spatial location of mineral phases) might play important role in determining the average dissolution rate and the evolution of cement paste pore structure during leaching.

Part II: Applications to cement based materials

Critical appraisal of experimental data and models for diffusivity of cement paste

5.1 Introduction

Varieties of degradation processes of cement based materials such as chloride ingress and corrosion, sulphate attack, carbonation and calcium leaching are associated with the transport of ions and gases. One of the important transport mechanisms of ion and gases is diffusion which refers to the transport of matter under concentration gradient. The rate of diffusion is characterized by the *diffusion coefficient or commonly referred to as diffusivity*. Diffusivity is an important parameter for modelling degradation processes for practical applications such as contaminant transport in cementitious barriers, assessment of long-term behaviour of nuclear waste disposal systems based on cementitious materials, prediction of rebar corrosion in civil concrete structures. Diffusivity is also a key durability parameter to define service life of concrete structures [135]. Diffusivity of a porous media at the macroscopic scale is given as [136]

$$D_e = \frac{\theta D_0 \delta}{\zeta^2} \tag{5.1}$$

D_e is the diffusivity of ion/gas in porous media also known as effective diffusivity, D_0 is the diffusivity of the ion/gas in pore water, θ is the water content which is equal to porosity for saturated media; δ is the constrictivity; and ζ is the geometric tortuosity factor. The ratio (D_e/D_0) is also referred to as *relative diffusivity* of the media [137]. Alternatively

Eq. (5.1) can also be represented as [136]

$$D_e = \theta \zeta_a D_0 \tag{5.2}$$

ζ_a is the apparent tortuosity factor. In case of sorption/binding of ions to porous media for e.g. binding of chloride ions in cement based materials, diffusivity is given as [136].

$$D_a = \frac{\theta D_0 \delta}{R_d \zeta^2} \tag{5.3}$$

D_a is the diffusivity accounting for retardation caused by binding/sorption also known as apparent diffusivity and R_d is the retardation factor. Geometric tortuosity factor takes into account that diffusion occurs only through the connected pathway. Constrictivity accounts for the narrowing of pores thus restricting the diffusion of species through the pore. Constrictivity depends on the ratio of the diameter of the diffusing particle to the pore diameter. Moreover phenomena such as anion exclusion and influence of adsorbed layer on diffusion is also lumped into constrictivity [138]. Thus both constrictivity and tortuosity depend on the morphology of the media. The morphology of the cement based material depends on several factors such as water to cement ratio (w/c), admixtures, initial composition of cement clinkers, curing conditions and degree of hydration and hence determination of diffusivity and its prediction is a formidable task.

During last decade efforts has been laid in understanding the process in diffusion and to measure diffusion coefficients. Varieties of methods have been proposed to measure the diffusivity and none of them seems to be univocally accepted. Moreover, different models have been developed to predict the diffusivity of cement based materials. In this chapter an overview on these developments is presented and in particular differences and similarities between different experiments and modelling approaches are highlighted. The scope of this chapter has been limited to steady state diffusivity (i.e. apparent diffusivity not considered) under saturated conditions for ordinary Portland cement (opc).

Section 5.2 gives an overview of experimental data obtained using different techniques and through collection of large amount of experimental data provides perspectives on differences in the values of diffusion coefficients obtained by different methods. Section 5.3 presents an overview on existing diffusivity models for opc. Section 5.4 presents a comparative analysis of cement paste diffusion models discussed in section 5.3. In section 5.5, summerize details on efforts made by different researchers for estimating diffusivity from the cement paste microstructures.

5.2   Comparison of relative diffusivities obtained by different techniques

The experimental methods used to measure diffusion coefficient can be grouped into four types: (i) through-diffusion based on measuring fluxes; (ii) in-diffusion based on measuring concentration profiles in the sample; (iii) electro-migration experiments, either by through- or in-diffusion, in which ion diffusion is accelerated by an electric field; and (iv) techniques in which proxy variables are used to determine diffusivity, e.g. electric resistivity techniques. Overview on these techniques can be found in [8]. Data for diffusion experiments on cement pastes as reported by different researchers using these techniques are compiled in this section. The data include measurements carried out using through-diffusion experiments for tritiated water (HTO) [5, 7, 139–142] and dissolved gases such as helium [8], oxygen [6, 141]; and electrical resistivity [9, 143–145]. Only the steady state diffusion coefficients of chloride ion determined by electro-migration technique [6, 146, 147] were included in this comparison as the chloride is known to bind with the hydration product and as a result non-steady state chloride diffusion varies with time.

Composition of the cement for the collected data is summarized in table 5.1. For the references where no direct values of capillary porosity are available, the capillary porosity(ϕ) is computed using Power's model [148].

$$\phi = \frac{\text{w/c} - 0.36\alpha}{\text{w/c} + 0.32} \tag{5.4}$$

where α is the degree of hydration. In cases where the degree of hydration was not available it was assumed that the paste has been hydrated to maximum achievable degree of hydration. The maximum degree of hydration (α_{max}) was computed using relationship given in [5].

$$\alpha_{max} = 0.239 + 0.745 \tanh[3.62(\text{w/c} - 0.095)] \tag{5.5}$$

Indeed based on the curing conditions used for majority of experiments (summarized in table 5.2) it can be assumed that the maximum degree of hydration has been attained. The compiled data is summarized in table 5.3 and table 5.4.

The relationship between relative diffusivity and w/c and capillary porosity for the collected data is shown in Fig. 5.1(a) and Fig. 5.1(b) respectively. Increase in relative diffusivity with respect to higher w/c and capillary porosity is consistent for all reported data. The relation of the relative diffusivity with w/c shows more scatter than the relation with capillary porosity. This is due to the fact that at a given w/c, the degree of hydration achieved might vary for reported data, which in turn can results in different porosities. Regardless of the use of different experimental techniques and authors, all reported data are fitted well to the exponential relationship correlating the relative diffusivity with

Table 5.1: Cement composition of the collected data

Reference	Bouges composition (in %)				Fineness(m^2/Kg)
	C$_3$S	C$_2$S	C$_3$A	C$_4$AF	
Phung [8]	65.43	15.14	9.19	10.24	435
Ma *et al.* [9]	62.6	17.03	9.73	10.06	-
Yamaguchi *et al.* [142]	51.79	26.72	11.53	9.95	-
Bejaoui and Bary [5]	67.36	21.46	3.75	7.43	310.5
Castellote *et al.* [141]	61.18	15.98	12.21	10.63	-
Delagrave *et al.* [7](w/c=0.45)	68.7	5.8	7.4	5.1	461.6
Delagrave *et al.* [7] (w/c=0.25)	68.7	6.9	7.7	5.4	535.1
Ngala and Page [6]	54.81	25.7	10.71	8.77	345
Christensen *et al.* [145]	73.48	19.96	5.36	1.19	-
Oh and Jang [146]	30.0	40.5	11.0	9.7	-
Sun *et al.* [147]	55.5	19.1	6.5	10.1	-

Table 5.2: Curing conditions for the collected data

Curing conditions	Reference
For 28 days in sealed condition in a controlled temperature of 22°C ± 2°C	Phung [8]
The samples were cured at 50°C under deionized water until peak of in XRD of unhydrated cement phase disappears	Yamaguchi *et al.* [142]
Samples are cured in saturated lime water incoroporating sodium and potassium hydroxide during 12 months	Bejaoui and Bary [5]
Samples are cured for 28 days under water. They were stored for 1 month immersed in a saturated Ca(OH)$_2$ solution	Castellote *et al.* [141]
The specimens were demolded and immersed in lime solution for 3 months	Delagrave *et al.* [7]
After curing at 22°C for 2 weeks and immersed in 35mM NaOH solution. They were then stored in a curing room at temprature of 38 ± 2°C for 10 weeks	Ngala and Page [6]
Cured for 28 days in a 100% relative humidity chamber at 25°C	Numata *et al.* [139]
Cured at 20°C till test was performed	Oh and Jang [146]
The samples were placed in a room at a temperature of 20 °C for 24 h and then moved to a standard curing room (temperature of 20 ± 3°C, relative humidity above 95 %). After three days of curing, the samples were removed and split into several parts. Finally, the samples were taken out for measurement of their degree of hydration and porosity at the required standard age	Sun *et al.* [147]

Table 5.3: Summary of data of diffusion coefficient collected from literature: electric resistivity technique

Reference	w/c	Degree of hydration	Capillary porosity	$D_e/D_0 (\times 10^{-2})$
Ma *et al.* [9]	0.3	0.28	0.321**	2.85
		0.431	0.24**	1.63
		0.522	0.18**	1.52
		0.61	0.13**	1.34
		0.65	0.11**	1.30
	0.4	0.33	0.39**	5.36
		0.51	0.30**	2.91
		0.631	0.24**	2.36
		0.70	0.21**	2.01
		0.72	0.2**	1.76
	0.5	0.36	0.45**	9.50
		0.56	0.37**	5.30
		0.67	0.32**	3.88
		0.74	0.29**	2.67
		0.79	0.27**	2.01
Tumidajski *et al.* [143]	0.25	0.54***	0.10	0.104
	0.3	0.63***	0.12	0.372
	0.4	0.6***	0.26	2.04
	0.5	0.68***	0.31	2.42
	0.8	0.42***	0.58	10.5
	1	0.65***	0.58	10.5
Taffinder and Batchelor [144]	0.4	0.84*	0.137*	0.476
	0.5	0.91*	0.211*	0.581
	0.6	0.946*	0.282*	1.03
	0.7	0.966*	0.345*	1.67
	0.8	0.975*	0.401*	1.82
	0.9	0.98*	0.449*	2.63
	1.0	0.982*	0.49*	3.70
Christensen *et al.* [145]	0.5	0.611**	0.31**	2.87
		0.511	0.36**	3.52
		0.491	0.37**	4.31
		0.451	0.39**	5.89
		0.431	0.40**	7.07
		0.391	0.42**	9.22
		0.311	0.46**	16.3
		0.291	0.47**	20.9
		0.211	0.51**	35.2
		0.171	0.53**	39.5
		0.091	0.57**	43.0
		0.011	0.61**	45.6

*Degree of hydration is taken as maximum degree of hydration computed using equation 5.5 and porosity computed using equation 5.4

**porosity was computed using relationship given in ref [149]

***Degree of hydration computed using equation 5.4

Table 5.4: Summary of data of diffusion coefficient collected from literature: Through diffusion and electro-migration techniques

Reference	Technqiue/ Tracer	w/c	Degree of hydration	Capillary porosity	$D_e/D_0 (\times 10^{-2})$
Phung [8]	Helium	0.425	0.85***	0.16	0.321
Sun *et al.* [147]	electro migration	0.23	0.573*	0.04*	0.0696
		0.35	0.734*	0.13*	0.2203
		0.53	0.861*	0.26*	0.723
Yamaguchi *et al.* [142]	HTO	0.45	0.908***	0.16	0.638
		0.6	0.926***	0.29	2.05
		0.75	0.953***	0.38	3.88
Bejaoui and Bary [5]	HTO	0.25	0.62*	0.048*	0.0251
		0.3	0.71*	0.072*	0.0505
		0.35	0.782*	0.103*	0.122
		0.38	0.817*	0.123*	0.146
		0.4	0.84*	0.137*	0.164
		0.42	0.856*	0.152*	0.178
		0.45	0.879*	0.174*	0.239
		0.5	0.91*	0.211*	0.404
		0.6	0.946*	0.282*	0.696
		0.65	0.958*	0.315*	0.937
Oh and Jang [146]	electro migration	0.35	0.673***	0.161	0.254
		0.45	0.788***	0.225	0.443
		0.55	0.83611***	0.286	1.061
Castellote *et al.* [141]	oxygen	0.4	0.84*	0.137*	0.453
Delagrave *et al.* [7]	HTO	0.45	0.879***	0.22	0.439
		0.25	0.55***	0.09	0.0281
Ngala and Page [6]	oxygen	0.4	0.84*	0.137*	0.449
		0.5	0.91*	0.211*	0.498
		0.6	0.946*	0.282*	0.653
		0.7	0.966*	0.345*	1.04
Ngala and Page [6]	electro migration	0.4	0.84*	0.137*	0.2703
		0.5	0.91*	0.211*	0.5068
		0.6	0.946*	0.282*	0.8108
		0.7	0.966*	0.345*	1.4864
Revertegat *et al.* [140]	HTO	0.37	0.625***	0.21	0.2
Numata *et al.* [139]	HTO	0.4	0.831***	0.14	0.228
		0.5	0.774***	0.27	0.424
		0.55	0.851***	0.28	0.504

*Degree of hydration is taken as maximum degree of hydration computed using equation 5.5 and porosity computed using equation 5.4

**porosity was computed using relationship given in ref [149]

***Degree of hydration computed using equation 5.4
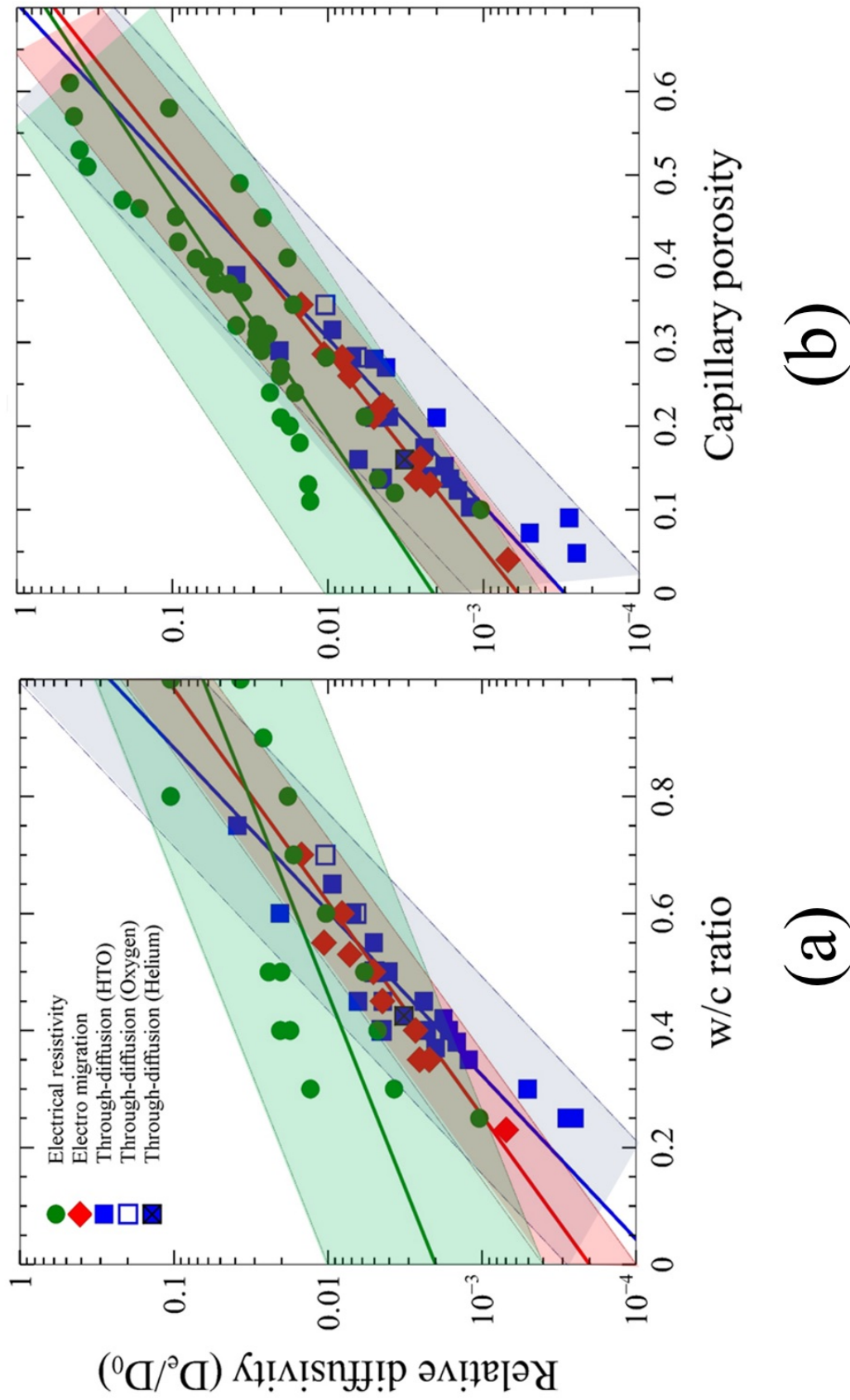
Figure 5.1: Relative diffusivity vs. (a) w/c and (b) capillary porosity – data is fitted to exponential relationship (bold solid lines); shaded regions represent the factor of five, two and four bounds for the exponential relationship fitted with data from electrical resistivity, electro-migration and through diffusion, respectively.

w/c or capillary porosity. However the data obtained by electrical resistivity shows most scatter (within factor of five bound[1]), whereas electro-migration data shows least scatter (within factor of two bound). Spragg *et al.* [150] have analysed in detail different factors affecting electrical resistivity measurements. They reported that several key parameters such as type of setup, temperature, sample storage and conditioning, frequency of current at which measurements are carried out, and the resistivity of pore water solution may result in large variations of the relative diffusivity obtained by the electrical resistivity measurements. The relative diffusivity obtained from electrical resistivity measurement is also higher than the ones from electro-migration and through-diffusion. The difference seems to diminish with the increase of w/c or capillary porosity. When the w/c is larger than 0.4, the differences between the different techniques diminishes.

5.3   Effective diffusivity models

In this section different constitutive relationships to predict diffusion coefficients are reviewed. Many relationships have been proposed to describe the link between diffusivity of cement paste and parameters such as porosity, w/c and volume fractions of different phases. These relationships can be broadly classified into empirical approaches, relationships derived from numerical models and analytical relationships which are based on effective media theories. Further classification can be made for models based on effective media theory into models considering morphology of cement paste in simplified form and models taking into account in details the morphological characteristics of cement paste. These relationships are summarized in Appendix F.

The empirical relationships between parameters (e.g. porosity, w/c) which link morphology and effective diffusivity through a set of constants are determined by fitting this relationship with the experimental data. The empirical relationships do not directly account for the morphology and connectivity of the pore structure and these considerations are lumped in fitting coefficients. Some of these relationship have been directly adapted from the soil science. For instance, Archie's power relationship [151] which was preliminary proposed for rocks and sand has been adapted for cement paste. Archie's relationship is originally presented in terms of total porosity. For cementitious materials it is usually assumed that the major effect on transport properties is due to capillary porosity and hence some authors [137, 146] express Archie's relationship in terms of capillary porosity. Moreover, porosity for cement paste is often determined by a Mercury Intrusion Porosimetry (MIP) which covers mainly capillary pore range [152]. Hence in this chapter all empirical relationships including Archie's relationship have been expressed in terms of capillary porosity. Applicability of Archie's relationship to cementitous materials has been argued

---

[1]The factor of five bound refers to the area in between the line drawn by multiplying and dividing five with the best fit value

Table 5.5: Values of coefficients and power for Archie's relationship as derived by different authors. *a* and *n* are coefficient and power which are to be fitted for Archie's relationship.

Reference	a	n
Tumidajski *et al.* [143]	1.89	2.55
Tumidajski *et al.* [143] using data of Christensen *et al.* [145]	0.14	4.8
Tumidajski *et al.* [143] using data of Taffinder and Batchelor [144]	7.71	3.32
Yamaguchi *et al.* [142]	0.18	0.94

by some authors [137, 145, 153]. Moreover, the fitting parameters obtained by different authors for Archie's relationship vary substantially. These values are summarized in Table 5.5. Despite these limitations, Archie's relationship is often used to simulate reactive transport processes in cement [13, 154]. To alleviate the inability of Archie's relationship to account for the percolation threshold Winsauer *et al.* [155] proposed the extension which sets the diffusivity to zero when the porosity is smaller than the threshold porosity (ϕ_c). For cement paste, the fitting parameters for this relationship have been obtained by Lee *et al.* [156]. The effective diffusivity can also be expressed as the exponential function of the porosity instead of power relationship as suggested in Refs. [139, 153, 157]. The exponential function is also used to describe the relationship between w/c ratio and effective diffusivity [158].

Garboczi and Bentz [137] proposed relationship between relative diffusivity and capillary porosity based on numerical computation of diffusivity from virtual microstructures of cement paste. Computation of diffusivity from virtual microstructure allows distinguishing contributions of different diffusive phases viz. C-S-H and capillary pores to diffusion. The first term in their relationship represents the contribution from the percolating fraction of capillary pores. The second term represents contribution of non-percolating capillary pores and C-S-H phase. The last term is the contribution of C-S-H when capillary porosity is zero. Through numerical simulations on virtual microstructure of hydrating C_3S paste they determined the values for the coefficients a_1, a_2 and a_3 as 1.8, 0.07 and 0.001 respectively (for mathematical expression see appendix F). The threshold porosity (ϕ_c) was determined as 0.18. Bentz *et al.* [159] re-determined the coefficients a_1, a_2 and a_3 for cement paste as 1.7, 0.03, and 0.0004 respectively. The threshold porosity for cement paste was determined as 0.2. The threshold porosity computed from the virtual microstructure of cement paste has been found to be independent of w/c. However, it strongly depends on the resolution of the microstructure and microstructure model used [160–162] and hence percolation threshold can be considered as an additional parameter that can be adjusted. Furthermore, many models discussed later in this paper base the percolation threshold on work of Garboczi and Bentz [137] and hence the percolation threshold is classified as an unknown parameter in this chapter.

The models presented till now are either empirical or have been derived from numerical computations. Alternatively the morphology of cement paste can be conceptualized into

a simple geometrical configuration for which analytical solution or theoretical model can be devised. These theories are known as effective media theory. The simplest geometrical configuration for which analytical solution exist is arranging different phases of the multiphase material such as cement paste in series or parallel. Bejaoui and Bary [5] presented a set of series/parallel configurations, to predict diffusivity of the cement paste as shown in Fig. 5.2. In their approach the percolating diffusive phases are placed in parallel. The non-percolating phases are placed in series. The degree of percolation was computed based on volume fraction. They assumed that the phase starts to percolate once its volume fraction is 15% and the amount of percolating fraction increases linearly and becomes fully percolated at 25% volume fraction. This function for degree of percolation is inspired from the analysis on CEMHYD3D generated microstructures reported by Bentz *et al.* [159]. Additionally to account for the tortuosity of capillary pores they used an exponential law. The tortuosity of LD and HD C-S-H phase and mixed fraction of LD C-S-H and capillary pores was taken into account using the effective media theory for single coated spheres [163]. The porosity of LD and HD C-S-H was taken as 20% and 31% respectively according to Jennings model [22]. The phase fractions needed for their model is determined using the Tennis and Jennings hydration model [15]. They determined the diffusion coefficient of LD C-S-H and HD C-S-H as 9×10^{12} m^2/s and 1×10^{12} m^2/s, respectively, for HTO by fitting the experimental data.

Another set of configuration for which theoretical models exist are the well-defined inclusions (such as spheres, cylinders, ellipsoids) distributed randomly throughout a matrix material. The basic idea behind these models have been discussed in appendix G. Several cement paste models have been proposed wherein cement paste has been conceptualized to be composed of inclusions in a matrix. Pivonka *et al.* [164] applied the differential media approximation to predict the effective diffusivity of cement paste. The cement paste morphology is conceptualized as a media composed of non-diffusive phase as spherical inclusions in matrix of capillary pores. The diffusion through gel (C-S-H) pores is thus neglected. Based on the comparison with the results of experiments for steady state chloride diffusivity, they found that the values obtained from differential effective media theory an one order higher than that of experiments. Hence they suggested to decrease the diffusivity of pore solution by factor of 10. They attributed the choice of lower diffusivity in the pore solution of cement paste to the higher viscosity of the pore solution which is due to the restructuring of water molecules along the charged pore surfaces. Under these assumptions the differential approximation reduces to Archie's law with values of coefficient and power as 0.1 and 1.5 respectively. Christensen *et al.* [145] have shown that for electric resistivity measurements, differential approximation provides good correlation only at early stages of hydration when capillary porosities are greater than 50%. However, at later stage of hydration, differential scheme breaks down. Oh and Jang [146] applied generalized effective media approximation to predict effective diffusivity of cement paste.
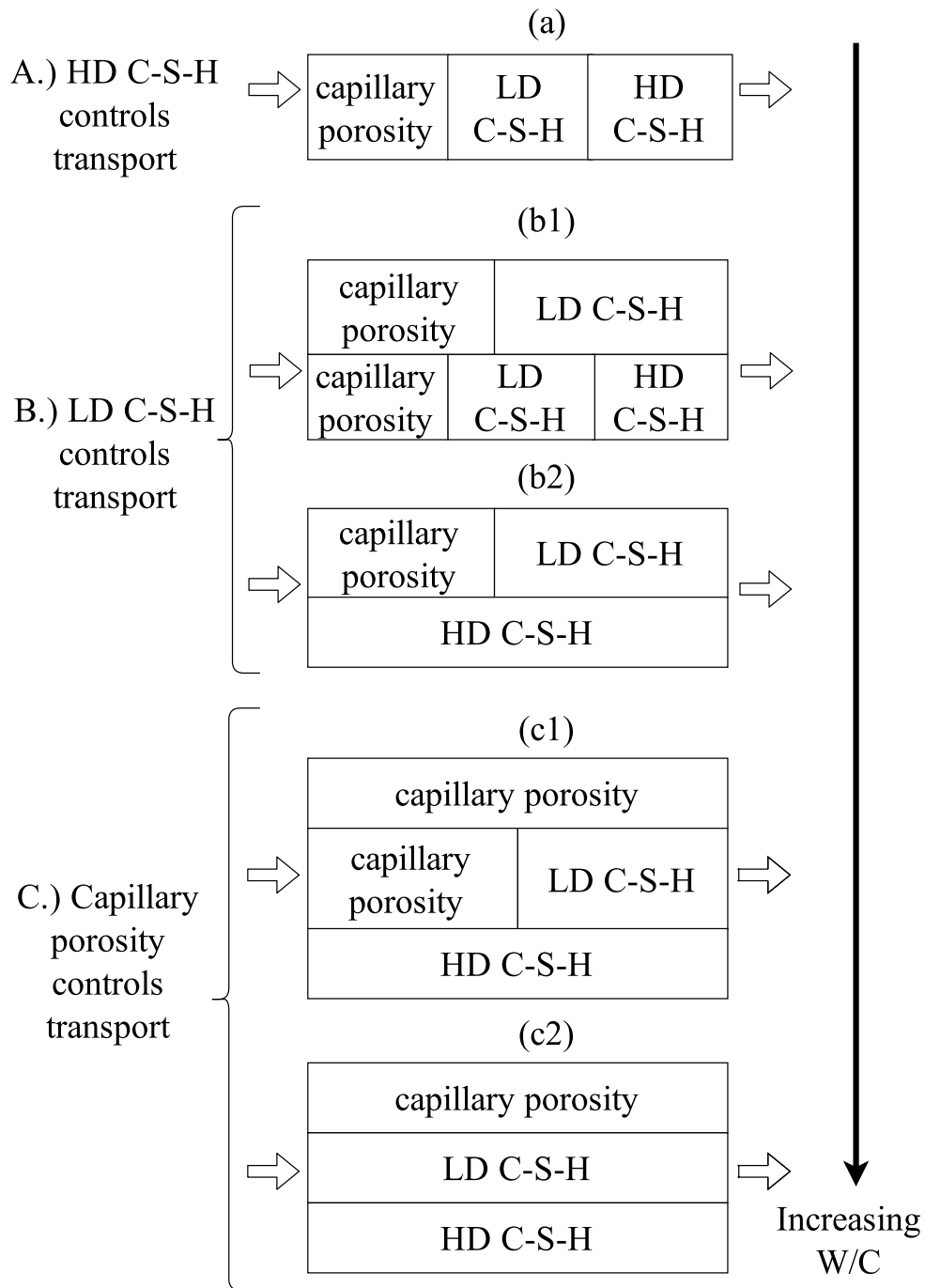
Figure 5.2: Simplified equivalent systems proposed by Bejaoui and Bary [5] for HCP

They considered that the cement paste consists of inclusions capillary pores and diffusive solid (C-S-H) in matrix of equivalent homogeneous media. According to this model, for the porosity smaller than threshold capillary porosity, diffusion occurs through the diffusive solid. They assumed threshold capillary porosity as 0.17. They determined the relative diffusivity of this solid phase by fitting with the experimental data as 2.0×10^{-4}. The relationship derived from the generalized effective media theory takes a similar form as that of modified Archie's relationship proposed by Winsauer *et al.* [155] when diffusivity of solid phase is zero. Therefore, modified Archie's law can also be viewed as a specific case of generalized effective media theory.

Models based on effective media theory so far described considered a very simplistic view on morphology of cement paste. Several models have been proposed which account for more detailed morphological description of cement paste. The cement paste morphology is represented in several levels and the effective media theories are then utilized for obtaining effective diffusivity at each level. Bary and Béjaoui [165] conceptualized morphology of cement paste as a three coated spheres with the core at the centre and three layers around this core viz., inner, intermediate and outer layers. The clinker forms the core and hydration products are represented as layers around the clinker phase. The hydration products are divided into two layers (inner and outer layers), in which other minor phases (portlandite (CH) and aluminate phases (AFm)) are inclusions. The inner layer is formed of HD C-S-H whereas outer layer is formed of LD C-S-H. The outer layer further contains inclusions of more diffusive capillary pores. They further divided outer layer into two parts where one part consists of non-percolated capillary pores and the other part contains percolated capillary pores. They assumed the fractions of non-percolated capillary pores as 8%. Both intermediate and outer layers have equal amount of CH and AFm inclusions. The fraction of portlandite and aluminate phases in inner and outer layer are distributed in the same proportion as the fractions of HD and LD C-S-H in cement paste. The effective diffusivity of this configuration is determined using the effective media theory for multi-coated spheres proposed by Milton [166]. This theory is based on self-consistent approximation. According to this theory, effective diffusion coefficient of the microstructure ($D_{e,n}$) consisting of n layer multi-coated sphere can be determined iteratively, wherein at each iteration the effective media is composed of single coated spheres with core consisting of effective media of previous iteration surrounded by the layer of the current iteration using following equation [166]

$$D_{e,n} = D_n + \left(1 - \frac{\phi_n}{\sum_{i=1}^{n} \phi_i}\right) \left[\frac{1}{D_{e,n-1} - D_n} + \frac{1}{3D_n} \frac{\phi_n}{\sum_{i=1}^{n} \phi_i}\right]^{-1} \qquad (5.6)$$

Where $D_{e,n}$ is the effective diffusivity determined for n^{th} layer [L^2,T^{-1}]; ϕ_i is the fraction of ith layer and $D_{e,n-1}$ is the effective diffusion coefficient of assembly of multi-coated spheres consisting of $n-1$ layers. The diffusion coefficient for inner and intermediate

layers in Bary and Béjaoui [165] model are then determined by Maxwell approximation and diffusion coefficient of external layer is determined using self-consistent scheme to better represent the effect of percolation. For intermediate and outer layer additionally they assume that D_{CSH}^{int}/D_0 and D_{CSH}^{out}/D_0 as zero to simplify the relationships. However, this assumption is not essential. The volume fractions of different phases needed are determined using Tennis and Jennings model [15]. Diffusivity of inner and outer C-S-H matrix were determined by fitting with the experimental data of Bejaoui and Bary [5] as 3.4×10^{-12} m^2/s and 8.3×10^{-13} m^2/s, respectively, for HTO.

Similar conceptualization has been made by Stora *et al.* [167] for cement paste morphology. However they did not divide the outer layer further in two parts as in case of Bary and Béjaoui [165]. Diffusivity of both layers were determined using Maxwell approximation. Moreover in order to obtain the effective diffusivity of LD and HD C-S-H they applied the *mixed coated sphere assemblage model* (MCSA) [168] which allows to capture sudden variations of effective diffusivity caused by percolation effects in a better way than self-consistent scheme. The MCSA model requires an additional fitting parameter known as the geometric parameter (f) which they determined as 0.805 and 0.546 for HD C-S-H and LD C-S-H respectively based on comparison with experimental data. This model has been further extended to simulate the leaching of cement paste [169]. Dridi [170] also utilized the effective media theory for assembly of multi-coated spheres to compute effective diffusivity of cement paste. He used similar morphological conceptualization as Stora *et al.* [167]. However, in case when LD C-S-H volume fractions are smaller than percolation threshold which is the case for low w/c, he represented cement paste as single coated spheres with LD C-S-H as inclusions in the layer of HD C-S-H. Similar to Stora *et al.* [167] the diffusivity of inner and outer layer is computed using generalized Maxwell approximation. Moreover in order to account for percolation behaviour of capillary pores he used self-consistent scheme for outer layer when capillary pores percolate. The percolation threshold for capillary pores was assumed to be 15%. He used the diffusivity of LD and HD C-S-H as 6.5×10^{12} m^2/s and 1.25×10^{12} m^2/s by fitting with experimental results of Bejaoui and Bary [5] rather than using MCSA model as in case of Stora *et al.* [167]. These values are in the similar range as the one fitted by Bary and Béjaoui [165].

Liu *et al.* [171] represented the morphology of cement paste in rather different way. They considered cement paste morphology in three levels . At level I they assumed the representation of two types of C-S-H, LD C-S-H and HD C-S-H. Both LD and HD C-S-H are composed of non-diffusive spherical solid phase as inclusions in the gel pore space. At level II the porous C-S-H gel is composed of spherical inclusion of HD C-S-H and capillary pores smaller than 1 μm in the matrix of LD C-S-H. Finally at level III the HCP is assumed to consist of spherical inclusion of unhydrated cement, portlandite, aluminates and capillary pores in the matrix of porous C-S-H gel. The diffusivity of LD and HD C-S-H at level I is determined using differential effective media scheme. The diffusivity

Table 5.6: Values of unknown parameter used for different relative diffusivity models of cement paste. The mathematical expression for this models can be found in appendix F.

Reference/ Model	Parameters used
Archies relationship	a : 0.0462, 0.1158, 0.5385 for electro migration, through-diffusion and electric resistivity respectively n: 1.3916, 2.0609, 2.3366 for electro migration, through-diffusion and electric resistivity respectively
Exponential form	a: 0.0006, 0.0003 and 0.0021 for electro migration, through-diffusion and electric resistivity respectively n: 9.7627, 11.507 and 8.2079 for electro migration, through-diffusion and electric resistivity respectively
Exponential form with respect to w/c	a: 0.002,0.00007 and 0.0002 for electro migration, through-diffusion and electric resistivity respectively n: 3.4779 , 8.2253 and 6.3193 for electro migration, through-diffusion and electric resistivity respectively
NIST model [159]	a_1: 1.7, a_2: 0.03, a_3: 0.0004 and ϕ_c: 0.2
Generalized self-consistent scheme [146]	D_s: $2 \times 10^{-5} D_0$, n: 2.7 and ϕ_c: 0.17
Bejaoui and Bary [5]	D_{LD-CSH} : $4.0179 \times 10^{-3} D_0$, D_{HD-CSH}: $4.4643 \times 10^{-4} D_0$
Bary and Béjaoui [165]	D_{LD-CSH} : $1.7 \times 10^{-3} D_0$, D_{HD-CSH} : $4.15 \times 10^{-4} D_0$
Stora *et al.* [167]	f_{gp}^{LD-CSH}: 0.675, f_{gp}^{HD-CSH}: 0.761
Dridi [170]	D_{LD-CSH}:$2.9018 \times 10^{-3} D_0$, D_{HD-CSH}: $5.35714 \times 10^{-4} D_0$
Liu *et al.* [171]	D_{gp}: $1.8634 \times 10^{-2} D_0$

at level II and level III are determined using Maxwell approximation and self-consistent scheme respectively. They determined the diffusivity of ions in gel pores through inverse analysis. For chloride ions they determined the value of diffusivity of ions in gel pores as 3×10^{-11} m^2/s. The volume fractions of different phases where determined using the hydration model proposed by Bernard *et al.* [172]. The porosity of LD C-S-H and HD C-S-H in their model were kept constant for different w/c with values as 0.37 and 0.24 respectively which is based on colloid model of C-S-H proposed by Jennings [23].

5.4 Comparison between effective diffusivity models

In this section comparisons are carried out for the models to obtain diffusivity as presented in previous section. The parameters needed for these relationships are taken as the one suggested in the respective references and are summarized in Table 5.6. For empirical relationships discussed in section 5.3 it is relevant to compare the quality of the relationship rather than their predictive capabilities. Hence for these relationships unknown parameters are first calibrated for experimental data collected in section 5.2 and then compared with the experimental data. The parameters of the calibrated model are summarized in Table 5.6. For models which require volume fractions of different phases the comparisons were

Table 5.7: Volume fractions (in %) of different phases of cement paste computed using Tennis and Jennings hydration model [15] for experiments used to compare models considering detailed morphological aspects of cement paste

references	w/c	Degree of hydration	clinkers	portlandite	aluminates	capillary porosity	HD C-S-H	LD C-S-H
Electro-migration								
Sun et al. [147]	0.23	0.573	22.3	10.83	17.19	4.5	35.75	8.36
	0.35	0.734	9.38	12.41	19.37	10.79	31.86	17.45
	0.53	0.861	2.66	10.92	17.42	20.01	10	40.84
Oh and Jang [146]	0.35	0.673	10.11	7.12	28.04	7.3	30.64	16.79
	0.45	0.788	4.91	6.77	25.01	12.28	20.67	30.37
	0.55	0.836	2.46	6.33	22.09	17.2	7.55	44.36
Through-diffusion								
Delagrave et al. [7]	0.45	0.879	4.93	15.79	14.67	13.6696	20.63	30.31
	0.25	0.55	21.21	14.52	14.84	4.4291	35.9451	9.05
Yamaguchi et al. [142]	0.45	0.908	4.87	10.6	23.17	13.2694	19.47	28.61
	0.6	0.926	1.79	9.21	19.63	20.7149	9.48	47.69
	0.75	0.953	0.83	8.05	16.85	27.3181	0	43.39
Ngala and Page [6]	0.4	0.84	6.99	11.33	21.93	10.44	26.09	23.02
	0.5	0.91	3.44	10.61	20.25	15.7	13.74	36.26
	0.6	0.946	1.79	9.69	18.03	20.5	0.97	49.02
	0.7	0.966	1.04	8.84	16.24	24.97	0	48.91
Phung [8]	0.425	0.85	5.83	13.18	19.48	12.71	22.9	25.91
Electrical resistivity								
Ma et al. [9]	0.3	0.522	24.3	9.05	15	16.95	22.6	12.16
	0.3	0.61	19.78	10.73	17.65	11.9	27.63	12.32
	0.3	0.65	17.71	11.5	18.83	9.64	30.08	12.23
	0.4	0.51	21.41	7.58	12.56	28.33	14.6	15.51
	0.4	0.631	16.06	9.57	15.7	21.9	18.45	18.31
	0.4	0.70	13.01	10.72	17.41	18.29	20.76	19.81
	0.4	0.72	12.13	11.05	17.89	17.25	21.44	20.23
	0.5	0.56	16.83	7.36	12.17	33.88	9.74	20.02
	0.5	0.67	12.57	8.95	14.62	28.38	11.02	24.46
	0.5	0.74	9.86	9.98	16.1	24.9	11.75	27.41
	0.5	0.79	7.93	10.71	17.12	22.43	12.23	29.58
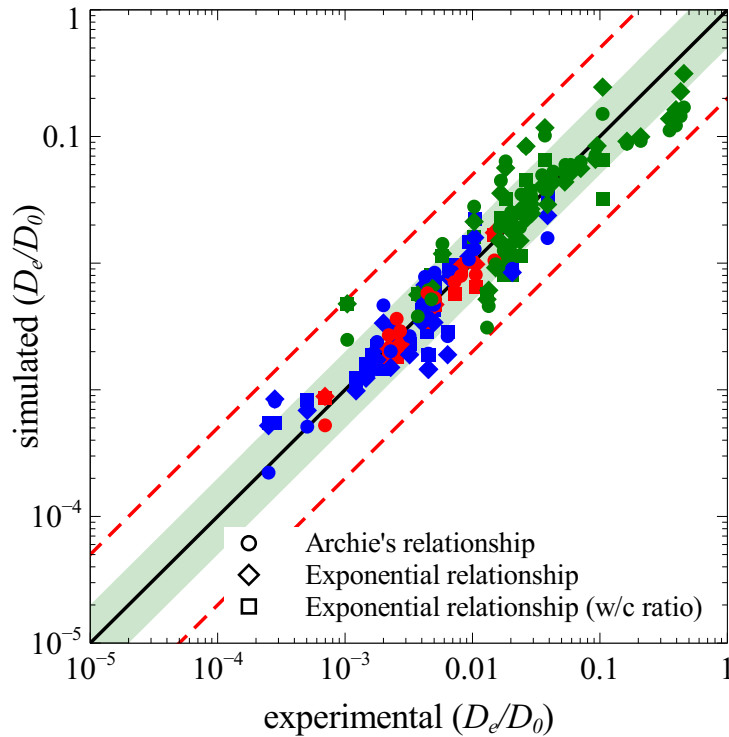
Figure 5.3: Comparison of relative diffusivity obtained from empirical relationships and experimental data. Marker colours represent different experimental techniques. Blue, red and green represents through-diffusion, electro migration, and electric resistivity respectively. Shaded green region shows factor of two bound and dashed line shows factor of five bounds.

carried out only for a selected set of experimental data as given in Table 5.7. Care has been taken that the experimental data selected does not include the ones which has been used to calibrate these relationships. The volume fractions of different phases were computed using Tennis and Jennings hydration model [15] and reported in Table 5.7. For Stora *et al.* [167] and Liu *et al.* [171] additionally porosity of LD C-S-H and HD C-S-H is needed. The porosity of LD C-S-H and HD C-S-H was taken as 0.37 and 0.24 respectively which is based on colloid model of C-S-H proposed by Jennings [23]. The parameters for Stora *et al.* [167] were recalibrated as these porosity values are different from the one used in their paper.

Fig. 5.3, Fig. 5.4, and Fig. 5.5 shows the comparison of the relative diffusivity obtained using different relationships for effective diffusivity and experimental data. Alike models are grouped together in each figure. For instance in Fig. 5.3 all the empirical relationships are compared with experimental data. In Fig. 5.4 models which account for morphological nature of cement paste in simplified way and express the relationship solely in terms of capillary porosity i.e. NIST model [137] and Oh and Jang model [146] based on generalized effective media theory are compared with experimental data. In Fig. 5.5 models which take into account detailed morphological aspects of cement paste are compared with the experimental data. Table 5.8 summarizes the percentage of data for which the relative diffusivity is within factor of two bounds. This serves as a good indicator to quantitatively
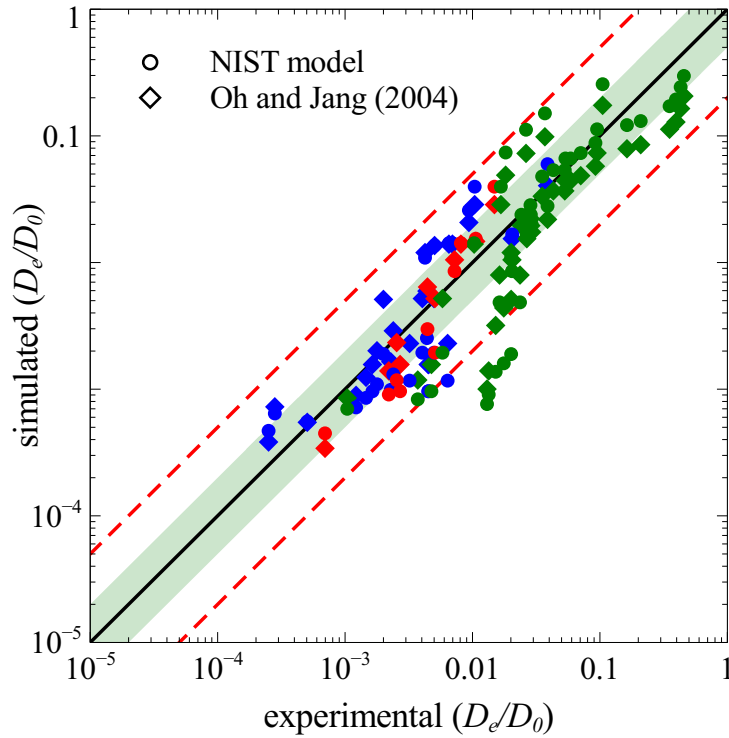
Figure 5.4: Comparison of relative diffusivity obtained from models which depend only on capillary porosity and experimental data. Blue, red and green represents through-diffusion, electro migration, and electric resistivity respectively. Shaded green region shows factor of two bound and dashed line shows factor of five bounds.
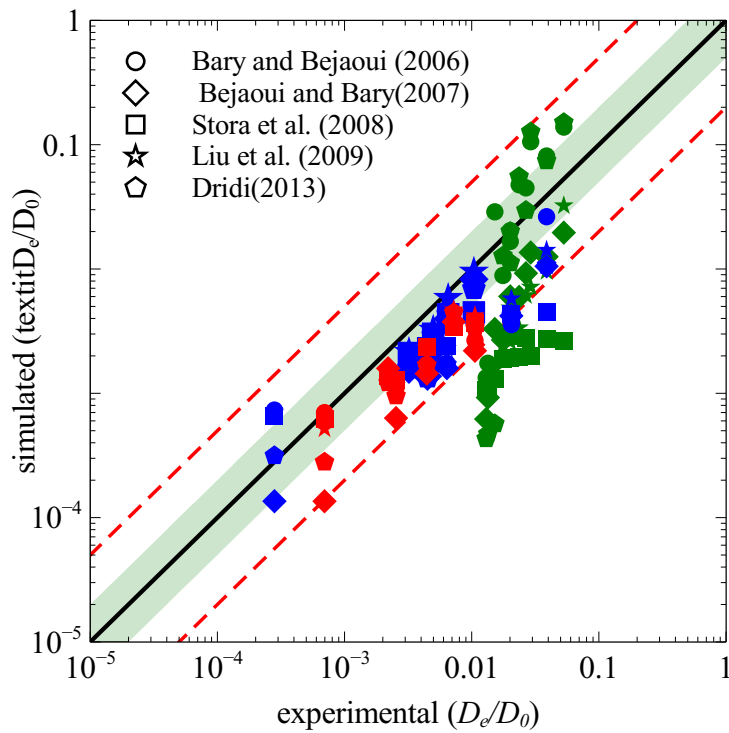
Figure 5.5: Comparison of relative diffusivity obtained from models which take into account morphology of cement paste in detail and experimental data. Blue, red and green represents through-diffusion, electric migration, and electric resistivity respectively. Shaded green region shows factor of two bound and dashed line shows factor of five bounds.

Table 5.8: Percentage of data lying between factor 2 bounds for different relationship of relative diffusivity of cement paste. The number of experimental data considered in each case is represented in brakets.

Reference/ Model	Electro-migration	through-diffusion	Electrical resistivity	Average
Archies relationship	100* (10)	72* (25)	65* (40)	72
Exponential form	100* (10)	76* (25)	65* (40)	73.3
Exponential form with respect to w/c	100* (10)	76* (25)	62.5* (16)	76.5
NIST model [137]	50(10)	44(25)	52.5(40)	49.3
Generalized self-consistent scheme [146]	90(10)	56(25)	55(40)	60
Bejaoui and Bary [5]	33.3(6)	20(10)	0(11)	14.8
Bary and Béjaoui [165]	50(6)	40(10)	45.5(11)	44.5
Stora *et al.* [167]	67.7(6)	40(10)	0(11)	29.9
Dridi [170]	33.3 (6)	40 (10)	45.5(11)	40.75
Liu *et al.* [171]	50(6)	50(10)	9.1(11)	33.3
*These models have been calibrated on the experimental data presented in this chapter and hence it shows good predictability compared to other models				

compare different models.

Fig. 5.3 reveals that all the empirical relationships show almost the same level of accuracy. This is confirmed by the values of percentage of data lying between factors of two bounds as given in Table 5.8. The percentage of data lying between factor of two bounds on average is above 70% for empirical models once they are calibrated. In case of simplified models, Oh and Jang model performs better than NIST model for electro migration as can be seen in Fig. 5.4. This can also be confirmed from Table 5.8. Very good correlation for Oh and Jang model for electro-migration tests is due to the fact that this model has been calibrated with electro-migration data. Oh and Jang model also performs slightly better than NIST model for other type of experiments. However, overall above 49% values predicted by both models (neglecting the performance of Oh and Jang model for electro-migration) lie between factor of two bounds. Hence it can be concluded that this model may need a recalibration to achieve better prediction. Moreover it can be seen in Fig. 5.4 that for electric resistivity data, both models under-predict at low relative diffusivity with some predictions lying even outside factor of five bounds. As mentioned in section 5.2 the relative diffusivity obtained from electric resistivity is higher than other methods at lower capillary porosity. Furthermore, these models have been calibrated with either data from through-diffusion or electro-migration. Thus poor predictions by these models can be attributed to the differences observed in the experimental values.

For the models taking into account the detailed morphological aspects, the Bary and Béjaoui [165] model shows the least agreement as shown in Table 5.8. For electro-migration prediction by models of Dridi [170], Stora *et al.* [167] and Liu *et al.* [171] 50% or more

data lie within factor of two bounds. For through diffusion all models except that of Bary and Béjaoui [165] have 40% or more data lying within factor of two bounds. For electric resistivity data only the models of Bary and Béjaoui [165] and Dridi [170] show good predictability with 45.5% data predicted lying between factor of two bounds. Fig. 5.5 shows that for low relative diffusivity all models perform badly with large set of predicted data lying beyond factor of five bounds. It must be noted that all these models have been calibrated on through diffusion or electro-migration. The calibration parameters in these models are associated with C-S-H diffusivity and at low capillary porosities (low relative diffusivities) the amount of C-S-H phase increases. Hence it can be speculated that differences between electric resistivity measurements and through-diffusion or electro-migration are associated with the diffusivity of C-S-H phase.

5.5 Obtaining effective diffusivity from microstructures

In this section modelling approaches to obtain diffusion coefficient from microstructures of cement paste and issues associated with it are discussed. Different approaches used to obtain diffusion coefficient from virtual microstructures generated from integrated kinetic models and 3D images such as tomography are presented in section 5.5.1 and section 5.5.2 respectively. The influence of resolution on obtained diffusion coefficient are discussed in 5.5.3 and studies carried out to determine representative element volume (REV) are presented in 5.5.4. Finally a discussion on the choice of C-S-H diffusion coefficient made by different researchers in order to obtain diffusion coefficient from the microstructures is given in section 5.5.5.

5.5.1 Diffusivity from virtual micro structures

Garboczi and Bentz [137] used the virtual microstructure of cement paste (obtained from earlier version of CEMHYD3D model) to obtain diffusivity of cement paste using random walk method. Based on their analysis they proposed an analytical relationship for diffusivity of cement paste as discussed in section 5.3. Christensen *et al.* [145] compared the diffusivity obtained with this model with the experimental values obtained from electric resistivity measurements. The simulated values showed a good agreement for the porosity above percolation threshold. However for very high porosity values the simulations and experiments show disagreement. Kamali-Bernard *et al.* [173] using finite element software *ABAQUS* computed diffusivity from virtual CEMHYD3D microstructures for experimental data of Delagrave *et al.* [7].

Different numerical approaches such as finite difference method [174], finite element method [175], random walk algorithim [176, 177] and lattice Boltzmann method [178] have

been used to obtain diffusivity from the micro structure obtained from HYMOSTRUC. Zhang *et al.* [175] and Liu *et al.* [177] showed that the diffusivity obtained from virtual HYMOSTRUC microstructure is around three times higher than that of experimental value and higher than that obtained for the CEMHYD3D microstructures.

5.5.2 Diffusivity from 3D images

Promentilla *et al.* [179] used images obtained from synchrotron based x-ray computed tomography (x-ray CT) with resolution of 0.5 μm to compute the relative diffusivity. They observed a sudden change in computed relative diffusivity at a porosity of around 20%. This observation suggests that at 20% capillary pores exhibits percolation transition from a disconnected phase to the connected phase. Karim and Krabbenhoft [180] used the computed tomography (CT) images available from NIST visible data set [181] to obtain diffusivity. The resolution of the image was 1 μm. They consider transport only through capillary pores. The capillary pore for the given resolution was less than one that can be estimated using Power's model [148]. Therefore in order to incorporate the influence of the unresolved porosity, they proposed to decrease the diffusivity of voxels linearly from D_0 up to the threshold gray value (42 in their case) which gives the same value of porosity as capillary pores. The voxels beyond this threshold values are considered to represent hydration products and clinkers and they are considered non-diffusive phases. With this treatment they found a good agreement with the NIST model [137]. It should be noted that the gray values in CT images are closely related material density. Therefore such thresholding may not directly correspond to unresolved capillary pores alone but mixture of unresolved pores and C-S-H phase. One of the reason for mismatch with the NIST model could also be due to the fact that they consider transport only through capillary pores. Zhang *et al.* [182] computed diffusivity of cement paste using image obtained from micro-tomography. The resolution of micro-tomography image was 0.5 μm. They considered transport through both C-S-H with relative diffusivity of C-S-H as 1/400 and capillary pores. The computed diffusivity were within the range of the experimental results. Kurumisawa *et al.* [183] constructed a three dimensional image from a 2D back scattered image using auto-correlation function to predict the diffusion properties of OPC and blended cement. They reported that the diffusivity of C-S-H in blended cement paste is two to five times smaller than that of OPC to achieve good correlation with experimental results. They attributed this observation to differences in C-S-H in blended cement and an electric charge effect of the pore surface.

5.5.3 Influence of resolution

Garboczi and Bentz [162] carried out study on influence of resolution on the computed diffusivity for CEMHYD3D model. They showed that the diffusivity increases with

increase in resolution. This is due to the fact that the capillary pores get better connected thus decreasing the percolation threshold for pores. They further reported that the influence of resolution is less prominent for lower porosity as the C-S-H phase governs the diffusion. They concluded that if the porosity of C-S-H phase is not resolved then the resolution of 1 μm can be considered as an appropriate resolution as it gives good prediction for percolation threshold for solid phases when compared with experiments [184, 185]. Ukrainczyk and Koenders [174] based on analysis of HYMOSTRUC generated microstructures with porosity of 6% concluded that the resolution does not influence the obtained diffusion coefficient which is indeed consistent with the results reported by Garboczi and Bentz [162].

5.5.4 Size of representative element volume (REV)

Hain *et al.* [186] carried out REV analysis using the cement paste microstructure obtained from CT images available at NIST visible data set [181]. To minimize the influence of boundary conditions they used a window boundary approach. Based on their analysis they obtained size of REV as 64 μm$\times$ 64 μm$\times$ 64 μm. Zhang *et al.* [187] used the microstructures generated from HYMOSTRUC to obtain REV for cement paste. Based on their analysis they suggest the size of REV to be around 100 μm$\times$ 100 μm$\times$ 100 μm. Ukrainczyk and Koenders [174] carried out detailed analysis of influence of particle size distribution of clinker phase, degree of hydration and porosity on size of REV using microstructure generated from HYMOSTRUC. They reported that the size of REV increases with the decrease in porosity and increase in degree of hydration and finer particle size distribution.

5.5.5 Diffusivity of C-S-H phase

Diffusivity of C-S-H phase is usually obtained by inverse modeling as it is difficult to measure it directly. Garboczi and Bentz [137] suggested the relative diffusivity of C-S-H paste as 0.0025 by comparing the diffusion cofficient obtained from CEMHYD3D microstructures with results of chloride diffusion experiments. Based on simulations using CEMHYD3D microstructures at w/c of 0.25, Kamali-Bernard *et al.* [173] fitted the relative diffusivity of C-S-H phase as 0.001 by comparing with the experimental data of Delagrave *et al.* [7]. Bentz *et al.* [188] suggested that the diffusivity of pozzolanic C-S-H should be five times lower for HTO diffusion and twenty five times lower for chloride ions relative to that of C-S-H in OPC. Ma *et al.* [9] proposed the value of relative diffusivity of C-S-H phase as 0.00775 based on electric conductivity measurements. Kurumisawa *et al.* [183] used Archie's relationship proposed originally by Bejaoui and Bary [5] to obtain diffusivity of chloride ions in low density C-S-H (D_{LD-CSH}) and high density C-S-H (D_{HD-CSH}).

This relationship is expressed as

$$D_{LD-CSH} = 1.34 \times 10^{-10} (\phi_p^{LD})^{2.09} \tag{5.7}$$

$$D_{HD-CSH} = 2.02 \times 10^{-11} (\phi_p^{HD})^{1.82}$$

where ϕ_p^{LD} and ϕ_p^{HD} is porosity of low density and high density C-S-H respectively.

5.6   Concluding remarks

In this chapter different experimental techniques and modelling approaches for opc cement based material under saturated condition have been reviewed. The relative diffusivity as reported by various authors have been collected and analysed for cement paste. For electric resistivity, through-diffusion and electro-migration all the data collected lie between factor of five bounds, factor of four and factor of two bounds from the best fit values (using exponential function). Further it is observed that at low to moderate w/c or capillary porosity the relative diffusivity for cement paste obtained by electric resistivity is always higher than other methods.

Varieties of models have been proposed to predict diffusivity of cement paste. However, none of these models are devoid of fitting parameters. Even the most advanced models needs parameters associated with C-S-H diffusivity. All the models proposed has been claimed to have good fitting with experimental data provided this fitting parameters are carefully determined. The empirical models were re-calibrated using the collected experimental data. All empirical models once calibrated show similar predictive behaviour. In terms of predictability it can be said that both models accounting for cement paste morphology in simplified way and advanced models show similar behaviour and may need re-calibration to improve the predictability. It was also observed that all these models were not able to well predict the electrical resistivity data and at low relative diffusivity (capillary porosity) the predicted data even lie beyond the factor of 5 bounds. As advanced models only have fitting parameters related to C-S-H diffusivity, it can be speculated that the differences observed between electric resistivity and other techniques are associated with C-S-H diffusivity.

At present it is known that different ions might have different diffusivity [153, 189] through cement paste. However, there is lack of experimental data on constrictivity factors in cement based materials. In absence of an appropriate description of constrictivity, sometimes the relationship for constrictivity factor defined for soils has been used to cementitious materials [190].

Obtaining diffusivity from virtual micro structure or 3D images can help to improve our understanding on the diffusion process of cement paste as the effect of tortuosity can be directly accounted for. For virtual microstructures the REV of 100 μm seems

to be appropriate for obtaining diffusivity. However what should be the appropriate resolution for the microstructure still remains the open question. It should be noted that this resolution has nothing to do with accuracy but with the size of pores that has to be resolved at the micro-scale. For virtual microstructures at lower porosity the resolution does not seem to play a crucial role, however, for higher porosity large differences can be observed with change in resolution. The key input parameter for obtaining diffusivity from the microstructure is the diffusivity of C-S-H phase. The relative diffusivity of C-S-H reported in literature ranges from 0.00775 to 0.001. The diffusivity of C-S-H is usually obtained by inverse analysis and does not have a rigorous theoretical basis as a result of which the estimation of diffusivity from the microstructure is not entirely devoid of fitting parameters.

Determination of effective diffusivity from integrated kinetic
models: role of morphology

6.1 Introduction

From the conclusions of chapter 5 it is clear that for obtaining diffusivity from virtual microstructures or even the most advanced effective diffusivity models, C-S-H diffusivity is the fitting parameter. Furthermore, it is concluded in chapter 5 that the differences in the measured relative diffusion coefficient between electric resistivity and other techniques might be associated with the diffusion coefficient of C-S-H. As a result a better description of diffusivity of C-S-H is essential to have reliable predictions.

In this chapter a numerical approach for solute transport presented in Chapter 3 is utilized to determine effective diffusivity from the microstructure of the cement paste generated using two different integrated kinetic models viz., HYMOSTRUC and CEMHYD3D which are vector based and voxel based approaches respectively. Both these models even for the same pore fractions, gives different connectivity and hence the role of connectivity of capillary pores can be explored by using these two different models. A two-scale approach based on effective media theory has been developed to obtain the diffusion coefficient of C-S-H phase. This approach allows to separate the contribution of low density and high density C-S-H pores. The numerical approach presented in this chapter thus allows to study the contribution of different types of pores in the cement paste on transport properties. Finally a one to one comparison has been carried out between selected experimental data (obtained from through diffusion and electric resistivity techniques) and numerical approach to validate the proposed approach. This validation is also of importance for the use of virtual microstructures generated using HYMOSTRUC and CEMHYD3D as

input to simulate degradation processes such as calcium leaching. Section 6.2 presents description of the numerical approach used to obtain the effective diffusion coefficient from the microstructure. The two scale model for diffusion coefficient of C-S-H is presented in section 6.3. The results and discussions are presented in section 6.5.

6.2 Computational approach to determine diffusion coefficient

The schematic description of the computational approach used to determine the effective diffusivity of a cement paste is presented in Fig. 6.1. The first step is to obtain the microstructure of cement paste from integrated kinetic models. The integrated kinetic models require basic inputs such as Bogue's composition, water-cement ratio (w/c) and specific surface area (Blaine's fineness). The microstructures can be then generated from these models for a required degree of hydration.

The effective diffusivity are obtained by solving the mass transport through the microstructure of the cement paste. All the hydration products except C-S-H are considered as non-diffusive. The mass transport equation in the microstructure is solved using the *multilevel TRT LB scheme with D3Q7 lattice and linear EDF* as presented in chapter 3. The anti-symmetric relaxation parameter (τ_-) was taken as one and the magic parameter (M) was taken as 1/4 for all simulations. The diffusivity of the capillary pores (D_0) is assigned as 1 as only the relative diffusivity was of interest in this study. The diffusion coefficient for C-S-H is determined using the two scale approach presented in next section. The Dirichlet boundary conditions are prescribed along boundary normal to the direction for which diffusivity is to be computed. The value of concentration was taken as 1 M at the inlet and 0 M at the outlet to achieve the constant gradient along the length. Other boundaries are assigned periodic condition. It should be noted that the Dirichlet boundary condition satisfies Hill's criteria necessary for the reliable volume averaging [191, 192]. The effective diffusion coefficient at steady state is then obtained using a volume averaging approach as follows

$$D_e = -\frac{\langle \hat{n} \cdot \vec{J} \rangle}{\langle \hat{n} \cdot \vec{\nabla} C \rangle} \tag{6.1}$$

Where $\hat{n}$ is the normal vector pointing to the direction in which the diffusion coefficient has to be determined. The volume average quantity $\langle \bullet \rangle$ is defined as

$$\langle \bullet \rangle = \frac{1}{|\Omega|} \int_\Omega \bullet \ \Omega$$

As LB scheme is an explicit time marching method simulation is stopped when the relative
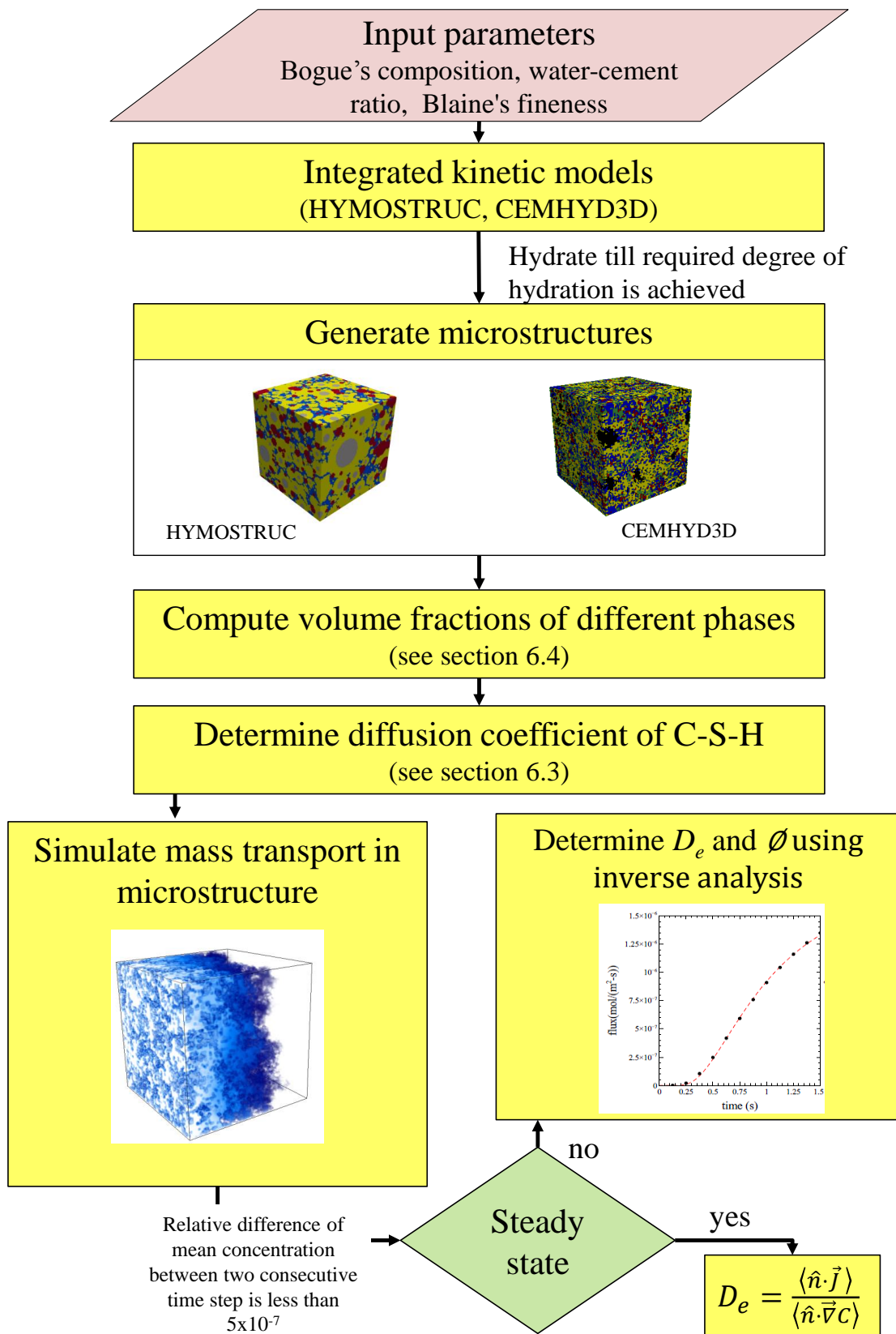
Figure 6.1: Numerical scheme to determine diffusion coefficient generated from integrated kinetics model
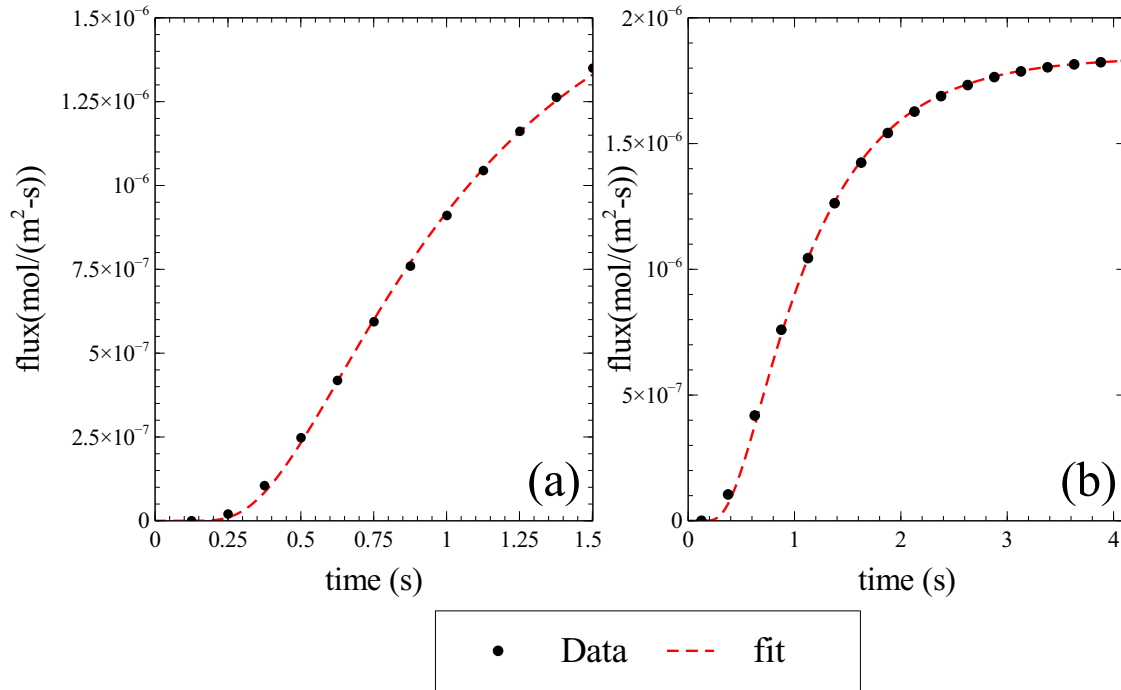
Figure 6.2: Fit for transient outlet flux curve in x-direction using (a) Only the initial portion (case a) (b) complete curve (case b)

change in average concentration in domain is less than 5×10^{-7}. In some cases the steady state was not reached (especially for low w/c) at the end of the simulation. In such cases, an equivalent one dimensional mass transport problem is solved to optimize the unknown parameters of equivalent homogeneous media i.e. porosity (ϕ) and effective diffusion coefficient(D_e) by fitting the transient outlet flux curve. All the fitting carried out in this study for transient outlet flux curve had coefficient of determination around 0.99, indicating that a good fit has been achieved. The optimization is carried out using the bounded least square minimization method [193, 194] implemented in *python*. The algorithm for bounded least square minimization which extends the non-bounded implementation available in *SciPy* [194] (a *Python* library) is presented in appendix H.

To validate this approach a microstructure of size 100 μm $\times$ 100 μm $\times$ 100 μm generated for cement composition of Phung [8] using HYMOSTRUC has been used as the steady state was achieved in this simulation. Fits were carried out for two cases (a) when only the initial portion of the transient outlet flux curve is used, which represents the case when steady state is not reached in a simulation (b) complete transient outlet flux curve is used. Fig. 6.2 shows the fit achieved in both cases for transient outlet flux curve in x direction and results for the fits are summarized in Tables 6.1 and 6.2. Note that the porosity fitted usually refers to the porosity that contributes to the transport (connected porosity) in the microstructure. For this microstructure the capillary porosity was found to be fully percolated. Moreover the diffusivity in capillary pores is much higher than gel

Table 6.1: Comparison between approach to obtain diffusion coefficient using transient outlet flux curve and Eq. (6.1) in case only the initial portion of curve is used (case a)

Axis	Actual capillary porosity	Fitted capillary porosity	D_e/D_0 using Eq. (6.1)	Fitted D_e/D_0	Relative error for D_e/D_0 in %	Relative error for capillary porosity in %
X	0.153	0.118	0.0229	0.0216	5.57	22.61
Y	0.153	0.130	0.0243	0.0242	0.53	14.82
Z	0.153	0.137	0.0244	0.0233	4.70	10.19
mean	0.153	0.129	0.0239	0.0231	3.56	15.87

Table 6.2: Comparison between approach to obtain diffusion coefficient using transient outlet flux curve and Eq. (6.1) in case the full curve is used (case b)

Axis	Actual capillary porosity	Fitted capillary porosity	D_e/D_0 using Eq. (6.1)	Fitted D_e/D_0	Relative error for D_e/D_0 in %	Relative error for capillary porosity in %
X	0.153	0.135	0.0229	0.0231	0.689	11.764
Y	0.153	0.135	0.0243	0.0246	1.23	11.764
Z	0.153	0.154	0.0244	0.0246	0.82	0.653
mean	0.153	0.141	0.0239	0.0241	0.913	8.06

pores. Thus capillary pores are the major contributor for the transport in this case. Hence the fitted porosity can be thought of as a capillary porosity. The mean relative difference between the capillary porosity and porosity fitted for case a and case b were found to be 15.87% and 8.06% respectively. The mean relative difference between the diffusion coefficient computed using volume averaging approach (i.e. Eq. (6.1)) and for case a and case b were found to be 3.56% and 0.913% respectively. Thus it can be concluded that the relative differences between two approaches for computing diffusivity is negligible with the value of maximum mean relative difference observed for these cases as 5.57% which corresponds to differences in the third digit after decimal (see Table 6.1).

6.3 Model to obtain diffusion of C-S-H phase

In this section an approach based on effective media theory is presented to determine the diffusivity of C-S-H phase. The basic idea behind effective media theories is briefly described in appendix G. Effective media theories provides an approximate effective diffusivity accounting for tortuosity for a morphology consisting of well-defined inclusions (such as spheres, cylinders, ellipsoids) distributed randomly throughout a matrix material. In order to obtain the effective diffusivity, the morphology of the C-S-H is considered over
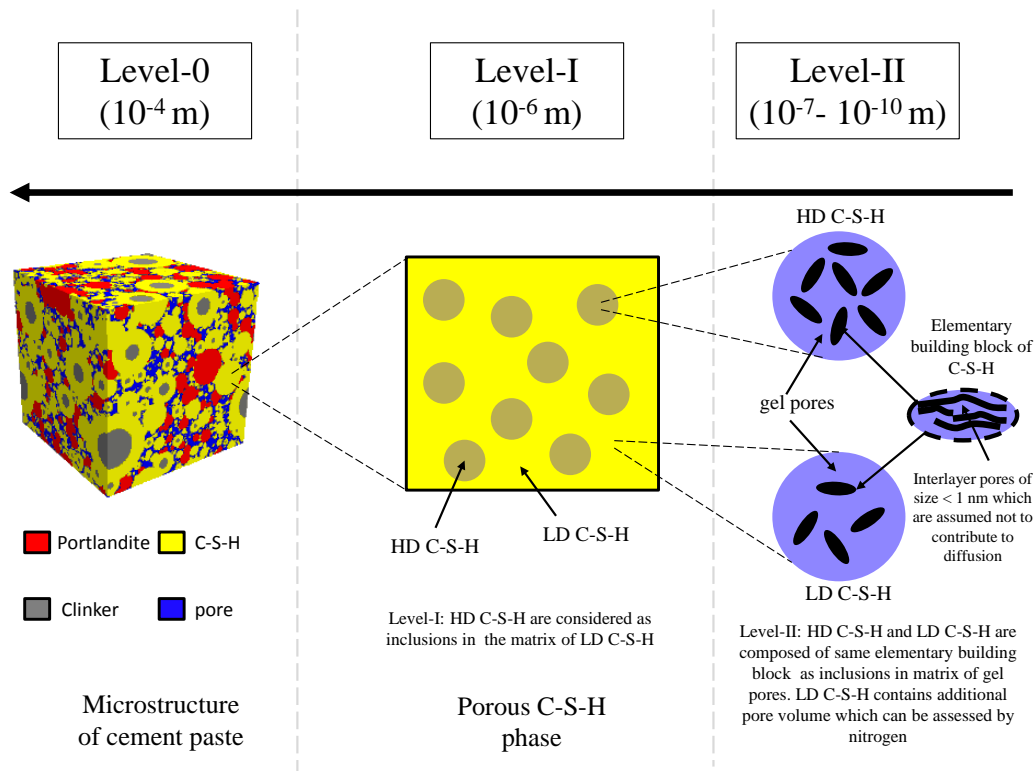
Figure 6.3: Morphological representation of porous C-S-H phase

two scales as shown in Fig. 6.3 and homogenization is carried out at each scale.

At the lowest scale (level-II) two distinct morphologies of C-S-H are considered viz., high density C-S-H (HD C-S-H) and low density C-S-H (LD C-S-H) as suggested in [15, 195]. Observations from nano-indentation measurements further suggest that the properties of LD and HD C-S-H are independent of cement fineness and w/c, thus being intrinsic for cement paste [196, 197]. Both HD and LD C-S-H are made of the same elementary building blocks but they differ in their packing [23]. These elementary building blocks contains inter-layer porosity (consisting of pores < 1 nm) of about 18% [198] as illustrated in Fig. 6.3). The water in this pores is chemically bounded to the C-S-H platelets. Hence, it is assumed that these pores *do not contribute to the diffusion process*. LD C-S-H has an additional porosity compared to HD C-S-H which is accessible by nitrogen and measurable during BET analysis [15, 195].

The elementary building block of C-S-H has been conceptualized by varieties of shapes. The simplest representation of the elementary building block is spheres with around 5 nm diameter which has been used in a colloidal model of C-S-H proposed by Jennings [23]. This model has been further modified based on the interpretation of water sorption isotherms to better describe the water present in pore space of C-S-H [199]. In the refined model the elementary building block of C-S-H has been considered as brick-shaped elements with around 4.5 nm thickness. Similarly, Garrault *et al.* [200] based on scanning electron microscopy (SEM) suggested that the C-S-H is made of elementary brick-shaped particles

of size 60 nm $\times$ 30 nm $\times$ 5 nm. They observed that the agglomeration of this particles takes place perpendicularly and parallel to the surface of the alite grains. Sanahuja *et al.* [201] based on these observation used the randomly distributed oblate spheres with aspect ratio of 0.12 ($\approx 5/\sqrt{30 \times 60}$) to represent C-S-H while proposing the multi-scale approach to obtain elasticity of hardening cement paste. On the other hand based on small angle neutron scattering, Chiang *et al.* [202] hypothesised that C-S-H is made of disk-shaped particles with a radius of 9.5nm and a thickness of 0.113 nm. Jennings *et al.* [203] provided a morphological classification of C-S-H formed during alite hydration based on images from the transmission electron microscope. They observed that C-S-H can be formed of varieties of basic bulding blocks such as 0.25 μm long cigar shaped tubes, tapered needles 0.75 - 1 μm long with aspect ratio of $\approx$ 10, crumpled foils based on the reactions occurring at different stages of hydration. Thus there is no general consensus on the shape of the elementary building block of C-S-H. *Therefore in this study the morphology of the elementary building block is considered brick shaped which is supported by the recent colloid model of Jennings [199] and SEM observations of Garrault* et al. *[200].* These bricks are represented through oblate spheres with *aspect ratio of 0.12.* Furthermore a parametric study on the influence of the shape of the elementary building block on the diffusivity of cement paste has been carried out in section 6.5 to better understand the role of this shape on mass transport.

At the scale of the smallest volume resolved in microstructure model i.e. level-I (1 μm^3), there are two approaches to represent different types of C-S-H. First approach as proposed by Smilauer and Bittnar [204] to explicitly represent LD C-S-H and HD C-S-H in the microstructure based on confinement conditions. In their approach during the beginning of hydration LD C-S-H is assigned to C-S-H volumes. During the progression of hydration, when the neighbourhood of an LD C-S-H volume (i.e., 26 volumes around a central volume) gets filled with solid phases, LD C-S-H volume is transformed to HD C-S-H volume. The volume fractions of LD and HD C-S-H obtained by this approach varied substantially with the model proposed by Tennis and Jennings [15]. The other approach, which is used in this study, considers C-S-H as a mixture of LD and HD C-S-H. As HD C-S-H is formed during later stage of hydration, HD C-S-H are assumed to be spherical inclusions in LD C-S-H as shown in Fig. 6.3. The volume fraction of LD and HD C-S-H are then determined using the model of Tennis and Jennings [15]. Details on computation of volume fractions are presented in section 6.4.

Out of the two effective medium approximations which allow to consider for the higher volume fractions (viz., self-consistent scheme and differential effective media approximation) the self-consistent scheme allows accounting for the effect of percolation of one phase in another. However when diffusivity of different phases vary substantially, the self-consistent approximation fails [163] and spurious percolation thresholds are imposed. On the other hand differential effective media ensures that the initial matrix always remains connected.

Furthermore, it has also been shown experimentally that differential effective media theory can provide reasonable estimates for differently shaped inclusions at higher volume fractions [205]. Hence in this study differential effective media theory was used to estimate effective diffusion coefficient at each scale. The estimation of the effective diffusion coefficient at each scale is described in detail below.

Level-II

At level-II the HD and LD C-S-H consist of non-diffusive spheroid inclusions in the matrix of gel pores. For this morphology the effective diffusion coefficient of LD C-S-H and HD C-S-H using differential effective media theory is given as [206]

$$D_{HD-CSH} = D_{gp}(\phi_p^{HD})^{1/(Y-X-Z)}, \qquad D_{LD-CSH} = D_{gp}(\phi_p^{LD})^{1/(Y-X-Z)}$$
$$X = 3\frac{R-R^2}{1+3R}, \quad Y = 3\frac{9R^2-2R+1}{(1+3R)^2}, \quad Z = 3\frac{4-24R+36R^2+3R^3-9R^4}{(5-3R)(1+3R)^2} \tag{6.2}$$

ϕ_p^{HD} and ϕ_p^{LD} are the fraction of gel pores in LD C-S-H and HD C-S-H repsectively. D_{gp}, D_{HD-CSH}, D_{LD-CSH} are the diffusion coefficient [L^{2}T^{-1}] of gel pores, HD C-S-H and LD C-S-H respectively. D_{gp} in this study is taken as *one order lower* than the one in capillary pores to account for the constrictivity effect in the small gel pores [165, 167]. R is the depolarization factor and can be computed as

$$R = \frac{1-\epsilon^2}{2\epsilon}\left(\ln\left(\frac{1+\epsilon}{1-\epsilon}\right) - 2\epsilon\right) \qquad \text{(prolate spheroids)}$$
$$R = \frac{1+\epsilon^2}{\epsilon^3}\left(\epsilon - \tan^{-1}\epsilon\right) \qquad \text{(oblate spheroids)} \tag{6.3}$$
$$\epsilon = \sqrt{|1-(a/c)^2|}$$

ϵ is the eccentricity, a is the equatorial radius of the spheroid [L], and c is the distance from centre to pole along the symmetry axis [L]. c is less than a for oblate spheroids and c is larger than a for prolate spheroids. For spheres c is equal to a. The ratio of c to a is often known as the aspect ratio. Oblate spheroids give good representation for platelet like inclusions whereas prolate spheroids can be used for fibrous inclusions. For asymptotic limits of aspect ratio equation 6.2 reduces to

$$D_{HD-CSH} = D_{gp}(\phi_p^{HD})^{5/3}, \qquad D_{LD-CSH} = D_{gp}(\phi_p^{LD})^{5/3} \quad \text{(fibres)} \tag{6.4}$$
$$D_{HD-CSH} = D_{gp}(\phi_p^{HD})^{16/9}, \qquad D_{LD-CSH} = D_{gp}(\phi_p^{LD})^{16/9} \quad \text{(disks)}$$

Figure 6.4 shows the pore diffusion coefficient ($D_p = \frac{D_e}{\phi D_{gp}}$) as predicted by differential scheme for different shapes of inclusions. Figure 6.4 reveals that the shape can influence on the diffusion coefficient, with the spherical shape giving the highest value of pore diffusion
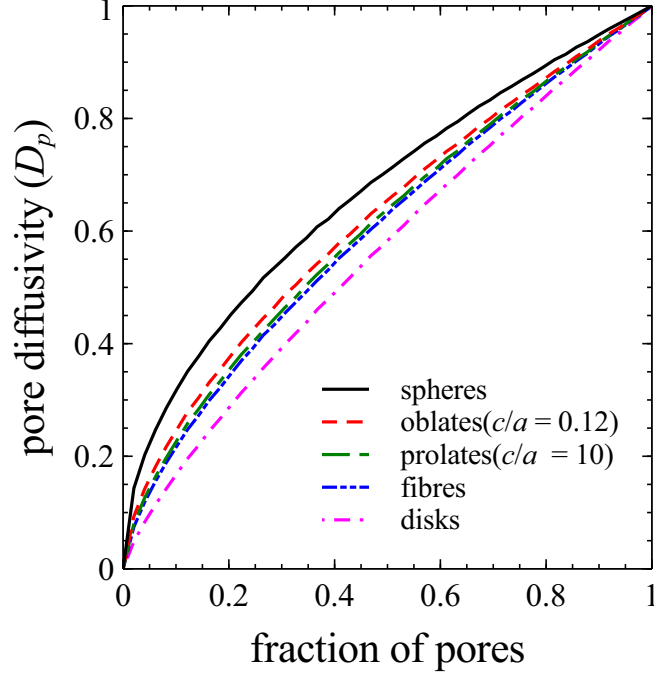
Figure 6.4: Pore diffusion coefficient predicted for different shapes by differential scheme

coefficient and disk shape giving the lowest value of the pore diffusion coefficient.

Level-I

At level-I HD C-S-H are considered as spherical inclusions in LD C-S-H matrix. The effective diffusion coefficient using differential scheme for this morphology is given by [163, 206]

$$\left(\frac{D_{HD-CSH} - D_{CSH}}{D_{HD-CSH} - D_{LD-CSH}}\right) \left(\frac{D_{LD-CSH}}{D_{CSH}}\right)^{1/3} = 1 - \phi_{HD}^{CSH} \qquad (6.5)$$

where D_{CSH} is the effective diffusion coefficient of C-S-H [L^{2}T^{-1}]. ϕ_{HD}^{CSH} is the fraction for HD C-S-H in the C-S-H volume.

As an illustration, the pore fraction in HD C-S-H (ϕ_p^{HD}) and LD C-S-H (ϕ_p^{LD}) are taken as 0.24 and as 0.37, respectively [198]. When only nitrogen accessible pores contribute to the diffusion process ϕ_p^{HD} becomes zero and ϕ_p^{LD} is 0.17 [15]. Diffusion coefficients of C-S-H (D_{CSH}) relative to the diffusion coefficient in capillary pores (D_0) computed using Eq. (6.5) for different fractions of HD C-S-H are shown in Fig. 6.5. Fig. 6.5(a) shows the result for the case in which only nitrogen accessible pores contribute in diffusion which is assumed to be the case for diffusion of ions and dissolved gases. Garboczi and Bentz [137] proposed the value of 0.0025 as relative diffusivity of C-S-H to be used for CEMHYD3D microstructures. This value is based on the comparison with the experimental data of Cl^- for w/c of 0.4 and greater as reported in references [153, 207]. On the other hand Kamali-Bernard *et al.* [173] obtained the optimal value of relative diffusivity of C-S-H phase to be used for the CEMHYD3D microstructure as 0.001. This value was obtained
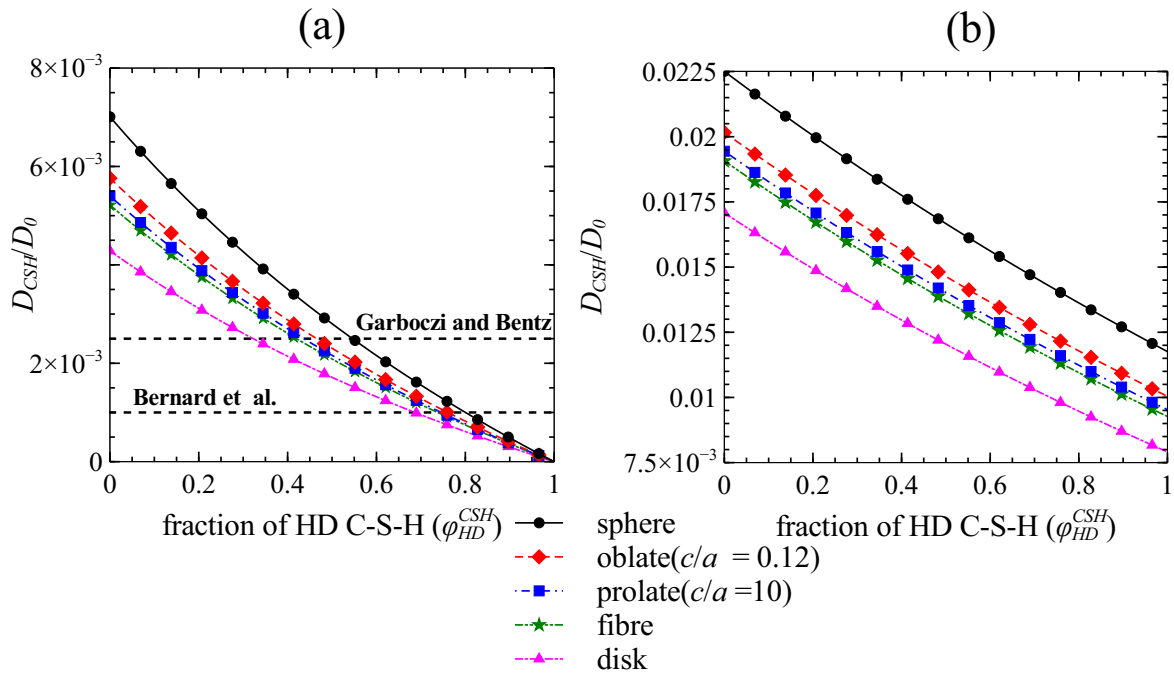
Figure 6.5: Diffusion coefficient for C-S-H volume as predicted by proposed model (a) Only nitrogen accessible pore contributes to diffusion coefficient (b) all pores contribute to diffusion coefficient

by comparison with the experimental result for cement paste with w/c 0.25 (reported in reference [7]. Differences between these values can be explained using the proposed model. At low w/c ϕ_{HD}^{CSH} is higher, resulting in lower diffusion coefficient of C-S-H phase.

Fig. 6.5(b) shows the relative diffusion coefficients as predicted by the proposed model in case when all the pores contribute in the diffusion process. It is interesting to note that the variability of diffusion coefficient for C-S-H phase as predicted by the proposed model is less (only upto 2 times) with respect to ϕ_{HD}^{CSH} when all porosity contributes in diffusion. Recently Ma *et al.* [9] proposed value of C-S-H diffusivity as 0.0075 based on inverse fitting of electric resistivity measurements with the diffusion model proposed by Oh and Jang [146]. Note that this value is for the fraction of C-S-H in cement paste and not for single C-S-H volume in a microstructure (for which this value would be higher). This high values for relative diffusivity of C-S-H phase can be explained taking into account the contribution of all pores. Fig. 6.5 also shows that the shape of elementary building block C-S-H influences the effective diffusivity estimated for C-S-H.

Summary of assumptions

The main assumptions used to derive the model for diffusion coefficient of C-S-H phase are summarized below

- The morphological picture of C-S-H as presented in figure 6.3 is valid

- The diffusion coefficients at each level can be homogenized using the differential

effective media theory.

- The elementary building block for C-S-H is considered to be an oblate sphere with an aspect ratio of 0.12 for all simulations unless specified.

- The diffusion coefficient in the pore space of C-S-H is taken as an order of magnitude lower than that in capillary pores to account for thewe constrictivity effects.

- Diffusion of tracers and dissolved gases only occurs through the nitrogen accessible pores whereas for electric resistivity all the gel pores contribute. This assumption is validated in section 6.5.

6.4 Computation of volume fractions of different phases

The approach to compute volume fractions of different phases used as input for the diffusion model of C-S-H is presented in this section. For virtual microstructure, fraction of C-S-H (ϕ_{CSH}) and capillary pores (ϕ_{CP}) in microstructure can be computed. Using Power's model [148] to compute fraction of total pores in microstructure, fraction of gel pores can be computed as

$$\phi_{gel} = \frac{\text{w/c} - 0.17\alpha}{\text{w/c} + 0.32} - \phi_{cp} \tag{6.6}$$

ϕ_{gel} denotes gel porosity. The fraction of gel pores in the C-S-H volume (ϕ_p^{CSH}) is given as $\frac{\phi_{gel}}{\phi_{CSH}}$. The fraction of solid phase in C-S-H (ϕ_s^{CSH}) is then $1 - \phi_p^{CSH}$. Tennis and Jennings [15] provided an empirical formula for the ratio of mass of LD C-S-H to the mass of total C-S-H phase (M_r) as

$$M_r = 3.017\alpha\text{w/c} - 1.347\alpha + 0.538 \tag{6.7}$$

α is the degree of hydration and M_r is equivalent to the volume ratio of solid phase in LD C-S-H ($\phi_{s,LD}^{CSH}$) to solid in total C-S-H volume ($\frac{\phi_{s,LD}^{CSH}}{\phi_s^{CSH}}$) as the density of solid phase is same for both types of C-S-H. The fraction of solid in HD C-S-H ($\phi_{s,HD}^{CSH}$) is then $\phi_s^{CSH} - \phi_{s,LD}^{CSH}$. As discussed in previous section, pores in C-S-H volume are divided into nitrogen accessible and inaccessible pores. Both LD and HD C-S-H contain the same volume of nitrogen inaccessible pores, however LD C-S-H has additional nitrogen accessible pores which result in lower bulk density of LD C-S-H [15].

$$\begin{aligned}
\phi_p^{CSH} &= \phi_{p,HD}^{CSH} + \phi_{p,LD}^{CSH} \\
&= \phi_{p,HD}^{CSH} + (\phi_{p,HD}^{CSH} + \phi_{p,nitro}^{CSH}) \\
&= 2\phi_{p,HD}^{CSH} + \phi_{p,nitro}^{CSH}
\end{aligned} \tag{6.8}$$

$\phi_{p,HD}^{CSH}$, $\phi_{p,LD}^{CSH}$, $\phi_{p,nitro}^{CSH}$ denotes fraction of HD pores, LD pores and nitrogen accessible pores in C-S-H volume. The fraction of nitrogen accessible pores in C-S-H is obtained as [15]

$$
\begin{aligned}
\phi_{p,nitro}^{CSH} &= \left(1 - \frac{\rho_{LD}}{\rho_{HD}}\right)\phi_{LD}^{CSH} \\
&= \left(1 - \frac{\rho_{LD}}{\rho_{HD}}\right)\left(\phi_{s,LD}^{CSH} + \phi_{p,LD}^{CSH}\right) \qquad (6.9)\\
&= \left(1 - \frac{\rho_{LD}}{\rho_{HD}}\right)\left(\phi_{s,LD}^{CSH} + \phi_{p}^{CSH} - \phi_{p,HD}^{CSH}\right)
\end{aligned}
$$

ρ_{LD} and ρ_{HD} are the dried densities of LD and HD C-S-H respectively [ML^{-3}] and ϕ_{LD}^{CSH} is the fraction of LD C-S-H in C-S-H volume. The values of ρ_{LD} and ρ_{HD} are 1.44 g/cm^3 and 1.75 g/cm^3 respectively[15]. Using Eq. (6.8) and Eq. (6.9) the fraction of $\phi_{p,HD}^{CSH}$ can be obtained as

$$
\phi_{p,HD}^{CSH} = \frac{\frac{\rho_{LD}}{\rho_{HD}}\phi_{p}^{CSH} - \left(1 - \frac{\rho_{LD}}{\rho_{HD}}\right)\phi_{s,LD}^{CSH}}{1 + \frac{\rho_{LD}}{\rho_{HD}}} \qquad (6.10)
$$

Finally ϕ_{LD}^{CSH} can be determined as $\phi_{s,LD}^{CSH} + \phi_{p,HD}^{CSH} + \phi_{p,nitro}^{CSH}$ and ϕ_{HD}^{CSH} can be determined as $\phi_{s,HD}^{CSH} + \phi_{p,HD}^{CSH}$. The fraction of pore space in LD C-S-H (ϕ_{p}^{LD}) and HD C-S-H (ϕ_{p}^{HD}) can be obtained as $\frac{\phi_{p,HD}^{CSH} + \phi_{p,nitro}^{CSH}}{\phi_{LD}^{CSH}}$ and $\frac{\phi_{p,HD}^{CSH}}{\phi_{HD}^{CSH}}$ respectively.

6.5 Results and discussions

The size of the microstructure for all simulations was taken as 100 μm $\times$ 100 μm $\times$ 100 μm which is a reasonable size for the REV (as discussed in chapter 5). In order to confirm that this size is representative, a set of simulations were carried out to test the influence of statistical variability of the virtual microstructure generated using CEMHYD3D and HYMOSTRUC on the obtained diffusion coefficients. Three microstructures were generated for each integrated kinetic model using different random seed for the cement composition of Phung [8]. Table 6.3 and table 6.4 summarize the results for HYMOSTRUC and CEMHYD3D respectively. The standard deviation for each simulation was found to be very small. Therefore, it can be considered that the size of REV is appropriate for the simulations. Furthermore the standard deviation for relative diffusion coefficient along different axis is very less which in term confirms that the microstructures generated are isotropic. Therefore for all the simulation presented in this study the relative diffusivity of microstructure was taken as an average over all the three directions.

Simulations were carried out for the selected set of data representing through diffusion with different tracers such as dissolved helium (refs. [8]), dissolved oxygen (refs.[6]) and HTO (refs. [5, 7]) and electric resistivity (refs. [9]) experimental techniques. These results have been summarized in Table 5.3 and 5.4. Fig. 6.6 shows the comparison between the relative diffusion coefficients obtained from the microstructures generated from integrated

Table 6.3: Influence of statistical variability: relative diffusivity obtained from HYMOSTRUC for the three simulations with different random seed

simulation number	X	Y	Z	mean	standard deviation
1	0.0229	0.0243	0.0244	0.0239	8.39e-4
2	0.0223	0.0226	0.0217	0.0222	4.58E-04
3	0.0244	0.025	0.0228	0.0241	1.14E-03
mean standard deviation	0.0232 1.08E-03	0.0240 1.23E-03	0.0230 1.36E-03	0.0234 1.02E-03	- -

Table 6.4: Influence of statistical variability: relative diffusivity obtained from CEMHYD3D for the three simulations with different random seeds

simulation number	X	Y	Z	mean	standard deviation
1	1.43E-03	1.41E-03	1.48E-03	1.44E-03	3.61E-05
2	1.44E-03	1.41E-03	1.40E-03	1.42E-03	2.08E-05
3	1.39E-03	1.40E-03	1.36E-03	1.38E-03	2.08E-05
mean standard deviation	1.42E-03 2.65E-05	1.41E-03 5.77E-06	1.41E-03 6.11E-05	1.41E-03 2.85E-05	- -
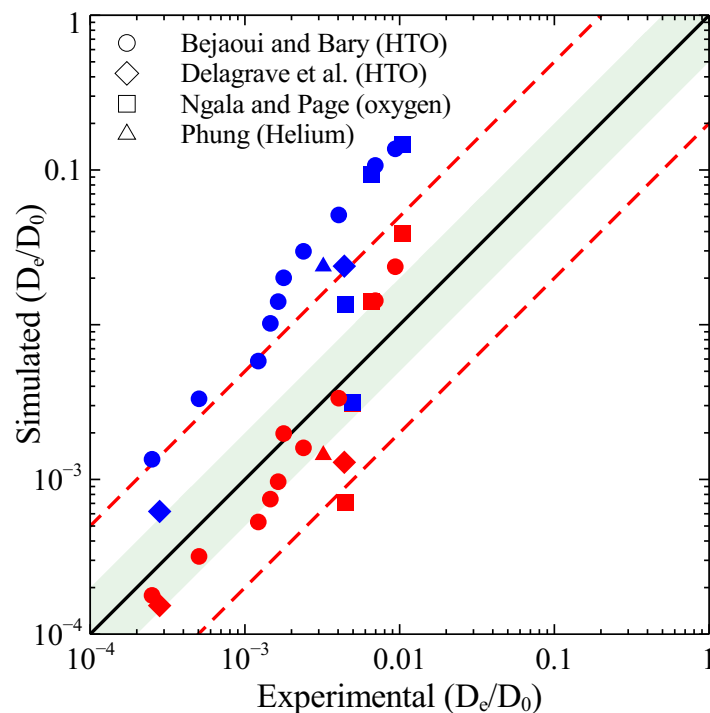
Figure 6.6: Comparison between relative diffusivity obtained using microstructures generated from integrated kinetic models for through diffusion experiments with tracers such as dissolved oxygen (refs. [6]), HTO (refs. [7], [5]) and dissolved helium (refs. [8]). The predictions from HYMOSTRUC and CEMHYD3D are marked blue and red respectively. Black line represents line of equality. Shaded green region shows factor of 2 bounds and dashed line in red shows factor of 5 bounds.
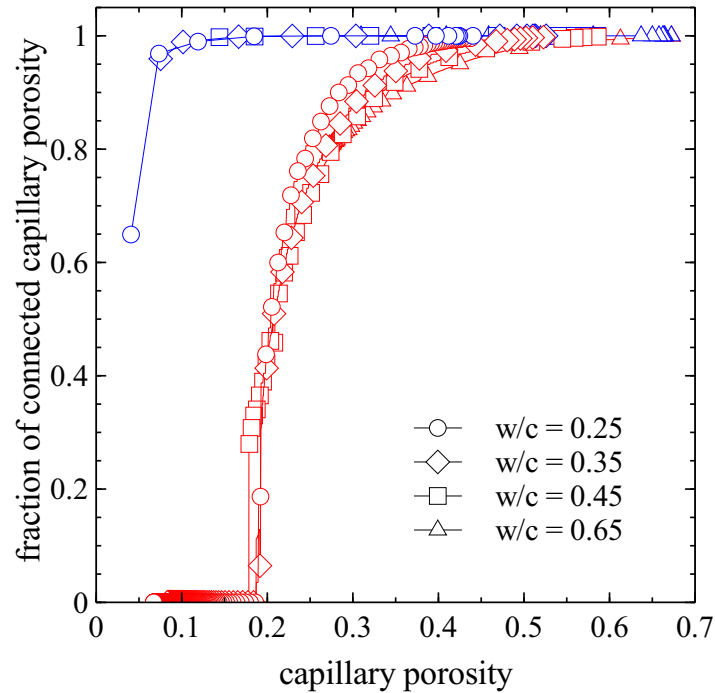
Figure 6.7: Fraction of capillary pores percolated at different w/c during hydration for cement composition of Bejaoui and Bary [5]. The results for HYMOSTRUC and CEMHYD3D are marked blue and red respectively.

kinetic models and experiments for through diffusion tests. It can be observed from Fig. 6.6 that both HYMOSTRUC and CEMHYD3D models give qualitatively similar trends. However, the relative diffusivity obtained from HYMOSTRUC are always higher compared to CEMHYD3D. Similar observation has been previously made by Liu *et al.* [177]. Zhang [208] on the other hand has used a one order lower value for diffusion coefficient of ions in pore water as proposed by Pivonka *et al.* [164] (discussion on this assumption is given in section 5.3) in order to achieve good comparison with the experimental data.

Very high predictions of the relative diffusion coefficient using HYMOSTRUC generated microstructure can be attributed to the very high degree of percolation of capillary pore even at low w/c. Fig. 6.7 shows the fraction of capillary pores connected for the microstructures generated from CEMHYD3D and HYMOSTRUC for cement composition of Bejaoui and Bary [5]. It can be seen from Fig. 6.7 that for HYMOSTRUC even at around 5% capillary porosity, 65% of the capillary pore are connected. As a result for HYMOSTRUC generated microstructure capillary pores are the dominant phase for transport to occur. For CEMHYD3D complete de-percolation of capillary pores occurs at around 18% capillary porosity and hence below 18% capillary porosity the C-S-H is the dominant phase for transport to occur. Therefore, the effective diffusion coefficient computed from CEMYHD3D are always lower compared to that for HYMOSTRUC. Further from Fig. 5.1 in chapter 5, it can be observed that at around 20-30% capillary porosity, sudden increase in the diffusion coefficient occurs, suggesting that at this point the capillary
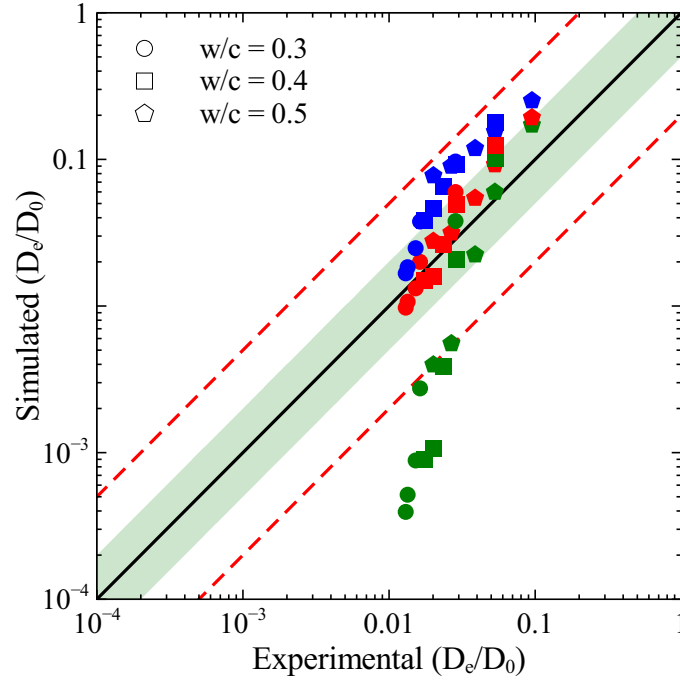
Figure 6.8: Comparison between relative diffusivity obtained using microstructures generated from integrated kinetic models for electric resistivity experiments of Ma *et al.* [9]. The predictions from HYMOSTRUC, CEMHYD3D and CEMYHD3D with only nitrogen accessible pores contributing to diffusion are marked blue, red and green respectively. Black line represents line of equality. Shaded green region shows factor of 2 bounds and dashed line in red shows factor of 5 bounds. The area within factor of two bound is represented by shaded region

porosity starts to percolate. This might also be the reason for a good predictions achieved by CEMHYD3D generated microstructure compared to HYMOSTRUC microstructure for low to moderate relative diffusivity.

For through diffusion experiments, all the predicted data points (expect one) for HYMOSTRUC fall outside the factor of two bounds. For CEMHYD3D around 53% (of 17 simulated data points) lie within factor of two bounds which is comparable with the performance of existing analytical models discussed in chapter 5. From Fig. 6.6 it can be seen that all the data points for low relative diffusivity falls within factor of two bounds for CEMHYD3D which validates the proposed two scale model with an assumption that only nitrogen accessible pores contribute to the diffusion of tracers. Furthermore, for higher relative diffusivity (w/c greater than 0.5), the relative diffusivity is always overestimated by microstructure models. A possible reason for the over prediction might be higher contribution from the C-S-H phase. Eq. (6.7) used to estimate the relative fraction of LD C-S-H is derived empirically for w/c upto 0.5 by Tennis and Jennings [15]. Beyond this w/c at higher degree of hydration the phase fraction of HD C-S-H according to Eq. (6.7) would be zero as a result of which C-S-H at that point is assumed to be composed of only LD C-S-H. This results in very high diffusivity of C-S-H (see Fig. 6.5).

Fig. 6.8 shows the comparison between the relative diffusion coefficient obtained from
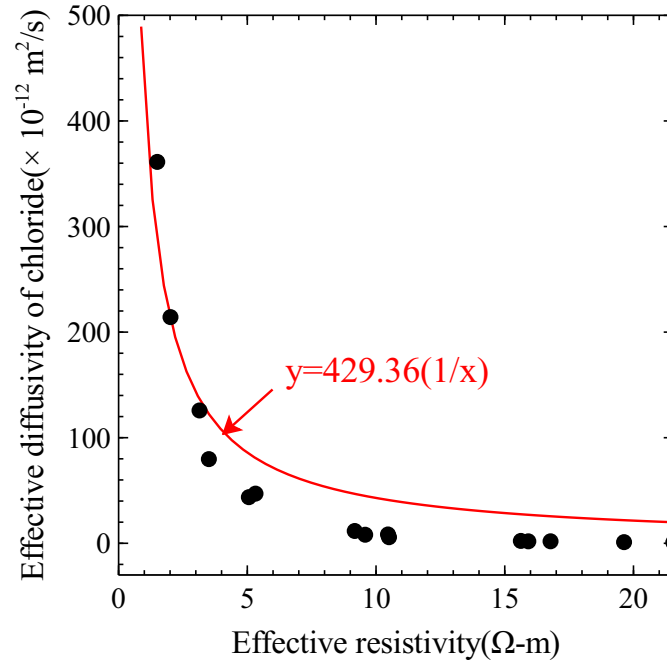
Figure 6.9: Relationship between the steady stated chloride diffusion coefficient and effective resistivity obtained for cement composition of Ma *et al.* [9].

the microstructures generated from integrated kinetic models and experiments for electric resistivity measurements of Ma *et al.* [9]. For the case of electric resistivity good predictions are observed under the assumption that all gel pores contribute to the measurement. In case only the nitrogen accessible pores in C-S-H contribute in diffusion the predicted relative diffusion coefficients are significantly lower than the experimental values as shown in Fig. 6.8. Thus it can be inferred that differences in measurements observed between electric resistivity measurements and through/electro migration is due to differences in contribution of C-S-H with only nitrogen accessible porosity of LD C-S-H allowing transport of tracers/ions whereas for electric resistivity all C-S-H pores contributes. The relationship between electric resistivity and chloride diffusivity is often related in literature as [209–211]

$$D_e = k_{Cl}\frac{1}{\varrho_e} \tag{6.11}$$

where k_{Cl} is a fitting factor and ϱ_e is the effective resistivity [ML^{3}T^{-1}Q^{-2}]. D_e in Eq. 6.11 is usually represented in terms of $\times 10^{-12}$ m^2/s. The relative diffusivity obtained from the microstructures for the Ma *et al.* [9] experiments in case only nitrogen accessible C-S-H pores contributing to transport can be converted into steady state effective diffusivity of chloride by multiplying with D_0 equal to 2.03×10^{-9} m^2/s for chloride [212]. Similarly, relative diffusivity obtained from the microstructures for the Ma *et al.* [9] experiments in case all pore contributes can be converted into effective resistivity by multiplying with the ϱ_0 equal to 0.21 Ohm-m, 0.25 Ohm-m and 0.29 Ohm-m for w/c equal to 0.3, 0.4 and 0.5 respectively. ϱ_0 being the resistivity of pore water [ML^{3}T^{-1}Q^{-2}]. Fig. 6.9 shows the
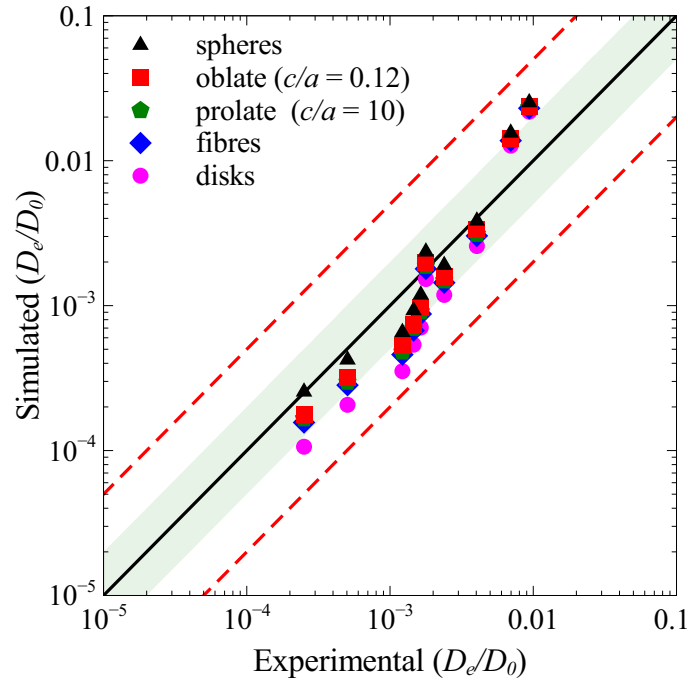
Figure 6.10: Comparison between relative diffusion coefficients obtained using microstructures generated from CEMHYD3D and experimental data of Bejaoui and Bary [5] highlighting the influence of shape of elementary building block of C-S-H.

relationship between electrical resistivity and steady state effective diffusivity of chlorides. The value of k_{Cl} was obtained as 429.36. For concrete the value of k_{Cl} as reported by different authors ranges from 103 to 297 [210, 211] which is lower than that for the cement paste as fitted for results in Fig. 6.9. This can be attributed to dilution effect in case of concrete. For instance if the volume fraction of cement paste in concrete is 50% than the k_{Cl} value can be converted to that for concrete by multiplying k_{Cl} for cement pate with paste fraction i.e. 0.5. The k_{Cl} for concrete with cement composition of Ma *et al.* [9] in this case would be 214.68 (429.36 × 0.5) which falls within the range of values as reported by different authors for concrete.

From Fig. 6.8 it can be inferred that the differences between the predictions from HYMOSTRUC and CEMHYD3D are lower compared to through diffusion. The possible reason for this observation is that in case when all gel pores are contributing to diffusion, the effective diffusivity of the C-S-H is relatively very large compared to C-S-H diffusivity with only nitrogen accessible pore contributing to diffusion (see Fig. 6.5). Therefore the effect of de-percolation is less compared to through diffusion experiments. For electric resistivity measurements, around 80% (of 15 simulated data points) fall within factor of two bounds for CEMHYD3D generated microstructure showing better performance compared to existing analytical models discussed in chapter 5.

Fig. 6.10 shows the influence of shape of elementary building block of C-S-H on relative diffusivity predicted from CEMHYD3D generated microstructure for experimental data of Bejaoui and Bary [5]. Influence of shape of elementary building block is only noticeable

at very low w/c (w/c = 0.25 and 0.3) where the transport essentially occurs through C-S-H. The estimates of effective diffusivity by different shape (except disks) fall within the factor of two bounds for these w/c, with spherical shape providing the best estimates. As discussed in section 6.3, the experimental observations suggest that C-S-H elementary building blocks do posses an aspect ratio. However, from the perspective of transport the shape of elementary building block might not be an influential factor.

6.6 Conclusions

The LB scheme presented in part I has been utilized to obtain diffusion coefficient from microstructures generated from integrated kinetics model. It should be noted that integrated kinetics models have been developed to obtain correct phase fractions and to provide microstructures for a given degree of hydration. However, extraction of diffusivity from these models is a "by product". For the same capillary pore fraction, these models can therefore provide different capillary pore connectivity. The C-S-H is treated as a porous media and its diffusivity is obtained using a two-scale model based on effective media theory. The effective media theory together with microstructures generated from integrated kinetics model and lattice Boltzmann scheme thus provides a framework to explore the influence of different morphological features of cement paste on transport properties. At present the reduction in diffusivity in gel pores was taken as 1/10 accounting for constrictivity effects for all type of tracers. However it has been observed that different ions diffuse differently in cement paste [153, 189] and these differences are associated with constrictivity. Hence in future a detailed experimental program is needed to accurately quantify the constrictivity parameter.

A series of simulations were carried out for through diffusion experiments using different tracers such as HTO, dissolved helium and dissolved oxygen and electric resistivity experiments to have one to one comparison with relative diffusivity obtained from microstructure generated using two integrated kinetics models viz., HYMOSTRUC and CEMHYD3D. It was observed that prediction from HYMOSTRUC was higher compared to CEMHYD3D especially for low relative diffusivity (i.e. low w/c and porosity). For higher diffusivities (i.e. for high w/c and porosity) and when the difference between diffusivity of C-S-H phase and capillary pores is small (i.e. in case of electric resistivity experiments), differences between the diffusivites obtained from microstructures generated using these models decreases. The possible explanation for this difference is the fact that even at porosity as low as 5%, 65% of the capillary pores are connected in case of HYMOSTRUC whereas in case of CEMHYD3D a complete de-percolation is noticed. Hence, at low w/c ratio in case of HYMOSTRUC capillary pores are dominant phase whereas for CEMHYD3D C-S-H is the dominant phase for transport to occur.

It should be noted that for microstructures generated from integrated kinetic models

percolation thershold is a function of resolution and degree of percolation increases with higher resolution [160, 162]. However, for diffusivity the curcial factor is the capillary porosity when depercolation occurs as at that point C-S-H phase becomes dominant. Experimental results show transition at around 17% of capillary pores. Therefore, the diffusivites predicted from CEMHYD3D generated models shows better co-relation with experimental data. Around 53% (of 17 simulated data points) and 80% (of 15 simulated data points) of predicted data points from microstructures generated from CEMHYD3D for through diffusion experiments and electric resistivity experiments respectively falls within factor of two bounds. The presented approach thus outperforms majority of the existing analytical models. Further, the results simulated for low relative diffusivity (low w/c or porosity) were within factor of two bounds indicating good predictive capability of the presented C-S-H diffusivity model. Simulations were also carried out to access the influence of the shape of the elementary building blocks on estimated relative diffusivity. It was observed that differences are only visible at very low w/c (i.e. w/c = 0.25 and 0.3). However, in general the shape of elementary building block does not have a major influence on predicted diffusivity.

The simulations further reveal that for the tracers such as HTO, dissolved helium and dissolved oxygen, transport occurs only through nitrogen accessible gel pores whereas for electric resistivity measurements all gel pores contributes. This in turn provides an explanation for higher relative diffusivity measured by electric resistivity experiments compared to the through diffusion technique. It was demonstrated that this can be further utilized to establish relationship between steady state chloride diffusivity and electric resistivity experiments. The question now arises whether this explanation is viable. Jennings [21] suggested that the nitrogen accessible pores represents the large gel pores of size 3-12 nm whereas the nitrogen inaccessible pores represents small gel pores of size 1-3 nm. The water in the small gel pores is physically bound (also known as "hindered water" or "constrained water") and has different physical properties compared to the bulk pore water. Hence, small gel pores might provide higher resistance to diffusion of tracers such as HTO, dissolved helium and dissolved oxygen and therefore do not contribute to transport. On other hand, due to high pH of pore water of cement paste the small gel pores should be rich in ions which in turn allows to transmit electric current through small gel pores. Hence even though the small gel pores do not contribute to diffusion of tracers it might contribute to the electric resistivity measurements. Alternatively, it can also be the case that the constrictivity in small gel pores is much higher compared to that in large gel pores. This hypothesis needs to be further explored by taking into account different constrictivities for LD C-S-H and HD C-S-H. It should be noted that in this case too the diffusivity of C-S-H should be in the range of the one predicted by the model presented in absence of contribution from small gel pores as for this values of diffusion coefficient good agreement is found with the experiments.

Leaching of cement paste: mechanisms, influence on properties and existing modelling approaches

---

7.1 Introduction

Leaching is a process in which ions get dissolved from the solid phases of cement based materials and are transported by concentration gradients (diffusion) or/and pressure gradients (convection). The leaching of calcium ions is of most importance compared to other leachable ions as calcium based solid phase forms the majority of solid volume in cement based materials. Therefore, *leaching* is the term commonly used to refer to *calcium leaching* in cement based materials. Hence in this thesis leaching refers to calcium leaching. Leaching causes dissolution of solid phases such as portlandite and aluminate phases and causes incongruent dissolution of C-S-H phase. This results in a more porous material with lower strength and higher permeability and diffusivity. Progression of leaching in cement based material is very slow (up to a few millimeters in hundred years [17, 18]). Hence for civil concrete structures with life span of few decades leaching is not considered an important deterioration mechanism. However, for structures which are in constant contact with water such as dams, foundations of offshore structures and bridges, water tanks, sewer pipes, subsurface nuclear waste disposal facility, leaching can be an important deterioration mechanism and should be taken into account for the service life evaluation of such structures.

The first half of this chapter provides a overview on current understanding of mechanisms of leaching, its influence on properties and microstructure of cement paste. The latter half of this chapter provides overview on the existing modelling approaches for leaching. Only opc is considered in this review. Section 7.2 gives a general overview on physical

and chemical mechanisms. The experimental observations on influence of leaching on pore structure and properties of concrete are presented in section 7.3. Section 7.4.1 gives an overview on modeling approaches at continuum scale. The modelling approaches resolving the microstructure of cement paste are presented in section 7.4.2.

7.2   Chemical and physical mechanisms

Leaching is triggered when cement based materials come in contact with low pH or low alkaline solution. The pH of pore water in OPC paste lies in the range of around 12.5-13 after hydration. Therefore, any solution with pH below this range (e.g. water) will initiate leaching and is considered as an *aggressive* solution. Due to the slow progression of leaching different techniques have been proposed to accelerate leaching some of which involves the use of aggressive solutions such as deionized water [13, 14, 213–215], ammonium nitrate solution [8, 14, 216–227] and ammonium chloride solution [228]. Amongst all, deionized water and ammonium nitrate are the most commonly used solutions. Leaching rate due to ammonium nitrate is much faster than deionized water and results in similar end products (i.e. removal of calcium hydroxide and decalcification of C-S-H) [14, 229]. Ammonium nitrate reacts with the cement minerals to form calcium nitrate which is highly soluble and nitro aluminate of calcium which is not very soluble. Calcium nitrate quickly dissolves in water forming ammonia (which escapes from the system) and releases hydronium ions. This decreases the pH of solution which accelerates the successive dissolution of calcium bearing phases. This inturn increases the calcium equilibrium concentration on the onset of portlandite dissolution from 21 mol/m^3 to around 2730 mol/m^3 [229]. Alternatively, the leaching process has also been accelerated in some studies using electric field [230, 231] or application of a pressurized flow[232].

As the diffusion process is slower in cement paste, the reactions during leaching are usually equilibrium based. The equilibrium between solid and liquid calcium content can be described in terms of solid-liquid equilibrium curve (or simply *equilibrium curve*) as shown in Fig. 7.1. Fig. 7.1(a) shows the equilibrium curve for leaching caused by deionized water. This curve marks three distinct stages as explained in [10, 157, 233]. The dissolution of portlandite occurs in cement paste once alkali such as Na and K are leached reducing pH of cement paste. The concentration of Ca is maintained at around 21 mol/m^3 due to dissolution of portlandite. On full dissolution the calcium to silica ratio (Ca/Si) in solid is around 1.65 to 1.8. At this stage incongruent dissolution of C-S-H is initiated. A dissolution of ettringite and AFm phases also occurs in that zone. The calcium concentration in liquid at the end of this stage is around 2 mol/m^3 and Ca/Si in solid reaches to 1. Further leaching leads to complete decalcification of C-S-H, transforming C-S-H into an amorphous silica gel. At this stage the amount of silica in liquid can be as high as 6 mol/m^3.

Jacques *et al.* [234] have noted a large variability in the reported experimental data for
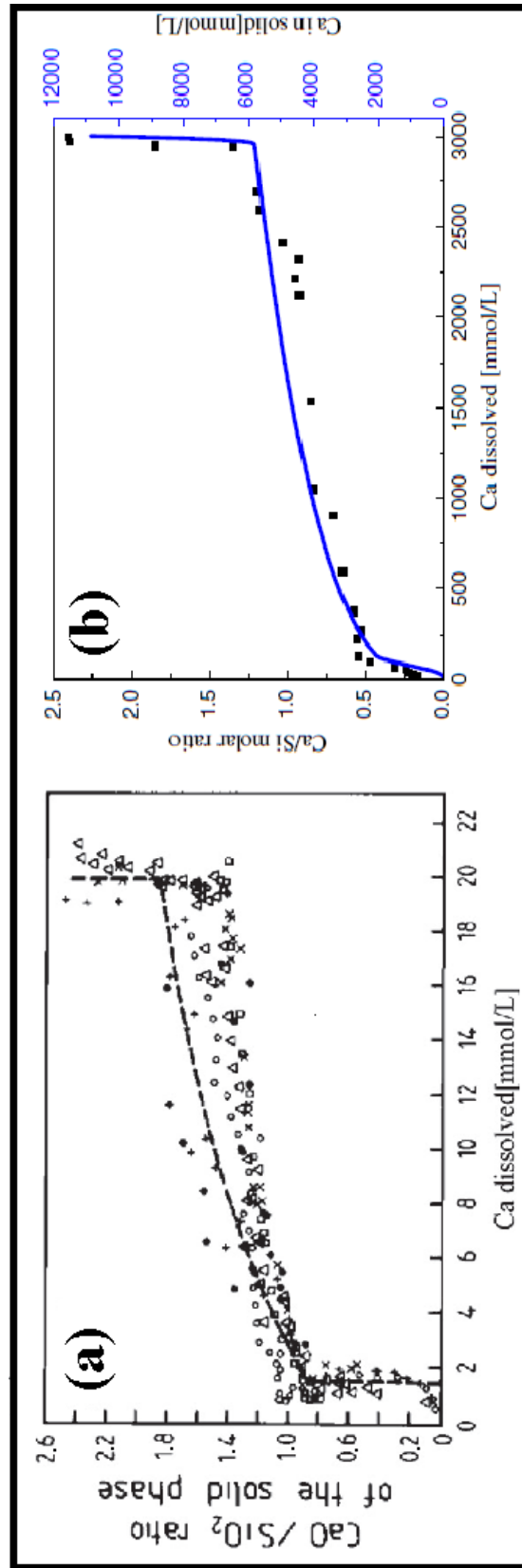
Figure 7.1: Evolution of ratio of solid calcium to silica content as a function of calcium concentration in the liquid (equilibrium curve) (a)deionized water as published by Buil *et al.* [10] . The points indicates the experimental data compiled by Berner [11] and solid line is fit to the data. (b) Ammonium nitrate as published by Wan *et al.* [12]. Points indicate the experimental data and solid line is fit to the data.

Table 7.1: Leaching kinetics parameter for ordinary portland cement paste as reported in literature

reference	leaching solution	w/c	temperature (°C)	a (mm/day$^{0.5}$)
Bellego *et al.* [216]	deionized water	0.4	-	0.12
	deionized water	0.25	-	0.084
	deionized water	0.45	-	0.288
Galle *et al.* [223]	ammonium nitrate	0.45	23	174
Kamali *et al.* [14]	deionized water	0.25	26	0.075
	deionized water	0.4	26	0.14
	deionized water	0.5	26	0.169
	deionized water	0.25	85	0.206
	deionized water	0.4	85	0.328
	deionized water	0.5	85	0.384
	ammonium nitrate	0.25	20	1.17
	ammonium nitrate	0.4	20	1.56
Yang *et al.* [228]	ammonium chloride	0.30	-	0.35

equilibrium curve as reported by different researchers for leaching due to deionized water. The large experimental variability is observed in the data especially for Ca when 1.25 < Ca/Si < 1.75 and for Si for when Ca/Si > 1.25. Less variability is present for the maximum Ca concentration (large Ca/Si) and pH. Several authors have listed different reasons for the variability in the experimental data, including the C-S-H synthesis process, reaction time and pathway followed to reach equilibrium amongst other things [219, 235]. As a consequence variability is observed between different reactions models of C-S-H for Ca when 1.25 < Ca/Si < 1.75 [234].

Wan *et al.* [12] determined the equilibrium curve for leaching under 6 M ammonium nitrate solution as shown in Fig. 7.1(b). It was found that leaching under 6 M ammonium nitrate occurs in three stages similar to that of water. The concentration of Ca in liquid is maintained at around 2950 mol/m^3 due to portlandite dissolution. On complete dissolution of portlandite the Ca/Si in solid is around 1.3 mol/m^3 and incongruent dissolution of C-S-H and dissolution of ettringite and AFm phase is initiated. The calcium concentration in liquid at the end of this stage is around 130 mol/m^3 and Ca/Si in solid is around 0.5. The values of Ca/Si at the end of stage one and two were observed to be lower than the typical values reported for leaching by deionized water.

Progression of the leaching front is governed by transport and is diffusion controlled (in absence of advection) as confirmed by many experimental studies [8, 13, 14, 216, 223, 236]. Therefore leaching depth at a given time can be expressed as

$$L_x = a\sqrt{t} \tag{7.1}$$

where, L_x is the leaching depth [L] and a [L^1 T$^{-1/2}$] is the leaching kinetics parameter. The popular approach to measure degraded depth is to use phenolphthalein. Phenolphthalein

turns from colourless in acidic solutions to pink in basic solutions with the transition occurring at pH around 9.5. However it should be noted that the leaching depth measured by phenolphthalein does not represent total leaching depth. The total leaching depth being defined as the distance at which the calcium in solid is the same as that for a reference unleached material. Bellego *et al.* [216] based on complementary microprobe analysis suggested that the degradation depth measured by phenolphthalein should be corrected by a factor of 1.16 to obtain total leaching depth. Table 7.1 shows the compiled data for leaching kinetics parameter of OPC paste. Higher w/c leads typically to higher leaching rate because of a higher porosity. Higher temperature also promotes leaching for both deionized water and ammonium nitrate. Leaching kinetic parameter in an ammonium nitrate solution is observed to be around 10 times higher compared to leaching in deionized water. Poyet *et al.* [237] have observed that the rate of leaching is sensitive to the frequency of renewal of leaching solution during test. In test setup where solution is not renewed the leaching rates observed are lower than that where solution is constantly renewed. Kamali *et al.* [238] has proposed a more general relationship to evaluate leaching depth as a function of time which accounts for a wide range of factors such a water-binder ratio (w/b), silica fume (SF), pH, temperature (T) and experimental protocol $(prot)$. Their relationship can be expressed as follows

$$L_x = a \times t^{1/n} \tag{7.2}$$

The leaching depth L_x is expressed in mm, time in days. The parameter n is 2 in absence of electric field and 1 in presence of electric field. The leaching kinetics parameter was expressed as

$$a = a_1 \times F(w/b) \times F(SF) \times F(pH) \times F(T) \times F(prot) \tag{7.3}$$

a_1 is a constant and $F(x)$ represents independent functions taking into account the influence of water-binder ratio (w/b), silica fume (SF), pH, temperature (T) and experimental protocol $(prot)$. All these functions have been determined by Kamali *et al.* [238] from their experimental results.

7.3 Changes in solid phase composition, pore structure and properties

As presented in the previous section, dissolution of different mineral phases occurs in several stages. This leads to formation of several distinct altered zones in a degraded sample such as a fully degraded zone with highly decalcified C-S-H gel at the surface, zone with a partially degraded C-S-H and fully dissolved ettringite and AFm phases, zone with fully dissolved

portlandite and a sound zone [213]. The progression of this zones is linear with square-root of time [213]. Faucon *et al.* [214] observed that the mineral composition of the surface in contact to the deionized water after leaching consisted of residual anhydrates, small quantity of hydrogarnet dissolved by leaching, iron substituted C-S-H, and magnesium precipitates in the form of hydrotalcite. The formation of hydrotalcite and ion substituted C-S-H was attributed to the change in pore water at the surface which increases influx of iron and magnesium from inner core. Partial leaching of silicon from C-S-H was also observed near the surface giving evidence of partial dissolution of C-S-H. Precipitation of ettringite has also been observed in some studies in the zones where portlandite has completely dissolved [13, 17, 239]. Scanning electron microscope (SEM) and X-ray imaging results by Phung [8] reveals the presence of portlandite in the transition zone between fully leached zone and the intact zone as shown in Fig. 7.2. The Ca/Si of solid phase drops gradually from sound zone to the leached surface as confirmed by X-ray diffraction [8], X-ray spectroscopy[240], tomography [240] and microprobe analysis [217, 239, 241]. The sample mass decrease is observed due to solid phase alteration during the leaching [8, 13]. A linear relationship exists between the mass loss due to leaching and square root of time similar to that for degradation depth [8, 217]. Decrease in mass subsequently leads to increase in surface area. Phung [8] observed that increase in surface area due to leaching was around 7 to 15 times and around 4 to 5 times for low and high water-binder ratio respectively. Such a high increase in surface area indicates the contribution of C-S-H in increase in surface area. Change in surface area of C-S-H due to decalcification has been studied in [222, 242]. An increase in surface area is observed on decalcification of C-S-H from Ca/Si of 1.7 to 1 using both small angle neutron scattering (SANS) and nitrogen sorption (BET). Further decalcification leads to decrease in surface area. The surface area measured by SANS is usually higher than the BET surface area. This result suggests that decalcification transforms the high density C-S-H into a structure with higher specific surface area i.e. low density C-S-H. The results from SANS reveals that the globule like morphology is transformed into a sheet like morphology due to decalcification.

Decalcification of C-S-H also induces irreversible shrinkage strains. A marked increase in shrinkage has been observed when the Ca/Si of C-S-H decreased below 1.2 which could be attributed to the changes in structure of C-S-H [220]. Chen *et al.* [220] based on their experimental investigation has postulated three mechanisms causing decalcification shrinkage

I *A polymerization-induced shrinkage can result if a siloxane bond, induced by the removal of inter layer Ca in C-S-H, bridges two adjacent regions or surfaces of C-S-H. Moreover, the enhanced mobility of C-S-H at these low Ca/Si (see mechanism II, below) facilitates the slight rotations necessary to align the silicate chains of C-S-H on adjacent surfaces before forming a siloxane bridge.*
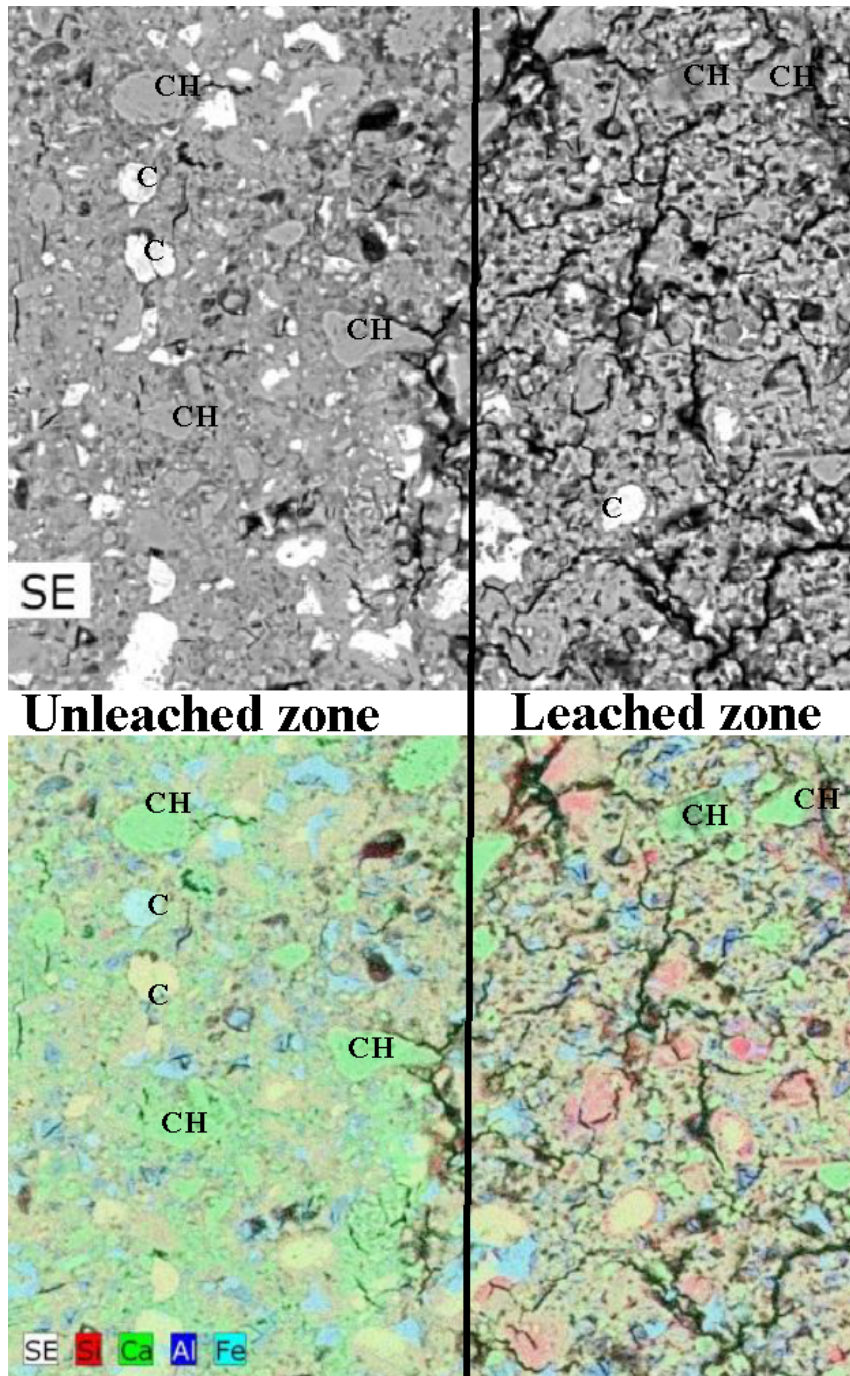
Figure 7.2: SEM image of transition zone of leached sample CH = portlandite, C = residual cement clinkers (top); element (Si, Ca, Al, Fe) mapping generated by X-ray imaging (bottom) (adapted from from [8])
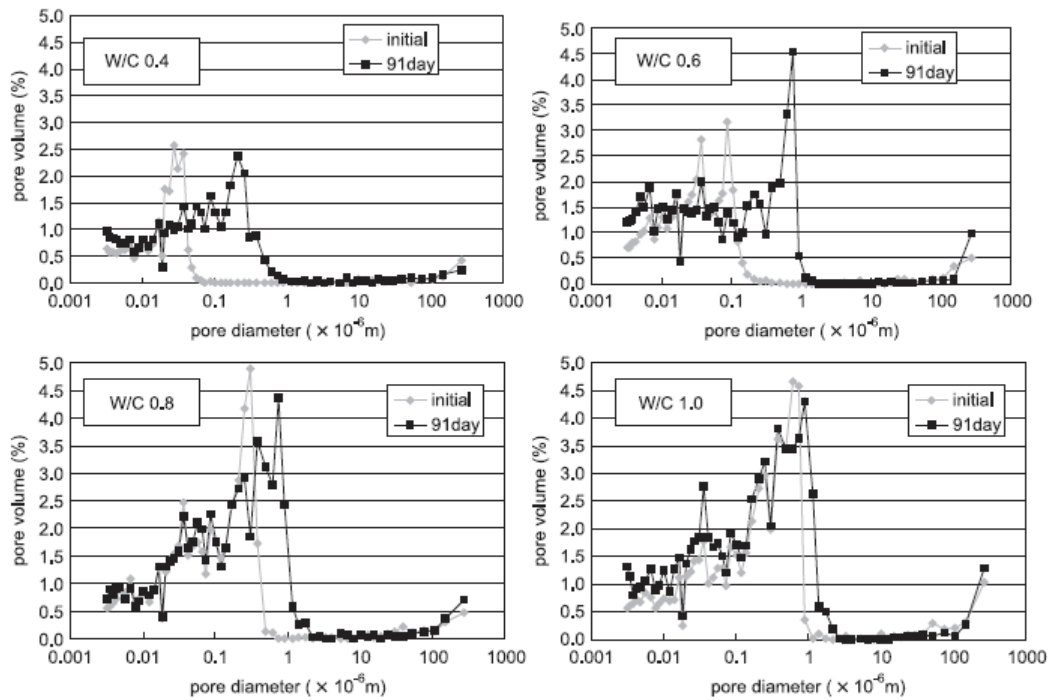
Figure 7.3: Pore size distribution of the initial sample and that leached for 91 days [13].

II *The loss of cohesion and subsequent increased mobility of induced shrinkage by encouraging the structural reorganization of C-S-H into dense morphologies, such as a progressively layered sheet-like morphology*

III *At extensive levels of decalcification (i.e., below Ca/Si 0.66), decomposition of the CaO sheets of C-S-H generates significant shrinkage due to the precipitation and subsequent polymerization of silica gel.*

Both porosity and pore size distribution are significantly altered after leaching. Phung [8] observed significant increase in number of pores with sizes between 60 nm to 500 nm and those with pore size less than 10 nm after leaching for cement paste. The increase in pore volume between 60 nm to 500 nm can be attributed to portlandite dissolution whereas increase in pore volume less than 10 nm is due to decalcification of C-S-H. Also, Bossa *et al.* [243] observed an increase in the volume of pores with sizes between 130 nm to 3.62 μm by a factor 3 using nano and micro tomography. Irrespective of w/c the pore size distribution is skewed towards larger pore sizes after leaching as shown in figure 7.3. The porosity of the fully leached zone in cement paste has been found to be around 60-80% as reported in several studies [157, 243, 244]. Similar to variation of Ca/Si, a gradient of increasing porosity is observed from sound zone towards degraded zone [8, 244].

Increase in both permeability and diffusivity is evident as leaching induces increase in porosity. Revertegat *et al.* [245] reported an increase in diffusivity by a factor 2 and 5 for tritium and cesium respectively after 30% decalcification. Phung [8] observed that the increase in permeability was much higher compared to that of diffusivity due to leaching.

Page 148

For the same sample after 28 days of leaching in ammonium nitrate solution the diffusivity of helium gas increased by 4 times whereas increase in permeability was 25 times. Galle *et al.* [223] have reported an increase in permeability by two orders of magnitude for fully leached (depleted from portlandite) cement paste.

Leaching causes loss of apparent stiffness, a decrease of maximal load (yield stress), and a decrease of fracture energy [216, 226, 246]. The triaxial behaviour of degraded cement paste is characterized by an overall strength loss, a loss of frictional performance and a high sensitivity to drained and undrained conditions [247]. Constantinides and Ulm [248] based on nano-indentation results suggested that the volumetric fraction of high and low density C-S-H remains unchanged during leaching. However low density C-S-H undergoes higher degradation compared to the high density C-S-H with decrease in stiffness of 41% for the former and 14% for the latter. Leached paste can undergo large plastic deformations which suggests the C-S-H with a low Ca/Si is highly plastically deformable [249]. Deformations at failure under tension also increases due to leaching [250]. Heukamp *et al.* [250] based on these results stated that the chemical damage of C-S-H matrix dominates over the increase in macroporosity and in the overall loss of stiffness. Carde *et al.* [251] on other hand observed that loss of strength due to the decalcification of C-S-H is only 6% and can be neglected in relation to the global loss of strength due to the dissolution of calcium hydroxide.

7.4   Modelling approaches

In this section existing modelling approaches are discussed. The models which do not resolve the microstructure of cement paste i.e. *continuum* models are reviewed in section 7.4.1 and models which explicitly resolve microstructure are presented in section 7.4.2

7.4.1   Continuum models

As leaching is a coupled transport and chemical reaction (reactive transport) phenomenon most models aim to simulate these processes. Many model found in literature consider only the mass conservation of aqueous calcium under saturated, isothermal condition [10, 13, 157, 227, 252–256]. This approach has been subsequently extended to account for advective flow in isothermal conditions [257] and non isothermal conditions [258] and coupled chemo mechanical effects during leaching [253, 259].The mass conservation of aqueous calcium can be written as

$$\frac{\partial \phi C_{Ca}}{\partial t} = \vec{\nabla} \cdot D_e \vec{\nabla} C_{Ca} - \frac{\partial C_{Ca}^s}{\partial t} \qquad (7.4)$$

where C_{Ca} is the aqueous Ca concentration, C_{Ca}^s is the solid Ca concentration, D_e is the effective diffusion coefficient of calcium in cement paste and ϕ is the porosity. C_{Ca} can be linked to C_{Ca}^s using the equilibrium curves as shown in Fig. 7.1 and therefore $\frac{\partial C_{Ca}^s}{\partial t}$ can be further expressed in terms of C_{Ca} as

$$\frac{\partial C_{Ca}^s}{\partial t} = \frac{\partial C_{Ca}^s}{\partial C_{Ca}} \frac{\partial C_{Ca}}{\partial t} \tag{7.5}$$

Different approaches have been proposed to describe chemical equilibrium under accelerated conditions in an ammonium nitrate solution. Gérard et al. [260] suggested to use the equilibrium curve for deionized water but to increase the diffusion coefficient 60 times to account for acceleration due to 6M ammonium nitrate solution. In references [10, 227, 229] an equilibrium curve for ammonium nitrate has been used. Phung [8] proposed to gradually adapt the equilibrium curve from one representative for deionized water to one representative for a high ammonium nitrate solution in order to account for influence of spatial-temporal variation of NO_3 concentration on chemical equilibrium.

Models coupling thermodynamics with multi-component transport are an alternative to simulate leaching [156, 261, 262]. The changes in calcium content in solid are obtained by solving the chemical equilibrium between the mineral and the ionic species in pore solution. One class of models (multi-component) attribute the same diffusion coefficient to all aqueous species; consequently electro-kinetic effects induced by a species-dependent diffusion coefficient are not accounted for [156, 262]. On the other hand, Maltais et al. [261] have considered electro-kinetic effects by solving Nernst-Planck equation for transport. Whereas only transport equations for so-called primary species have to be solved for the former, a transport equation is needed for each aqueous species in the latter making it computationally expensive. For leaching, Maltais et al. [261] have considered following 8 aqueous species to be transported: K^+, Na^+, Mg^{2+}, Ca^{2+}, SO_4^{2-}, OH^-, $Al(OH)_4^-$ and Cl^-. Stora et al. [262] further coupled the multi-component reactive transport model to a mechanical model to account for coupled chemo-mechanical effects during leaching. One of the main factors contributing to uncertainty in modelling leaching with a thermodynamic approach is the dissolution model for C-S-H [234]. During the last decades, several C-S-H dissolution models have been proposed with different thermodynamic representation of C-S-H. The detailed review on these models has been presented in [263, 264]. The selection of a single C-S-H dissolution model is not straightforward because of the large variability in experimental solubility data and the fact that all the models seem to reproduce the experimental data within this experimental variability [234, 263].

An important aspect in modelling leaching is to account for reaction-induced changes in porosity and diffusion coefficients. For thermodynamics based modeling approaches changes in porosity are directly determined from the changes in mineral composition during leaching and molar volumes. However, for simplified models accounting only for Ca

transport different approaches have been utilized. Empirical relationship between porosity and C_{Ca}^s derived from experiments is used in references [157, 252, 265]. In references [10, 13, 227, 254] both portlandite and C-S-H are leached out in the form of portlandite and porosity change is therefore described as

$$\phi = \phi_0 + V_m^{CH} \left[C_{Ca,0}^s - C_{Ca}^s \right] \tag{7.6}$$

where V_m^{CH} is the molar volume of portlandite, ϕ_0 is the initial porosity and $C_{Ca,0}^s$ is the initial Ca concentration. Phung [8] used Eq. 7.6 to obtain change in porosity due to dissolution for portlandite. The porosity change caused by decalcification of C-S-H in his model was obtained using a linear relationship between molar volume and calcium in solid of C-S-H as proposed by Morandeau $et\ al.$ [266]. This relationship is given as follows

$$\phi_{CSH} = \phi_{CSH,0} + 0.04 C_{CSH} \left(1 - \frac{[Ca/Si]_{CSH}}{[Ca/Si]_{CSH,0}} \right) \tag{7.7}$$

where $\phi_{CSH,0}$ is initial porosity of C-S-H, C_{CSH} is the concentration of C-S-H phase and $[Ca/Si]_{CSH}$ is Ca/Si of C-S-H and $[Ca/Si]_{CSH,0}$ is the initial Ca/Si of C-S-H. During leaching the concentration of C-S-H is assumed to be constant by Phung [8] and the increase in porosity is accounted by the decrease in molar volume due to change in Ca/Si of C-S-H.

Different types of empirical relationships have been used to account for change in diffusivity due to leaching. Empirical relationships such as exponential relationship and modified Archie's relationship have been used in [157, 267] and Lee $et\ al.$ [156] respectively. The fitting parameters for these relationships have been derived from unleached cement paste data. Haga $et\ al.$ [13] proposed an Archie's relationship type of model as given below

$$D_e = \left(\frac{\phi}{\phi_0} \right)^n D_{e,0} \tag{7.8}$$

where ϕ is the porosity and $D_{e,0}$ is the effective diffusion coefficient of the unleached cement paste. The coefficient n was fitted as 2 based on inverse analysis to match the solid calcium concentration computed from the model and experiments. Delagrave $et\ al.$ [268] proposed the following form of empirical relationship to update diffusivity due to leaching

$$D_e = D_{e,0} \left(\frac{D_e^{leach}}{D_{e,0}} \right)^{\frac{\beta\phi_{CH}+\alpha\phi_d}{\phi_{CH}+\phi_s}} \tag{7.9}$$

with

$$\alpha = 1 + (1 - \beta)\frac{\phi_{CH}}{\phi_s}$$

where D_e^{leach} is the effective diffusion coefficient of a fully leached sample, ϕ_{CH} is the

fraction of portlandite in the cement paste, ϕ_d is the volume fraction of hydrates other than portlandite, ϕ_s is the volume fraction of the hydrates calculated by subtracting the volume occupied by the portlandite and SiO_2 fractions from the total volume of hydrates in a fully hydrated cement paste. β is the fitting parameter. Gérard *et al.* [260] suggested the values of D_e^{leach} as $0.4 \times 10^{-9} m^2/s$ and β as 1.3 for w/c ratio of 0.25 and 2.4 for w/c of 0.4.

Analytical relationships for diffusivity based on effective media theory proposed for sound paste has been extended/utilized to account for change in diffusivity due to change in porosity. Perko *et al.* [264] used the relationship proposed by Oh and Jang [146] (See chapter 5) which is based on generalized effective media theory. Bejaoui and Bary [5] further extended their series/parallel model (See section 5.3) to apply to leaching. They assumed an Archie's relationship type of model to account for changes in diffusivity of low density and high density C-S-H (which is input parameter in their model) due to increase in porosity. Similarly, Stora *et al.* [262] extended multi-coated sphere assemblage model (See section 5.3) to account for leaching. The changes in the diffusivity of low and high density C-S-H were accounted for in their model using following relationship

$$\text{if Ca/Si} > 0.8, \qquad D_{e,i} = \left(1 - \frac{Ca/Si - 0.8}{1.65 - 0.8} \right) D_{e,i}^{leach} + \left(\frac{Ca/Si - 0.8}{1.65 - 0.8} \right) D_{e,0,i} \quad (7.10)$$

$$\text{if Ca/Si} \leq 0.8, \qquad D_{e,i} = D_{e,0,i}$$

$$i \in \{\text{LD C-S-H, HD C-S-H}\}$$

Diffusivity relationships derived from numerical models have also been proposed for leaching. Marchand *et al.* [241] used the microstructure generated using CEMHYD3D to study the influence of the degree of portlandite leaching from cement paste on diffusivity. Based on their analysis, they proposed a relationship between diffusivity and degree of portlandite leaching from cement paste as follows

$$\frac{D_e(\phi_{leach}^{CH}) - D_e(\phi_{leach}^{CH} = 0)}{D_e(\phi_{leach}^{CH} = 100) - D_e(\phi_{leach}^{CH} = 0)} = \frac{1.1 \phi_{leach}^{CH}{}^2}{0.28 + 0.79 \phi_{leach}^{CH}} \quad (7.11)$$

where ϕ_{leach}^{CH} is the fraction of portlandite leached and $D_e(\phi_{leach}^{CH})$ represents effective diffusivity when the volume fraction of portlandite leached is ϕ_{leach}^{CH}. The $D_e(\phi_{leach}^{CH} = 100)$ required for this model was derived from the microstructure generated from CEMHYD3D. $D_e(\phi_{leach}^{CH} = 0)$ was obtained from same model after converting portlandite voxels in fluid voxel.

Snyder and Clifton [269] adapted the NIST relationship (see chapter 5) for unleached cement paste to account for leaching as follows

$$\frac{D_e(\phi_{leach})}{D_0} = 2 D_R^{NIST}(\phi_{leach}) - D_R^{NIST}(\phi) \quad (7.12)$$

where ϕ_{leach} is the porosity of leached material, and D_R^{NIST} is the relative diffusivity as computed with the NIST model for unleached cement paste (see section 5.3). van Eijk and Brouwers [270] used this model to simulate diffusivity changes during leaching with additional modifications. They used a percolation threshold for leached material of 0.16 compared to 0.18 in sound material. The second modification was to increase contribution of C-S-H to diffusivity (the third term in NIST model) from 0.001 (for unleached cement paste) to 0.0025 (which is the relative diffusivity assigned to C-S-H phase while obtaining diffusion coefficient from CEMHYD3D microstructure [271]). However, this term represents the contribution of C-S-H which also account for connectivity of C-S-H in the cement paste microstructures and hence should be smaller than 0.0025. The final form the model of van Eijk and Brouwers [270] can be expressed as

$$\frac{D_e}{D_0} = 0.0025 - 0.07\phi^2 - 1.8H(\phi - 0.18)(\phi - 0.18)^2 + 0.14\phi_{leach}^2 + 3.6H(\phi_{leach} - 0.16)(\phi_{leach} - 0.16)^2$$
(7.13)

It should be noted that equation 7.12 has been derived considered leaching of only portlandite phase and henceforth equation 7.13 does not account for C-S-H leaching. This relationship has been used by Wan *et al.* [227] and Phung [8] to model leaching. To account for the contribution of C-S-H leaching on the diffusion coefficient, Phung [8] considered that 50% of the volume change in C-S-H during leaching contributes to the capillary porosity.

7.4.2 Models to simulate leaching through microstructure

Several attempts have been made to explicitly simulate the changes in microstructure during leaching. Bentz and Garboczi [271] studied the influence of calcium hydroxide leaching on transport properties. They first simulated the microstructure of hydrated cement paste using CEMHYD3D. The leaching process is then modelled as a random dissolution process. For each leaching cycle, the three dimensional microstructure is scanned to identify all voxels of portlandite which are in contact with pore space. For each of these voxels, a one-step random walk to one of their six neighbouring sites is executed. If the step lands in a pore space voxel, that voxel is converted to pore space. Their study showed that the percolation threshold due to leaching reduced to 16% from 18% for hydration. This in turn led to higher increase in diffusivity while leaching compared to decrease in diffusivity during the formation of hydration product. Thus showing that the diffusivity porosity relationship during leaching do not follow same curve as one during hydration (a *hysteresis behaviour*). The modified NIST model for diffusion proposed by van Eijk and Brouwers [270] discussed in previous section tries to account for this observation by changing percolation threshold for leached paste from 18% to 16%.

Feng *et al.* [272] carried out a similar study with the microstructures generated from THAMES hydration model [273]. This model links microstructure evolution to the

thermodynamic equilibrium model GEMIPM2K. Similar to CEMHYD3D, microstructure evolution during hydration in this model is based on stochastic rules. This model improves the approach to dissolve and precipitate mineral phases. The probability of dissolution or precipitation of a voxel is further based on a predefined tendency for a phase to adopt particular morphologies to achieve realistic crystal shape. The leaching in the approach of Feng *et al.* [272] was simulated as a batch reaction using GEMIPM2K thermodynamic model [121]. By flushing small amounts of pore solution at a given time step, the dissolved volume fractions of solid phases are computed using the thermodynamic model. Their approach accounts for changes in microstructure due to dissolution of portlandite, aluminate and C-S-H phases compared to dissolution of only portlandite phase in the approach of Bentz and Garboczi [271].Their simulation results revealed very little hysteresis behaviour between hydration and leaching in contrast to the study of Bentz and Garboczi [271]. They attributed the differences between the two models to the different stochastic rules used to generate initial microstructures. They also computed the transport and mechanical properties of the leached microstructure using finite difference and finite element methods respectively. The change in diffusion coefficient of C-S-H phase and mechanical properties of C-S-H due to leaching were not taken into account while estimating transport and mechanical properties. They observed that a sudden change in slope is observed for the plot of diffusion coefficient with respect to porosity once portlandite is dissolved. Similar change in the slope is also observed for the plot of elastic modulus with respect to porosity. The porosity at which the change in slope occurs depends on the w/c. They also observed that the slope of plot of stiffness with respect to porosity was much stiffer than hydration. This was due to the loss of portlandite which is much stiffer than C-S-H.

Moranville and co-authors [224, 274] proposed an approach to simulate the changes in microstructure due to leaching in which they considered a continuum the three dimensional domain is discretized into 100 μm^3 volume elements. The continuum reactive transport equations are solved along this domain. Transport of ions is solved using the finite volume method whereas the reaction terms are computed using *PHREEQC*. The changes in the diffusion coefficient due to leaching in the transport model is accounted using NIST model for unleached cement paste. Each of the discritized volume element of the continuum domain is either associated with boundary fluid or cement paste microstructure generated using CEMHYD3D. The microstructure is updated during leaching by randomly removing phases that are in contact with pore fluid to match the dissolved volume fraction.

Bernard and Kamali-Bernard [275] proposed a multiscale approach to determine the mechanical and transport properties of leached cement paste. They assumed that leaching progresses in three distinct unleached zone, zone without portlandite and zone without portlandite and aluminate phases. The thickness of each zone is determined through empirical relationships obtained through experiments. The transport and mechanical properties of each zone is determined directly from their microstructure. The initial

microstructures of hydrated cement paste were obtained using CEMHYD3D. The leached microstructures from each zone were determined by turning the dissolved phases into pore spaces. Their numerical results showed that the complete leaching of portlandite decreases the compressive strength of a w/c = 0.4 cement paste by a factor of 1.33. The complete dissolution of portlandite and aluminate phases leads to decrease in compressive strength by factor of 1.86. Complete leaching of portlandite leads to an increase in diffusion coefficient by around 30 times. The dissolution of portlandite and aluminate phases leads to an increase in diffusion coefficient by two orders of magnitude

The models presented above do not simulate the ion transport in the microstructure. Leaching in those models is carried out by uniformly dissolving the phases in the entire microstructure to get the required volume fractions. Recently, Gaitero *et al.* [276] and Ukrainczyk and Koenders [277] presented models which simulate leaching considering ion transport in the resolved microstructure. Gaitero *et al.* [276] presented a pore-scale reactive transport model for leaching due to ammonium nitrate. The initial microstructure for a fully hydrated cement paste in their model was generated with HYMOSTRUC. The solid phases considered in their simulations were, clinkers inner-product C-S-H, outer product C-S-H and overlapping C-S-H. For describing C-S-H reaction, they assumed that C-S-H consist of leachable portlandite and non-leachable C-S-H with Ca/Si equal to one. Hence the reaction due to leaching in their model is represented solely in terms of portlandites dissolution. Gaitero *et al.* [276] accounted for the increase in diffusivity of C-S-H phase due to dissolution through a linear relationship with respect to porosity. The transport equation (in their case Nernst-Planck equation) was solved using a finite element method. Ukrainczyk and Koenders [277] similarly used the HYMOSTRUC model to generate intial microstructure and considered only C-S-H dissolution in presence of deionized water using an equilibrium curve similar to one shown in Fig. 7.1. The diffusivity of C-S-H was evolved in their model as a function of Ca/Si in solid phase. A linear interpolation was carried out between the known points. They considered following known points: Ca/Si 1.7, 1, 0, the assumed diffusion coefficients were $D_0/200$, $D_0/3$ and D_0 respectively. The transport equation (diffusion equation) was solved using implicit finite difference scheme and diffusion of only calcium ions was considered.

7.5 Conclusions

An overview on experimental observations on leaching mechanisms, its influence on microstructure and properties of opc paste and existing modeling approaches not resolving microstructure (continuum approaches) and ones resolving microstructure has been presented. Leaching due to its slow progression is usually studied experimentally under accelerated conditions. The two most commonly used leaching solutions are ammonium nitrate and deionized water. For both solution equilibrium curve shows three distinct parts

viz., marking complete dissolution of portlandite, start of decalcification of C-S-H and dissolution of aluminate phases and complete dissolution of aluminate phases and further decalcification of of C-S-H phases. The progression of the leaching front for both aggressive solutions is diffusion controlled. However, the kinetic rate parameter for leaching under ammonium nitrate solution is ten times higher than that for deionized water.

Leaching leads to formation of zones in the altered material. The outer most zone contains highly decalcified iron substituted C-S-H surface with residual unhydrated cement particles, hydrogarnet (only small quantity dissolved) and hydrotalcite; the zone with fully leached portlandite and the zone next to the unleached cement paste which might contain small amount of portlandite. Decalcification leads to increase in surface area, decrease in the bulk density and results in shrinkage due to decalcification of C-S-H. C-S-H undergoes structural changes due to decalcification and based on SANS data different researchers have concluded that C-S-H morphology is transformed from globule like morphology into sheet like morphology.

Leaching causes an increase in porosity and the pore size distribution is skewed towards higher pores. Leaching causes an increase in permeability and diffusion coefficient and a loss of stiffness. The nano-indentation tests on leached C-S-H reveals that the low density C-S-H undergoes higher degradation than high density C-S-H. However the volume fraction of both high density and low density C-S-H was observed to be constant.

At continuum scale, simplified reactive transport models accounting for only mass transport of Ca and multi-component transport models coupled with thermodynamic models have been used to simulate leaching. The porosity change due to leaching in case of simplified model is computed either through empirical relationships or considering C-S-H reaction in terms of portlandite. Different types of relationships have been used to account for changes in diffusion coefficient due to leaching. All these relationships have some form of fitting parameters which need to be determined. For some relationships these parameters have been determined from the experimental data of unleached cement paste. For others these parameters have been determined by comparison with experimental and predicted leaching profiles. However, due to the lack of experimental data on changes on diffusion coefficient due to leaching it is difficult to access the predictability of these models.

Models explicitly resolving the microstructure and simulating changes in microstructure due to leaching have been developed. Two types of approaches exist in literature. In a first approach, the dissolution of different phases is carried out by dissolving mineral phase in contact with pore water in a stochastic way. Such an approach leads to a uniform microstructure rather than different zones that are observed during leaching. The alternative approach is to use a coupled reactive transport framework to simulate leaching through microstructure. Two models have been proposed recently which only account for dissolution of C-S-H in microstructure. The changes in diffusion coefficient of C-S-H due to change in porosity in these models have been accounted for through simple

empirical relationships. There is still a lack of a robust model to simulate changes in microstructure during leaching. Such a model will not only pave a way forward towards a multi-scale framework, but also serve as an important tool to understand changes in material properties during leaching for which very little experimental data exist.

Modelling changes in microstructure of cement paste under
calcium leaching

8.1 Introduction

Modeling of reactive transport processes using a transport model coupled with geochemical
solver is computationally expensive. For instance, solving the benchmark on C-S-H
dissolution as presented in section 4.5.3 takes around 2 days using a desktop computer
with 3 GHz Intel Xenon processor. Hence in order to simulate reactive transport processes
for a three dimensional microstructure for a longer duration of leaching it is essential
to develop an alternate approach. In this chapter, a simplified reactive transport model
which is deduced from a geochemical model has been developed. This model considers
transport of only Ca and Si components. The reactions are implemented as look-up tables
which have been pre-computed with the geochemical solver *PHREEQC* thus eliminating
a need of invoking the geochemical model at each time step. The equivalence of the
simplified model to coupled reactive transport model has been established through a set
of benchmarks. Further the two-scale model for C-S-H diffusivity as proposed in Chapter
6 has been extended to account for changes in C-S-H structure during leaching. Finally
the simulations of leaching are carried out on the microstructures generated from both
CEMHYD3D and HYMOSTRUC. Section 8.2 details the simplified modeling approach
developed for leaching. Finally the results of the simulation for calcium leaching on
microstructures generated from CEMHYD3D and HYMOSTRUC are presented in section
8.3.

8.2 Simplified reactive transport model for leaching and its implementation

The flow chart for the approach to simulate calcium leaching through the microstructure of the cement paste is presented in Fig. 8.1. The transport of Ca and Si components are described using the advection-diffusion-reaction equation under similar assumptions as discussed in Section 4.1. The advection-diffusion-reaction equation is solved using the *TRT LB scheme for multilevel porous media* with a D2Q5 lattice and a linear EDF as described in section 3.2.2 with an additional source/sink term as explained in section 4.3. For the reactive transport problem (with explicit coupling), the time step should respect the Neumann criteria in order to ensure reliable solutions (as discussed in chapter 4). However, this results in a very small time steps. For instance, for the benchmark on C-S-H dissolution as presented in section 4.5.3 the time step is kept around 3 μs to respect the Neumann criteria. This makes it computationally expensive to simulate leaching during the longer time span. To overcome this limitation, an adaptive relaxation scheme was used which is inspired from the PID (proportional, integral, differential) adaptive time stepping scheme used for conventional numerical methods [278–282]. The adaptation of PID scheme in terms of relaxation parameters for LB method is described in appendix I. This approach allows to safely increase the relaxation time and in turn the time step, while keeping the errors below certain tolerance value.

The molecular diffusion coefficient for both Ca and Si is taken as $2.2 \times 10^{-9} \mathrm{m}^2/\mathrm{s}$ [157]. The diffusion coefficient in capillary pores D_p is equal to the molecular diffusion in water (D_0) and porosity ϕ is equal to one. Only portlandite, clinkers and C-S-H phase are explicitly represented in microstructure for reasons of simplicity. In case of CEMHYD3D, hydration products other than portlandite and C-S-H are also represented as C-S-H. Portlandite and clinker phases are non-diffusive whereas the effective diffusion coefficient D_e for the C-S-H phase is computed using the two-scale diffusion model as described in section 6.3. In this model, the C-S-H is assumed to be composed of HD C-S-H as an inclusion in the matrix of LD C-S-H. Input parameters for this model are the volume fractions of pores and solids in LD C-S-H and HD C-S-H. The approach to compute these volume fractions for initial microstructure has been described in section 6.4. During leaching, solid and pore fractions of HD C-S-H and LD C-S-H have to be updated. Using the updated phase fractions, the diffusion coefficient is updated using the two-scale diffusion model. The approach to update the volume fraction of solid and pore space in LD and HD C-S-H due to dissolution is presented in section 8.2.1. Due to the lack of experimental data on the influence of constricitivity on ion transport in gel pores, the diffusivity of ions in gel pores is assumed to a order of magnitude lower than molecular diffusion coefficient in pure water (see also chapter 6). When Ca/Si in C-S-H becomes less than one, the constrictivity effects are neglected and the diffusivity in the gel pores is taken as the
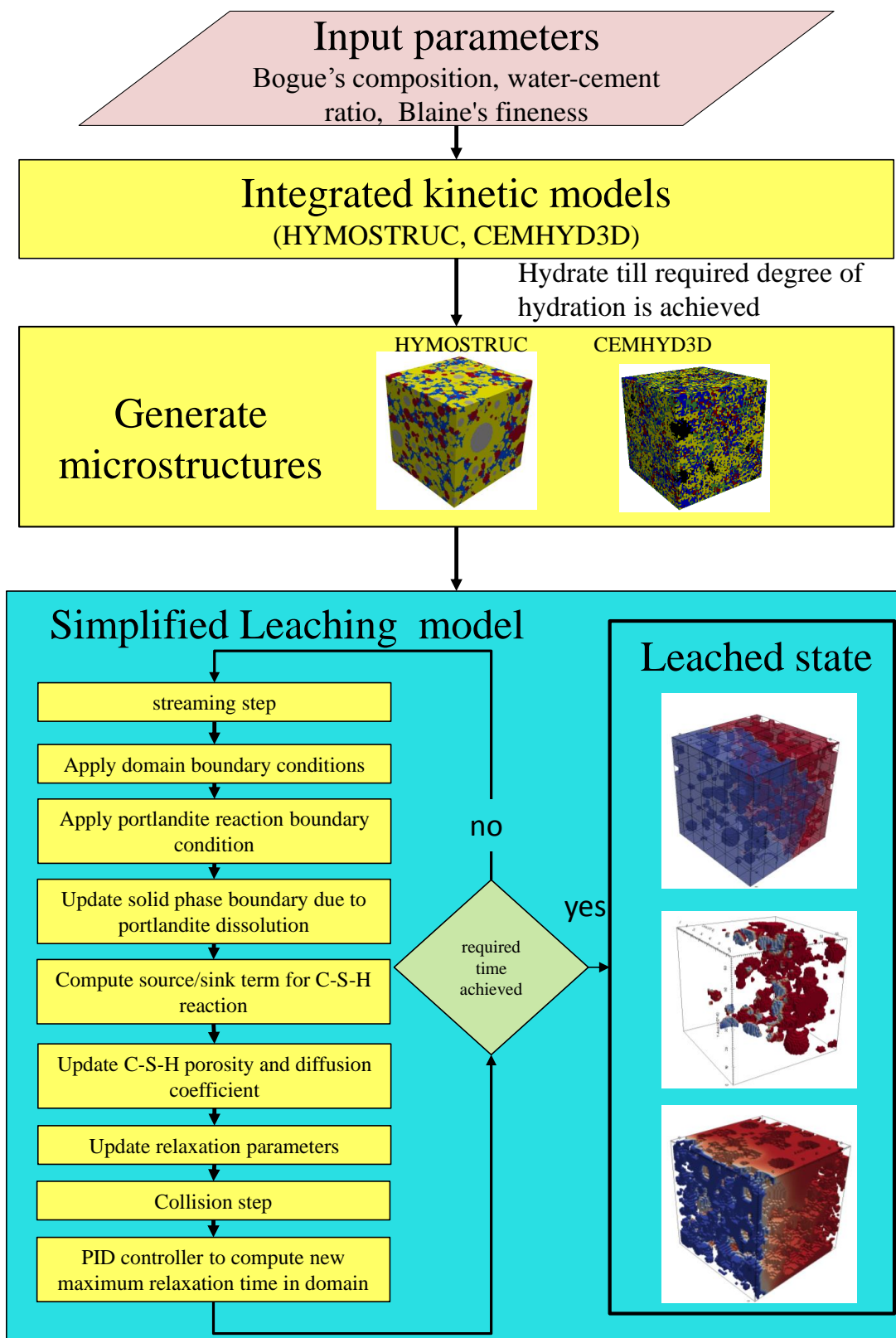
Figure 8.1: Overall approach to simulate leaching through hardened cement paste microstructures generated using integrated kinetics models
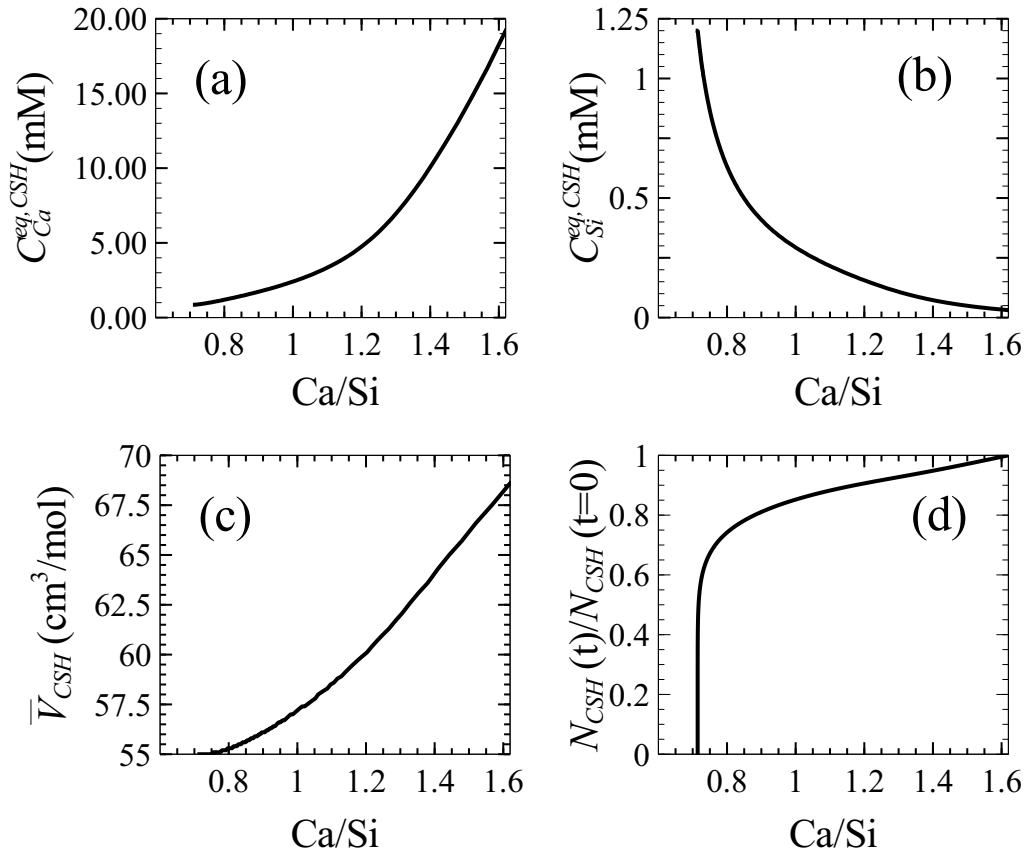
Figure 8.2: Relationships between Ca/Si in C-S-H and (a) Equilibrium Ca concentration (b) Equilibrium Si concentration (c) Molar volume (d) ratio of moles of C-S-H to initial moles of C-S-H

molecular diffusion coefficient in the water. This assumption is justified by the fact that C-S-H starts to undergo drastic structural changes at Ca/Si below one,which is observed in both experiments (see discussion section 7.3) and in thermodynamic model (see Fig 8.2 (d) where at Ca/Si below one the sudden decrease in number of moles is seen). As a result at this point it can be assumed that the pores in C-S-H are large enough to neglect constrictivity effect.

As mentioned previously, leaching of only portlandite and C-S-H due to *deionized water* is considered presently and other minor mineral phases such as ettringite and aluminate phases in case of CEMHYD3D generated microstructures which also undergoes dissolution are treated as C-S-H phase. The dissolution reactions for C-S-H and portlandite are considered through equilibrium chemistry as the leaching is diffusion controlled process (see discussion in chapter 7). Dissolution reaction of C-S-H results in the additional source/sink term for Ca and Si transport equation at the volume element where C-S-H is

present. This source/sink term is computed as follows

$$R_{hom,CSH}^{Ca} = \phi\frac{(C_{Ca}^{eq,CSH} - C_{Ca})}{\Delta t}, \qquad R_{hom,CSH}^{Si} = \phi\frac{(C_{Si}^{eq,CSH} - C_{Si})}{\Delta t} \qquad (8.1)$$

where $R_{hom,CSH}^{Ca}$ and $R_{hom,CSH}^{Si}$ are homogeneous source/sink term of Ca and Si components respectively due to C-S-H dissolution [$N^1L^{-3}T^{-1}$]. C_{Ca} and C_{Si} are the aqueous concentration of Ca and Si components [N^1L^{-3}]. ϕ is the porosity and Δt is the time step [T] which is one for LB scheme. $C_{Ca}^{eq,CSH}$ and $C_{Si}^{eq,CSH}$ are the equilibrium concentrations for Ca and respectively which depend on Ca/Si in the solid of C-S-H phase as described later. As C-S-H undergoes incongruent dissolution the change in porosity due to dissolution is preliminarily due to the change in the molar volume which is given as

$$\phi_{CSH} = \frac{N_{CSH}}{V}(\bar{V}_{CSH}(\vec{r}, t + \Delta t) - \bar{V}_{CSH}(\vec{r}, t)), \qquad \vec{r} \in \Omega_{CSH} \qquad (8.2)$$

where V is the volume of the element, Ω_{CSH} represents the C-S-H domain, ϕ_{CSH} is the porosity of the C-S-H, $\bar{V}_{CSH}$ is the molar volume [$N^{-1}L^3$] and N_{CSH} is the moles of C-S-H phase [N]. N_{CSH} during the initial stage of C-S-H (Ca/Si > 1) dissolution does not vary significantly. However, during later stage N_{CSH} can vary (see Fig. 8.2). The dissolution of portlandite is a heterogeneous reaction and at the boundary of the portlandite, following condition is applied

$$C_{ca}|_{\Gamma=\Gamma_{port}} = C_{Ca}^{eq,port} \qquad (8.3)$$

where Γ_{port} represents the boundary of the portlandite, $C_{Ca}^{eq,port}$ is the equilibrium concentration for Ca component. This boundary condition is implemented using the approach described in section 4.2. The change in geometry due to dissolution is carried out using the approach given in section 4.4. The molar volume of portlandite phase is taken as 33 cm^3/mol.

The relationships for equilibrium concentrations, change in molar volumes and change in moles as a function of Ca/Si in solids for C-S-H and the equilibrium concentration for portlandite were determined using flush-type geochemical simulations [1] using *PHREEQC*. The thermodynamic database CEMDATA07 [126, 283–285] was used to obtain the relevant thermodynamic constants. C-S-H phase in the geochemical reaction model is represented as an ideal solid solution using the CSHQ solid solution model proposed by Kulik [131]. The CSHQ solid solution model is more consistent in terms of reproducing the solubility curves and it gives a more realistic prediction of C-S-H gel densities and volume changes compared to two phase solid solution model as proposed by Kulik and Kersten [286] which is part of CEMDATA07. From the geochemical model, the equilibrium concentration for

---

[1]A flush-type reaction path simulation calculates equilibrium between aqueous and solid phase during different steps (or water-cycles). After each step, an increment of unreacted fluid is added to the system displacing the existing fluid and leaving the reacted minerals in place. Such a type of simulation is also called a mixing-flow reaction in chemical engineering
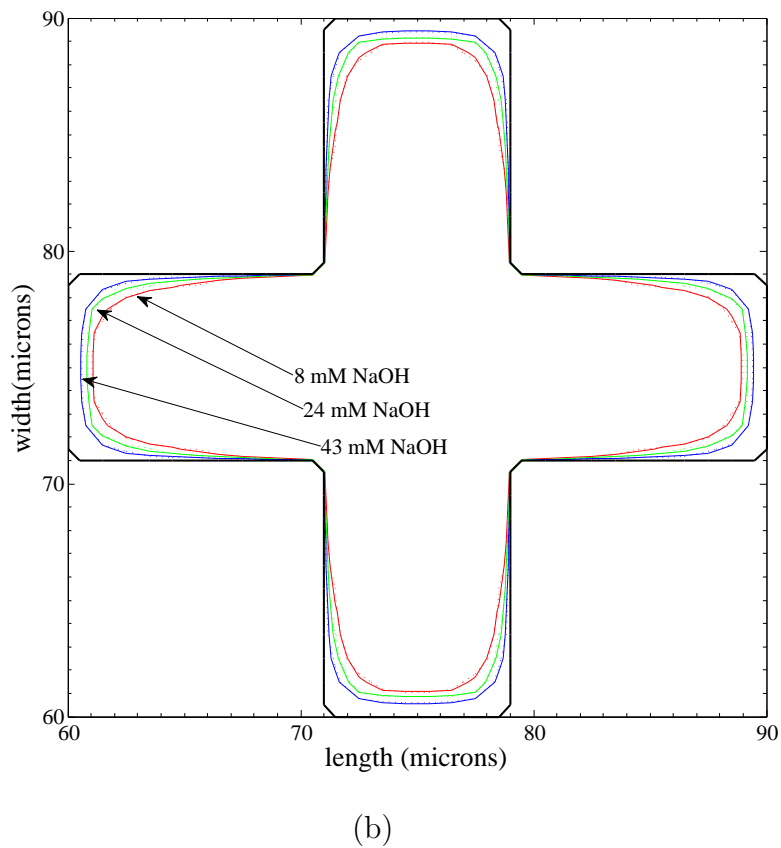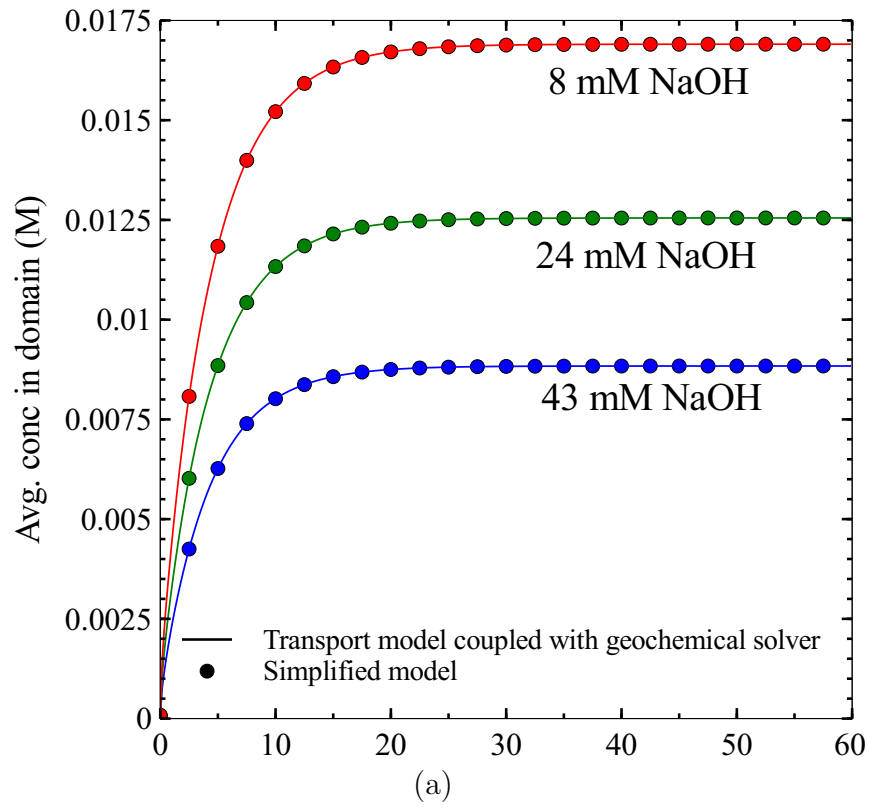
Figure 8.3: Portlandite dissolution benchmark: (a) evolution of average Ca concentration in aqueous phase. (b) Final shape of grain at the end of 60 s. Dotted line represents simplified model and solid lines represents the model coupled with geochemcial solver.

portlandite ($C_{Ca}^{eq,port}$) is ~19.48 mM for leaching under deionized water. The relationships for equilibrium concentrations, change in molar volumes and change in moles as a function of Ca/Si in solids for C-S-H for leaching under deionized water are shown in Fig. 8.2. Experimental data show that there exist an unique relationship between Ca/Si and the parameters such as equilibrium concentrations and change in molar volumes [233, 266] which was also confirmed by simulating flush-type reactions with different initial concentrations of CaO and SiO$_2$. These relationships are implemented in the simplified model as a look-up table and a second order Lagrange polynomial is used for interpolation between the tabulated values. When the C-S-H voxel is in contact with portlandite, portlandite is dissolved first in order to equilibrate the aqueous Ca concentration. This can be simply implemented by applying the portlandite boundary condition before the collision step of LB scheme as shown in Fig. 8.1. This simplified approach can thus be viewed as a scheme in which the chemical reactions (state) are precomputed and tabulated thus eliminating the need to solve the complex geochemical system which in turn increases the computational efficiency.

To validate the proposed approach for portlandite reaction, the example on portlandite dissolution as presented in section 4.6.1 was used. In this example dissolution of a fictional portlandite grain is carried out at different pH values which are obtained by introducing different NaOH concentrations. The equilibrium Ca concentration for portlandite for 8 mM, 24 mM and 43 mM NaOH solutions used in this example were found to be 16.89 mM, 12.53 mM and 8.818 mM respectively. Fig. 8.3 shows the comparison between the results using the transport model coupled with the geochemical model and the simplified approach presented in this section. Good agreement is observed between both models thus validating the portlandite dissolution model for leaching.

To validate the model for C-S-H dissolution, the example presented in section 4.5.3 was simulated using the simplified model. Using the simplified model, this example takes around 15 minutes using a desktop computer with 3 GHz Intel Xenon processor. The comparison between the transport model coupled with the geochemical model for reaction and the simplified model are shown in Fig. 8.5. Fig. 8.4 shows the change in relaxation parameter carried out through PID scheme during this simulation. Good agreement is observed between the two approaches. It is also of interest to compare the results obtained with a simplified model considering only the transport of Ca component, as it is commonly used approach for simulating leaching [10, 157, 260, 264]. In this model further, the change in number of moles of C-S-H due to leaching is not accounted for (i.e. relationship Fig. 8.2 not used). Fig. 8.6 shows that in case of only Ca transport, good agreement is not observed between Ca in solid and liquid phase at inlet of the domain where considerable leaching has occurred.
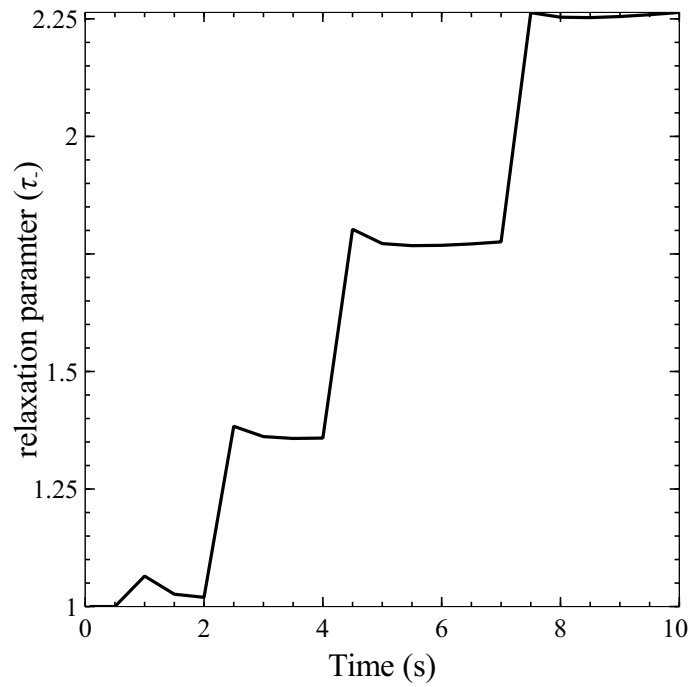
Figure 8.4: C-S-H dissolution benchmark: change in relaxation parameter as controlled by PID scheme
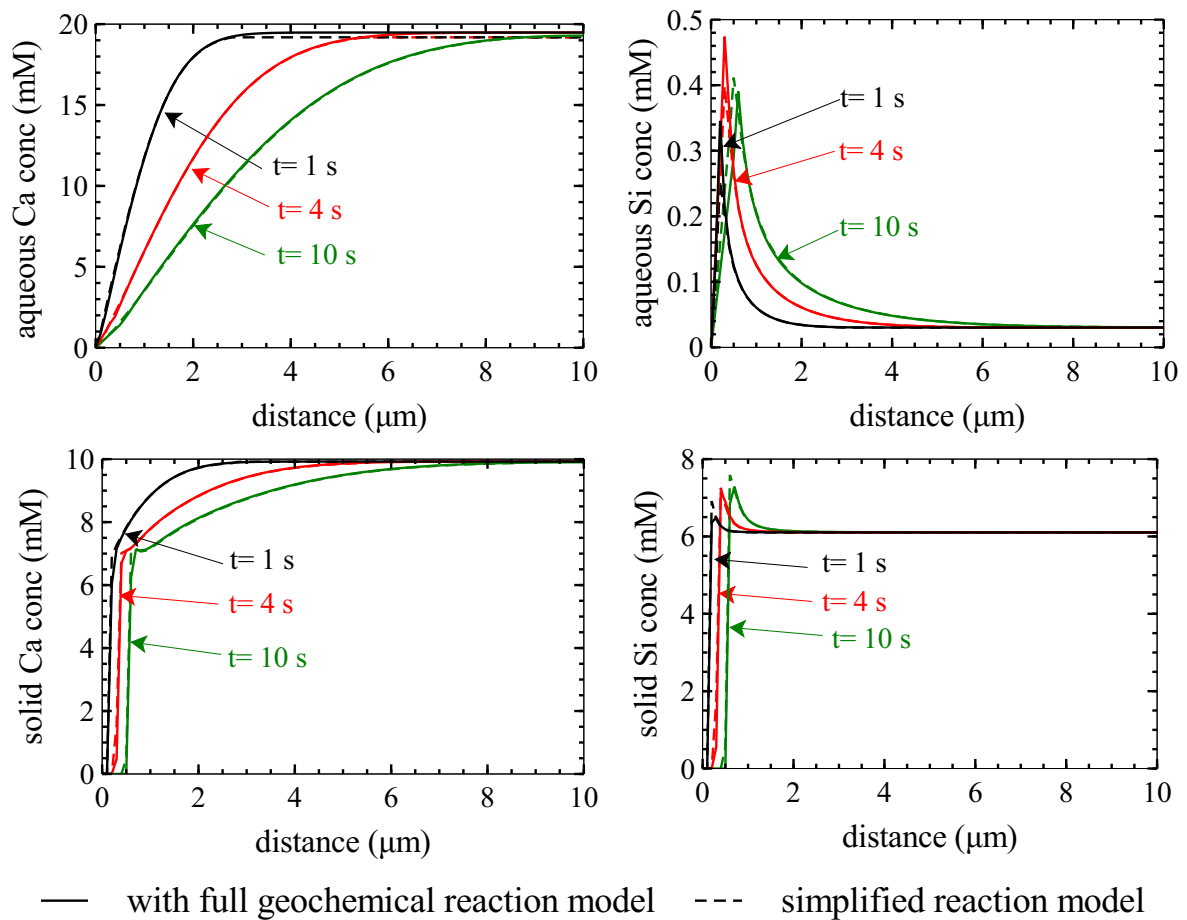
Figure 8.5: C-S-H dissolution benchmark: profiles for Ca and Si concentration in aqueous and solid phases at different times. In this case transport of both Ca and Si is considered
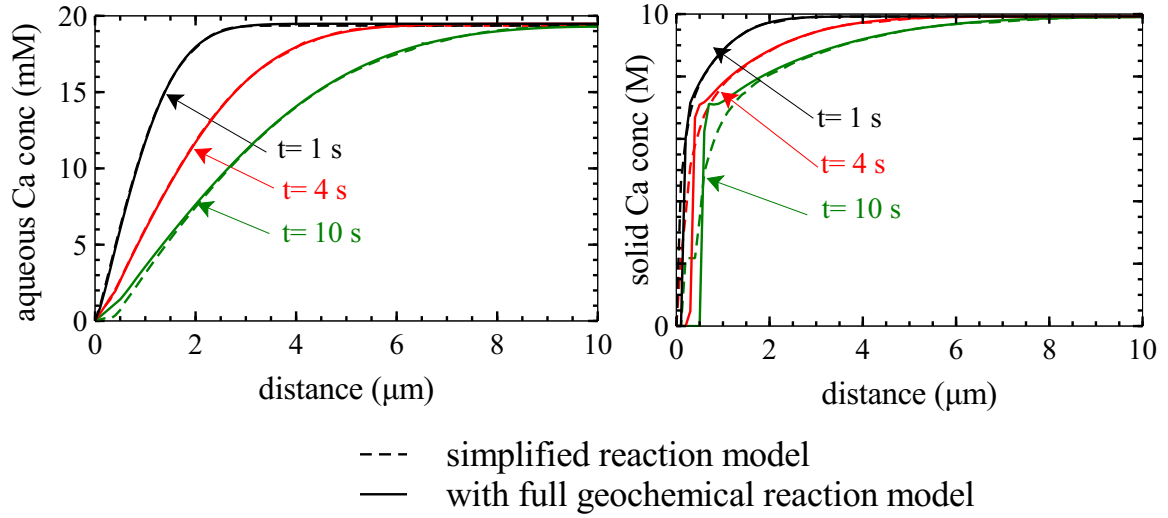
Figure 8.6: C-S-H dissolution benchmark: profiles for Ca concentration in aqueous and solid phases at different times. In this case transport of only Ca considered

8.2.1 Updating of volume fractions due to leaching

As a result of dissolution the C-S-H, an additional pore space is created as a result of which volume fractions of solids in LD C-S-H and HD C-S-H and pore fraction of LD C-S-H and HD C-S-H need to be updated which are inputs for the two-scale C-S-H model presented in section 6.3. To update these volume fractions, additional assumptions are made

I *The fractions of HD C-S-H and LD C-S-H remain unchanged during leaching.* Based on nano-indentation test, Constantinides and Ulm [287] have shown that during leaching the volume fractions of HD C-S-H and LD C-S-H remain unchanged.

II *The degradation rate of LD C-S-H is different from HD C-S-H.* More specifically, LD C-S-H degrades faster than HD C-S-H [287]. Constantinides and Ulm [287] reported an elastic modulus of LD C-S-H and HD C-S-H as 21.7 ± 2.2GPa and 29.4 ± 2.4GPa for sound paste and 3.0 ± 0.8GPa and 12.0 ± 1.2GPa respectively for leached paste. The residual values of elastic modulus thus being 41% and 14% for LD C-S-H and HD C-S-H respectively of the initial ones.

III *The ratio of change in porosity of LD C-S-H and HD C-S-H remains constant during leaching.*

$$\frac{\Delta \phi_p^{LD}}{\Delta \phi_p^{HD}} = R_{LD}^{HD} \tag{8.4}$$

R_{LD}^{HD} denotes the relative change in LD C-S-H porosity with respect to HD C-S-H porosity. Further, by definition the ratio of change in solid fractions of LD C-S-H and HD C-S-H $\left(\frac{\Delta \phi_s^{LD}}{\Delta \phi_s^{HD}} \right)$ is also equal to R_{LD}^{HD}. Assuming that a linear relationship

exists between porosity and elastic modulus as suggested in refs. [196, 288], R_{LD}^{HD} can be determined as

$$R_{LD}^{HD} \approx \frac{\Delta E_{LD}}{\Delta E_{HD}} \approx \frac{21.7 - 3.0}{29.4 - 12.0} \approx 1.075 \tag{8.5}$$

E_{LD} and E_{HD} being the elastic modulus of LD C-S-H and HD C-S-H respectively. This assumption can be verified by carrying out nano-indentation tests on C-S-H with different Ca/Si and if found wrong, should be suitability modified.

The change in the fractions of solids of LD C-S-H and HD C-S-H phases in a C-S-H volume can then be determined as

$$\Delta\phi_{s,HD}^{CSH} = \left(\frac{\Delta\phi_s^{CSH}}{\phi_{HD}^{CSH} + R_{LD}^{HD}\phi_{LD}^{CSH}} \right) \phi_{HD}^{CSH} \tag{8.6}$$
$$\Delta\phi_{s,LD}^{CSH} = \Delta\phi_s^{CSH} - \Delta\phi_{s,HD}^{CSH}$$

Correspondingly the volume fraction of solids of LD C-S-H and HD C-S-H in C-S-H volume can be determined as $\phi_{s,LD}^{CSH} + \Delta\phi_{s,LD}^{CSH}$ and $\phi_{s,HD}^{CSH} + \Delta\phi_{s,HD}^{CSH}$ respectively. The fractions of pores in HD C-S-H and LD C-S-H can be determined as

$$\phi_{p,HD}^{CSH} = \phi_{HD}^{CSH} - \phi_{s,HD}^{CSH}, \qquad \phi_{p,LD}^{CSH} = \phi_{LD}^{CSH} - \phi_{s,LD}^{CSH} \tag{8.7}$$

The porosity of HD C-S-H and LD C-S-H and nitrogen accessible porosity in LD C-S-H can finally be determined as

$$\phi_p^{HD} = \frac{\phi_{p,HD}^{CSH}}{\phi_{HD}^{CSH}}, \qquad \phi_p^{LD} = \frac{\phi_{p,LD}^{CSH}}{\phi_{LD}^{CSH}}, \qquad \phi_{nit}^{LD} = \frac{\phi_p^{CSH} - 2\phi_{p,HD}^{CSH}}{\phi_{LD}^{CSH}} \tag{8.8}$$

8.3   Results and Discussions

Simulations of leaching due to deionized water were carried out on the microstructures generated from HYMOSTRUC and CEMHYD3D for OPC with composition used by Kamali *et al.* [14] (Bogue's composition: 73.4%, 10.3%, 3.9% and 5.8% for C_3S, C_2S, C_3A, C_4AF respectively) who carried out leaching experiments with deionized water. Simulations were carried out for two different w/c viz., 0.25 and 0.4. The size of the generated microstructure was taken as 65 μm $\times$ 65 μm $\times$ 65 μm which is smaller than the REV (100 μm $\times$ 100 μm $\times$ 100 μm) used for diffusion computations, however it still represents a reasonable size[2]. The microstructures generated were hydrated for up to 3 months (similar to curing time used in experiments) before subjecting to leaching. To simulate leaching, a additional layer of nodes which represent the leaching fluid is added to

---

[2]Similar size has been determine has been determined as REV for Hain *et al.* [186]. See section 5.5 on discussion on REV.

left side of the simulation domain. The concentration of both Ca and Si at this boundary are set to zero to represent deionized water. All other boundaries are set as zero flux boundaries. Simulations were carried out for 800 s.

Fig. 8.7 shows the evolution of average Ca in the aqueous phase, solid phase, C-S-H and portlandite content with time. As expected, the cement paste with w/c equal to 0.4 undergoes faster leaching because of its higher initial diffusivity and capillary porosity compared to cement paste with w/c equal to 0.25. Fig. 8.7 also shows that irrespective of the integrated kinetic model or w/c, the relative (with respect to initial content) amount of protlandite dissolved is much more compared to the amount of Ca leached from C-S-H. Hence leaching of portlandite is often considered more significant in some models and is also commonly observed in experiments (see chapter 7). Further from Fig. 8.7, it can be clearly seen that the microstructure generated from HYMOSTRUC undergoes higher leaching compared to CEMHYD3D. This is due to the fact that HYMOSTRUC generated microstructures exhibits lower percolation threshold for capillary pores compared to CEMHYD3D (as discussed in section 6.5).

Fig. 8.8 shows the profiles of average Ca concentration in solid phase, C-S-H and portlandite content at the end of 800 s. Leaching clearly leads to the formation of distinct zones viz., intact zone (where no leaching has occurred), transition zone (where portlandite is partially dissolved) and zone where portlandite is completely dissolved and C-S-H has considerably dissolved. Fig. 8.8 further shows that in the transition zone, the leaching of C-S-H is also initiated. The presence of portlandite and partially leached C-S-H has been found experimentally through SEM images by Phung [8] (see Fig. 7.2). In a well-mixed system at thermodynamic equilibrium, C-S-H leaching only initiates after the portlandite is completely dissolved. However in the cement paste microstructure, portlandite grains can also be embedded in the C-S-H matrix and C-S-H can leach first. Hence the presence of portlandite and partial leaching of C-S-H is plausible in the transition zone due to the morphological characteristics of cement paste. Fig. 8.8 also shows that the transition zone is much wider for w/c equal to 0.25 than 0.4 irrespective of the integrated kinetic models use to generate microstructure. For w/c of 0.25 the transition zone is found from around 0 μm to 30 μm for CEMHYD3D and around 5 μm to 40 μm for HYMOSTRUC. For w/c of 0.4 the transition zone ranges from around 30 μm to 45 μm for CEMHYD3D and 30 μm to 50 μm for HYMOSTRUC.

Fig. 8.9 shows the porosities profiles at 800 s. From Fig. 8.9 and Fig. 8.8 it can be inferred that, for w/c of 0.25, alterations in microstructure has occurred upto 30 μm and 40 μm for CEMHYD3D and HYMOSTRUC respectively. Similarly for w/c of 0.4, alterations in microstructure has occurred upto 45 μm and 50 μm for CEMHYD3D and HYMOSTRUC respectively. From the leaching kinetic parameters determined by Kamali *et al.* [14] (as summarized in table 7.1) the depth of the leaching front can be determined as 7.2 μm and 13.45 μm for w/c of 0.25 and 0.4 respectively after 800 s. The leaching depth in the
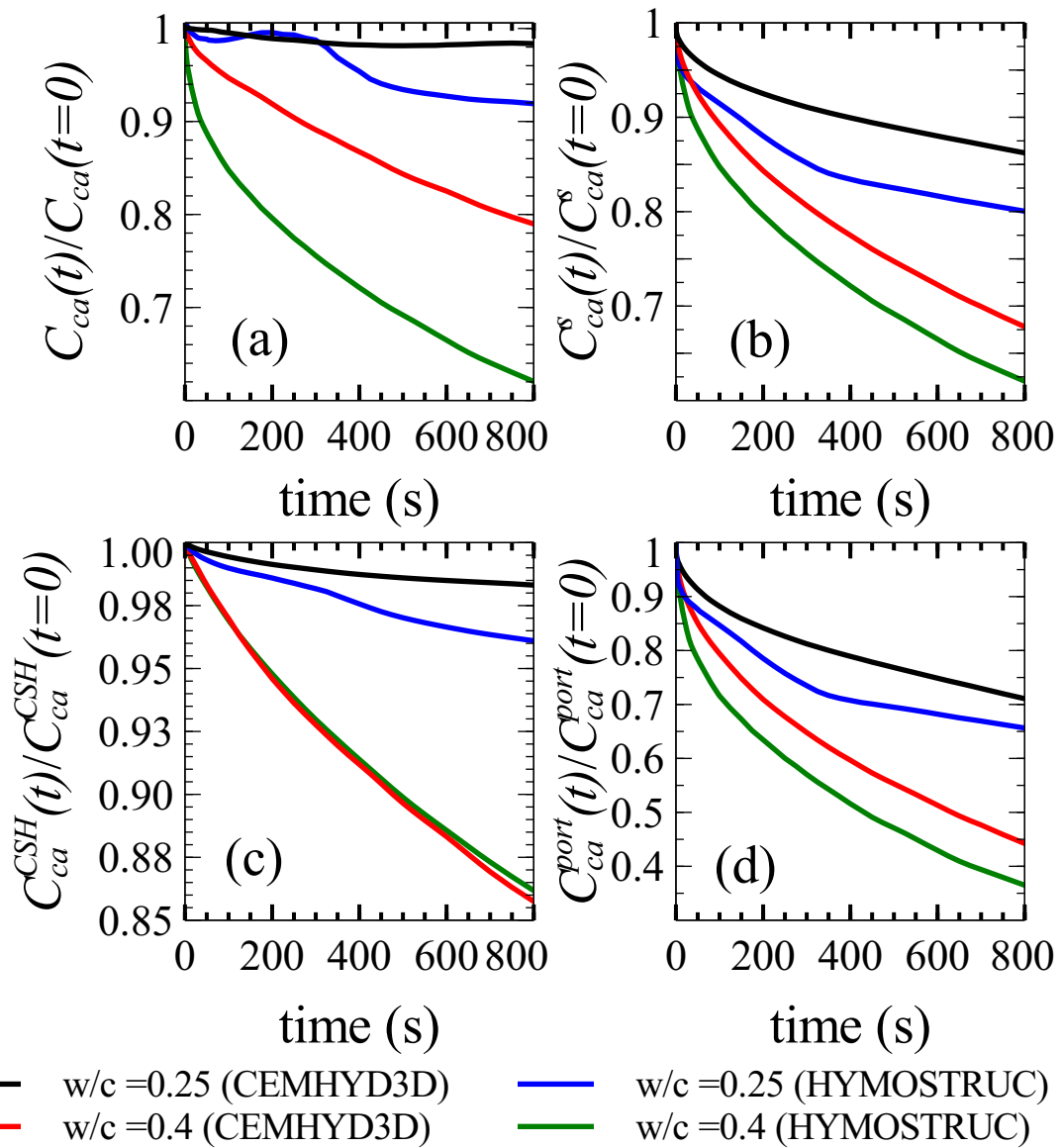
Figure 8.7: Evolution of (a) average total calcium concentration in aqueous phase (b) average total calcium concentration in solid phase (c) average calcium concentration in C-S-H phase (d) average portlandite content over time.
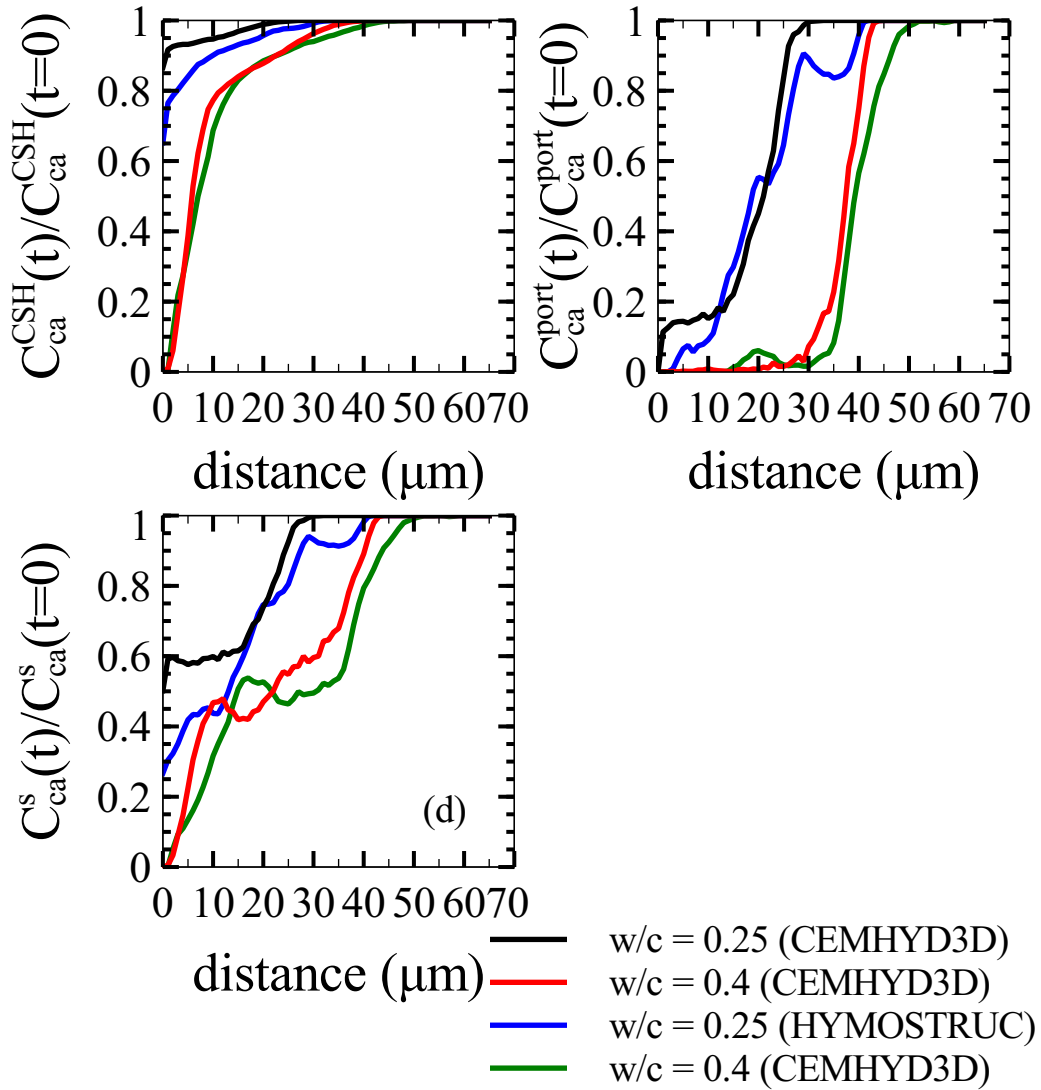
Figure 8.8: Profiles of (a) average Ca concentration in C-S-H phase (b) average portlandite content (c) average Ca concentration in solid phase at the end of 800 s. Average is taken over the plane perpendicular to direction of leaching.
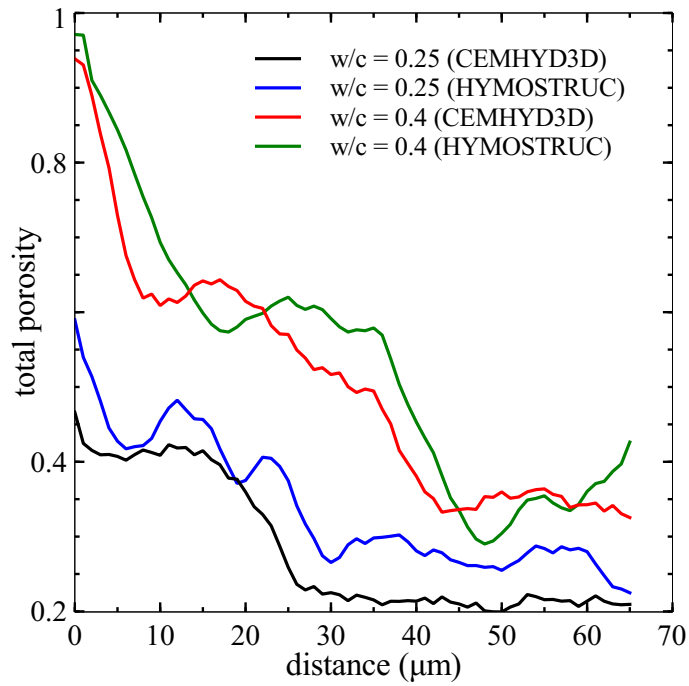
Figure 8.9: Average total porosity profile at the end of 800 s. Average is taken over the plane perpendicular to direction of leaching.
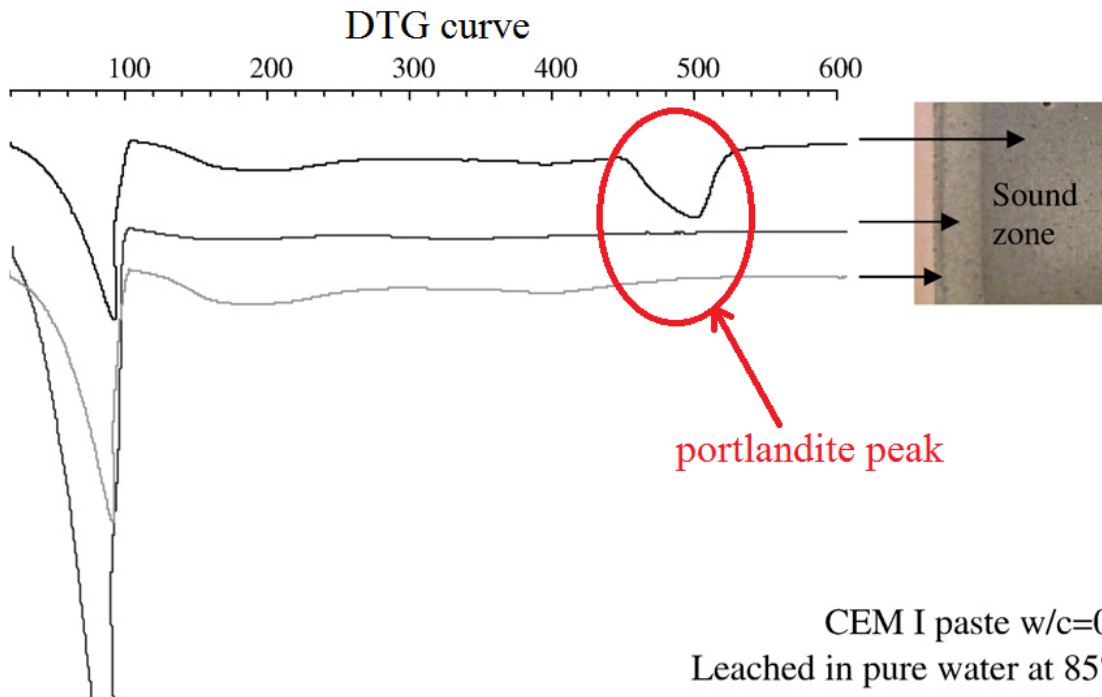
Figure 8.10: Example of cement paste sample along with corresponding TGA results after leaching (adapted from Kamali *et al.* [14]).

(a)

(b)
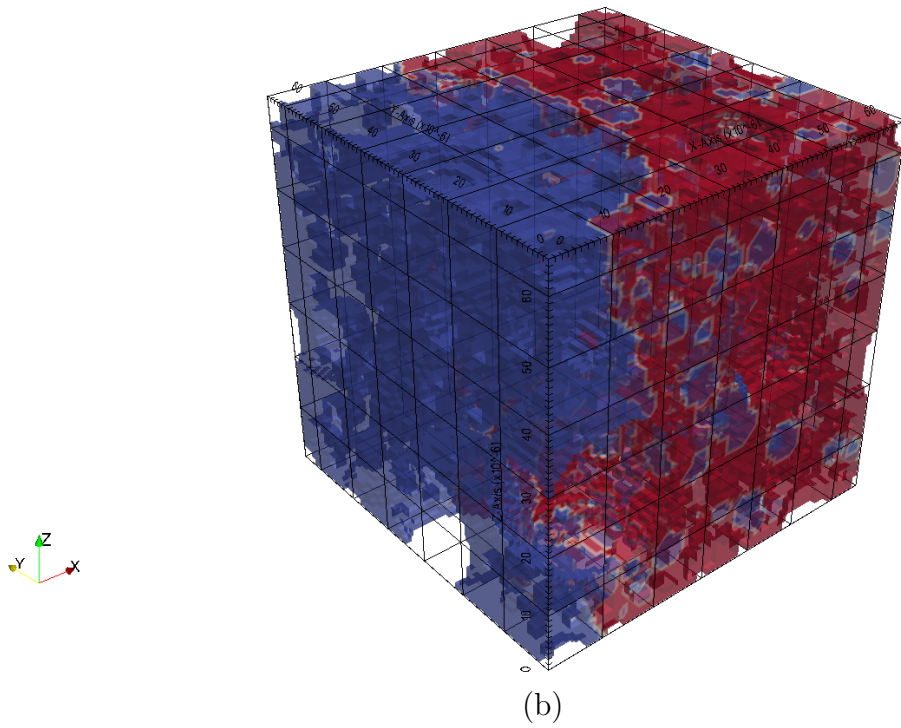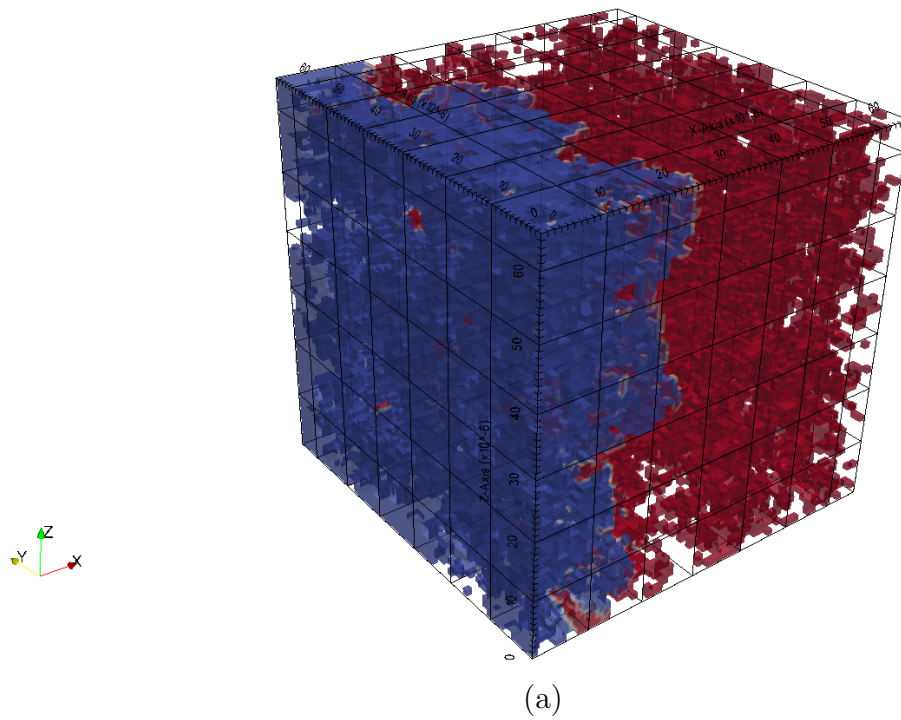
Figure 8.11: Three dimensional veiw of Ca front for w/c=0.25. Region in red and blue represents region with Ca $\geq$ 19mM and Ca $<$ 19mM respectively. a) CEMHYD3D b) HYMOSTRUC
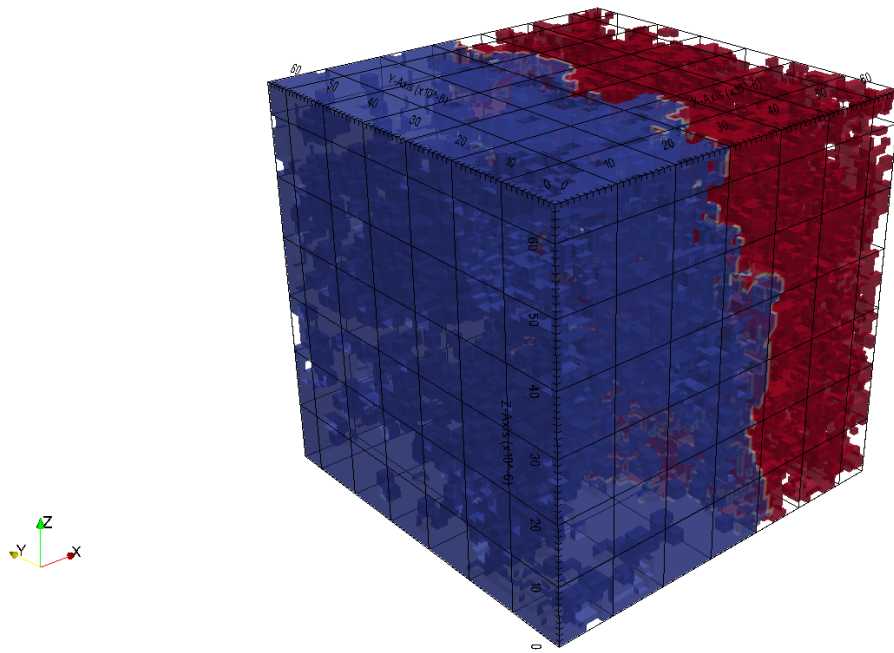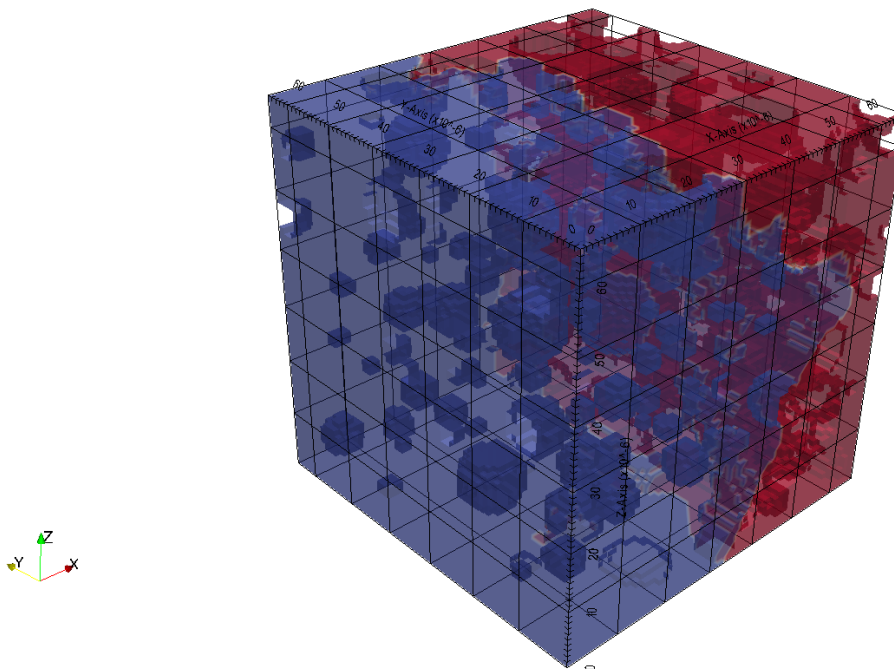
Figure 8.12: Three dimensional veiw of Ca front for w/c=0.4. Region in red and blue represents region with Ca $\geq$ 19mM and Ca $<$ 19mM respectively. a) CEMHYD3D b) HYMOSTRUC
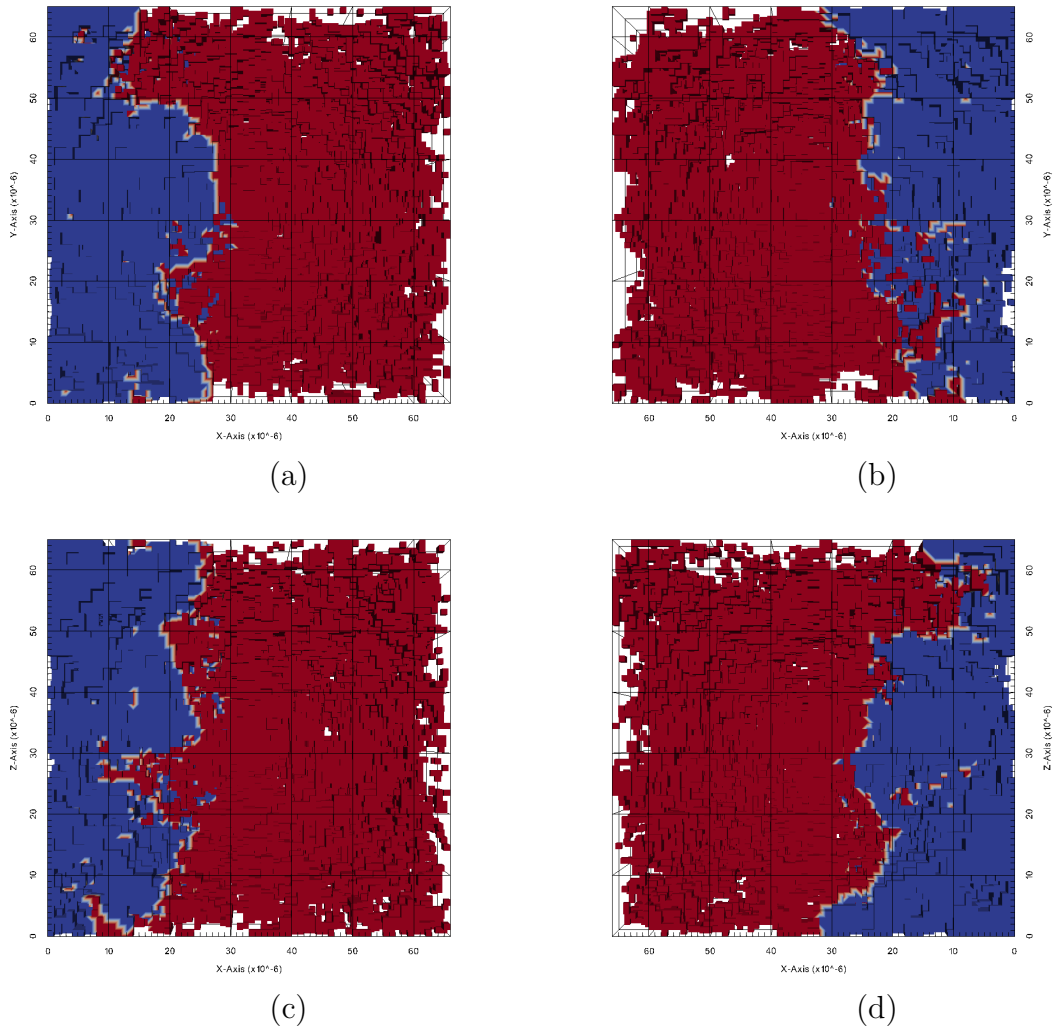
Figure 8.13: Ca front for w/c=0.25 CEMHYD3D microstructure. Region in red and blue represents region with Ca $\geq$ 19mM and Ca $<$ 19mM respectively. a) back view b) front view c) bottom view d) top view
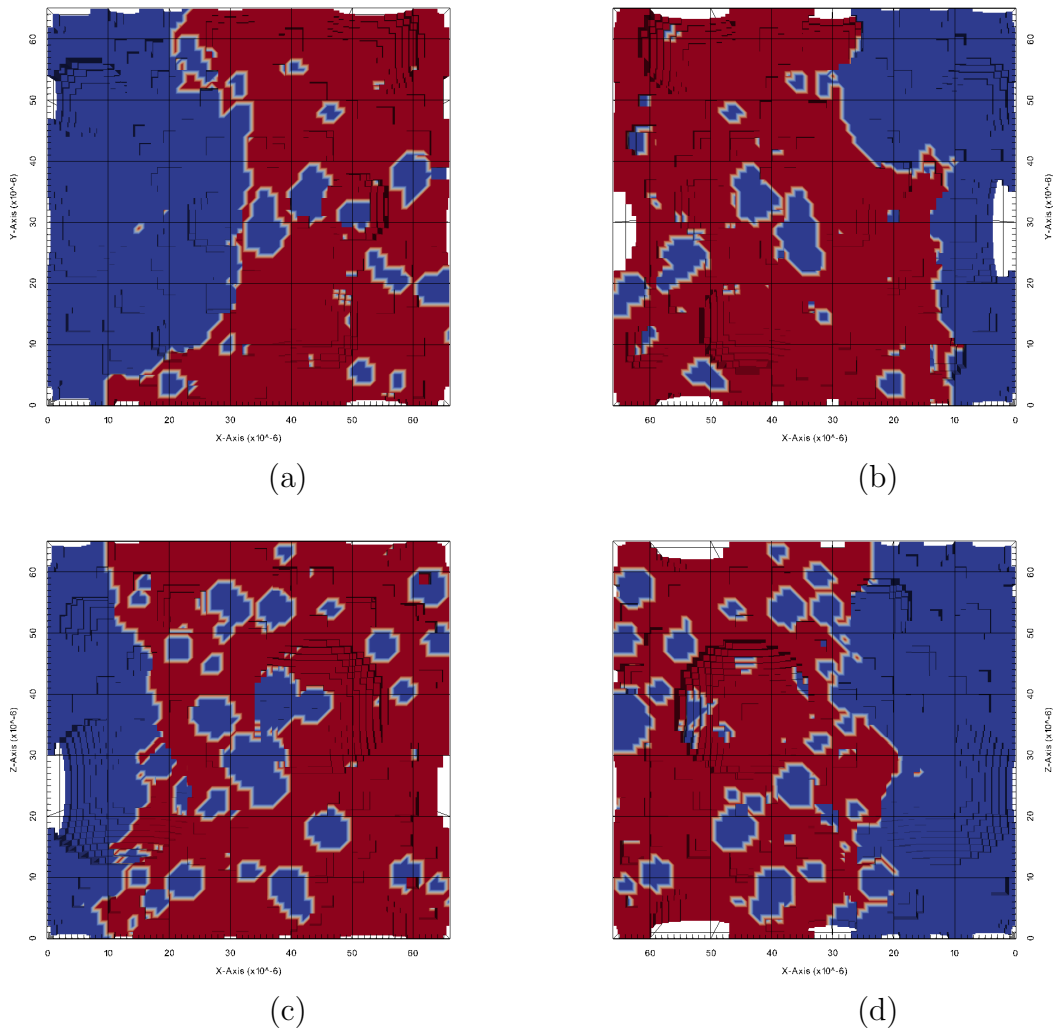
Figure 8.14: Ca front for w/c=0.25 HYMOSTRUC microstructure. Region in red and blue represents region with Ca $\geq$ 19mM and Ca $<$ 19mM respectively. a) back view b) front view c) bottom view d) top view
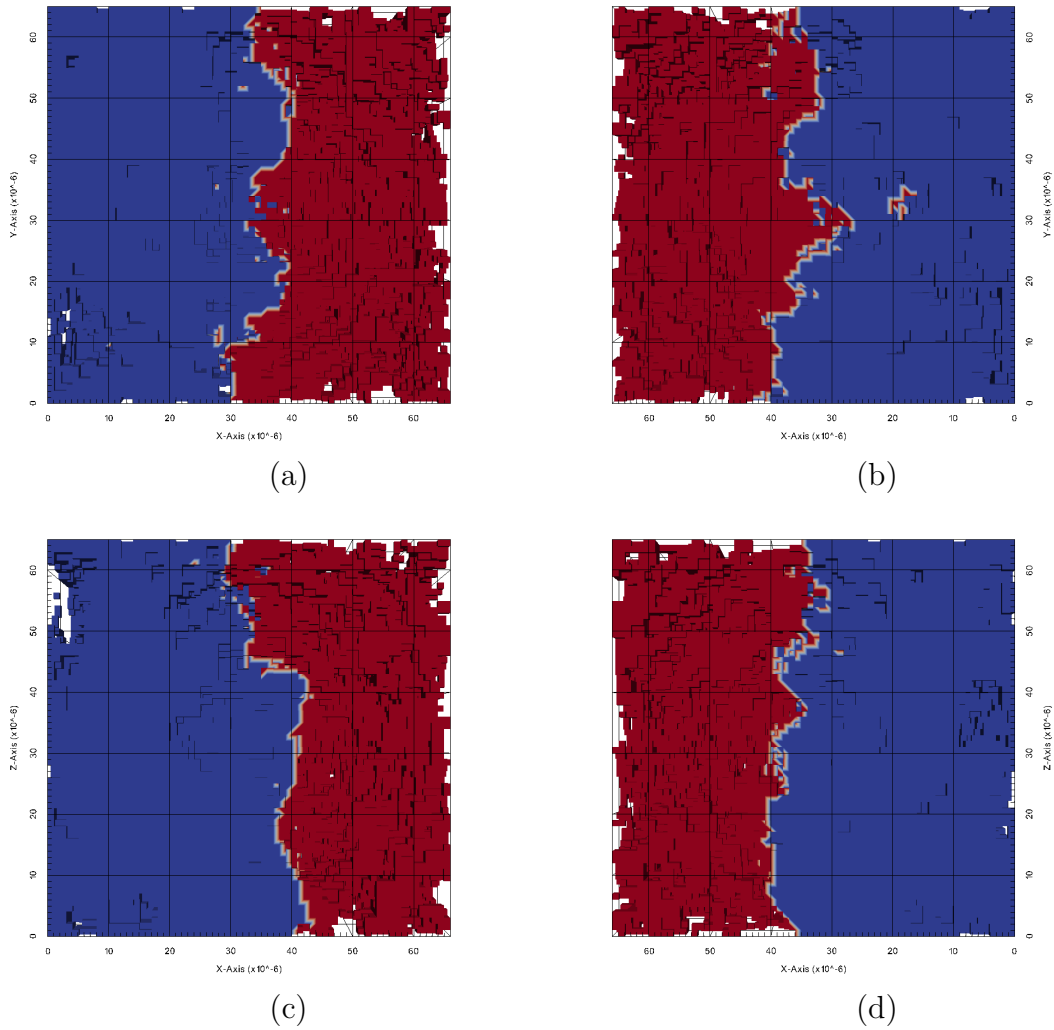
Figure 8.15: Ca front for w/c=0.4 CEMHYD3D microstructure. Region in red and blue represents region with Ca $\geq$ 19mM and Ca $<$ 19mM respectively. a) back view b) front view c) bottom view d) top view
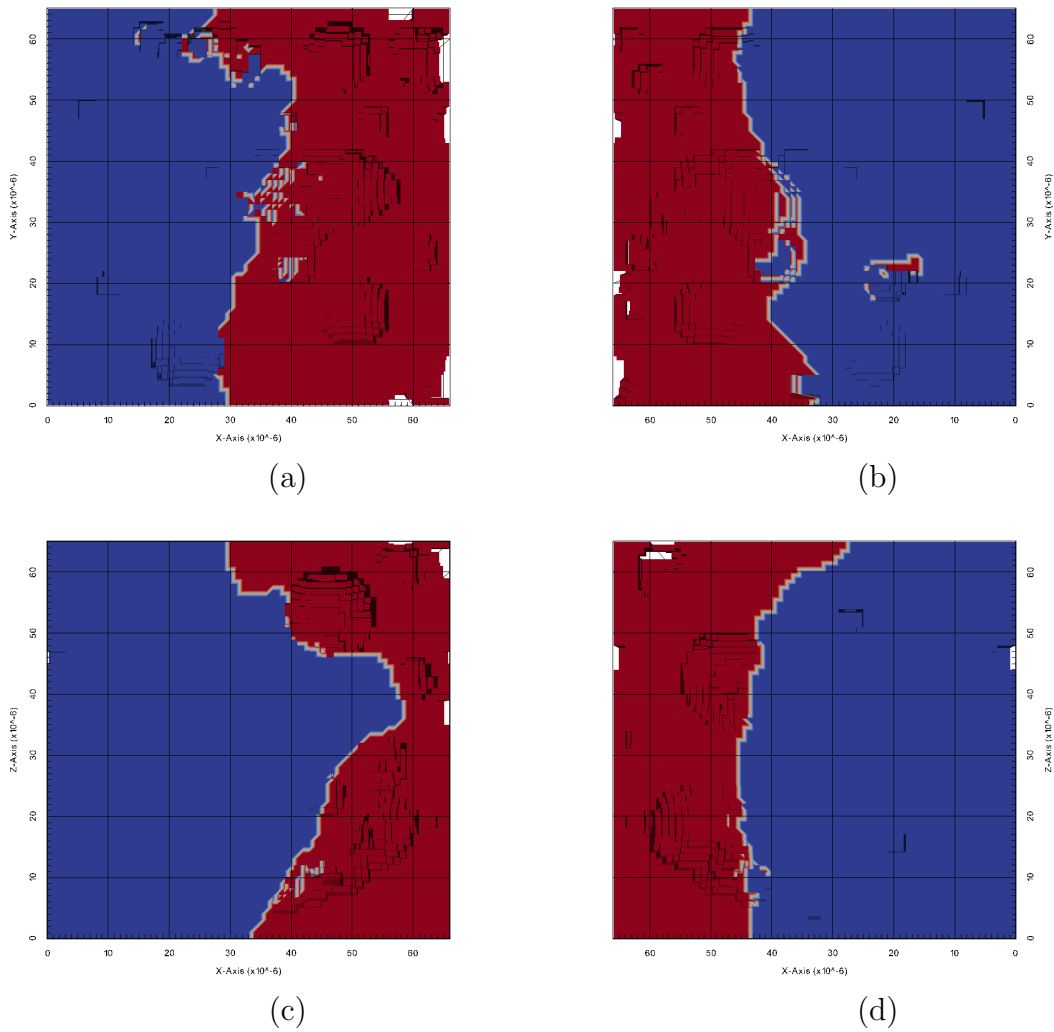
Figure 8.16: Ca front for w/c=0.4 HYMOSTRUC microstructure. Region in red and blue represents region with Ca $\geq$ 19mM and Ca $<$ 19mM respectively. a) back view b) front view c) bottom view d) top view

work of Kamali *et al.* [14] was determined visually. Fig 8.10 shows the leached sample obtained from the experiments of Kamali *et al.* [14] where the leached zone can be clearly distinguished from unleached zone. The TGA analysis further supports that the leached zone does not contain portlandite, thus suggesting that the leaching depth determined form their experiment corresponds to portlandite dissolution front. The experimental leaching depth thus closely corresponds to the depth that mark beginning of the transition zones in the microstructure simulation. From Fig. 8.8 it can be seen that the beginning of the transition zone is roughly marked at around 0 μm and 3 μm for CEMHYD3D and HYMOSTRUC respectively for w/c of 0.25 and around 25 μm and 30 μm for CEMHYD3D and HYMOSTRUC respectively for w/c of 0.4 which is more closer to the experimental values. This relatively large (compare to the size of the simulation domain) transition zone observed in simulations might be due to small size of REV used for this simulations. In future detailed analysis of REV for leaching should be carried out. Fig. 8.11 - Fig. 8.16 shows the leaching fronts which differentiate the zones where the Ca concentration is aqueous phase < 19 mM and $\geq$ 19 mM. These figures clearly show that for this size of REV large undulations are observed in the front.

8.4 Conclusions

In this chapter an efficient model has been developed to simulate leaching through cement paste microstructure. The efficiency of this simplified model is achieved firstly by development of a new adaptive relaxation scheme which allows to have larger time steps while keeping errors within certain bounds and secondly by replacing the geochemical computations with precomputed relationships implemented in the form of a look up table. The simplified model only considers transport of two components viz., Ca and Si. The comparison with the reactive transport model coupled with the geochemical solver confirms the accuracy of the simplified model. Further it was found that the commonly used approach, wherein only transport of Ca is considered was unable to capture the profile in the initial part of the domain where considerable leaching has occurred. Thus transport of both Ca and Si was found to be essential. The two-scale diffusion model for C-S-H has been further extended for leaching. Certain heuristic assumptions were to made to update the volume fractions of pores in LD C-S-H and HD C-S-H onsite of leaching. Further detailed experimental investigation might be necessary to confirm or modify these assumptions.

The developed model was used to simulate leaching from the microstructure of OPC paste with two different w/c viz. 0.25 and 0.4. It was found that the cement paste with the higher w/c undergoes more leaching. The relative amount (with respect to initial) of portlandite dissolved is much higher compared to the calcium leached from the to C-S-H for both w/c. It was further observed that HYMOSTRUC generated microstructures

undergoes more leaching compared to CEMHYD3D. This is due to the fact that the capillary pores percolation threshold for HYMOSTRUC is much lower compared to CEMYHD3D as a result of which capillary pores are dominant phase for transport in case of HYMOSTRUC. Formation of distinct zones viz., an unleached intact zone, a trasition zone where portlandite is partially leached and a zone where portlandite is fully leached and C-S-H undergoes considerable leaching was observed in the leached microstructures. In the transition zone portlandite is partially leached and initiation of leaching of C-S-H is observed. Thus unlike common presumption, the leaching of portlandite and C-S-H can occur at the same time. Bigger transition zones are observed for lower w/c. The leaching depth observed (depth till the intact zone) was much larger compared to values determined from experiments. However, the leaching depth obtained from experiment closely correspond to depth marking the beginning of transition zone. The reason for the difference in experimental observation and simulation can be the large width of the transition zone as a result of which sharp front was not observed in the simulations. This in turn might be associated with the small size of microstructure used in this study. In future an REV analysis for leaching should be carried out in order to determine the appropriate size of REV needed for leaching simulations.

Retrospection, Conclusions and Way forward

9.1   Retrospection

As highlighted in the introduction of this thesis, the specific need for this project arose from the necessity to understand how concrete would age over a very long period of time in a near surface Belgian nuclear waste disposal system. Due to the large time scale involved and the slow nature of physio-chemical processes which degrade concrete, it is extremely difficult to experimentally study the process of ageing. As a result a need for a *computational suite* which can simulate the changes in morphology due to ageing was identified. Indeed the altered morphology generated from this model can be further used to estimate changes in properties due to ageing and hence such a tool could prove to be a useful *virtual probe* to investigate ageing processes.

Based on this view point the specific objectives of this thesis were identified viz., to develop a numerical framework that is able to simulate changes in morphology due to physico-chemical processes and to apply this framework to first predict the diffusivity of cement paste and secondly to simulate the leaching process. The prediction of diffusivity of cement paste further requires development of the description of C-S-H diffusivity based on morphological parameters. The prediction of diffusivity with a reasonable accuracy is essential as it defines the susceptibility of the cement paste to undergo physico-chemical degradation. It is also regarded as an important parameter in service life prediction of concrete structures. The leaching process is one of the important detrimental processes to be considered for the service life assessment of the structures are in contact with water or can come in contact with water such as ear surface Belgian nuclear waste disposal system. Further due to its slow nature, very few studies exists on the influence of leaching on the properties (especially transport properties) of cement paste. Hence the successful

demonstration of the ability of the developed framework to simulate leaching can pave a way forward to develop a comprehensive knowledge on influence of leaching on the properties of the cement paste.

In order to achieve these goals a lattice Boltzmann (LB) method based framework was developed in this study. The developed framework can simulate mass transport and reactive transport processes through the pore-scale and multilevel systems. Specific developments were made in field of LB methods viz., development of a local second order convergent generalized boundary condition for advection-diffusion equation, development of a new PID based relaxation scheme to allow for higher time-step while keeping errors in check and a new diffusion velocity LB scheme which allows to fix the relaxation parameter to a value that best suites the stability and accuracy while allowing for variability of both the time step and spatial heterogeneity of diffusion coefficients. A consistent approach was developed to link LB schemes with external geochemical solver wherein heterogeneous reactions are treated as pseudo-homogeneous reactions. This approach allows to account for heterogeneous reactions and homogeneous reaction in same way which made coupling of LB scheme with the external geochemical solver *PHREEQC* possible using sequential non-iterative approach. The developed framework has been implemented in a newly developed LB method based multi-physics tool called *Yantra*.

To achieve the second goal of obtaining *reliable* prediction of diffusivity of cement paste, a new two-scale diffusivity model of C-S-H based on effective media theory has been developed. This model has been further extended to account for leaching. This model along with the LB framework to simulate mass transport and microstructures generated from integrated kinetic models presents a tool to explore the role of morphology and pore spaces in cement paste on diffusivity. Finally in order to simulate leaching, a simplified model has been developed which considers transport of only Ca and Si components and the reaction of C-S-H in this model was implemented as a look up table. This approach has the same level of accuracy as the transport model coupled with the geochemical solver however, it reduces the computational times from days to minutes. This made the simulation of the reactive transport processes (resulting in dissolution of portlandite and decalcification of C-S-H) due to calcium leaching through the microstructure of reasonable size feasible.

9.2   Conclusions

The main conclusions that can be drawn from the work carried out in this thesis are summarized below —

- LB method provides an efficient numerical framework to simulate mass transport and reactive transport processes through a pore-scale and multilevel systems. The voxelized pore structures generated from integrated kinetic models or computed tomography can be used as an direct input in the LB methods.

- The pseudo-homogeneous treatment of heterogeneous reactions, even though slightly less accurate compared to the conventional approach to treat boundary conditions, presents an ability to treat both homogeneous and heterogeneous reactions in the same way thus allowing the use of a single source/sink term. This allows for coupling of the LB method and an external geochemical solver.

- A series of simple examples highlighting the influence of parameters such as solution composition, surface area and spatial arrangement of mineral phases on dissolution of fictitious portlandite grain reveals that, under diffusive transport conditions and a thermodynamic equilibrium approach, different initial pH conditions do not influence the overall reaction rate (time needed to reach equilibrium is the same). However, lower pH values increase the amount of dissolved portlandite resulting in smaller grains at the end of simulation. Further, spatial arrangement of mineral grains is more important than the surface area. The spatial arrangement of grains may cause local equilibrium in certain parts of the domain inhibiting local dissolution processes at the grain surface.

- From the study of influence of pore network on portlandite dissolution, four cases consisting of random porous media with same portlandite fraction but differing in particle sizes or total porosity (by introducing inert material), it was observed that for diffusion controlled dissolution the tortuosity and the porosity of the porous media have a more pronounced effect compared to particle size and surface area.

- Using the developed two-scale model for C-S-H diffusivity, the LB scheme and integrated kinetic models, it is possible to estimate the diffusivity of cement paste within the uncertainty band defined by the experimental results complied from literature.

- It was found from the wide range of experimental data complied from literature, that relative diffusivity measured by electrical resistivity is always higher compared to through-diffusion techniques (measured using HTO or dissolved gases as tracer). Using the two-scale model for diffusivity, it was found that this difference is due to different contribution of gel pores. In case of the tracers such as HTO, dissolved helium and dissolved oxygen, transport occurs through nitrogen accessible gel pores (present in LD C-S-H) whereas for electric resistivity measurements all gel pores contribute resulting in higher measurements for electric resistivity. This observation can be used in future to establish the link between diffusivity of tracers and electric resistivity [1].

- The influence of the shape of C-S-H elementary bricks on relative diffusivity is only visible at very low w/c (i.e. w/c = 0.25 and 0.3). For varities of shapes (except disks)

---

[1]Electric resistivity is easy to measure and often used as non-destructive in-situ technique.

the predicted values for low w/c lies within factor of 2 bounds. Therefore, it can be presumed that the shape of C-S-H elementary bricks may not be of importance for transport properties.

- By comparison between different integrated kinetic models, it was found that the diffusivity predicted from microstructures generated from HYMOSTRUC (a vector based hydration model) is always higher compared to that from CEMYHD3D (a voxel based hydration model). These differences are more pronounced for low to moderate w/c and diminishes at higher w/c ratios. Further when difference of diffusivity between C-S-H phase and capillary pores is less (i.e. electric resistivity experiments) the differences between diffusivity predicted from microstructures generated from HYMOSTRUC and CEMHYD3D is less. The reason for these differences is due to the very low percolation threshold for HYMOSTRUC. In case of HYMOSTRUC, even at porosity as low as 5%, 65% of the capillary pores are connected, whereas in case of CEMHYD3D a complete depercolation is observed at porosity lower than 18%. Similarly in case of leaching, the microstructure generated from HYMOSTRUC undergoes more leaching compared to CEMHYD3D.

- Using the simplified model developed for leaching it is possible to simulate the leaching through microstructures of reasonable size. Qualitatively correct microstructures of the leached sample can be obtained from the developed model.

- From simulations of leaching carried out on microstructures of cement paste, it was observed that cement paste with higher w/c undergoes more leaching. The relative amount (with respect to initial) of portlandite dissolved in much higher compared to the amount of calcium leached from C-S-H. Further, leaching leads to formation of distinct zones viz., an intact unleached zone, a transition zone where protlandite is partially leached and a zone where protlandite is fully leached and C-S-H undergoes considerable leaching. In the transition zone, the initiation of leaching of C-S-H was also observed. Thus unlike common presumption, the leaching of portlandite and C-S-H can occur together at the same time. Bigger transition zones are observed for lower w/c. The leaching depth observed (depth till the intact zone) was much larger compared to the values determined from experiments. However, the leaching depths obtained from experiments closely correspond to depth marking the beginning of transition zone. The reason for the difference in experimental observation and simulation can be the large width of the transition zone as a result of which a sharp front was not observed in the simulations. Further simulations with larger microstructures can be carried out in future in order to reduce the width of transition zone (in terms of overall sample size) and to achieve sharp front.

9.3 Way forward

In this thesis for the first time (as per the author's knowledge) the simulation of leaching through the microstructure of cement paste considering both reaction and transport processes have been achieved. This in turn is a first step towards the development of a computational suite that can simulate physico-chemical changes occurring in cement paste during ageing and the development of multi-scale, multi-physics approach to mimic the ageing of concrete. In order to further attain this goal following aspects need to be addressed in future

- The algorithms implemented in *Yantra* can be also be used to investigate the role of ITZ in the leaching of mortar and to develop an suitable upscaling framework for leaching of concrete.

- Changes in microstructure due to other physico-chemical processes such as carbonation, sulphate attack, occurring during the ageing of concrete can be explored with the developed framework.

- The approach of pre-tabulating geochemical computations provides a lucrative alternative to transport solver coupled with thermodynamic calculations and can be further explored for other reaction networks commonly encountered in the ageing of concrete (such as sulphate attack, carbonation).

- To extend the developed approach to variably saturated porous media. Indeed, in most cases concrete is under saturated and hence this is an essential extension in future. Variable saturation is also important to simulate degradation processes such as carbonation which are often studied in experiments at unsaturated conditions (60-70% relative humidity).

- For ion transport electro-kinetic effects can be important and hence a transport solver accounting for electro-kinetic effects (Nerst-Planck equation solver) should be implemented in future in *Yantra* and further coupled with *PHREEQC*.

- The capabilities of *Yantra* should be further extended to include/couple different physics such as thermal transport, mechanics (fracture propagation) and water flow. Depending on the applications, these different physics may play a crucial role in simulating aging of concrete.

- At present there is very little information on constrictivity of cement paste and hence experiments focusing on the study of constrictivity parameter are needed to better predict transport of different ions or tracers. The constrictivity effects can also be studied by coupling molecular dynamics simulations with single pore transport simulations (see for instance [289, 290]).

- Heurstic assumptions have been made in this thesis with regard to how the phase fractions of LD C-S-H, HD C-S-H and pores in LD C-S-H and HD C-S-H evolve during leaching. Further experimental investigation on nano-indentation tests and BET tests at different Ca/Si ratio of C-S-H can provide more insights into the changes of these volume fractions (see for instance [15, 248]).

A

Yantra: A lattice Boltzmann method based tool for multi-physics simulations in hetergoenous porous media

---

The algorithms presented in this thesis have been implemented in a newly developed lattice Boltzmann method based framework for multi-physics simulation named as *Yantra* (in sanskrit it means a tool or a device). The outline of *Yantra* framework is shown in Fig. A.1. The object oriented framework of *Yantra* is implemented in *Python* with computationally intensive tasks and LB solvers implemented in *FORTRAN*. Python also act as a communicator between two different solvers (e.g. LB solver and *PHREEQC*). At the heart of *Yantra* lies three main modules *preprocessor*, *physics* and *postprocessor* which users can use to define their model. The *preprocessor* module provides two objects *mesh2d* and *mesh3d* which can be used to generate 2d or 3d domain respectively. The the most important variable in mesh class is the array called *nodetype* which marks whether the node is treated as solid or liquid. The nodes with *nodetype* values less than or equal to zero are treated as liquid nodes and greater than zero are treated as solid nodes. The *nodetype* can take any value and can be used as in indicator to differentiate between different material types. Further this objects contain specific methods to import microstructures from integrated kinetic models or to mark simple shapes such as sphere, circle, rectangle or a box in the *nodetype* array with a specific indicator value. These objects are initialized by specifying domain bounds (rectangle in case of 2D and box in case of 3D). The *mesh2D* and *mesh3D* objects are weakly associated to physics.

physics module contain specific kernels to solve certain type of physics. physics module is further divided into *continuum*, *pore* and *multilevel* referring to solver solving physics at continuum scale, pore scale or multilevel scale respectively. At present in *pore* and *multilevel* modules their exists two physics implementations viz., *transport* and *reactivetransport*.
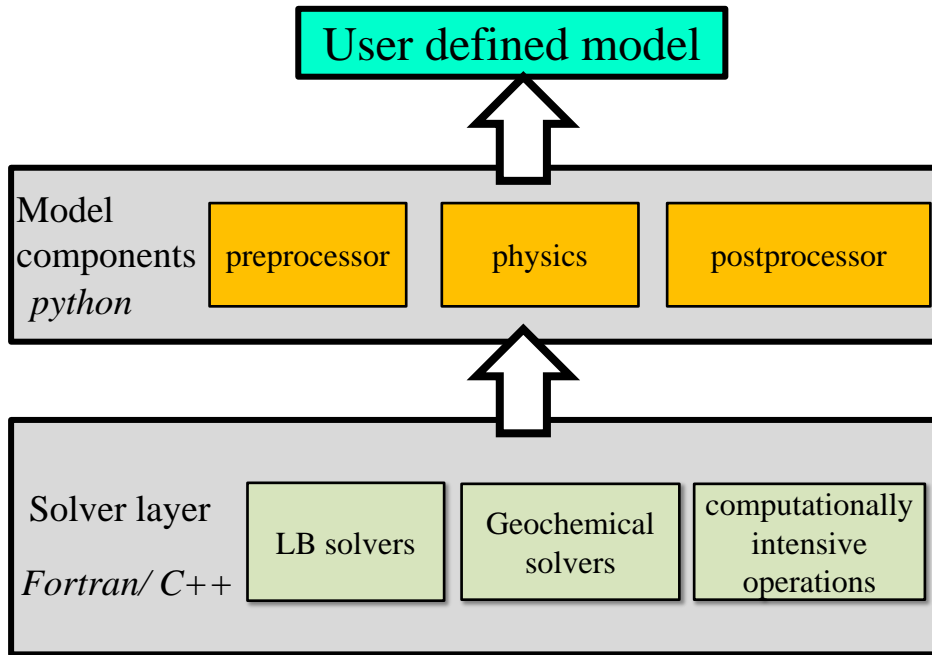
Figure A.1: Outline of *Yantra* framework

The *transport* module contains solvers to solve advection-diffusion and diffusion equation whereas *reactivetransport* module contain transport solver coupled with phreeqc and simplified models. The initialization of any object in *physics* class requires passing of instance of mesh object, a dictionary data structure for domain parameters and a dictionary data structure for domain boundary conditions. Default initialization of different parameters have been implemented for users not familiar with LB schemes and sanity check on initialization are incorporated to avoid erroneous input. Additional parameter required to initialize physics object are *blocksize* and *nprocs*. The LB solvers are implemented with a blocking scheme[1] to make it *cache efficient* and *blocksize* can be used to specify the size of the block. The implementation of LB solvers includes *openMP* directives and *nprocs* can be used to specify the number of threads (processors) to be used. The collision step in LB solvers have been further optimized[2]. The streaming step is implemented using swap technique to avoid need for two different copies of distribution functions [76]. The association of mesh object instance to physics object instance can be further exploited to parallelize a simulation on a multi-core architecture using message passing interface (MPI). The parallelization of *Yantra* physics instance using MPI has been demonstrated but is not included in the current version.

Post-processing of results can be carried out using *Matplotlib* [291] a python library in case of 2D plots. For 3d post-processing output can be obtained from *Yantra* in *vtk* format which can be visualized in Paraview [292]. The *postprocessor* module at present

---

[1]The idea of the blocking scheme is to divide data into chunks that can fit the L1 cache.
[2]The collision term is expanded in order to reduce the number of floating point operations
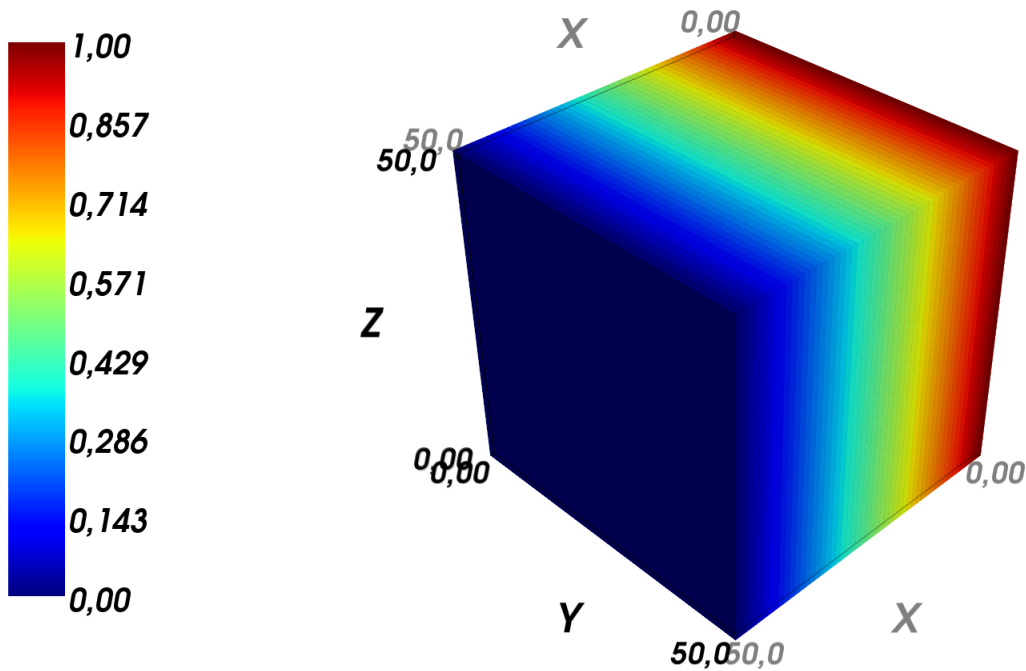
Figure A.2: Output of *Yantra*

contains a *plot3d* module which is a wrapper written on top of *Mayavi2* library [293], which provides basic three dimensional visualization functionality. *Yantra* requires only one time compilation which can be carried out with automatic setup file accompanied with it. For installation *Yantra* requires python 2.6 or higher distribution, a *FORTRAN* compiler and python packages viz., *SciPy* and *NumPy*. This packages can be installed using a full python installer such as *Python (x,y)* [294]. All the implementations of *Yantra* are accompanied with series of benchmarks. At present around 20 benchmarks are included with *Yantra*. To develop a model in *Yantra* first a mesh instance is created and then a physics instance is created. The simulation can be ran up to require time using *run* method in physics instance. The example code for a simple model to simulate the a diffusion in 3D domain is given below and the output of the code is plotted in Fig. A.2

```
1   """
2   An example code to create a model in Yantra
3   """
4   import Yantra #imports Yantra
5   #------lets begin with creating instances of this objects--------
6   #mesh instance
7   #50x50x50 domain with 1 as dx
8   m = Yantra.preprocessor.mesh3d(0, 50, 0, 50,  0, 50,1, loc='nodal')
9   #physics instance
10  dp ={'D':1./6.} #diffusion coefficient taken as 1/6
```

```
11  bc ={'left':['conc' ,1.0],
12      'right':['conc',0.0],
13      'top': ['flux',0],
14      'bottom':['flux',0],
15      'front': ['flux',0],
16      'back':['flux',0],
17      } #left and right as concentration boundary and all other are flux boundaries
18  #use SRT D3Q7 LB solver for diffusion equation
19  physics= Yantra.physics.pore.transport.diff.SD3Q7
20  p = physics(m,dp,bc,8) #number of processors taken as 8
21  p.run(tf=5000) #final time for run as 5000
22  #plotting simulation
23  #get x,y,z co-ordinates
24  x,y,z=m.get_coordinates()
25  Yantra.postprocessor.plot3D.contour3d(x,y, z, p.conc ,m.nodetype, m.dx)
```

From Boltzmann equation to lattice Boltzmann equation

Lattice Boltzmann method can be derived by discretizing Boltzmann equation in terms of directional velocity [295, 296]. The Boltzmann equation is given as follows

$$\frac{\partial f}{\partial t} + \vec{e} \cdot \vec{\nabla} f = \Omega \tag{B.1}$$

where f is the distribution function $[\text{NL}^{-3}]$, $\vec{e}$ is the directional velocity $[\text{L}^1, \text{T}^{-1}]$ and Ω represents the collision term. Discretizing Boltzmann equation in terms of directional velocity gives

$$\frac{\partial f_i}{\partial t} + \vec{e_i} \cdot \vec{\nabla} f_i = \Omega_i, \qquad i = 1, 2, ..., q \tag{B.2}$$

Here q is the number of discrete velocities. Discretizing time using forward finite difference scheme we get

$$\frac{\partial f_i}{\partial t} = \frac{f_i(\vec{r}, t + \Delta t) - f_i(\vec{r}, t)}{\Delta t} \tag{B.3}$$

$\vec{r}$ is the position vector. substituting Eq. (B.3) in Eq. (B.2) we get,

$$\frac{f_i(\vec{r}, t + \Delta t) - f_i(\vec{r}, t)}{\Delta t} = -\vec{e_i} \cdot \vec{\nabla} f_i(\vec{r}, t) + \Omega_i(\vec{r}, t) \tag{B.4}$$

Eq. (B.4) shows that in order to obtain the lattice boltzmann equation from the discrete boltzmann equation the right hand side has to be subjected to the upwind treatment. Upwind schemes use an adaptive or solution-sensitive finite difference stencil to numerically simulate the direction of propagation of information in a flow field. The upwind schemes attempt to discretize hyperbolic partial differential equations by using differencing biased in the direction determined by the sign of the characteristic speeds. The upwind scheme is

stable if it satisfy the Courant-Friedrichs-Lewy condition

$$\text{Courant number:} \frac{e\Delta t}{\Delta r} \leq 1$$

For conventional lattice Boltzmann implementations e, Δt and Δr are usually set to 1 and hence this condition is satisfied. In case of discrete boltzmann equation velocities $\vec{e_i}$ define upwind and downwind directions, a characteristic line is defined by $\vec{e_i}$. The upwind treatment in the case of discrete boltzmann equation means that RHS term at time t in Eq. (B.4) is evaluated at $\vec{r} - \vec{e_i}\Delta t$. From there the information travels along characteristic line in time Δt and arrive point r. That is $\vec{\nabla} f_i(\vec{r}, t) = \vec{\nabla} f_i(\vec{r} - \vec{e_i}\Delta t, t)$ and $\vec{\Omega}(\vec{r}, t) = \vec{\Omega}(\vec{r} - \vec{e_i}\Delta t, t)$,

$$\frac{f_i(\vec{r}, t + \Delta t) - f_i(\vec{r}, t)}{\Delta t} = -\vec{e_i} \cdot \vec{\nabla} f_i(\vec{r} - \vec{e_i}\Delta t, t) + \Omega_i(\vec{r} - \vec{e_i}\Delta t, t) \qquad \text{(B.5)}$$

replacing $\vec{r}$ with $\vec{r} + \vec{e_i}\Delta t$ we get

$$\frac{f_i(\vec{r} + \vec{e_i}\Delta t, t + \Delta t) - f_i(\vec{r} + \vec{e_i}\Delta t, t)}{\Delta t} = -\vec{e_i} \cdot \vec{\nabla} f_i(\vec{r}, t) + \Omega_i(\vec{r}, t) \qquad \text{(B.6)}$$

using forward difference for the space derivative

$$\vec{e_i} \cdot \vec{\nabla} f_i(\vec{r}, t) = \frac{f(\vec{r} + \vec{e_i}\Delta t, t) - f_i(\vec{r}, t)}{\Delta t} \qquad \text{(B.7)}$$

substituting Eq. (B.7) in Eq. (B.6) and rearranging we get

$$f_i(\vec{r} + \vec{e_i}\Delta t, t + \Delta t) = f_i(\vec{r}, t) + \Delta t \Omega_i(\vec{r}, t) \qquad \text{(B.8)}$$

Eq. (B.8) represents the general form of the lattice botlzmann equation. If the collision term is replaced with the BGK term a well known single relaxation time lattice boltzmann scheme can be obtained from above equation. The BGK collision operator (Ω^{BGK}) is given as

$$\Omega_i^{BGK}(\vec{r}, t) = -\frac{1}{\tau} \left(f_i(\vec{r}, t) - f_i^{eq}(\vec{r}, t) \right) \qquad \text{(B.9)}$$

and the single relaxation time lattice boltzmann scheme is given as

$$f_i(\vec{r} + \vec{e_i}\Delta t, t + \Delta t) = f_i(\vec{r}, t) - \frac{1}{\tau} \left(f_i(\vec{r}, t) - f_i^{eq}(\vec{r}, t) \right) \qquad \text{(B.10)}$$

f_i^{eq} is the equilibrium distribution function.

Equilibrium distribution function in lattice Boltzmann method

Equilibrium distribution function satisfies Maxwell-Boltzmann distribution given as

$$f^{eq}(\vec{e}, C, \vec{u}) = C \left(\frac{m}{2\pi kT} \right)^{3/2} \exp \left(\frac{-m(\vec{e} - \vec{u}) \cdot (\vec{e} - \vec{u})}{2kT} \right) \tag{C.1}$$

where m is the particle mass and kT is the product of Boltzmann's constant and temperature. Replacing $kT/m = e_s^2/\gamma$ we get

$$f^{eq}(\vec{e}, C, \vec{u}) = C \left(2\pi \frac{e_s^2}{\gamma} \right)^{-3/2} \exp \left(\frac{-(\vec{e} - \vec{u}) \cdot (\vec{e} - \vec{u})}{\frac{2e_s^2}{\gamma}} \right) \tag{C.2}$$

e_s represents the speed of sound and γ is the adiabatic constant. Eq. (C.2) can be rewritten as

$$f^{eq}(\vec{e}, C, \vec{u}) = C w(\vec{e}) F_1(\vec{e}, \vec{u}) F_2(\vec{u})$$

$$w(\vec{e}) = \left(2\pi \frac{e_s^2}{\gamma} \right)^{-3/2}$$

$$F_1(\vec{e}, \vec{u}) = \exp \left(\frac{2\vec{e} \cdot \vec{u}}{2\frac{e_s^2}{\gamma}} \right) \tag{C.3}$$

$$F_2(\vec{e}, \vec{u}) = \exp \left(\frac{-\vec{u} \cdot \vec{u}}{2\frac{e_s^2}{\gamma}} \right)$$

Substituting the Taylor series expansion for the exponents in eq. (C.3) we get

$$\exp(x) = 1 + x + \frac{x^2}{2!} + \frac{x^3}{3!} + \cdots \tag{C.4}$$

and

$$f^{eq}(\vec{e}, C, \vec{u}) = w(\vec{e})C \left[1 + \gamma \frac{\vec{e} \cdot \vec{u}}{e_s^2} + \gamma \frac{(\vec{e} \cdot \vec{u})^2}{2e_s^2} - \gamma \frac{(\vec{u} \cdot \vec{u})}{2e_s^4} \right] + O(\vec{u}^3) \qquad \text{(C.5)}$$

In general the above equilibrium distribution function can be written as

$$f^{eq}(\vec{e}, C, \vec{u}) = w(\vec{e})C \left[A_1 + A_2(\vec{e} \cdot \vec{u}) + A_3(\vec{e} \cdot \vec{u})^2 + A_4(\vec{u} \cdot \vec{u}) \right] + O(\vec{u}^3) \qquad \text{(C.6)}$$

The unknown coefficients A_1, A_2, A_3, and A_4 are determined based on fact that equilibrium distribution function must satisfy conservation of mass, momentum, energy. The order up to which terms must be considered in f^{eq} is generally determined by governing equation intend to be solve. For eg., to arrive to Naiver-Stokes we need terms up to order of $\vec{u}^2$. However to arrive to advection diffusion equation terms up to order of $\vec{u}$ suffice requirement.

Remark C.0.1 (pseudo lattice speed of sound) *For $\gamma = 1$ the equilibrium distribution function given by Eq. (C.5) can be rewritten as*

$$f^{eq}(\vec{e}, C, \vec{u}) = w(\vec{e})C \left[1 + \frac{\vec{e} \cdot \vec{u}}{e_s^2} + \frac{(\vec{e} \cdot \vec{u})^2}{2e_s^2} - \frac{(\vec{u} \cdot \vec{u})}{2e_s^4} \right]$$

Using this equilibrium distribution function to recover the Naiver-Stokes equation the relationship between pressure (P) and density (ρ) can be recovered as [297]

$$P = e_s^2 \rho$$

Therefore e_s is generally referred to as lattice speed of sound. However the term e_s has no physical significance for advection-diffusion equation and hence in this thesis e_s is referred to as pseudo lattice speed of sound.

Multiscale Chapman-Enskog expansion

The governing partial differential equation can be recovered from the lattice Boltzmann equation using the a multiscale Chapman-Enskog expansion. The lattice Boltzmann equation is given as

$$f_i(\vec{r} + \vec{e_i}\Delta t, t + \Delta t) = f_i(\vec{r}, t) + \Delta t \Omega_i(\vec{r}, t) \tag{D.1}$$

Expanding $f_i(\vec{r} + \vec{e_i}\Delta t, t + \Delta t)$ using taylor series expansion

$$f_i(\vec{r} + \vec{e_i}\Delta t, t + \Delta t) = f_i(\vec{r}, t) + \sum_{n=1}^{n=\infty} \frac{1}{n!} \left[\Delta t \left(\frac{\partial}{\partial t} + \vec{e_i} \cdot \vec{\nabla} \right) \right]^n f_i(\vec{r}, t) \tag{D.2}$$

Substituting Eq. (D.2) in Eq. (D.1) we get

$$\sum_{n=1}^{n=\infty} \frac{1}{n!} \left[\Delta t \left(\frac{\partial}{\partial t} + \vec{e_i} \cdot \vec{\nabla} \right) \right]^n f_i(\vec{r}, t) = \Delta t \Omega_i(\vec{r}, t) \tag{D.3}$$

Retaining only terms upto second order in Eq. (D.3)

$$\left[\frac{\partial}{\partial t} + \vec{e_i} \cdot \vec{\nabla} + \frac{\Delta t}{2} \left(\frac{\partial^2}{\partial t^2} + 2\frac{\partial}{\partial t}\vec{e_i} \cdot \vec{\nabla} + \vec{e_i}\vec{e_i} : \vec{\nabla}\vec{\nabla} \right) \right] f_i(\vec{r}, t) = \Omega_i(\vec{r}, t) + O(\Delta t^3) \tag{D.4}$$

In Chapman-Enskog expansion space and time derivatives are expanded with respect to a small perturbation ε. The time derivative is expanded as

$$\frac{\partial}{\partial t} = \varepsilon \frac{\partial}{\partial t_1} + \varepsilon^2 \frac{\partial}{\partial t_2} + O(\varepsilon^3) \tag{D.5}$$

and space derivative is expanded as

$$\vec{\nabla} = \varepsilon\vec{\nabla}^* + O(\varepsilon^2) \tag{D.6}$$

The distribution function and collision term is likewise expanded starting from zeroth order.

$$f_i = f_i^{(0)} + \varepsilon f_i^{(1)} + \varepsilon^2 f_i^{(2)} + O(\varepsilon^3) \tag{D.7}$$

$$\Omega_i = \Omega_i^{(0)} + \varepsilon\Omega_i^{(1)} + \varepsilon^2\Omega_i^{(2)} + O(\varepsilon^3) \tag{D.8}$$

Substituting, Eq. (D.5), Eq. (D.6), Eq. (D.7) and Eq. (D.8) in Eq.(D.4) and neglecting $O(\varepsilon^3)$ terms we get

$$\left[\varepsilon\frac{\partial}{\partial t_1} + \varepsilon^2\frac{\partial}{\partial t_2} + \varepsilon\vec{e_i}\cdot\vec{\nabla}^* + \varepsilon^2\frac{\Delta t}{2}\frac{\partial^2}{\partial t_1^2} + \varepsilon^2\Delta t\frac{\partial}{\partial t_1}\vec{e_i}\cdot\vec{\nabla}^* + \varepsilon^2\frac{\Delta t}{2}\vec{e_i}\vec{e_i}:\vec{\nabla}^*\vec{\nabla}^*\right]\left(f_i^{(0)} + \varepsilon f_i^{(1)}\right)$$
$$= \Omega_i^{(0)} + \varepsilon\Omega_i^{(1)} + \varepsilon^2\Omega_i^{(2)} \quad \text{(D.9)}$$

Finally grouping the terms to same order the conservation laws at different scales can be discussed separately.

$$O(\varepsilon^0):\Omega_i = 0 \tag{D.10}$$

$$O(\varepsilon^1):\left[\frac{\partial}{\partial t_1} + \vec{e_i}\cdot\vec{\nabla}^*\right]f_i^{(0)} = \Omega_i^{(1)} \tag{D.11}$$

$$O(\varepsilon^2):\left[\frac{\partial}{\partial t_2} + \frac{\Delta t}{2}\frac{\partial^2}{\partial t_1^2} + \Delta t\frac{\partial}{\partial t_1}\vec{e_i}\cdot\vec{\nabla}^* + \frac{\Delta t}{2}\vec{e_i}\vec{e_i}:\vec{\nabla}^*\vec{\nabla}^*\right]f_i^{(0)} + \left[\frac{\partial}{\partial t_1} + \vec{e_i}\cdot\vec{\nabla}^*\right]f_i^{(1)} = \Omega_i^{(2)} \tag{D.12}$$

The macroscopic variables are defined as the moments of the distribution function and the macroscopic dynamics can be expressed by means of the conservation laws applied to some of this moments. A global conservation of a macroscopic quantity is expressed locally by a collision invariant. For example, conservation of mass is enforced by a local conservation of mass during the collision between particles. At the level of lattice Boltzmann equation this means that the $\sum_i \Omega_i$ should be zero.

Quasi stationary assumption for heterogeneous reactions

The change in concentration of jth species in solid ($C^{j,s}$) due to heterogeneous reaction can be written as

$$\frac{\partial C^{j,s}}{\partial t} = -R_{het}^{j} \tag{E.1}$$

R_{het}^{j} in above equation represents source/sink term in aqueous concentration corresponding to heterogeneous reaction. Correspondingly the mass balance for aqueous concentration (C^{j}) at fluid-solid interface in terms of aqueous concentrations can be written as

$$\frac{\partial C^{j}}{\partial t} = \vec{\nabla} \cdot \vec{J^{j}} + R_{het}^{j} \tag{E.2}$$

Only small change in solid concentration is sufficient to greatly affect the solution composition in liquid phase. As a result at the fluid-solid interface the aqueous solution spends much of its time in stationary state. This implies that $\frac{\partial C^{j}}{\partial t} \approx 0$. This is commonly referred to as quasi-state approximation [110]. As a consequence Eq.(E.2) can be written as

$$\vec{\nabla} \cdot \vec{J^{j}} = -R_{het}^{j} \tag{E.3}$$

Taking volume integral over the volume of the solid domain Eq. (E.3) we get

$$\int_{V_s} \vec{\nabla} \cdot \vec{J^{j}} dV_s = \int_{V_s} -R_{het}^{j} dV_s \tag{E.4}$$

Using Gauss's divergence theorem we get

$$\int_{\Gamma_s} \hat{n} \cdot \vec{J^{j}} d\Gamma_s = \int_{V_s} -R_{het}^{j} dV_s \tag{E.5}$$

Assuming the flux and reaction terms to be constant over the solid surface we get

$$\hat{n} \cdot \vec{J^j} = -\frac{V_s}{A_s} R^j_{het} \tag{E.6}$$

where V_s is the volume of the solid and A_s is the surface area of the solid. Thus the heterogeneous reactions occurring at the fluid-solid interface can be represented as the boundary conditions using Eq. (E.6).

Summary of mathematical expressions for different effective diffusivity models for cement paste

---

The mathematical expressions and the fitting parameter involved for the different models to predict effective diffusivity of cement paste are summarized below :

F.1 Empirical model

Archies relationship

$$\frac{D_e}{D_0} = a\phi^n$$

D_e is the effective diffusion of cement paste [L^2 T^{-1}], D_0 is the diffusion in pore water [L^2 T^{-1}], ϕ is capillary porosity

Fitting parameters: a, n

Modified Archie's relationship

$$\frac{D_e}{D_0} = a(\phi - \phi_c)^n \qquad \qquad \forall \phi > \phi_c$$
$$\frac{D_e}{D_0} = 0 \qquad \qquad \forall \phi \leq \phi_c$$

ϕ_c is the threshold capillary porosity

Fitting parameters: a, n, ϕ_c

Exponential form

$$\frac{D_e}{D_0} = a \exp(n\phi)$$

Fitting parameters: a, n

Exponential form with respect to water-cement ratio

$$\frac{D_e}{D_0} = a \exp(n\text{w/c})$$

w/c is the water-cement ratio
Fitting parameters: a, n

F.2   Relationships derived from numerical models

NIST model Garboczi and Bentz [137]

$$\frac{D_e}{D_0} = a_1 H(\phi - \phi_c)(\phi - \phi_c)^2 + a_2\phi^2 + a_3$$

Fitting parameters: a_1, a_2, a_3, ϕ_c

F.3   Effective media theories

F.3.1   Models conceptualizing morphology of cement paste in simplified way

Differential effective media [164]

$$\frac{D_e}{D_0} = \phi^{1.5}$$

Assumptions: non-diffusive solid as inclusion in matrix capillary porosity
Fitting parameters: Free water diffusion should be taken an order of magnitude lower to apply this model to cement paste [164].

Generalized self-consistent scheme [146] (Oh and Jang model)

$$\frac{D_e}{D_0} = \left(m_\phi + \sqrt{m_\phi^2 + \frac{\phi_c}{1 - \phi_c}\left(\frac{D_{CSH}}{D_0}\right)^{\frac{1}{n}}} \right)^n$$

$$m_\phi = \frac{1}{2}\left[\left(\frac{D_{CSH}}{D_0}\right)^{1/n} + \frac{\phi}{1 - \phi_c}\left(1 - \left(\frac{D_{CSH}}{D_0}\right)^{1/n}\right) - \frac{\phi_c}{1 - \phi_c} \right]$$

where D_{CSH} is diffusivity of C-S-H phase.

Assumptions: diffusive solid and capillary porosity as inclusion in matrix of equivalent homogenous media

Fitting parameters: D_{CSH}, n, ϕ_c

Bejaoui and Bary [5]

Uses different set of series parallel configurations as shown in Fig. 5.2 of chapter 5. The tortuosity of capillary pores is computed through

$$\zeta_a^{CP} = 0.0067 \exp(5\phi)$$

ζ_a^{CP} is apparent tortuosity for capillary pores.

The tortuosity of LD C-S-H, HD C-S-H and mixed fraction of LD C-S-H and capillary porosity is computed using effective media theory for single coated sphere which can be written as

$$\zeta_a^i = \phi_p^i - \frac{\phi_p^i(1 - \phi_p^i)}{3 - \phi_p^i} \qquad i \in \{LD - CSH, HD - CSH, LD - CSH + HD - CSH\}$$

ϕ_p^i is the fraction of pores in i^{th} phase and ζ_a^i is apparent tortuousity of ith phase

Fitting parameters: D_{LD-CSH}, D_{HD-CSH}

D_{LD-CSH} and D_{HD-CSH} are the diffusion coefficients of LD C-S-H and HD C-S-H respectively.

F.3.2 Models conceptualizing in detail the morphology of cement paste

Bary and Béjaoui [165]

$$D_{e,n} = D_n + \left(1 - \frac{\phi_n}{\sum\limits_{i=1}^{n} \phi_i}\right)\left[\frac{1}{D_{e,n-1} - D_n} + \frac{1}{3D_n}\frac{\phi_n}{\sum\limits_{i=1}^{n} \phi_i}\right]$$

$$D_{inn} = 2D_{HD-CSH}\left(\frac{1 - \phi_{AF}^{inn} - \phi_{CH}^{inn}}{2 + \phi_{AF}^{inn} + \phi_{CH}^{inn}}\right)$$

under the Assumptions $D_{CSH}^{out}/D_0 \approx 0$

$$D_{int} = 2D_{LD-CSH} \left(\frac{1 + 2\phi_{CP}^{int} - \phi_{AF}^{int} - \phi_{CH}^{int}}{1 - \phi_{CP}^{int} + 0.5\left(\phi_{AF}^{int} + \phi_{CH}^{int}\right)} \right)$$

$$D_{out} = D_{LD-CSH} \left(\frac{1 - \frac{3}{2}\left(\phi_{AF}^{out} + \phi_{CH}^{out}\right)}{1 - 3\phi_{CP}^{out}} \right)$$

where $D_{e,n}$ is the effective diffusivity of n coated layers, ϕ_n is the fraction of $n * th$ phase, ϕ_{AF}^{inn}, ϕ_{AF}^{int}, ϕ_{AF}^{out} are fractions of aluminate phases in inner, intermediate and outer shells respectively, ϕ_{CH}^{inn}, ϕ_{CH}^{int}, ϕ_{CH}^{out} are fractions of portlandite in inner, intermediate and outer shells respectively. ϕ_{CP}^{int} and ϕ_{CP}^{out} are the fraction of capillary pore in intermediate shell and outer shell respectively

Assumptions: cement paste is assembly of three coated sphere with inner shell made of inclusion of other hydration products in matrix of HD C-S-H. Intermediate and outer shell containing capillary pores in addition to other hydration products as inclusions in matrix of LD C-S-H

Fitting parameters: D_{LD-CSH}, D_{HD-CSH}

Stora *et al.* [167]

$$D_i = D_{gp} \left(\frac{-1 + (f_{gp}^i + \phi_{gp}^i) + |1 - (f_{gp}^i + \phi_{gp}^i)|}{1 + (2f_{gp}^i - \phi_{gp}^i)} \right), i \in \{LD - CSH, HD - CSH\}$$

where ϕ_{gp} denotes fraction of gel pores and f_{gp} is the geometric parameter. D_{gp} is the diffusivity in gel pores $[L^2T^{-1}]$ which is taken as one order lower than that in pore water

$$D_{inn} = 2D_{HD-CSH} \left(\frac{1 - \phi_{CH}^{inn} - \phi_{AF}^{inn}}{2 + \phi_{CH}^{inn} + \phi_{AF}^{inn}} \right)$$

$$D_{out} = 2D_{LD-CSH} \left(\frac{1 - \phi_{CH}^{out} - \phi_{AF}^{out} + 2\phi_{cp}^{out}\beta_{cp}^{LD-CSH}}{2 + \phi_{CH}^{out} + \phi_{AF}^{out} - \phi_{cp}^{out}\beta_{cp}^{LD-CSH}} \right)$$

$$\beta_i^j = \frac{D_i - D_j}{D_i + 2D_j}$$

$$D_e = 2D_{LD-CSH} \left(\frac{3}{2 + \phi_{UC} - 2\phi_{inn}\beta_{inn}^{out}} - 1 \right)$$

ϕ_{uc} is fraction of unhydrated clinker phase in cement paste.

Assumptions: cement paste is assembly of two coated sphere with inner shell made of inclusion of other hydration products in matrix of HD C-S-H. Outer shell containing capillary pores in addition to other hydration products as inclusions in matrix of LD C-S-H

Fitting parameters: f_{gp}^{LD-CSH}, f_{gp}^{HD-CSH}, ϕ_{gp}^{HD-CSH}

Dridi [170]

$$D_{e,n} = D_n + \left(1 - \frac{\phi_n}{\sum\limits_{i=1}^{n} \phi_i}\right) \left[\frac{1}{D_{e,n-1} - D_n} + \frac{1}{3D_n}\frac{\phi_n}{\sum\limits_{i=1}^{n} \phi_i}\right]$$

$$D_{inn} = 2D_{HD-CSH}\left(\frac{1 - \phi_{AF}^{inn} - \phi_{CH}^{inn}}{2 + \phi_{AF}^{inn} + \phi_{CH}^{inn}}\right)$$

$$D_{out} = 2D_{LD-CSH}\left(\frac{1 + 2\phi_{CP}^{out} - \phi_{AF}^{out} - \phi_{CH}^{out}}{1 - \phi_{CP}^{out} + 0.5\left(\phi_{AF}^{out} + \phi_{CH}^{out}\right)}\right) \qquad \text{if}\phi_{cp}^{out} < \phi_c$$

$$\sum_i \frac{\phi_i^{out}}{\phi_{CP}^{out} + \phi_{AF}^{out} + \phi_{CH}^{out} + \phi_{CSH}^{out}}\frac{D_i - D_{out}}{D_i + 2D_{out}} = 0 \qquad \text{if}\phi_{cp}^{out} \geq \phi_c$$

$$i \in \{CP, CH, CSH_{out}, AF\}$$

Assumptions: cement paste is assembly of two coated sphere with inner shell made of inclusion of other hydration products in matrix of HD C-S-H. Outer shell containing capillary pores in addition to other hydration products as inclusions in matrix of LD C-S-H. When LD C-S-H doesnot percolate cement paste is considered as assembly of single coated spheres.

Fitting parameters: D_{LD-CSH}, D_{HD-CSH}

Liu et al. [171]

$$D_{HD-CSH} = (\phi_{gp}^{HD-CSH})^{1.5}D_{gp}, \qquad D_{LD-CSH} = (\phi_{gp}^{LD-CSH})^{1.5}D_{gp}$$

$$\frac{D_{CSH} - D_{LD-CSH}}{D_{CSH} + 2D_{LD-CSH}} = \sum_i \phi_i^{out}\left[\frac{D_j - D_{LD-CSH}}{D_j + D_{LD-CSH}}\right] \qquad i \in \{CP, HD-CSH\}$$

$$\sum_i \phi_i^p \frac{D_i - D_e}{D_i + 2D_e} = 0 \qquad i \in \{CP, CH, AF, UC, CSH\}$$

Assumptions: Microstructure of cement paste divided in three level. At level I two types of C-S-H considered where each C-S-H type is represented as inclusion in matrix of gel pore. At level II, HD C-S-H and small capillary pores are inclusions in matrix of LD C-S-H. At level III, capillary pores, CSH and other hydration products as inclusions in matrix of equivalent continuum media.

Fitting parameters: D_{gp}

A overview on effective media theories

Effective media theories [1] provides a set of approximate solutions for effective diffusion coefficients for a well defined inclusions (such as spheres, cylinders, ellipsoids) distributed randomly throughout a matrix material.The effective media approximations only take into account the basic morphological information such as shape and volume fractions of inclusion. To derive the effective media approximation it is essential to formulate a well defined boundary value problem for the micro-scale (i.e. a system with inclusion and matrix). This boundary value problem is often referred to as localization problem [198, 299] or Eshelby's inclusion problem [300] after the thought process devised by John D. Eshelby in 1957 [301] . Following assumptions are made to define localization problem for diffusion at level of the representative element volume(REV):

   I The steady state has been reached in REV

  II The uniform concentration gradient (H) boundary condition are considered on REV

 III No mass exchange at a fluid-solid interface is considered

Thus the simplified localization problem is formulated as

$$\vec{\nabla} \cdot \vec{J}(x) = 0 \quad \forall x \in \Omega$$
$$\vec{J}(x) = -D(x)\vec{\nabla}C(x) \quad \forall x \in \Omega \qquad \text{(G.1)}$$
$$C(x) = Hx \quad \forall x \in \Gamma$$

---

[1]The effective media theories are analytically derived by applying continuum mechanics at the micro-level and hence this field of study is often referred to as continuum micro-mechanics after the celebrated article of Hill published in 1965 titled *"Continuum micro-mechanics of elastoplastic polycrystals"*[298]

$C(x)$ and $\vec{J}(x)$ are concentration field $[N^1 L^{-3}]$ and flux vector field $[N^1 L^{-2} T^{-1}]$ respectively. $D(x)$ is the diffusion coefficient $[L^2 T^{-1}]$. Ω and Γ represents the domain and boundary of REV respectively. The average concentration gradient in the REV would then be

$$\langle \vec{\nabla} C(x) \rangle = H \tag{G.2}$$

$\langle \bullet \rangle$ represents the volume average. The dependence of the microscopic gradient with respect to the macroscopic gradient can be expressed through the localization factor $A(x)$ as follows

$$\vec{\nabla} C(x) = A(x) H \tag{G.3}$$

$A(x)$ takes into account the morphology of the microstructure. From equations G.2 and G.3 it can be shown that

$$\langle A \rangle = \sum_{i=1}^{n} \phi_i A_i = \mathbb{1} \tag{G.4}$$

n represents number of different phases in REV. The macroscopic flux can be obtained by taking volume average over the microscopic flux

$$\langle \vec{J} \rangle = -\langle D(x) \vec{\nabla} C(x) \rangle = -\langle D(x) A(x) \rangle H \tag{G.5}$$

Therefore,

$$D_e = \langle D(x) A(x) \rangle \tag{G.6}$$

D_e is the effective diffusion coefficient $[L^2 T^{-1}]$ of REV. For a composite with inclusions of non-diffusive phase (solid) in matrix of diffusive phase (pore space), from Eq. (G.4) and Eq. (G.6) it can be deduced that

$$D_e = D_0 \phi A_p = D_0 (\mathbb{1} - (1 - \phi) A_s) \tag{G.7}$$

where ϕ is the fraction of pore space, A_p and A_s are the localization factor for pore space and solid phase respectively, and D_p is diffusion coefficient $[L^2 T^{-1}]$ in pores. By definition of pore diffusion coefficient the, pore diffusion coefficient (D_p) $[L^2 T^{-1}]$ of the REV is given as

$$D_p = D_0 A_p \tag{G.8}$$

Thus if the localization factor is known, the effective diffusion coefficient for the REV can be determined. However, the exact analytical determination of localization factor is a complex task and therefore different approximations are used to obtain the localization tensor.

The most commonly used estimates are Generalized Maxwell approximation (which is analogue of Mori-Tanaka scheme used for elastic modulus [163]), self-consistent scheme (and its variants are also referred as effective media approximation [302]) and differential

effective media scheme. These approximations differ in the underlying assumptions used to derive the effective diffusivity. To understand the assumptions involved in these theories let us consider a case of composite media made of two phases. In generalized Maxwell approximation one phase is considered as inclusions in the matrix of another matrix in an infinite domain of same shape as inclusion so that a constant gradient can be assumed inside the domain. The inclusions are considered to be well separated such that they do not interact with each other. With this assumption the analytical solution for single inclusion can be directly applied to obtain effective media of the composite. The applicability of generalized Maxwell approximation is limited to dilute range of volume fraction. On other hand, in the self-consistent scheme, the phases are considered as inclusion in matrix of media with diffusivity equivalent to that of effective diffusivity of composite. It is further ensured in self-consistent scheme that the local perturbations in concentration field caused by these inclusions on average cancel out. The self-consistent scheme thus treats all the phases of a heterogeneous media in same way and hence allows accounting for the effect of percolation of one phase in another. However, when properties of different phases varies substantially, the self-consistent approximation fails [163]. In differential effective media, one phase is taken as matrix and another phase is added incrementally such that the volume fraction added is always in the dilute limit with respect to current effective media. This assumption leads to differential equation integration of which gives the effective diffusivity of the composite. Hence this scheme is named as a differential effective media theory. The differential effective media ensures that the initial matrix always remains connected. This in turn allows the differential effective media to recover Archies relationship [303]. Formulas for these effective media theories for the case of composite with inclusions as non-diffusive spheres (solid) in a matrix of diffusive phase (pores) are given in Table G.1. The formula for generalized Maxwell scheme is explicit whereas self-consistent and differential effective media scheme have implicit formula. For detail description of these schemes readers are referred to Ref. [163, 304]. The diffusion coefficient obtained from this estimates are shown in Fig. G.1

Table G.1: Different effective media approximation schemes. phase 1 is the pore space and phase 2 is non-diffusive solid inclusions

Scheme	Assumptions	D_e	References
Maxwell approximation	Phase 2 are inclusions in matrix of phase 1	$\frac{2\phi}{3-\phi}D_0$	[163, 304]
Self -consistent	Phase 2 and phase 1 are inclusions in matrix of equivalent homogeneous media	$\frac{3\phi-1}{2}D_0$ $(\phi \geq 1/3)$	[163, 304]
Differential	Phase 1 is taken as matrix and phase 2 is added incrementally such that the volume fraction added is always in the dilute limit with respect to current effective media	$\phi^{3/2}D_0$	[163, 304]
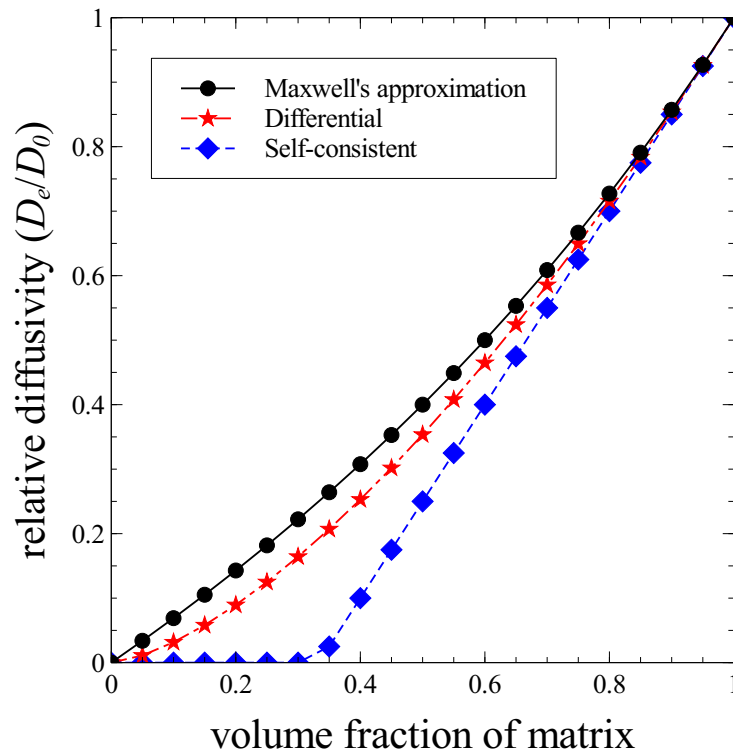
Figure G.1: Effective diffusion coefficients relative to diffusion coefficient in matrix (D_0) as computed from different effective media theories for composite with insulated spherical inclusions in matrix of diffusive phase

H

Extension of SciPy least square minimization method to account for bounds

Below is the code to extend *SciPy* non-constrained least square method to bounded least square method. This algorithm is taken from the discussion on [305]

```python
# leastsq_bounds.py
from __future__ import division
import numpy as np
from scipy.optimize import leastsq
def leastsq_bounds( func, x0, bounds, boundsweight=10, **kwargs ):
    """
    leastsq with bound conatraints lo <= p <= hi
    run leastsq with additional constraints to minimize the sum of squares of
    [func(p) ...]
    + boundsweight * [max( lo_i - p_i, 0, p_i - hi_i ) ...]

    Parameters
    ----------
    func() : a list of function of parameters 'p', [err0 err1 ...]
    bounds : an n x 2 list or array '[[lo_0,hi_0], [lo_1, hi_1] ...]'.
        Use e.g. [0, inf]; do not use NaNs.
        A bound e.g. [2,2] pins that x_j == 2.
    boundsweight : weights the bounds constraints
    kwargs : keyword args passed on to leastsq

    Returns
    -------
    exactly as for leastsq of SciPy

```

```
25      Notes
26      -----
27      The bounds may not be met if boundsweight is too small;
28      check that with e.g. check_bounds( p, bounds ) below.
29
30      To access 'x' in 'func(p)', 'def func( p, x=xouter )'
31      or make it global, or 'self.x' in a class.
32
33
34      """
35
36      if bounds is not None  and  boundsweight > 0:
37          check_bounds( x0, bounds )
38          if "args" in kwargs:
39              args = kwargs["args"]
40              del kwargs["args"]
41          else:
42              args = ()
43          funcbox = lambda p: \
44              np.hstack(( func( p, *args ),
45                          _inbox( p, bounds, boundsweight )))
46      else:
47          funcbox = func
48      return leastsq( funcbox, x0, **kwargs )
49
50
51  def _inbox( X, box, weight=1 ):
52      """ -> [tub( Xj, loj, hij ) ... ]
53          all 0  <=>  X in box, lo <= X <= hi
54      """
55      assert len(X) == len(box), \
56          "len X %d != len box %d" % (len(X), len(box))
57      return weight * np.array([
58          np.fmax( lo - x, 0 ) + np.fmax( 0, x - hi )
59              for x, (lo,hi) in zip( X, box )])
60
61  def check_bounds( X, box ):
62      """ print Xj not in box, loj <= Xj <= hij
63          return nr not in
64      """
65      nX, nbox = len(X), len(box)
66      assert nX == nbox, \
67          "len X %d != len box %d" % (nX, nbox)
68      nnotin = 0
69      for j, x, (lo,hi) in zip( range(nX), X, box ):
70          if not (lo <= x <= hi):
71              print "check_bounds: x[%d] %g is not in box %g .. %g" % (j, x, lo, hi)
72              nnotin += 1
```

```
73        return nnotin
```
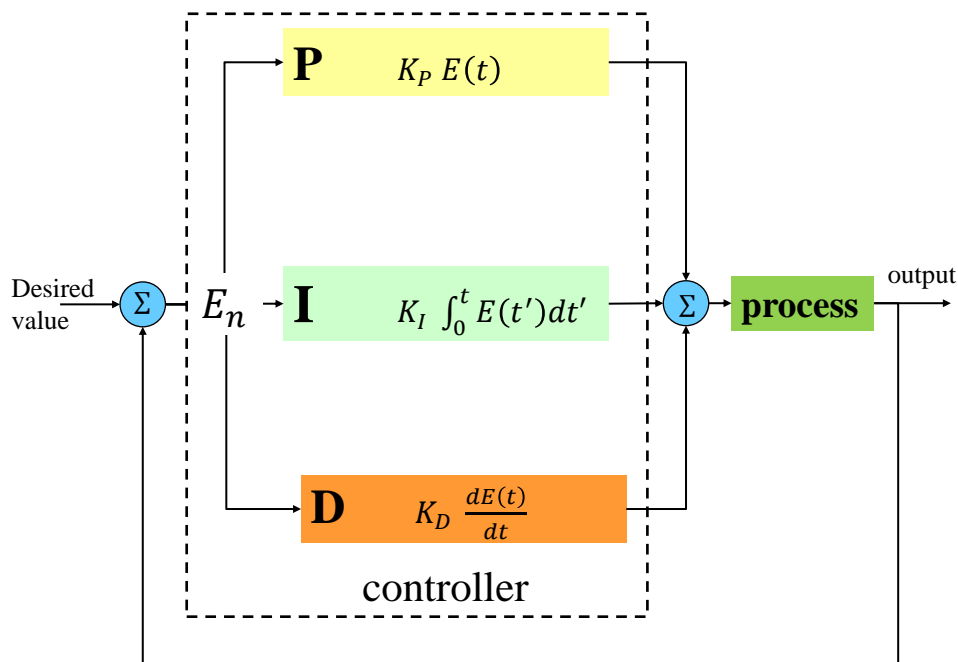
Figure I.1: Schematic diagram of PID-controller

The PID (proportional,integral,derivative) time stepping scheme is inspired from the PID controller commonly used in industrial control systems [278, 279]. The advantage of PID scheme is its simplistic structure and robust performance in a wide range of operating conditions [281]. The schematic diagram of PID controller is shown in Fig. I.1. An PID controller continuously calculates an error value and attempts to minimize the error over time by adjustment of a control variable. The controller performs P, I and D mathematical

functions on the error and can be tuned by adjusting the parameters corresponding to this operations viz., K_P, K_I and K_D respectively. By tuning K_P the overall error can be controlled. K_I can be tuned to remove the residual error at the steady state. Since the integral term responds to accumulated errors for the past, it can cause the present value to overshoot the desired value. K_D counteracts the K_P and K_I terms when the output changes quickly. This helps to reduce an overshoot [278].

Time step selection can be viewed as an automatic control problem with PID controller defined as [278–282]

$$\Delta t_{n+1} = \left(\frac{E_{n-1}}{E_n} \right)^{K_P} \left(\frac{1}{E_n} \right)^{K_I} \left(\frac{E_{n-1}^2}{E_n E_{n-2}} \right)^{K_D} \Delta t_n \tag{I.1}$$

where E is the error term and Δt_{n+1} and Δt_n are time step at $n+1^{th}$ iteration and n^{th} iteration respectively. Additionally the time step limits Δt_{max} and Δt_{min} can be supplied to the controller to avoid excessive growth or reduction of the time step. The error in this study is defined as follows

$$E = \frac{1}{TOL} \max_j \left(\frac{\|C_n^j - C_{n-1}^j\|}{\|C_n^j\|} \right) \tag{I.2}$$

where TOL is the specified tolerance, C^j is the concentration of jth component and $\| \bullet \|$ represents euclidean norm. For a given time step the time integration using PID scheme can be given as —

1 Given Δt_{min}, Δt_{max}, TOL, K_P, K_I, K_D and initializing E_n, E_{n-1}, and E_{n-2} as 1 and initial time step as $\Delta t_n = \Delta t_{min}$

2 compute E_n

3 if $E_n > 1$ reject the time step:

   - $t_{n+1} = t_n - \Delta t_n$
   - $\Delta t_{n+1} = \max(\frac{1}{E_n} \Delta t_n, \Delta t_{min})$
   - $C_n^j = C_{n-1}^j$

   else

   - calcuate Δt_{n+1} using Eq. (I.1)
   - $\Delta t_{n+1} = \max(\Delta t_{n+1}, \Delta t_{min})$
   - $\Delta t_{n+1} = \min(\Delta t_{n+1}, \Delta t_{max})$

4 $E_{n-2} = E_{n-1}$, $E_{n-1} = E_n$

In case of LB schemes from Eq. (2.76) it can be deduced that $\Delta t \propto (\tau - \frac{1}{2})$. Hence the PID controller can be heuristically rewritten in terms of relaxation parameter as

$$\left(\tau_{n+1} - \frac{1}{2}\right) = SF \left(\frac{E_{n-1}}{E_n}\right)^{K_p} \left(\frac{1}{E_n}\right)^{K_I} \left(\frac{E_{n-1}^2}{E_n E_{n-2}}\right)^{K_D} \left(\tau_n - \frac{1}{2}\right) \tag{I.3}$$

In LB scheme resetting to previous time step in case of rejection requires an additional storage of distribution functions which can be expensive in terms of memory. As a result an additional safety factor SF is introduced in Eq. I.3 which can be tweaked to avoid rejections. In case of rejection (if $E_{n+1} > 1$), in present study the relaxation parameter is taken as $\min(\tau_n, \tau_{n+1})$.

Determination of PID control parameters is based on trial and error. In this study in depth analysis of the PID parameters on accuracy of LB scheme was not carried out. However based on preliminary investigation it was found that, the values PID parameters (0.075, 0.175, and 0.08 for K_P, K_I and K_D respectively) used by Valli *et al.* [281] for the reactive flow and transport using finite element methods worked well for LB scheme too and hence this values were used in this study. The value of relative tolerance was chosen as 0.05 for C-S-H benchmark performed in chapter 8 and for the simulations of leaching through micorstructures in chapter 8 the tolerance was further relaxed to 0.1. The value of SF was taken as 0.9.

Bibliography

[1] NIRAS, *The cAt project in Dessel. A long-term solution for Belgian category A waste*, Tech. Rep. (NIRAS, 2010).

[2] NIRAS, *Synthese van het veiligheidsrapport voor de opervlaktebergingsinrichting van categorie-A afval in Dessel*, Tech. Rep. (NIRAS, 2012).

[3] `http://www.niras-cat.be/`, accessed: 2015-09-24.

[4] P. K. Mehta and P. J. M. Monteiro, *Concrete: microstructure, properties, and materials* (McGraw-Hill New York, 2006) p. 684.

[5] S. Bejaoui and B. Bary, *Modeling of the link between microstructure and effective diffusivity of cement pastes using a simplified composite model,* Cement and Concrete Research **37**, 469 (2007).

[6] V. Ngala and C. Page, *Effects of Carbonation on Pore Structure and Diffusional Properties of Hydrated Cement Pastes,* Cement and Concrete Research **27**, 995 (1997).

[7] A. Delagrave, J. Marchand, and M. Pigeon, *Influence of microstructure on the tritiated water diffusivity of mortars,* Advanced Cement Based Materials **7**, 60 (1998).

[8] Q. T. Phung, *Effects of carbonation and calcium leaching on microstructure and transport properties of cement pastes*, Ph.D. thesis, Ghent University (2015).

[9] H. Ma, D. Hou, J. Liu, and Z. Li, *Estimate the relative electrical conductivity of C-S-H gel from experimental results,* Construction and Building Materials **71**, 392 (2014).

[10] M. Buil, E. Revertegat, and J. Oliver, *A model of the attack of pure water or undersaturated lime solution cement,* in *Stabilization and Solidification of Hazardous, Radioactive, and Mixed Wastes,* edited by T. M. Gilliam and C. C. Wiles (American society for testing and materials, Philadelphia, 1992) 2nd ed., pp. 227–241.

[11] U. R. Berner, *Modelling the incongruent dissolution of hydrated cement minerals,* Radiochimica Acta **44/45**, 387 (1988).

[12] K. Wan, L. Li, and W. Sun, *Solidliquid equilibrium curve of calcium in 6mol/L ammonium nitrate solution,* Cement and Concrete Research **53**, 44 (2013).

[13] K. Haga, S. Sutou, M. Hironaga, S. Tanaka, and S. Nagasaki, *Effects of porosity on leaching of Ca from hardened ordinary Portland cement paste,* Cement and Concrete Research **35**, 1764 (2005).

[14] S. Kamali, M. Moranville, and S. Leclercq, *Material and environmental parameter effects on the leaching of cement pastes: Experiments and modelling,* Cement and Concrete Research **38**, 575 (2008).

[15] P. D. Tennis and H. M. Jennings, *A model for two types of calcium silicate hydrate in the microstructure of portland cement pastes,* Cement and Concrete Research **30**, 855 (2000).

[16] G. De Schutter, *No concrete is sustainable without being durable,* in *International Conference on Durability of Building Materials and Components - XIII DBMC,* edited by M. Quattrone and V. M. John (2015) p. 7.

[17] J. Tragaardh and B. Lagerblad, *TR-98-11 Leaching of 90-year old concrete mortar in contact with stagnant water,* (1998).

[18] K. Yokozeki, K. Watanabe, N. Sakata, and N. Otsuki, *Modeling of leaching from cementitious materials used in underground environment,* Applied Clay Science **26**, 293 (2004).

[19] H. M. Jennings, J. J. Thomas, J. S. Gevrenov, G. Constantinides, and F. J. Ulm, *A multi-technique investigation of the nanoporosity of cement paste,* Cement and Concrete Research **37**, 329 (2007).

[20] J. J. Thomas and H. M. Jennings, *A colloidal interpretation of chemical aging of the C-S-H gel and its effects on the properties of cement paste,* Cement and Concrete Research **36**, 30 (2006).

[21] H. M. Jennings, *Refinements to colloid model of C-S-H in cement: CM-II,* Cement and Concrete Research **38**, 275 (2008).

[22] H. M. Jennings, *Colloid model of C-S-H and implications to the problem of creep and shrinkage,* Materials and Structures **37**, 59 (2003).

[23] H. M. Jennings, *A model for the microstructure of calcium silicate hydrate in cement paste,* Cement and Concrete Research **30**, 101 (2000).

[24] H. M. Jennings, J. W. Bullard, J. J. Thomas, J. E. Andrade, J. J. Chen, and G. W. Scherer, *Characterization and Modeling of Pores and Surfaces in Cement Paste,* Journal of Advanced Concrete Technology **6**, 5 (2008).

[25] H. M. Jennings and J. W. Bullard, *From electrons to infrastructure: Engineering concrete from the bottom up,* Cement and Concrete Research **41**, 727 (2011).

[26] D. Bentz, E. Garboczi, H. Jennings, and D. Quenard, *Multi-scale digital-image-based modelling of cement-based materials,* in *MRS Proceedings*, Vol. 370 (Cambridge Univ Press, 1994) p. 33.

[27] K. V. Breugel, *Modelling of cement-based systems the alchemy of cement chemistry,* Cement and Concrete Research **34**, 1661 (2004).

[28] J. S. Dolado and K. van Breugel, *Recent advances in modeling for cementitious materials,* Cement and Concrete Research **41**, 711 (2011).

[29] K. Maekawa, T. Ishida, and T. Kishi, *Multi-scale Modeling of Concrete Performance Integrated Material and Structural Mechanics,* Journal Of Advanced Concrete Technology **1**, 91 (2003).

[30] E. A. B. Koenders, E. Schlangen, and K. V. Breugel, *MULTI-SCALE MODELLING : THE DELFTCODE,* in *International RILEM Symposium on Concrete Modelling CONMOD08*, May (2008) pp. 251–258.

[31] http://www.nist.gov/el/building_materials/electronic-monograph.cfm, accessed: 2015-09-24.

[32] Z. Qian, *Multiscale Modeling of Fracture Processes in Cementitious Materials*, Ph.D. thesis, TU Delft (2012).

[33] M. Zhang, *Multiscale lattice Boltzman- finite element modelling of transport properties in cement-based materials*, Ph.D. thesis, TU Delft (2013).

[34] K. V. Breugel, *Durability : Key issues in perspective,* in *1st International Conference on Microstructure Related Durability of Cementitious Composites 13-15 October 2008*, October (2008) pp. 323–332.

[35] S. Molins, D. Trebotich, C. I. Steefel, and C. Shen, *An investigation of the effect of pore scale flow on average geochemical reaction rates using direct numerical simulation,* Water Resources Research **48**, 1 (2012).

[36] L. Li, C. a. Peters, and M. a. Celia, *Upscaling geochemical reaction rates using pore-scale network modeling,* Advances in Water Resources **29**, 1351 (2006).

[37] A. Raoof, H. Nick, T. Wolterbeek, and C. Spiers, *Pore-scale modeling of reactive transport in wellbore cement under CO2 storage conditions,* International Journal of Greenhouse Gas Control **11**, S67 (2012).

[38] E. M. Ryan, A. M. Tartakovsky, and C. Amon, *Pore-scale modeling of competitive adsorption in porous media.* Journal of contaminant hydrology **120-121**, 56 (2011).

[39] A. M. Tartakovsky, P. Meakin, T. D. Scheibe, and B. D. Wood, *A smoothed particle hydrodynamics model for reactive transport and mineral precipitation in porous and fractured porous media,* Water Resources Research **43**, W05437 (2007).

[40] G. O'Brien and C. Bean, *A comparison of published experimental data with a coupled lattice Boltzmann-analytic advection-diffusion method for reactive transport in porous media,* Journal of Hydrology **268**, 143 (2002).

[41] R. Verberg and A. J. C. Ladd, *Simulation of chemical erosion in rough fractures,* Physical Review E **65**, 1 (2002).

[42] H. Yoon, A. J. Valocchi, C. J. Werth, and T. Dewers, *Pore-scale simulation of mixing-induced calcium carbonate precipitation and dissolution in a microfluidic pore network,* Water Resources Research **48**, 1 (2012).

[43] D. Yu and A. J. C. Ladd, *A numerical simulation method for dissolution in porous and fractured media,* Journal of Computational Physics **229**, 6450 (2010).

[44] Q. Kang, P. C. Lichtner, and D. Zhang, *Lattice Boltzmann pore-scale model for multicomponent reactive transport in porous media,* Journal of Geophysical Research: Solid Earth **111**, 1 (2006).

[45] Q. Kang, P. C. Lichtner, and D. Zhang, *An improved lattice Boltzmann model for multicomponent reactive transport in porous media at the pore scale,* Water Resources Research **43**, 1 (2007).

[46] Q. Kang, P. C. Lichtner, and D. R. Janecky, *Lattice boltzmann method for reacting flows in porous media,* Advances in Applied Mathematics and Mechanics **2**, 545 (2010).

[47] S. Sullivan, F. Sani, M. Johns, and L. Gladden, *Simulation of packed bed reactors using lattice Boltzmann methods,* Chemical Engineering Science **60**, 3405 (2005).

[48] X. Zhang, J. W. Crawford, and I. M. Young, *Does pore water velocity affect the reaction rates of adsorptive solute transport in soils? Demonstration with pore-scale modelling,* Advances in Water Resources **31**, 425 (2008).

[49] F. Verhaeghe, S. Arnout, B. Blanpain, and P. Wollants, *Lattice-Boltzmann modeling of dissolution phenomena,* Physical Review E - Statistical, Nonlinear, and Soft Matter Physics **73**, 036316 (2006).

[50] F. Verhaeghe, J. Liu, M. Guo, S. Arnout, B. Blanpain, and P. Wollants, *Dissolution and diffusion behavior of Al2O3 in a CaO- Al2O3-SiO2 liquid: An experimental-numerical approach,* Applied Physics Letters **91**, 124104 (2007).

[51] A. Hiorth, E. Jettestuen, L. Cathles, and M. Madland, *Precipitation, dissolution, and ion exchange processes coupled with a lattice Boltzmann advection diffusion solver,* Geochimica et Cosmochimica Acta **104**, 99 (2013).

[52] K. Van Breugel, *Simulation of hydration and formation of structure in hardening cement-based materials*, Ph.D. thesis, TU Delft (1991).

[53] J. Thomas, J. Biernacki, and J. Bullard, *Modeling and simulation of cement hydration kinetics and microstructure development,* Cement and Concrete Research **41**, 1257 (2011).

[54] G. Ye, *Experimental Study and Numerical Simulation of the Development of the Microstructure and Permeability of Cementitious Materials*, Ph.D. thesis, TU Delft (2003).

[55] S. Bishnoi and K. Scrivener, *Micro-Structural Modelling of cementitious materials using vector approach,* in *Congress on the Chemistry of Cement* (2007).

[56] S. Bishnoi and K. L. Scrivener, *μic : A new platform for modelling the hydration of cements,* Cement and Concrete Research **39**, 266 (2009).

[57] C. Pignat, P. Navi, and K. Scrivener, *Simulation of cement paste microstructure hydration, pore space characterization and permeability determination,* Materials and Structures **38**, 459 (2005).

[58] P. Navi and C. Pignat, *Three-dimensional characterization of the pore structure of a simulated cement paste,* Cement and Concrete Research **29**, 507 (1999).

[59] D. Bentz, P. Coveney, E. Garboczi, M. Kleyn, and P. Stutzman, *Cellular automaton simulations of cement hydration and microstructure development,* Modelling and Simulation in Materials Science and Engineering **2**, 783 (1994).

[60] J. W. Bullard, E. Enjolras, W. L. George, S. G. Satterfield, and J. E. Terrill, *A parallel reaction-transport model applied to cement hydration and microstructure development,* Modelling and Simulation in Materials Science and Engineering **18**, 025007 (2010).

[61] `http://www.citg.tudelft.nl/index.php?id=17650&L=1`, accessed: 2015-09-24.

[62] `http://www.nist.gov/el/building_materials/evcctl.cfm`, accessed: 2015-09-24.

[63] N. Van Tuan, *Rice husk ash as a mineral admixture for ultra high performance concrete*, Ph.D. thesis, Tu Delft (2011).

[64] D. L. Parkhurst and C. Appelo, *Description of Input and Examples for PHREEQC Version 3 A Computer Program for Speciation , Batch-Reaction , One-Dimensional Transport , and Inverse Geochemical Calculations Chapter 43 of,* in *Modeling Techniques* (2013) Chap. chap. A43, pp. 1–678.

[65] U. Frisch, B. Hasslacher, and Y. Pomeau, *Lattice-Gas Automata for the Navier-Stokes Equation,* Physical Review Letters **56**, 1505 (1986).

[66] F. J. Higuera and J. Jimenez, *Boltzmann Approach to Lattice Gas Simulations,* Europhysics Letters (EPL) **9**, 663 (1989).

[67] F. Higuera, S. Succi, and R. Benzi, *Lattice gas dynamics with enhanced collisions,* Europhysics Letters (EPL) **9**, 345 (1989).

[68] Y. Qian, D. D'Humieres, and P. Lallemand, *Lattice BGK models for Navier-Stokes equation,* Europhysics Letters (EPL) **17**, 479 (1992).

[69] P. Bhatnagar, E. Gross, and M. Krook, *A model for collision processes in gases. I. Small amplitude processes in charged and neutral one-component systems,* Physical review **94**, 511 (1954).

[70] D. D'Humieres, I. Ginzburg, M. Krafczyk, P. Lallemand, and L.-S. Luo, Philosophical Transactions of the Royal Society of London A: Mathematical, Physical and Engineering Sciences **360**, 437 (2002).

[71] E. Flekkoy, *Lattice Bhatnagar-Gross-Krook models for miscible fluids,* Physical Review E **47**, 4247 (1993).

[72] H. Chen, I. Goldhirsch, and S. A. Orszag, *Discrete Rotational Symmetry, Moment Isotropy, and Higher Order Lattice Boltzmann Models,* Journal of Scientific Computing **34**, 87 (2007).

[73] I. Ginzburg, *Equilibrium-type and link-type lattice Boltzmann models for generic advection and anisotropic-dispersion equation,* Advances in Water Resources **28**, 1171 (2005).

[74] B. Servan-Camas, *Lattice Boltzmann modeling for mass transport equations in porous media*, Ph.D. thesis, Louisiana State University and Agricultural and Mechanical College (2008).

[75] J. Latt, *Hydrodynamic limit of lattice Boltzmann equations*, Ph.D. thesis, Universite De Geneve (2007).

[76] J. Latt, *Technical report : How to implement your DdQq dynamics with only q variables per node (instead of 2q)*, Tech. Rep. 1 (2007).

[77] K. Mattila, J. Hyvaluoma, J. Timonen, and T. Rossi, *Comparison of implementations of the lattice-Boltzmann method,* Computers & Mathematics with Applications **55**, 1514 (2008).

[78] M. Wittmann, T. Zeiser, G. Hager, and G. Wellein, *Comparison of different propagation steps for lattice Boltzmann methods,* Computers & Mathematics with Applications **65**, 924 (2013).

[79] S. Suga, *Numerical schemes obtained From lattice Boltzmann equations for advection Diffusion Equations,* International Journal of Modern Physics C **17**, 1563 (2006).

[80] P. Lallemand and L.-S. Luo, *Theory of the lattice Boltzmann method: dispersion, dissipation, isotropy, Galilean invariance, and stability,* Physical review. E **61**, 6546 (2000).

[81] H. Yoshida and M. Nagaoka, *Multiple-relaxation-time lattice Boltzmann model for the convection and anisotropic diffusion equation,* Journal of Computational Physics **229**, 7774 (2010).

[82] R. Cornubert, D. D'Humières, and D. Levermore, *A Knudsen layer theory for lattice gases,* Physica D: Nonlinear Phenomena **47**, 241 (1991).

[83] D. Ziegler, *Boundary conditions for lattice Boltzmann simulations,* Journal of Statistical Physics **71**, 1171 (1993).

[84] M. A. Gallivan, D. R. Noble, J. G. Georgiadis, and R. O. Buckius, *an Evaluation of the BounceBack Boundary Condition for Lattice Boltzmann Simulations,* International Journal for Numerical Methods in Fluids **25**, 249 (1997).

[85] D. Kandhai, A. Koponen, A. Hoekstra, M. Kataja, J. Timonen, and P. Sloot, *Implementation aspects of 3D lattice-BGK: boundaries, accuracy, and a new Fast relaxation method,* Journal of Computational Physics **150**, 482 (1999).

[86] C. Pan, L.-S. Luo, and C. T. Miller, *An evaluation of lattice Boltzmann schemes for porous medium flow simulation,* Computers & Fluids **35**, 898 (2006).

[87] L. Talon, D. Bauer, N. Gland, S. Youssef, H. Auradou, and I. Ginzburg, *Assessment of the two relaxation time Lattice-Boltzmann scheme to simulate Stokes flow in porous media,* Water Resources Research **48** (2012), 10.1029/2011WR011385.

[88] S. Khirevich, I. Ginzburg, and U. Tallarek, *Coarse- and fine-grid numerical behavior of MRT/TRT lattice-Boltzmann schemes in regular and random sphere packings,* Journal of Computational Physics **281**, 708 (2015).

[89] I. Ginzburg, D. D'Humières, and A. Kuzmin, *Optimal stability of advection-diffusion lattice boltzmann models with two relaxation times for positive/negative equilibrium,* Journal of Statistical Physics **139**, 1090 (2010).

[90] B. Servan-Camas and F. T. C. Tsai, *Lattice Boltzmann method with two relaxation times for advection-diffusion equation: Third order analysis and stability analysis,* Advances in Water Resources **31**, 1113 (2008).

[91] A. Kuzmin, I. Ginzburg, and A. Mohamad, *The role of the kinetic parameter in the stability of two-relaxation-time advectiondiffusion lattice Boltzmann schemes,* Computers & Mathematics with Applications **61**, 3417 (2011).

[92] I. Ginzburg, *Consistent lattice Boltzmann schemes for the Brinkman model of porous flow and infinite Chapman-Enskog expansion,* Physical Review E - Statistical, Nonlinear, and Soft Matter Physics **77**, 1 (2008).

[93] J. Perko and R. A. Patel, *Single relaxation time lattice Boltzmann scheme for advective-diffusion problems with large diffusion coeffcient heterogeneities and high advective transport,* Physical Review E **89**, 053309 (2014).

[94] *Lattice dependence of reaction-diffusion in lattice Boltzmann modeling,* Computer Physics Communications **129**, 256 (2000).

[95] P. K. Smolarkiewicz, *A simple positive definite advection scheme with small implicit diffusion,* Monthly Weather Review **11**, 479 (1983).

[96] E. Wexler, *Analytical solutions for one-, two-, and three-dimensional solute transport in ground-water systems with uniform flow*, Tech. Rep. ([Washington, D.C.] :, 1992).

[97] D. D'Humieres and P. Lallemand, *Numerical simulations of hydrodynamics with lattice gas automata in two dimensions,* Complex Systems **1**, 599 (1987).

[98] P. Lavallee, J. P. Boon, and N. Alain, *Lattice Boltzmann Equation for Laminar Boundary flow,* Complex Systems **3**, 317 (1989).

[99] T. Zhang, B. Shi, Z. Guo, Z. Chai, and J. Lu, *General bounce-back scheme for concentration boundary condition in the lattice-Boltzmann method,* Physical Review E **85**, 016701:1 (2012).

[100] I. Ginzburg, *Generic boundary conditions for lattice Boltzmann models and their application to advection and anisotropic dispersion equations,* Advances in Water Resources **28**, 1196 (2005).

[101] Z. Guo, C. Zheng, and B. Shi, *An extrapolation method for boundary conditions in lattice Boltzmann method,* Physics of Fluids **14**, 2007 (2002).

[102] Z. Guo, B. Shi, and C. Zheng, *A coupled lattice BGK model for the Boussinesq equations,* International Journal for Numerical Methods in Fluids **39**, 325 (2002).

[103] J. Latt, B. Chopard, O. Malaspinas, M. Deville, and A. Michler, *Straight velocity boundaries in the lattice Boltzmann method,* Physical Review E - Statistical, Nonlinear, and Soft Matter Physics **77** (2008), 10.1103/PhysRevE.77.056703.

[104] H.-B. Huang, X.-Y. Lu, and M. C. Sukop, *Numerical study of lattice Boltzmann methods for a convectiondiffusion equation coupled with NavierStokes equations,* Journal of Physics A: Mathematical and Theoretical **44**, 055001 (2011).

[105] J. Vazquez, *The Porous Medium Equation: Mathematical Theory*, Oxford Mathematical Monographs (Clarendon Press, 2007).

[106] S. Ghosh, K. Lee, and P. Raghavan, *A multi-level computational model for multiscale damage analysis in composite and porous materials,* International Journal of Solids and Structures **38**, 2335 (2001).

[107] A. Vikhansky and I. Ginzburg, *Taylor dispersion in heterogeneous porous media: Extended method of moments, theory, and modelling with two-relaxation-times lattice Boltzmann scheme,* Physics of Fluids **26**, 022104 (2014).

[108] X. Zhang, a. G. Bengough, L. K. Deeks, J. W. Crawford, and I. M. Young, *A novel three-dimensional lattice Boltzmann model for solute transport in variably saturated porous media,* Water Resources Research **38**, 6 (2002).

[109] S. D. C. Walsh and M. O. Saar, *Macroscale lattice-Boltzmann methods for low Peclet number solute and heat transport in heterogeneous porous media,* Water Resources Research **46**, W07517 (2010).

[110] P. Lichtner, *Continuum formulation of multicomponent-multiphase reactive transport,* Reviews in Mineralogy and Geochemistry **34**, 1996 (1996).

[111] C. Appelo and D. Postma, *Geochemistry, Groundwater and Pollution*, 2nd ed. (CRC Press, 2005).

[112] C. I. Steefel, C. A. J. Appelo, B. Arora, D. Jacques, T. Kalbacher, O. Kolditz, V. Lagneau, P. C. Lichtner, K. U. Mayer, J. C. L. Meeussen, S. Molins, D. Moulton, H. Shao, J. Šimnek, N. Spycher, S. B. Yabusaki, and G. T. Yeh, *Reactive transport codes for subsurface environmental simulation,* Computational Geosciences **19**, 445 (2014).

[113] M. Dentz, T. Le Borgne, A. Englert, and B. Bijeljic, *Mixing, spreading and reaction in heterogeneous media: a brief review.* Journal of contaminant hydrology **120-121**, 1 (2011).

[114] C. I. Steefel and K. Maher, *Fluid-Rock Interaction: A Reactive Transport Approach,* Reviews in Mineralogy and Geochemistry **70**, 485 (2009).

[115] C. I. Steefel and K. T. B. MacQuarrie, *Approaches to modeling of reactive transport in porous media,* Reviews in Mineralogy and Geochemistry **34**, 85 (1996).

[116] P. J. Dellar, *An interpretation and derivation of the lattice Boltzmann method using Strang splitting,* Computers and Mathematics with Applications **65**, 129 (2013).

[117] R. A. Patel, J. Perko, D. Jacques, G. De Schutter, K. Van Breugel, and G. Ye, *A versatile pore-scale multicomponent reactive transport approach based on lattice Boltzmann method: Application to portlandite dissolution,* Physics and Chemistry of the Earth **70-71**, 127 (2014).

[118] R. A. Patel, J. Perko, D. Jacques, G. De Schutter, G. Ye, and K. V. Breugel, *Lattice Boltzmann based multicomponent reactive transport model coupled with geochemical solver for pore scale simulations,* in *V International Conference on Computational Methods for Coupled Problems in Science and Engineering, COUPLED PROBLEMS 2013*, edited by S. Idelsohn, M. Papadrakakis, and B. Schrefler (CIMNE, Barcelona, Ibiza, Spain, 2013) pp. 806–817.

[119] J. Allison, D. Brown, and K. Novo-Gradac, *MINTEQA2/PRODEFA2, A Geographical Assessment Model For Environmental Systems: Version 3.0 User's Manual*, Tech. Rep. (Environmental Research Laboratory, Georgia, USA, 1991).

[120] Bethke, C.M., and Yeakel, *The Geochemist's Workbench User's Guides, Version 9.0.*, Tech. Rep. (Aqueous Solutions LLC, Champaign, IL, 2011).

[121] D. A. Kulik, T. Wagner, S. V. Dmytrieva, G. Kosakowski, F. F. Hingerl, K. V. Chudnenko, and U. R. Berner, *GEM-Selektor geochemical modeling package: Revised algorithm and GEMS3K numerical kernel for coupled simulation codes,* Computational Geosciences **17**, 1 (2013).

[122] H. S. Carslow and J. C. Jaeger, *Conduction of Heat in Solids* (Oxford Uni. Press, Newyork, 1986) p. 378.

[123] D. Jacques, L. Wang, E. Martens, and D. Mallants, *Modelling chemical degradation of concrete during leaching with rain and soil water types,* Cement and Concrete Research **40**, 1306 (2010).

[124] B. Lothenbach, *Thermodynamic equilibrium calculations in cementitious systems,* Materials and Structures **43**, 1413 (2010).

[125] D. Jacques, *Benchmarking of the cement model and detrimental chemical reactions including temperature dependent parameters*, Tech. Rep. (NIROND-TR report 200830 E, SCK•CEN, 2009).

[126] B. Lothenbach, T. Matschei, G. Moschner, and F. Glasser, *Thermodynamic modelling of the effect of temperature on the hydration and porosity of Portland cement,* Cement and Concrete Research **38**, 1 (2008).

[127] S. R. Charlton and D. L. Parkhurst, *Modules based on the geochemical model PHREEQC for use in scripting and programming languages,* Computers & Geosciences **37**, 1653 (2011).

[128] H. Aaron, D. Fainstein, and G. Kotler, *DiffusionLimited Phase Transformations: A Comparison and Critical Evaluation of the Mathematical Approximations,* Journal of applied physics **41**, 4404 (1970).

[129] L. Wissmeier and D. Barry, *Simulation tool for variably saturated flow with comprehensive geochemical reactions in two- and three-dimensional domains,* Environmental Modelling & Software **26**, 210 (2011).

[130] R. J. Millington and J. P. Quirk, *Permeability of porous solids,* Transactions of the Faraday Society **57**, 1200 (1961).

[131] D. A. Kulik, *Improving the structural consistency of C-S-H solid solution thermodynamic models,* Cement and Concrete Research **41**, 477 (2011).

[132] D. Jacques, J. Simnek, D. Mallants, and M. T. van Genuchten, *Operator-splitting errors in coupled reactive transport codes for transient variably saturated flow and contaminant transport in layered soil profiles.* Journal of contaminant hydrology **88**, 197 (2006).

[133] R. A. Patel, J. Perko, D. Jacques, G. De Schutter, G. Ye, and K. V. BREUGEL, *application of porescale reactive transport model to study the influence of pore network characteristics on calcium leaching in cementitious material,* in *CONMOD 2014* (Beijing, China, 2014) pp. 359–366.

[134] M. Wang, J. Wang, N. Pan, and S. Chen, *Mesoscopic predictions of the effective thermal conductivity for microscale random porous media,* Physical Review E **75**, 036702 (2007).

[135] G. Van Der Wegen, R. B. Polder, and K. Van Breugel, *Guideline for service life design of structural concrete - A performance based approach with regard to chloride induced corrosion,* Heron **57**, 153 (2012).

[136] C. D. Shackelford and D. E. Daniel, *Diffusion in Saturated Soil. I: Background,* Journal of Geotechnical Engineering **117**, 467 (1991).

[137] E. J. Garboczi and D. P. Bentz, *Computer simulation of the diffusivity of cement-based materials,* Journal of Materials Science **27**, 2083 (1992).

[138] Y. Ichikawa, K. Kawamura, N. Fujii, and T. Nattavut, *Molecular dynamics and multiscale homogenization analysis of seepage/diffusion problem in bentonite clay,* International Journal for Numerical Methods in Engineering **54**, 1717 (2002).

[139] S. Numata, H. Amano, and K. Minami, *Diffusion of tritiated water in cement materials,* Journal of Nuclear Materials **171**, 373 (1990).

[140] E. Revertegat, C. Richet, and P. Gégout, *Effect of pH on the durability of cement pastes,* Cement and Concrete Research **22**, 259 (1992).

[141] M. Castellote, C. Alonso, C. Andrade, G. a. Chadbourn, and C. L. Page, *Oxygen and chloride diffusion in cement pastes as a validation of chloride diffusion coefficients obtained by steady-state migration tests,* Cement and Concrete Research **31**, 621 (2001).

[142] T. Yamaguchi, K. Negishi, S. Hoshino, and T. Tanaka, *Modeling of diffusive mass transport in micropores in cement based materials,* Cement and Concrete Research **39**, 1149 (2009).

[143] P. Tumidajski, A. S. Schumacher, S. Perron, P. Gu, and J. Beaudoin, *On the relationship between porosity and electrical resistivity in cementitous systems,* Cement and Concrete Research **26**, 539 (1996).

[144] G. G. Taffinder and B. Batchelor, *Measurement of effective diffusivities in solidified wastes,* Journal of Environmental Engineering **119**, 17 (1993).

[145] B. J. Christensen, T. O. Mason, H. M. Jennings, D. P. Bentz, and E. J. Garboczi, *Experimental and computer simulation results for the electrical conductivity of portland cement paste,* Materials Research Society Symposium Proceeding **245**, 259 (1992).

[146] B. H. Oh and S. Y. Jang, *Prediction of diffusivity of concrete based on simple analytic equations,* Cement and Concrete Research **34**, 463 (2004).

[147] G.-W. Sun, W. Sun, Y.-s. Zhang, and Z.-y. Liu, *Relationship between chloride diffusivity and pore structure of hardened cement paste,* Journal of Zhejiang University SCIENCE A **12**, 360 (2011).

[148] T. C. Hansen, *Physical structure of hardened cement paste,* Materials and Structures **19**, 423 (1986).

[149] D. P. Bentz and E. J. Garboczi, *Percolation of phases in a tiiree-dimensional cement paste microstructural model,* Cement and Concrete Research **21**, 325 (1991).

[150] R. Spragg, C. Villani, K. Snyder, D. Bentz, J. W. Bullard, and J. Weiss, *Factors that influence electrical resistivity measurements in cementitious Systems,* Transportation Research Record: Journal of the Transportation Research Board **2342**, 90 (2013).

[151] G. Archie, *The electrical resistivity log as an aid in determining some reservoir characteristics,* Trans.Transactions of the American institute of mineralogy and metallurgy **146**, 54 (1942), arXiv:942054-G [10.2118] .

[152] K. K. Aligizaki, *Pore structure of cement-based materials: testing, interpretation and requirements* (CRC Press, 2005) p. 432.

[153] A. Atkinson and A. K. Nickerson, *The diffusion of ions through water-saturated cement,* Journal of Materials Science **19**, 3068 (1984).

[154] J. M. Galíndez and J. Molinero, *Assessment of the long-term stability of cementitious barriers of radioactive waste repositories by using digital-image-based microstructure generation and reactive transport modelling,* Cement and Concrete Research **40**, 1278 (2010).

[155] W. O. Winsauer, H. M. Shearin Jr., P. H. Masson, and M. Williams, *Resistivity of Brine-Saturated Sands in Relation to Pore Geometry*, (1952).

[156] J. V. D. Lee, L. D. Windt, and V. Lagneau, *Application of reactive transport models in cement based porous media,* in *International RILEM Symposium on Concrete Modelling CONMOD08*, May (2008) pp. 463–470.

[157] M. Mainguy, C. Tognazzi, J. M. Torrenti, and F. Adenot, *Modelling of leaching in pure cement paste and mortar,* Cement and Concrete Research **30**, 83 (2000).

[158] J. Walton, L. Plansky, and R. Smith, *Models for estimation of service life of concrete barriers in low-level radioactive waste disposal*, Tech. Rep. (Idaho National Engineering Laboratory (United States), 1990).

[159] D. P. Bentz, E. J. Garboczi, C. J. Haecker, and O. M. Jensen, *Effects of cement particle size distribution on performance properties of Portland cement-based materials,* Cement and Concrete Research **29**, 1663 (1999).

[160] G. Ye, *Percolation of capillary pores in hardening cement pastes,* Cement and Concrete Research **35**, 167 (2005).

[161] G. Ye and K. Van Breugel, *Three-dimensional microstructure simulation model of cement based materials,* Heron **48**, 251 (2003).

[162] E. J. Garboczi and D. P. Bentz, *The effect of statistical fluctuation, finite size error, and digital resolution on the phase percolation and transport properties of the NIST cement hydration model,* Cement and Concrete Research **31**, 1501 (2001).

[163] S. Torquato, *Random Heterogeneous Materials: Microstructure and Macroscopic Properties* (Springer Science & Business Media, 2013) p. 703.

[164] P. Pivonka, C. Hellmich, and D. Smith, *Microscopic effects on chloride diffusivity of cement pastes-a scale-transition analysis,* Cement and Concrete Research **34**, 2251 (2004).

[165] B. Bary and S. Béjaoui, *Assessment of diffusive and mechanical properties of hardened cement pastes using a multi-coated sphere assemblage model,* Cement and Concrete Research **36**, 245 (2006).

[166] G. W. Milton, *Concerning bounds on the transport and mechanical properties of multicomponent composite materials,* Applied Physics A Solids and Surfaces **26**, 125 (1981).

[167] E. Stora, B. Bary, and Q. C. He, *On estimating the effective diffusive properties of hardened cement pastes,* Transport in Porous Media **73**, 279 (2008).

[168] E. Stora, Q.-C. He, and B. Bary, *A mixed composite spheres assemblage model for the transport properties of random heterogeneous materials with high contrasts,* Journal of Applied Physics **100**, 084910 (2006).

[169] E. Stora, B. Bary, Q.-C. He, E. Deville, and P. Montarnal, *Modelling and simulations of the chemo-mechanical behaviour of leached cement-based materials,* Cement and Concrete Research **39**, 763 (2009).

[170] W. Dridi, *Analysis of effective diffusivity of cement based materials by multi-scale modelling,* Materials and Structures , 313 (2012).

[171] X. Liu, R. Lackner, and C. Pichler, *Highlighting the effect of gel-Pore diffusivity on the effective diffusivity of cement paste A multiscale investigation,* in *Computational Structural Engineering,* edited by Y. Uan, J. Cui, and H. A. Mang (Springer Netherlands, 2009) pp. 973–981.

[172] O. Bernard, F. J. Ulm, and E. Lemarchand, *A multiscale micromechanics-hydration model for the early-age elastic properties of cement-based materials,* Cement and Concrete Research **33**, 1293 (2003).

[173] S. Kamali-Bernard, F. Bernard, and W. Prince, *Computer modelling of tritiated water diffusion test for cement based materials,* Computational Materials Science **45**, 528 (2009).

[174] N. Ukrainczyk and E. A. B. Koenders, *Representative elementary volumes for 3D modeling of mass transport in cementitious materials,* Modelling and Simulation in Materials Science and Engineering **22**, 035001 (2014).

[175] M. Zhang, G. Ye, and K. Van Breugel, *Microstructure-based modeling of water diffusivity in cement paste,* Construction and Building Materials **25**, 2046 (2011).

[176] L. Liu, H. Chen, W. Sun, and G. Ye, *Microstructure-based modeling of the diffusivity of cement paste with micro-cracks,* Construction and Building Materials **38**, 1107 (2013).

[177] L. Liu, W. Sun, G. Ye, H. Chen, and Z. Qian, *Estimation of the ionic diffusivity of virtual cement paste by random walk algorithm,* Construction and Building Materials **28**, 405 (2012).

[178] M. Zhang, G. Ye, and K. Van Breugel, *Modeling of ionic diffusivity in non-saturated cement-based materials using lattice Boltzmann method,* Cement and Concrete Research **42**, 1524 (2012).

[179] M. a. B. Promentilla, T. Sugiyama, T. Hitomi, and N. Takeda, *Quantification of tortuosity in hardened cement pastes using synchrotron-based X-ray computed microtomography,* Cement and Concrete Research **39**, 548 (2009).

[180] M. Karim and K. Krabbenhoft, *Extraction of effective cement paste diffusivities from x-ray microtomography scans,* Transport in Porous Media **84**, 371 (2010).

[181] D. Bentz, S. Mizell, S. Satterfield, J. Devaney, W. George, P. Ketcham, J. Graham, J. Porterfield, D. Quenard, F. Vallee, H. Sallee, E. Boller, and J. Baruchel, *The Visible Cement Data Set,* Journal of Research of the National Institute of Standards and Technology **107**, 137 (2002).

[182] M. Zhang, Y. He, G. Ye, D. a. Lange, and K. V. Breugel, *Computational investigation on mass diffusivity in Portland cement paste based on X-ray computed microtomography (uCT) image,* Construction and Building Materials **27**, 472 (2012).

[183] K. Kurumisawa, T. Nawa, and H. Owada, *Prediction of the diffusivity of cement-based materials using a three-dimensional spatial distribution model,* Cement and Concrete Composites **34**, 408 (2012).

[184] R. A. Olson, B. J. Christensen, R. T. Coverdale, S. J. Ford, G. M. Moss, H. Jennings, and T. O. Mason, *Interpretation of the impedance spectroscopy of cement paste via computer modelling Part lll Microstructural analysis of frozen,* Journal of Materials Science **30**, 5078 (1995).

[185] D. P. Bentz, *Capillary porosity depercolation/repercolation in hydrating cement pastes via low-temperature calorimetry measurements and CEMHYD3D modeling,* Journal of the American Ceramic Society **89**, 2606 (2006).

[186] M. Hain, K. Krabbenhoft, and P. Wriggers, *Computation of effective cement paste diffusivities from microtomographic images,* (2007).

[187] M. Z. Zhang, G. Ye, and K. Van Breugel, *A numerical-statistical approach to determining the representative element volume (REV) of cement paste for measuring diffusivity,* Materiales de Construcción **60**, 7 (2010).

[188] D. P. Bentz, O. M. Jensen, A. M. Coats, and F. P. Glasser, *Influence of silica fume on diffusivity in cement-based materials I. Experimental and computer modeling studies on cement pastes,* Cement and Concrete Research **30**, 953 (2000).

[189] S. Goto and D. M. Roy, *Diffusion of ions through hardened cement pastes,* Cement and Concrete Research **11**, 751 (1981).

[190] K. Nakarai, T. Ishida, and K. Maekawa, *Modeling of calcium leaching from cement hydrates coupled with micro-pore formation,* Journal Of advanced concrete technology **4**, 395 (2006).

[191] K. Markov and L. Preziosi, *Heterogeneous media micromechanics modeling methods and simulations* (Springer Science Business Media, 2000) p. 477.

[192] R. Hill, *Elastic properties of reinforced solids: Some theoretical principles,* Journal of the Mechanics and Physics of Solids **11**, 357 (1963).

[193] P. E. Gill and W. Murray, *Algorithms for the solution of the nonlinear least-squares problem,* SIAM Journal on Numerical Analysis **15**, 977 (1978).

[194] `http://docs.scipy.org/doc/scipy/reference/tutorial/optimize.html`, accessed: 2015-09-24.

[195] H. Jennings and P. Tennis, *Model for the developing microstructure in Portland cement pastes,* Journal of the American Ceramic Society **77**, 3161 (1994).

[196] H. Jennings, J. Thomas, J. Gevrenov, G. Constantinides, and F. Ulm, *A multi-technique investigation of the nanoporosity of cement paste,* Cement and Concrete Research **37**, 329 (2007).

[197] G. Constantinides and F.-J. Ulm, *The nanogranular nature of CSH,* Journal of the Mechanics and Physics of Solids **55**, 64 (2007).

[198] F. Ulm and G. Constantinides, *Is concrete a poromechanics material ? - A multiscale investigation of poroelastic properties,* Materials and structures **37**, 43 (2004).

[199] H. Jennings, *Refinements to colloid model of C-S-H in cement: CM-II,* Cement and Concrete Research **38**, 275 (2008).

[200] S. Garrault, E. Finot, E. Lesniewska, and A. Nonat, *Study of C-S-H growth on C_3S surface during its early hydration,* Materials and Structures **38**, 435 (2005).

[201] J. Sanahuja, L. Dormieux, and G. Chanvillard, *Modelling elasticity of a hydrating cement paste,* Cement and Concrete Research **37**, 1427 (2007).

[202] W.-S. Chiang, E. Fratini, P. Baglioni, D. Liu, and S.-H. Chen, *Microstructure Determination of Calcium-Silicate-Hydrate Globules by Small-Angle Neutron Scattering,* The Journal of Physical Chemistry C **116**, 5055 (2012).

[203] H. M. Jennings, B. J. Dalgleish, and P. L. Pratt, *Morphological development of hydrating tricalcium silicate as examined by electron microscopy techniques,* Journal of the American Ceramic Society **64**, 567 (1981).

[204] V. Smilauer and Z. Bittnar, *Microstructure-based micromechanical prediction of elastic properties in hydrating cement paste,* Cement and Concrete Research **36**, 1708 (2006).

[205] L. Weber, J. Dorn, and A. Mortensen, *On the electrical conductivity of metal matrix composites containing high volume fractions of non-conducting inclusions,* Acta Materialia **51**, 3199 (2003).

[206] N. Phan-Thien and D. Pham, *Differential multiphase models for polydispersed spheroidal inclusions: thermal conductivity and effective viscosity,* International Journal of Engineering Science **38**, 73 (2000).

[207] C. Page, N. Short, and A. El Tarras, *Diffusion of chloride ions in hardened cement pastes,* Cement and Concrete Research **11**, 395 (1981).

[208] M. Zhang, *Multiscale lattice Boltzman- finite element modelling of transport properties in cement-based materials*, Ph.D. thesis, TU Delft (2013).

[209] C. Andrade and R. Andrea, *Electrical resistivity as microstructural parameter for modelling of service life of reinforced concrete structures,* in *2nd International Symposium on Service Life Design for Infrastructure*, October, edited by K. van Breugel, G. Ye, and Y. Yuan (RILEM Publications SARL, Delft, Netherlands, 2010) pp. 379–388.

[210] T. Luping, L.-O. Nilsson, and P. A. M. Basheer, *Resistance of chlorides to chloride Ingress: testing and modelling* (2012) p. 241.

[211] V. Baroghel-Bouny, K. Kinomura, M. Thiery, and S. Moscardelli, *Easy assessment of durability indicators for service life prediction or quality control of concretes with high volumes of supplementary cementitious materials,* Cement and Concrete Composites **33**, 832 (2011).

[212] V. Ngala, C. Page, L. Parrott, and S. Yu, *Diffusion in cementitious materials: II, further investigations of chloride and oxygen diffusion in well-cured OPC and OPC/30%PFA pastes,* Cement and Concrete Research **25**, 819 (1995).

[213] F. Adenot and M. Buil, *Modelling of the corrosion of the cement paste by deionized water,* Cement and Concrete Research **22**, 489 (1992).

[214] P. Faucon, P. Le Bescop, F. Adenot, P. Bonville, J. F. Jacquinot, F. Pineau, and B. Felix, *Leaching of cement: Study of the surface layer,* Cement and Concrete Research **26**, 1707 (1996).

[215] J. Jain and N. Neithalath, *Analysis of calcium leaching behavior of plain and modified cement pastes in pure water,* Cement and Concrete Composites **31**, 176 (2009).

[216] C. L. Bellego, B. Gerard, and G. Pijaudier-Cabot, *Chemo-Mechanical Effects in Mortar Beams Subjected to Water Hydrolysis,* Journal of Engineering Mechanics **126**, 266 (2000).

[217] C. Carde and R. François, *Effect of the leaching of calcium hydroxide from cement paste on mechanical and physical properties,* Cement and Concrete Research **27**, 539 (1997).

[218] C. Carde and R. Franćois, *Effect of ITZ leaching on durability of cement-based materials,* Cement and Concrete Research **27**, 971 (1997).

[219] J. Chen, J. J. Thomas, H. F. Taylor, and H. M. Jennings, *Solubility and structure of calcium silicate hydrate,* Cement and Concrete Research **34**, 1499 (2004).

[220] J. Chen, J. Thomas, and H. Jennings, *Decalcification shrinkage of cement paste,* Cement and Concrete Research **36**, 801 (2006).

[221] N. Burlion, D. Bernard, and D. Chen, *X-ray microtomography: Application to microstructure analysis of a cementitious material during leaching process,* Cement and Concrete Research **36**, 346 (2006).

[222] J. J. Thomas, J. J. Chen, A. J. Allen, and H. M. Jennings, *Effects of decalcification on the microstructure and surface area of cement and tricalcium silicate pastes,* Cement and Concrete Research **34**, 2297 (2004).

[223] C. Galle, P. Le Bescop, and H. Peycelon, *Effect of an accelerated chemical degradation on water permeability and pore structure of cementbased materials,* Advances in Cement Research **16**, 105 (2004).

[224] M. Moranville, S. Kamali, and E. Guillon, *Physicochemical equilibria of cement-based materials in aggressive environments - Experiment and modeling,* Cement and Concrete Research **34**, 1569 (2004).

[225] F. Bernard and S. Kamali-Bernard, *Performance simulation and quantitative analysis of cement-based materials subjected to leaching,* Computational Materials Science **50**, 218 (2010).

[226] V. Nguyen, H. Colina, J. Torrenti, C. Boulay, and B. Nedjar, *Chemo-mechanical coupling behaviour of leached concretePart I: Experimental results,* Nuclear Engineering and Design **237**, 2083 (2007).

[227] K. Wan, Y. Li, and W. Sun, *Experimental and modelling research of the accelerated calcium leaching of cement paste in ammonium nitrate solution,* Construction and Building Materials **40**, 832 (2013).

[228] H. Yang, L. Jiang, Y. Zhang, Q. Pu, and Y. Xu, *Predicting the calcium leaching behavior of cement pastes in aggressive environments,* Construction and Building Materials **29**, 88 (2012).

[229] M. Mainguy and O. Coussy, *Propagation Fronts during Calcium Leaching and Chloride Penetration,* Journal of Engineering Mechanics **126**, 250 (2000).

[230] H. Saito and S. Nakane, *Comparison between Diffusion Test and Electrochemical Acceleration Test for Leaching Degradation of Cement Hydration Products,* , 208 (1999).

[231] A. Babaahmadi, L. Tang, Z. Abbas, T. Zack, and P. Martensson, *Development of an electro-chemical accelerated ageing method for leaching of calcium from cementitious materials,* Materials and Structures , 1 (2015).

[232] T. Ekström, *leaching of concrete The leaching process and its effects*, Ph.D. thesis, Lund university.

[233] U. R. Berner, *Evolution of pore water chemistry during degradation of cement in a radioactive waste repository environment,* Waste Management **12**, 201 (1992).

[234] D. Jacques, J. Perko, S. Seetharam, and D. Mallants, *A cement degradation model for evaluating the evolution of retardation factors in radionuclide leaching models,* Applied Geochemistry **49**, 143 (2014).

[235] P. Blanc, X. Bourbon, A. Lassin, and E. Gaucher, *Chemical model for cement-based materials: Temperature dependence of thermodynamic functions for nanocrystalline and crystalline CSH phases,* Cement and Concrete Research **40**, 851 (2010).

[236] M. Moranville, S. Kamali, and E. Guillon, *Physicochemical equilibria of cement-based materials in aggressive environmentsexperiment and modeling,* Cement and Concrete Research **34**, 1569 (2004).

[237] S. Poyet, P. Le Bescop, M. Pierre, L. Chomat, and C. Blanc, *Accelerated leaching of cementitious materials using ammonium nitrate (6M): influence of test conditions,* European Journal of Environmental and Civil Engineering **16**, 336 (2012).

[238] S. Kamali, B. Gérard, and M. Moranville, *Modelling the leaching kinetics of cement-based materialsinfluence of materials and environment,* Cement and Concrete Composites **25**, 451 (2003).

[239] K. Haga, M. Shibata, M. Hironaga, S. Tanaka, and S. Nagasaki, *Change in pore structure and composition of hardened cement paste during the process of dissolution,* Cement and Concrete Research **35**, 943 (2005).

[240] K. Wan, Y. Li, and W. Sun, *Application of tomography for solid calcium distributions in calcium leaching cement paste,* Construction and Building Materials **36**, 913 (2012).

[241] J. Marchand, D. P. Bentz, E. Samson, and Y. Maltais, *Influence of calcium hydroxide dissolution on the transport properties of hydrated cement systems,* Reactions of calcium hydroxide in concrete. Westerville, OH: American Ceramic Society , 113 (2001).

[242] A. Trapote-Barreira, L. Porcar, J. Cama, J. M. Soler, and A. J. Allen, *Structural changes in CSH gel during dissolution: Small-angle neutron scattering and Si-NMR characterization,* Cement and Concrete Research **72**, 76 (2015).

[243] N. Bossa, P. Chaurand, J. Vicente, D. Borschneck, C. Levard, O. Aguerre-Chariol, and J. Rose, *Micro- and nano-X-ray computed-tomography: A step forward in the characterization of the pore network of a leached cement paste,* Cement and Concrete Research **67**, 138 (2015).

[244] K. Wan, Q. Xu, L. Li, and W. Sun, *3D porosity distribution of partly calcium leached cement paste,* Construction and Building Materials **48**, 11 (2013).

[245] E. Revertegat, C. Richet, and P. Gégout, *Effect of pH on the durability of cement pastes,* Cement and Concrete Research **22**, 259 (1992).

[246] B. Huang and C. Qian, *Experiment study of chemo-mechanical coupling behavior of leached concrete,* Construction and Building Materials **25**, 2649 (2011).

[247] F. Heukamp, F.-J. Ulm, and J. Germaine, *Mechanical properties of calcium leached cement paste: triaxial stress states and the influence of pore pressure,* Cement and Concrete Research **31**, 767 (2001).

[248] G. Constantinides and F.-J. Ulm, *The effect of two types of C-S-H on the elasticity of cement-based materials: Results from nanoindentation and micromechanical modeling,* Cement and Concrete Research **34**, 67 (2004).

[249] F. H. Heukamp, F.-J. Ulm, and J. T. Germaine, *Does Calcium Leaching Increase Ductility of Cementitious Materials? Evidence from Direct Tensile Tests,* Journal of Materials in Civil Engineering **17**, 307 (2005).

[250] F. H. Heukamp, F. J. Ulm, and J. T. Germaine, *Poroplastic properties of calcium-leached cement-based materials,* Cement and Concrete Research **33**, 1155 (2003).

[251] C. Carde, R. François, and J. M. Torrenti, *Leaching of both calcium hydroxide and C-S-H from cement paste: Modeling the mechanical behavior,* Cement and Concrete Research **26**, 1257 (1996).

[252] M. Mainguy and O. Coussy, *Propagation Fronts during Calcium Leaching and Chloride Penetration,* Journal of Engineering Mechanics **126**, 250 (2000).

[253] F. Bangert, S. Grasberger, D. Kuhl, and G. Meschke, *Au th o r ' s co py Au th o co,* **70**, 891 (2003).

[254] D. Kuhl and F. Bangert, *Coupled chemo-mechanical deterioration of cementitious materials . Part I : Modeling,* **41**, 15 (2004).

[255] V. Nguyen, B. Nedjar, and J. Torrenti, *A computational setting of calcium leaching in concrete and its coupling with continuum damage mechanics,* Computers and Concrete **1**, 131 (2004).

[256] K. Nakarai, T. Ishida, K. Maekawa, and T. Kishi, *Modeling of calcium leaching from cement hydrates coupled with microstructure formation,* in *International RILEM Symposium on Concrete Modelling CONMOD08,* May (2008) pp. 385–392.

[257] D. Gawin, F. Pesavento, and B. A. Schrefler, *Modeling of cementitious materials exposed to isothermal calcium leaching, considering process kinetics and advective water flow. Part 1: Theoretical model,* International Journal of Solids and Structures **45**, 6221 (2008).

[258] D. Gawin, F. Pesavento, and B. Schrefler, *Modeling deterioration of cementitious materials exposed to calcium leaching in non-isothermal conditions,* Computer Methods in Applied Mechanics and Engineering **198**, 3051 (2009).

[259] D. Kuhl and G. Meschke, *Computational modeling of transport mechanisms in reactive porous media-application to calcium leaching of concrete,* Computational Modelling of Concrete , 473 (2003).

[260] B. Gérard, C. Le Bellego, and O. Bernard, *Simplified modelling of calcium leaching of concrete in various environments,* Materials and Structures **35**, 632 (2002).

[261] Y. Maltais, E. Samson, and J. Marchand, *Predicting the durability of Portland cement systems in aggressive environmentsLaboratory validation,* Cement and Concrete Research **34**, 1579 (2004).

[262] E. Stora, B. Bary, Q.-C. He, E. Deville, and P. Montarnal, *Modelling and simulations of the chemomechanical behaviour of leached cement-based materials,* Cement and Concrete Research **39**, 763 (2009).

[263] J. M. Soler, *Thermodynamic Description of the Solubility of C-S-H Gels in Hydrated Portland Cement*, Tech. Rep. Working Report 2007-88 (2007).

[264] J. Perko, D. Jacques, S. C. Seetharam, and D. Mallants, *Long-term evolution of the near surface disposal facility at Dessel. Project near surface disposal of category A waste at Dessel*, Tech. Rep. (ONDRAF/NIRAS Report. NIRONDTR 201004 E V 1.0, 2010).

[265] V. Nguyen, B. Nedjar, H. Colina, and J. Torrenti, *A separation of scales homogenization analysis for the modelling of calcium leaching in concrete,* Computer Methods in Applied Mechanics and Engineering **195**, 7196 (2006).

[266] A. Morandeau, M. Thiéry, and P. Dangla, *Investigation of the carbonation mechanism of CH and C-S-H in terms of kinetics, microstructure changes and moisture properties,* Cement and Concrete Research **56**, 153 (2014).

[267] M. Mainguy, F. J. Ulm, and F. H. Heukamp, *Similarity properties of demineralization and degradation of cracked porous materials,* International Journal of Solids and Structures **38**, 7079 (2001).

[268] A. Delagrave, B. Gerard, and J. Marchand, *Modeling the calcium laeching mechanisims in hydrated cement paste,* in *Mechanisms of Chemical Degradation of Cement-based Systems*, edited by K. Scrivener and J. Young (CRC Press, 1997) pp. 38–49.

[269] K. A. Snyder and J. Clifton, *4sight manual: A computer program for modelling degradation of underground low level waste concrete vaults*, Tech. Rep. (NISTIR 5612, U.S. Dept. of Commerce, 1995).

[270] R. van Eijk and H. Brouwers, *Study of the relation between hydrated Portland cement composition and leaching resistance,* (1998).

[271] D. Bentz and E. J. Garboczi, *Modelling the leaching of calcium hydroxide from cement paste : effects on pore space percolation and diffusivity,* Materials and Structures **25**, 523 (1992).

[272] P. Feng, C. Miao, and J. W. Bullard, *A model of phase stability, microstructure and properties during leaching of portland cement binders,* Cement and Concrete Composites **49**, 9 (2014).

[273] J. W. Bullard, B. Lothenbach, P. E. Stutzman, and K. a. Snyder, *Coupling thermodynamics and digital image models to simulate hydration and microstructure development of portland cement pastes,* Journal of Materials Research **26**, 609 (2011).

[274] E. Guillon, M. Moranville, and S. Kamali, *Characterization of the mechanical damage of a chemically degraded cement paste,* Materials and Structures **39**, 401 (2006).

[275] F. Bernard and S. Kamali-Bernard, *Performance simulation and quantitative analysis of cement-based materials subjected to leaching,* Computational Materials Science **50**, 218 (2010).

[276] J. J. Gaitero, J. S. Dolado, C. Neuen, F. Heber, and E. Koenders, *Computational 3D simulation of calcium leaching in cement matrices,* in *2nd International conference on Microstructural-related Durability of Cementitious Composites*, April, edited by G. Ye, K. V. Breugel, W. Sun, and C. Miao (2013) pp. 901 – 909.

[277] N. Ukrainczyk and E. A. B. Koenders, *3D simulation of cement paste aging due to reactive transport,* in *RILEM international symposium on concrete modelling (CONMOD 2014)*, edited by K. Li, P. Yan, and R. Yang (RILEM Publications, Beijing, China, 2014) pp. 305–313.

[278] J. Geiser and C. Fleck, *Adaptive step-size control in simulation of diffusive CVD processes,* Mathematical Problems in Engineering **2009**, 1 (2009).

[279] E. Hairer, S. P. Norsett, and G. Wanner, *Solving ordinary differential equations II: stiff and differential-algebraic problems* (Springer Science & Business Media, 1993) p. 614.

[280] G. Soderlind, *Automatic control and adaptive time-stepping,* Numerical Algorithms **31**, 281 (2002).

[281] A. M. P. Valli, G. F. Carey, and A. L. G. A. Coutinho, *Control strategies for timestep selection in finite element simulation of incompressible flows and coupled reaction-convection-diffusion processes,* International Journal for Numerical Methods in Fluids **47**, 201 (2005).

[282] A. M. P. Valli, G. F. Carey, and A. L. G. A. Coutinho, *On decoupled time step/-subcycling and iteration strategies for multiphysics problems,* Communications in Numerical Methods in Engineering **24**, 1941 (2008).

[283] T. Matschei, B. Lothenbach, and F. Glasser, *Thermodynamic properties of Portland cement hydrates in the system CaO-Al_2O_3-SiO_2 $CaSO_4$-$CaCO_3$-H_2O,* Cement and Concrete Research **37**, 1379 (2007).

[284] D. Jacques, *Benchmarking of the cement model and detrimental chemical reactions including temperature dependent parameters*, Tech. Rep. (NIROND-TR report 200830 E, SCK·CEN, 2009).

[285] `http://www.empa.ch/plugin/template/empa/*/62204/---/l=1`, accessed: 2015-09-24.

[286] D. A. Kulik and M. Kersten, *Aqueous solubility diagrams for cementitious waste stabilization systems: II, end-member stoichiometries of ideal calcium silicate hydrate solid solutions,* Journal of the American Ceramic Society **84**, 3017 (2001).

[287] G. Constantinides and F. J. Ulm, *The effect of two types of C-S-H on the elasticity of cement-based materials: Results from nanoindentation and micromechanical modeling,* Cement and Concrete Research **34**, 67 (2004).

[288] F.-J. Ulm and H. M. Jennings, *Does C-S-H particle shape matter? A discussion of the paper Modelling elasticity of a hydrating cement paste, by Julien Sanahuja, Luc Dormieux and Gilles Chanvillard. CCR 37 (2007) 14271439,* Cement and Concrete Research **38**, 1126 (2008).

[289] N. Modi, M. Winterhalter, and U. Kleinekathöfer, *Computational modeling of ion transport through nanopores,* Nanoscale **4**, 6166 (2012).

[290] M. Tagliazucchi and I. Szleifer, *Transport mechanisms in nanopores and nanochannels: can we mimic nature?* Materials Today **18**, 131 (2015).

[291] http://matplotlib.org/, accessed: 2015-10-10.

[292] http://www.paraview.org/, accessed: 2015-10-10.

[293] http://code.enthought.com/projects/mayavi/, accessed: 2015-10-10.

[294] http://python-xy.github.io/, accessed: 2015-10-10.

[295] X. He and L.-S. Luo, *Theory of the lattice Boltzmann method: From the Boltzmann equation to the lattice Boltzmann equation,* **56**, 6811 (1997).

[296] K. Mattila, *Implementation Techniques for the Lattice Boltzmann Method,* Ph.D. thesis (2010).

[297] B. Chopard, A. Dupuis, A. Masselot, and P. Luthi, *cellular automata and lattice Boltzmann techniques: an approach to model and simulate complex systems,* Advances in Complex Systems **05**, 103 (2002).

[298] R. Hill, *Continuum micro-mechanics of elastoplastic polycrystals,* Journal of the Mechanics and Physics of Solids **13**, 89 (1965).

[299] A. Zaoui, *Continuum Micromechanics: Survey,* Journal of Engineering Mechanics (2002).

[300] L. Dormieux, D. Kondo, and F.-J. Ulm, *Microporomechanics* (2006) p. 344.

[301] J. D. Eshelby, *The determination of the elastic field of an ellipsoidal inclusion, and related problems,* Proceedings of the Royal Society A: Mathematical, Physical and Engineering Sciences **241**, 376 (1957).

[302] A. Norris, *A differential scheme for the effective moduli of composites,* Mechanics of Materials **4**, 1 (1985).

[303] P. N. Sen, C. Scala, and M. H. Cohen, *A self-similar model for sedimentary rocks with application to the dielectric constant of fused glass beads,* Geophysics **46**, 781 (1981).

[304] L. Dormieux and D. Kondo, *Diffusive transport in disordered media. Application to the determination of the tortuosity and the permeability of cracked materials.* in *Applied Micromechanics of Porous Materials*, CISM International Centre for Mechanical Sciences, Vol. 480, edited by L. Dormieux and F.-J. Ulm (Springer Vienna, Vienna, 2005) pp. 83–106.

[305] `http://stackoverflow.com/questions/9878558/scipy-optimize-leastsq-with-bound-constraints`, accessed: 2015-09-24.

Ravi A. Patel ✉ ravee.a.patel@gmail.com

Personal

Date of birth	7th March 1988
Nationality	Indian
Martial status	Single

Education

2011 — **M.Tech. Civil engineering. Specialization: Geotechnical engineering**, *Indian Institute of Technology Guwahati(IIT Guwahati)*, Guwahati, India.
CPI:*9.58/10*

2009 — **B.E. Civil Engineering. Elective: Structural engineering**, *The Maharaja Sayajirao University of Baroda*, vadodara, India.
C.GPA:*3.73/4*

2005 — **Class XII (Gujarat State Board)**, *Bright English Medium School*, vadodara, India.
Aggregate percentage :*75.83%*

2003 — **Class X (Gujarat State Board)**, *Bright English Medium School*, vadodara, India.
Aggregate percentage :*83.57%*

Languages

Gujarati	**Native**	*Mother Tongue*
English	**Fluent**	*first language during education*
Hindi	**Fluent**	*second language during education*
German	**Beginner**	*completed A1 course in German*
Dutch	**Beginner**	*completed A1 course in Dutch*

Achievements

- Co-chair of mini symposium MS 2.10.: Challenges in pore scale reactive transport modelling organized as a part of inter pore conference 2015.

- Received scholarship from Belgian nuclear research center (SCK•CEN) to carry out PhD at University of Ghent from period of 15th Nov 2011 till 15th Nov 2015
- Got DAAD scholarship to carry out M Tech. Project at IGTH, university of Hannover, Germany for 9 months duration form 1st Sept. 2010 to 31st May 2011.
- Received fully funded scholarship from Ministry of Human Resource Development India to carry out M Tech. at Indian Institute of Technology Guwahati
- Obtained All India Rank of 390 with 95.46 for General Aptitude test for Engineering (GATE)
- Got merit scholarship from Prof R. H. Shah felicitation committee for ranking 3rd amongst 120 students in third year of B.E.(civil) at MSU Baroda

Research Interests

Geomaterials
- Durability of cementitious materials
- Multiscale/multi-physics modeling of geomaterials
- Soil mechanics (constitutive models for soils)
- Damage/fracture mechanics of cement based materials
- Alternate cement based materials and self healing of cement based materials
- Development of new (multi-functional) building materials
- Material ecology

Numerical methods
- Lattice Boltzmann methods
- Particle based methods
- Cellular automata and its application for solving PDEs
- Finite element methods

Experience

2009
2010

Teaching assistant, *Indian Institute of Technology Guwahati*, Guwahati, India.
Assisted in teaching of soil mechanics laboratory to undergraduate students and conducting courses under Quality Improvement Programme in Environmental Geotechnics.

Journal Publications(3)

2014 Patel, Ravi A., Janez Perko, Diederik Jacques, Geert De Schutter, Klaas Van Breugel, and Guang Ye. "A versatile pore-scale multicomponent reactive transport approach based on lattice Boltzmann method: Application to portlandite dissolution". In: *Physics and Chemistry of the Earth* 70-71, pp. 127–137.

2014 Perko, Janez and Ravi A. Patel. "Diffusion velocity lattice Boltzmann formulation applied to transport in macroscopic porous media". In: *International Journal of Modern Physics C* 25.12, p. 1441006.

2014 Perko, Janez and Ravi A. Patel. "Single-relaxation-time lattice Boltzmann scheme for advection-diffusion problems with large diffusion-coefficient heterogeneities and high-advection transport". In: *Physical Review E* 89.5, p. 053309.

Conference Publications(10)

2014 Patel, Ravi A., Janez Perko, Diederik Jacques, Geert De Schutter, Klaas Van Breugel, and Guang Ye. "Simulating evolution in cement microstructure during chemical degradation". In: *The 10th international PhD symposium in civil engineering.* Quebec, Canada, pp. 173–178.

2014 Patel, Ravi A., Janez Perko, Diederik Jacques, Geert De Schutter, Guang Ye, and K. Van Breugel. "application of porescale reactive transport model to study the influence of pore network characteristics on calcium leaching in cementitious material". In: *CONMOD 2014.* Beijing, China, pp. 359–366.

2013 Jacques, Diederik, Norbert Maes, Perko Janez, Suresh C. Seetharam, Quoc Tri Phung, Ravi A. Patel, Albert Soto, Sanheng Liu, Lian Wang, Geert De Schutter, Guang Ye, and Klaas Van Breugel. "Concrete in engineered barriers for radioactive waste disposal facilities – phenomenological study and assessment of long term performance". In: *Proceedings of the ASME 2013 15th International Conference on Environmental Remediation and Radioactive Waste Management ICEM2013.* Brussels: ASME, pp. 1–10.

2013 Patel, Ravi A., J. Perko, D. Jacques, G. De Schutter, G. Ye, and Klaas V. Breugel. "Lattice Boltzmann based multicomponent reactive transport model coupled with geochemical solver for pore scale simulations". In: *V International Conference on Computational Methods for Coupled Problems in Science and Engineering, COUPLED PROBLEMS 2013.* Ed. by S. Idelsohn, M. Papadrakakis, and B. Schrefler. Ibiza, Spain: CIMNE, Barcelona, pp. 806–817.

2013 Patel, Ravi A., Janez Perko, Diederik Jacques, Geert De Schutter, Guang Ye, and K. Van Breugel. "Application of pore scale modelling approach for long term durability assessment of concrete". In: *Transcend conference,Guildford, UK.* Guildford, UK.

2011 Patel, Ravi A., Martin Achmus, and Baleshwar Singh. "DEM simulations of soil-pile interface under static and cyclic loading". In: *II International Conference on Particle-based Methods – Fundamentals and Applications PARTICLES 2011.* CIMNE, Barcelona, pp. 287–294.

2010 Singh, Baleshwar, Birju Mistri, and Ravi A. Patel. "A reivew of constitutive models and their applications in geotechnical engineering". In: *International conference on earth science an engineering.* hyderabad, India.

2010 Singh, Baleshwar, Birju Mistri, and Ravi A Patel. "A study on pullout capacity of horizontal and inclined plate anchors for offshore Installations". In: *Martec-2010*. Dhaka, Bangladesh.

2010 Singh, Baleshwar, Birju Mistri, and Ravi A. Patel. "Comparision of foundation systems for offshore wind turbine installation". In: *International conference on technological trends*. kerala, India.

2010 Singh, Baleshwar, Birju Mistri, and Ravi A. Patel. "Study on load capacity behavior of plate anchors". In: *International conference on earth science an engineering*. hyderabad, India.

Thesis(1)

2011 Patel, Ravi A. "Behaviour of tension pile under cyclic loading". M Tech. Guwahati, India: Indian Institute of Technology Guwahati (IITG).

Posters and presentations(10)

2014 Patel, Ravi A. *Generalized boundary conditions for advection-diffusion equation in lattice Boltzmann methods*. presentation presented at DSFD 2014, Paris, France.

2014 Patel, Ravi A. and Janez Perko. *Pore scale reactive transport modelling approach: Developments and application to microstructure evolution of cement paste under calcium leaching*. Poster presented at PhD day, October 2014, SCK•CEN, Mol, belgium.

2014 Patel, Ravi A., Janez Perko, Diederik Jacques, Geert De Schutter, Guang Ye, and K. Van Breugel. *A generic Lattice Boltzmann based reactive transport approach for pore scale simulations*. presentation presented at 4th PhD workshop on reactive transport modelling and experiments,May 2014, KIT, karlsruhe,Germany.

2014 Perko, Janez and Ravi A Patel. *A single-relaxation time lattice Boltzmann formulation anisotropic advection-dispersion transport problems*. Poster presented at DSFD 2014, France.

2013 Patel, Ravi A. and Janez Perko. *Approach for modelling chemically induced changes in hardened cement microstructure*. presentation presented at PhD day, October 2013, SCK•CEN, Mol, belgium.

2013   Patel, Ravi A., Janez Perko, Diederik Jacques, Geert De Schutter, Guang Ye, and K. Van Breugel. *Modelling approach to evaluate changes in hardened cement paste microstructure under influence of aggressive pore water*. presentation presented at 3rd international workshop on mechanisims and modelling of waste/cement interactions, May 2013, Ghent, Belgium.

2013   Patel, Ravi A., Janez Perko, Diederik Jacques, Geert De Schutter, Guang Ye, and K. Van Breugel. *Serendipitous encounters with lattice Boltzmann advective-diffusive-reactive transport model*. presentation presented at ICMMES 2013, July 2013, Oxford, UK.

2013   Phung, Quoc Tri, Ravi A. Patel, Albert Soto, Suresh Seetharam, Norbert Maes, Janez Perko, Diederik Jacques, Guang Ye, K. Van Breugel, and Geert De Schutter. *long term degradation processes on concrete: An overview*. poster presented at Ageing center launch event, Delft, Netherlands.

2012   Patel, Ravi A. and Janez Perko. *Microstructural modelling of hardened cement pastefor long-term durability assessment*. Poster presented at PhD day, October 2012, SCK•CEN, Mol, belgium.

2012   Patel, Ravi A., Janez Perko, Diederik Jacques, Geert De Schutter, Guang Ye, and K. Van Breugel. *SCK•CEN concrete durability project*. presentation presented at 23rd NIST computer modelling workshop, July 2012, gaithersburg , MD, USA.